

Synthesis of functionalized graphene and its strengthening effect in aluminum metal matrix nanocomposite

BY

Rachit Ranjan

(Admission No: 17DR000316)



THESIS

SUBMITTED TO

**INDIAN INSTITUTE OF TECHNOLOGY
(INDIAN SCHOOL OF MINES) DHANBAD**

For the award of the degree of

DOCTOR OF PHILOSOPHY

MAY, 2022



CERTIFICATE FOR CLASSIFIED DATA
(To be submitted at the time of Thesis Submission)

This is to certify that the thesis entitled “ **Synthesis of functionalized graphene and its strengthening effect in aluminium metal matrix nanocomposite** ” being submitted to the Indian Institute of Technology (Indian School of Mines), Dhanbad by **Mr Rachit Ranjan** for award of Doctor of Philosophy (Ph.D) Degree in **Mechanical Engineering** does not contains any classified information. This work is original and yet not been submitted to any institution or university for the award of any degree.

Virek Bhardwaj

Signature of Supervisor (s)

Rachit Ranjan
25/05/2022

Signature of Scholar



CERTIFICATE REGARDING ENGLISH CHECKING
(To be submitted at the time of Thesis Submission)

This is to certify that the thesis entitled “**Synthesis of functionalized graphene and its strengthening effect in aluminium metal matrix nanocomposite**” being submitted to the Indian Institute of Technology (Indian School of Mines), Dhanbad by **Mr Rachit Ranjan**, Admission No **17DR000316** , for the award of Doctor of Philosophy (Ph.D.) Degree has been thoroughly checked for quality of English and logical sequencing of topics.

It is hereby certified that the standard of English is good and that grammar and typos have been thoroughly checked.

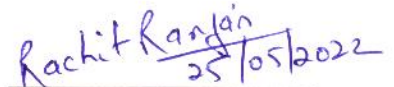
It is now worthy for evaluation by the panel of examiners.

 25.5.22

Signature of Supervisor (s)

Name: Vivek Bajpai

Date: 25/05/2022

 25/05/2022

Signature of Scholar

Name: Rachit Ranjan

Date: 25/05/2022



CERTIFICATE FROM THE SUPERVISOR(S)
(To be submitted at the time of Thesis Submission)

This is to certify that the thesis entitled “**Synthesis of functionalized graphene and its strengthening effect in aluminium metal matrix nanocomposite**” being submitted to the Indian Institute of Technology (Indian School of Mines), Dhanbad by **Mr Rachit Ranjan**, Admission No **17DR000316**, for the award of Doctor of Philosophy (Ph.D.) Degree is a bonafide work carried out by him/her, in the **Department of Mechanical Engineering**, IIT (ISM), Dhanbad, under my supervision and guidance. The thesis has fulfilled all the requirements as per the regulations of this Institute and, in my/our opinion, has reached the standard needed for submission. The results embodied in this thesis have not been submitted to any other university or institute for the award of any degree or diploma.

A handwritten signature in blue ink, appearing to read 'Vivek Bajpai', is written over a horizontal line.

Signature of Supervisor (s)

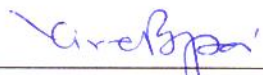
Name: Vivek Bajpai


Date: 25/05/2022



CERTIFICATE FOR FINAL VERSION OF THESIS
(To be submitted after Final Viva-Voce Examination)

This is to certify that the soft copy of thesis entitled “**Synthesis of functionalized graphene and its strengthening effect in aluminum metal matrix nanocomposite**” submitted by **Mr Rachit Ranjan** for award of Doctor of Philosophy (Ph.D.) Degree in **Mechanical Engineering** incorporates all corrections/modifications including those suggested during viva-voce.


Signature of Supervisor (s)


Signature of Scholar

Name: VIVEK BAJPAI

Name: RACHIT RANJAN

Date: 25.5.22

Date: 25/05/2022



COPYRIGHT AND CONSENT FORM
(To be submitted at the time of Thesis Submission)

To ensure uniformity of treatment among all contributors, other forms may not be substituted for this form, nor may any wording of the form be changed. This form is intended for original material submitted to the IIT (ISM), Dhanbad and must accompany any such material in order to be published by the ISM. Please read the form carefully and keep a copy for your files.

TITLE OF THESIS: SYNTHESIS OF FUNCTIONALIZED GRAPHENE AND ITS STRENGTHENING EFFECT IN ALUMINIUM METAL MATRIX NANOCOMPOSITE.

AUTHOR'S NAME & ADDRESS: RACHIT RANJAN

**DEPARTMENT OF MECHANICAL ENGINEERING,
INDIAN INSTITUTE OF TECHNOLOGY (INDIAN SCHOOL
OF MINES), DHANBAD-826004, JHARKHAND, INDIA**

COPYRIGHT TRANSFER

1. The undersigned hereby assigns to Indian Institute of Technology (Indian School of Mines), Dhanbad all rights under copyright that may exist in and to: (a) the above Work, including any revised or expanded derivative works submitted to the ISM by the undersigned based on the work; and (b) any associated written or multimedia components or other enhancements accompanying the work.

CONSENT AND RELEASE

2. In the event the undersigned makes a presentation based upon the work at a conference hosted or sponsored in whole or in part by the IIT (ISM) Dhanbad, the undersigned, in consideration for his/her participation in the conference, hereby grants the ISM the unlimited, worldwide, irrevocable permission to use, distribute, publish, license, exhibit, record, digitize, broadcast, reproduce and archive; in any format or medium, whether now known or hereafter developed: (a) his/her presentation and comments at the conference; (b) any written materials or multimedia files used in connection with his/her presentation; and (c) any recorded interviews of him/her (collectively, the "Presentation"). The permission granted includes the transcription and reproduction of the Presentation for inclusion in products sold or distributed by IIT(ISM) Dhanbad and live or recorded broadcast of the Presentation during or after the conference.
3. In connection with the permission granted in Section 2, the undersigned hereby grants IIT (ISM) Dhanbad the unlimited, worldwide, irrevocable right to use his/her name, picture, likeness, voice and biographical information as part of the advertisement, distribution and sale of products incorporating the Work or Presentation, and releases IIT (ISM) Dhanbad from any claim based on right of privacy or publicity.
4. The undersigned hereby warrants that the Work and Presentation (collectively, the "Materials") are original and that he/she is the author of the Materials. To the extent the Materials incorporate text passages, figures, data or other material from the works of others, the undersigned has obtained any necessary permissions. Where necessary, the undersigned has obtained all third party permissions and consents to grant the license above and has provided copies of such permissions and consents to IIT (ISM) Dhanbad.

GENERAL TERMS

- * The undersigned represents that he/she has the power and authority to make and execute this assignment.
- * The undersigned agrees to indemnify and hold harmless the IIT (ISM) Dhanbad from any damage or expense that may arise in the event of a breach of any of the warranties set forth above.
- * In the event the above work is not accepted and published by the IIT (ISM) Dhanbad or is withdrawn by the author(s) before acceptance by the IIT(ISM) Dhanbad, the foregoing copyright transfer shall become null and void and all materials embodying the Work submitted to the IIT(ISM) Dhanbad will be destroyed.
- * For jointly authored Works, all joint authors should sign, or one of the authors should sign as authorized agent for the others.

Rachit Ranjan

Signature of the Author

The Dedication

Lord Krishna: *For his countless blessings, strength, Knowledge and above all, his faithfulness and love from the beginning of my academic life*

*My father and mother: **Anil Kumar Sinha** and **Rina Sinha***

&

Prof. Vivek Bajpai: *For his blessings and supervision*

ACKNOWLEDGEMENTS

*The completion of this study could not have been possible without the expertise and guidance of **Prof. Vivek Bajpai**, our beloved dissertation advisor. I take this opportunity to express my deep sense of gratitude towards my guides and mentors for their kind support, cooperation and constant guidance during my Ph.D. work. I enjoyed the excellence in research, freedom and love they have given to me. I want to express my sincere thanks to the Director of Indian Institute of Technology (ISM) Dhanbad, India, **Prof. Rajeev Shekhar**, for providing the necessary research facility at the institute.*

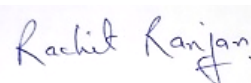
*I would also like to thank **Prof. Amit Rai Dixit**, **Prof. Randip Kumar Das** and **Prof. Rahul MR** for sitting on our panel and taking the time to read our thesis. I would like to thank **Prof. Amit Rai Dixit** over and over again for his support, love and guidance throughout my master's and Ph.D. I would also like to thank **Prof. Rashmi Ranjan Das** for sitting on our panel and taking the time to evaluate my progress during Ph.D. A debt of gratitude is also owed to **Prof. Nirmal Kumar Singh**, former in-charge of the central workshop, **Alok Kumar Das**, present in charge of the central workshop and **Prof. K. K. Singh** and **Prof. K Priya Ajit**, who stands with the scholars to provide all the research facilities needed to complete this research work for their endless love, support, and guidance. I would also like to thank **Prof. G.C. Nayak**, Associate Professor, Department of Chemistry, for extending their cooperation in order to complete the research work.*

I am thankful to my senior, Dr Md. Alamgir and Dr Amit Kumar to support the experimental activities for my thesis work at IIT (ISM) Dhanbad. I extend my gratitude to my batchmates Dr Mohan, Dr Kamlesh, Mr Harish, Mr Deepak, Mr Vikas, Mr Sachindra, Mr Surja, and Mr Mahesh. I want to extend my gratitude and love to my friends and juniors Ankit, Shashank, Ravi Shankar, Chitransh, Arnab, Vivek, Ratnesh, Anubhav and Nitesh for helping hand always during this period. The services and help of the staff of the central workshop are remarkable and must be acknowledged to Ashish sir, Murmu sir, Mr Shakil, Mr Ganesh, and Mr Sarfaraj.

Finally, I have no words to express my greatest gratitude towards my mother, Rina Sinha, my bother Amit Ranjan, my sister Priya Rangoli, My brother-in-law Santosh Kumar Sinha; without their love, support, respect, and care, it is not possible to complete this journey. Most of all, I would like to thank GOD the Almighty for giving me the strength to remain on the path of success, At last, a note of appreciation is extended to all those who helped in one way or the other during this research.

Date: 24-05-2022

Place: Dhanbad



Rachit Ranjan

Abstract

Graphene has a wide range of applications in electronics, electrical, engineering and sensor manufacturing industries and has also increased the mechanical performance of composite material. However, achieving proper interfacial bonding between graphene as reinforcement and matrix-like aluminum is a challenging task. Lower wettability and reaction product formation at the site of active carbon atoms makes the task difficult to achieve desired properties from graphene reinforced composites. Functionalized graphene, such as graphene oxide (GO) and reduced graphene oxide (rGO), has improved wettability and lowered the risk of aluminum carbide formation, resulting in a composite having higher strength than that of pure graphene reinforced composites. However, despite the improved performance of functionalized graphene (in this example, GO and rGO), there remains a scarcity of literature on the subject. As a result, the research focuses on synthesising and characterising functionalized graphene and analysing its effectiveness in strengthening aluminum metal matrix composite material.

Nitrogen-doped graphene, sulphur doped, and antimony doped graphene were synthesized via the ball milling technique. Melamine, sulphur and antimony to be used as a source of doping material were mixed with graphite in definite proportion and milled for 72 hours at 300 rpm to get nitrogen, sulphur and antimony doped graphene, respectively. Functionalized graphene is characterised by XPS, XRD, HRTEM, FESEM and RAMAN spectroscopic analytical techniques. The characterization of composite has revealed that graphene synthesized is multi-layered graphene having 6 to 10 layer thickness and has a flakier structure. Raman spectroscopy has shown that nitrogen-doped graphene has large D-band peaks, illustrating higher disorder in graphitic structure. In contrast, sulphur and antimony doped graphene have a lower I_D/I_G ratio. XPS and EDX spectrum of sulphur doped graphene have shown the presence of nitrogen and sulphur, illustrating that nitrogen may have been absorbed from the environment, creating sulphur-nitrogen co-doped graphene (S-NDG).

NDG/Al, S-NDG/Al and ADG/Al composite were synthesized by mixing 0.05, 0.1, 0.2 and 0.5 wt.% of reinforcement in aluminium matrix via powder metallurgy technique. The powder was cold compacted at 450 MPa, sintered at 600° C under an argon gas environment and extruded at 350° C to get a 10 mm diameter cylindrical specimen. After

the detailed experimental characterization of sulfur, nitrogen, and antimony doped graphene, sulfur doping improved wettability while increasing strength by 118.81%. Nitrogen and antimony doping have increased strength by 124.05% and 134.37%, respectively, compared to pure aluminum samples. Doped graphene also possesses lubricating capabilities, which has increased wear performance by 71% with just 0.5 wt.% NDG.

Table of Contents

CHAPTER 1: Introduction	1
1.1. Composites	1
1.2. A brief introduction to different carbonaceous reinforcement	3
1.2.1. Carbon nanotubes	3
1.2.2. Woven carbon fibres	5
1.2.3. Graphene nanoplatelets	6
1.3. Introduction to graphene-based MMC.....	8
1.4. Applications	9
1.4.1. Overview of applications of GNP/metal matrix composites.....	9
1.4.2. Application of graphene.....	10
1.5. Problem definition.....	14
1.6. Aim of existing project	15
1.7. Organization of the report.....	16
CHAPTER 2: Literature review	18
2.1. Graphene: Preparation, processing and dispersion techniques.....	18
2.1.1. Preparation methods	19
2.1.2. Processing techniques	27
2.1.3. Recent dispersion methods and challenges	37
2.2. Functionalization by ball milling technique	40
2.3. Graphene reinforced composites.....	41
2.3.1. Graphene reinforced aluminum matrix composites.....	41
2.3.2. Graphene reinforced magnesium matrix composite	45
2.3.3. Graphene reinforced iron matrix composites	48
2.3.4. Graphene in copper matrix composites.....	48
2.3.5. Other graphene metal matrix composites	52
2.4. Strengthening methods in metal matrix composites	52

2.4.1. Load transfer mechanism.....	55
2.4.2. Orowan strengthening.....	56
2.4.3. Thermal mismatch	57
2.4.4. Hall-Petch strengthening mechanism	57
2.5. The conclusion from the literature survey	58
2.5.1. Current issues:.....	58
2.5.2. Scope.....	58
2.6. Objectives.....	59
CHAPTER 3: Analytical approach for high energy milling process	60
3.1. Introduction	60
3.2. Motivation and approach.....	60
3.3. Mathematical formulations.....	61
3.4. Mathematical calculation: The energy supplied during ball milling.....	63
3.4.1. Kinetic energy transfer from a collision of similar balls and dissimilar balls.....	64
3.5. Experimental characterization of zirconium balls.....	66
3.6. Conclusion	67
CHAPTER 4: Synthesis of nitrogen-doped graphene and its strengthening effect on aluminum metal matrix composite.....	68
4.1. Introduction	68
4.2. Motivation, objective and approach	68
4.3. Experimental Methods.....	70
4.3.1. Material selection	70
4.3.2. Synthesis of Nitrogen-Doped graphene (NDG).....	70
4.3.3. Synthesis of NDG reinforced metal matrix composite material.....	70
4.4. Results and discussion	70
4.4.1. Physico-chemical characterization of N-doped graphene	71
4.4.2. Mechanical Properties	78

4.4.3. Characterization of composite material	82
4.5. Conclusion	85
CHAPTER 5: Synthesis of ball-milled edge-functionalized sulfur-nitrogen co-doped graphene: their influence on aluminum metal matrix composite	86
5.1. Introduction	86
5.2. Motivation, objective and approach	86
5.3. Experimental	88
5.3.1. Material Selection.....	88
5.3.2. Preparation of Sulfur-doped graphene	88
5.3.3. Preparation of metal matrix composite material.....	88
5.4. Result and discussion	89
5.4.1. Physicochemical characterization of sulfur-doped graphene.....	90
5.4.2. Mechanical Characterization of Al/S-NDG composite.....	95
5.5. Conclusion	98
CHAPTER 6: Synthesis of ball-milled edge-functionalized Antimony-doped graphene and its influence on aluminum metal matrix composite.....	100
6.1. Introduction	100
6.2. Motivation, objective and approach	100
6.3. Experimental Methods.....	101
6.3.1. Material	101
6.3.2. Preparation of functionalized Graphene	102
6.3.3. Preparation of ADG reinforced metal matrix composite	103
6.4. Result and discussion	104
6.4.1. Characterization of synthesized ADG	104
6.4.2. Mechanical characterization of Al/ADG composites	109
6.4.3. Morphological analysis of composite material	110
6.5. Conclusion	112

CHAPTER 7: Conclusion and Future Scope	114
7.1. Key conclusions:	114
7.1.1. Analytical approach to the high energy milling process	114
7.1.2. Characterization of NDG and its effect on aluminum matrix composite.....	115
7.1.3. Characterization of S-NDG and its effect in aluminum matrix composite.....	116
7.1.4. Characterization of ADG and its effect in aluminum matrix composite	117
7.2. Contributions.....	118
7.3. Future Scope	118

List of Figures

Figure 1-1: Classification of composites.	2
Figure 1-2: Percentage of aircraft mass built by composites material.....	2
Figure 1-3: Overview of the synthesis of metal matrix nanocomposites.....	3
Figure 1-4: (a) Single, double and multiwall CNT, (b) Number of publications on Carbon nanotube (CNT) since 2009 (Source: web of knowledge).....	5
Figure 1-5: (a) Liquid infiltration squeeze casting (b) Laminate squeeze casting.	7
Figure 1-6: (a) Graphene nanosheet, (b) The number of publications in graphene-based composites since the year 2009 (source: web of knowledge).....	8
Figure 1-7: Number of publications on graphene-based MMC at various fields (2009-2019, source: web of knowledge).....	9
Figure 1-8: Task list.....	16
Figure 2-1: Synthesis of graphene by different techniques.	18
Figure 2-2: Acoustic representation of shock wave formation and different dominant inside the bubble ^{125,126}	20
Figure 2-3: a) Graphene exfoliated in isopropyl alcohol and water solution and b) Graphene exfoliated in pure water solution ¹³⁵	22
Figure 2-4: Diagram of Low-pressure CVD system for graphene synthesis ¹⁴⁶	23
Figure 2-5: (a) Chemical structure of graphene oxide (b) Chemical structure of reduced graphene oxide ¹⁵⁷	25
Figure 2-6: (a) The non-wetting condition of liquid Al-droplet on the graphite surface, and (b) Schematic diagram of a liquid metal droplet onto the solid surface ²⁰⁵	29
Figure 2-7: Schematic diagram of spark plasma sintering machine ²¹¹	30
Figure 2-8: (a) Dimension of container used for consolidation, (b) & (c) sample before and after rolling process, (d) SEM image of the sample after rolling showing Al/Al and Al/GNP interface ²²³	33
Figure 2-9: (a) HRTEM image of synthesized composites, and (b) Stress-strain diagram for composites milled for 90 min and 30 min, respectively ²²⁶	35
Figure 2-10: (a) Schematic of MMNC fabricated by FSP using GO/Water colloid ²²⁸	36
Figure 2-11: (a) Schematic showing the area affected by FSP pin, and(b) Top-view for the prepared composite sample ²²⁹	37
Figure 2-12: (a) Schematic representation of S-GNP's preparation, (b) & (c) The deposition of ~10 nm sulfur particles/amorphous sulfur into the GNP multi-layered structure ²⁵⁷	42
Figure 2-13: (a) Wear loss, and (b) Coefficient of friction as load function ²⁷⁹	45

Figure 2-14: Ambient temperature tensile test for Mg-matrix composites at various reinforcement concentrations ^{283,284}	46
Figure 2-15: Graphical representation for GNP/Cu composites.....	50
Figure 2-16: (a) HRTEM image of graphene Cu composites and (b) Yield and tensile strength of graphene/Cu composites versus graphene derived volume fraction ^{284,314}	50
Figure 2-17: (a) & (b) HRTEM micrographs of the 1% HRDSR Cu composite showing nano-sized MLG particles in grain interiors (c) & (d) TEM micrographs of the 1% ESR Cu composites ²³	54
Figure 3-1: Schematic representation of milling balls during the ball milling process.....	64
Figure 3-2: Graphical representation of total energy transferred using three different types of ball.....	65
Figure 3-3: (a) Crack propagation in 4.46 mm ball and (b) Fracture surface of the ball.....	66
Figure 4-1: Nitrogen-doped graphene by solid-state ball-milling of graphite with melamine.....	71
Figure 4-2: FESEM image for, (a) Graphite powder before milling, (b) & (c) N-doped graphene at different magnification.....	72
Figure 4-3: Particle size distribution for 48h and 72h-milled sample.....	72
Figure 4-4: HRTEM image of N-doped graphene at (a) Lower magnification, (b) & (c) Higher magnification illustrating the number of layers of graphene and edge defects.....	74
Figure 4-5: SAED diffraction of NDG.....	75
Figure 4-6: XPS survey scan for NDG.....	75
Figure 4-7: XPS high-resolution spectra of Nitrogen, (a) Carbon and (b) Oxygen.....	76
Figure 4-8: XRD of nitrogen-doped graphene milled for 24h, 48h and 72h, respectively.....	76
Figure 4-9: Raman spectroscopy of nitrogen-doped graphene milled for 24h, 48h and 72h, respectively.....	77
Figure 4-10: (a) Tensile strength for pure Al, 0.05, 0.1, 0.2, 0.5 wt. % of NDG and 0.5 wt.% GNP and (b) Compressive stress-strain curve for NDG/Al composite.....	80
Figure 4-11: Mechanical properties of composites post, (a) Tensile and (b) Compressive test..	81
Figure 4-12: (a) Coefficient of friction (COF) and (b) Wear rate of NDG/Al composite material having different NDG concentrations.....	82
Figure 4-13: FESEM image of fractured surface after tensile test having NDG concentration of (a) 0.1 wt.% , (b) 0.2wt.% , (c) 0.5 wt.% respectively.....	83
Figure 4-14: EDX image of the Al/NDG composite material.....	84
Figure 4-15: XRD of Al/NDG metal matrix composite showing peaks for ALN and Al ₂ O ₃	85
Figure 5-1: Schematic diagram for the synthesis of sulfur-nitrogen co-doped graphene.....	89

Figure 5-2: FESEM image of sulfur-nitrogen co-doped graphene (a) Milled for 72h, (b) sulfur nanoparticles deposited on all over the graphene sheet, (c) Fractured graphite surface after 24h milling.....	91
Figure 5-3: EDAX spectrum of sulfur-nitrogen co-doped graphene showing S, C, O and N peaks.	91
Figure 5-4: XPS high-resolution XPS survey scan of S-NDG.....	92
Figure 5-5: : High-resolution XPS spectra of sulfur-nitrogen co-doped graphene (SDG) (a) XPS high-resolution spectra of C 1s, (b) N 1s and (c) S 2p.....	93
Figure 5-6: HRTEM image of sulfur-nitrogen co-doped graphene of (a) lower magnification (b) Higher magnification image with SAED diffraction.....	93
Figure 5-7: (a) STEM image at lower magnification with, (b) TEM surface mapping of oxygen, (c) Carbon and (d) Sulfur.....	94
Figure 5-8: Raman spectroscopy of pure graphite and S-NDG milled for 24h and 72 hours.....	95
Figure 5-9: Stress-strain graphs of the composite after (a) Tensile test and (b) Compressive test.	97
Figure 5-10: FESEM image after tensile fractured.....	98
Figure 5-11: EDX spectrum of S-NDG fractured surface	98
Figure 6-1: Schematics for the mechanochemical synthesis of antimony doped graphene.	103
Figure 6-2: Tensile and compressive test specimen.....	104
Figure 6-3: FESEM image of; (a) ADG shown average particle size, and (b) Particle under higher magnification.	105
Figure 6-4: HRTEM image showing (a) Exfoliated ADG particle and (b) High magnification image of ADG.....	106
Figure 6-5: XPS high-resolution survey scan for ADG.....	107
Figure 6-6: XPS high-resolution spectrum for (a) Carbon and (b) Antimony (Sb).	108
Figure 6-7: Raman spectroscopy of ADG.....	109
Figure 6-8: Stress-strain curve for (a) Tensile test and (b) Compressive test.	110
Figure 6-9: FESEM image after tensile fracture for 0.5 wt. % composite material.....	111
Figure 6-10: (a) Surface morphology of 0.5 wt. % ADG/Al composite and (b) Corresponding EDAX.....	112

List of Tables

Table 1-1: Overview for applications of GNP/Metal matrix composites. ^{14,22,59-61,25,52-58}	10
Table 2-1: List of reagent used for GO reduction ^{161,162,171-177,163-170,178-186,187,188,197,198,189-196}	26
Table 2-2: Overview of graphene reinforced aluminum matrix composites ^{42,46,268-273,47,54,238,263-267}	43
Table 2-3: Overview of graphene reinforced magnesium matrix composites ^{54,283,293-300,285-292} ...	47
Table 2-4: An overview of graphene reinforced iron-oxide matrix composites. ^{303,309-313}	49
Table 2-5: Overview of graphene reinforced Copper matrix composites ^{53,235,322,323,314-321}	51
Table 2-6: Strengthening mechanism and its governing equation for MMC strength evaluation ^{54,265,351-354,296,314,345-350}	55
Table 3-1: Summarized input parameters to calculate the total energy	64

Nomenclature

GO	Graphene oxide
rGO	Reduced graphene oxide
GNP	Graphene nano platelets
FLG	Few layer graphene
CNT	Carbon nanotube
MWCNT	Multiple wall carbon nanotube
GMMNC	Graphene metal matrix nanocomposites
UHMWPE	Ultra-high molecular weight polyethylene
Al	Aluminium
CF	Carbon fibre
WCF	Woven carbon fibre
Al ₄ C ₃	Aluminium carbide
Al ₂ O ₃	Aluminium oxide
Al	Aluminium
Cu	Copper
Mg	Magnesium
Au	Gold
Ag	Silver
S	Sulphur
Sb	Antimony
N	Nitrogen
ZnO	Zinc oxide
Fe ₃ O ₄	Iron oxide
WC	Tungsten carbide
NaCl	Sodium chloride
FET	Field effect transistors
MEGO	Microwave exfoliated graphene oxide
NEMS	Nano electromechanical systems
DLC	Diamond-like carbon
COF	Coefficient of friction
CVD	Chemical vapour deposition
NDG	Nitrogen-doped graphene
S-NDG	Sulphur nitrogen co-doped graphene
ADG	Antimony doped graphene
LPE	Liquid phase exfoliation
GrF	Graphite fluoride
CHx	Carbon-free radicals
XPS	X-ray photoelectron spectroscopy
SPS	Spark plasma sintering
HIP	Hot isostatic pressing
OHVF	High-velocity spray forming
FSP	Friction stir processing
C-C	Carbon-carbon
ECG	Edge-carboxylate graphite
LSB	Lithium-sulphur batteries
SiC	Silicon carbide
GRP	Glassfiber reinforced plastics

GND	Geometrically necessary dislocations
CTE	Coefficient of thermal expansion
k	Thermal conductivity
γ_{sv}	Surface tension of solid-vapour
γ_{sl}	Surface tension of solid-liquid
Γ_{lv}	Surface tension of liquid-vapour
σ_{yc}	Yield strength in nanocomposites
σ_{yc}	Yield strength in matrix
E_c	Young's modulus
γ_m	Poisson ratio
A	Volume fraction
S	Aspect ratio
μ	Modulus of rigidity
m_b	Average mass of grinding balls
V_b	Velocity of the balls
ω_p	Angular velocity of balls
ω_{jar}	Angular velocity of jar
d_b	Average diameter of grinding balls
R_p and R_{jar}	Radius of ball mill plate and inside radius of jar
K_a	Energy release ratio in collision of wet ball milling
E_b	Total energy dissipated per ball
N_b	Number of balls
E_{total}	Total energy transferred
XRD	X-ray powder diffraction
FESEM	Field emission scanning electron microscopy
HRTEM	High-resolution transmission electron microscopy
EDX	Energy Dispersive X-Ray Spectroscopy
JCPD	Joint Committee on Powder Diffraction Standards
TPa	Terapascal
GPa	Gigapascal
MPa	Megapascal

CHAPTER 1: Introduction

1.1. Composites

Composites are the macro or nano-physical amalgamation of distinct materials to achieve superior material. Hence, the knowledge of the distinct materials is, therefore very much required to fabricate the composites material. This material exhibits two or more phases in which one acts as a primary load carrying component. The softer phase matrix has specific mechanical and physical properties, whereas stronger reinforcement carries the principal amount of load applied to the material. Composites may be classified into various types, depending on the reinforcement and matrix material used, as illustrated in Figure 1-1. Matrix and the reinforcements together decide the performance of the composite, which is further dependent upon the morphology, particle interface, bonding between the materials and distribution of the reinforcement¹. The advantages of the composites material, which may be micro, nano, polymer or metal matrix composites, are their high strength, lightweight and improved mechanical or electronic properties. For instance, Boeing 787 (Dreamliner family) used the maximum amount of composites material in their prime structure and airframe than any other commercial aeroplane. So, the structure offered 20% savings in weight compared to the conventional design². Apart from the use of composites in the secondary structure of the aeroplane, the use of composite material in the primary structural frames such as wings has drastically increased. The scatter plot in Figure 1-2 shows the percentage use of the composite material in various aircraft on a time scale. The graph shows that with increasing time, the use of composite has increased on fighter planes and commercial aircrafts³⁻⁶.

In today's era, materials play an important role in emerging technologies for their unique and better performances, such as biomedical implants, new sensitive and miniaturized sensors, electronics for making diodes or solar cells, aerospace industries, etc. So, composite materials have better properties than the parent material and are better options as they have enhanced properties which can be further increased as per the need.

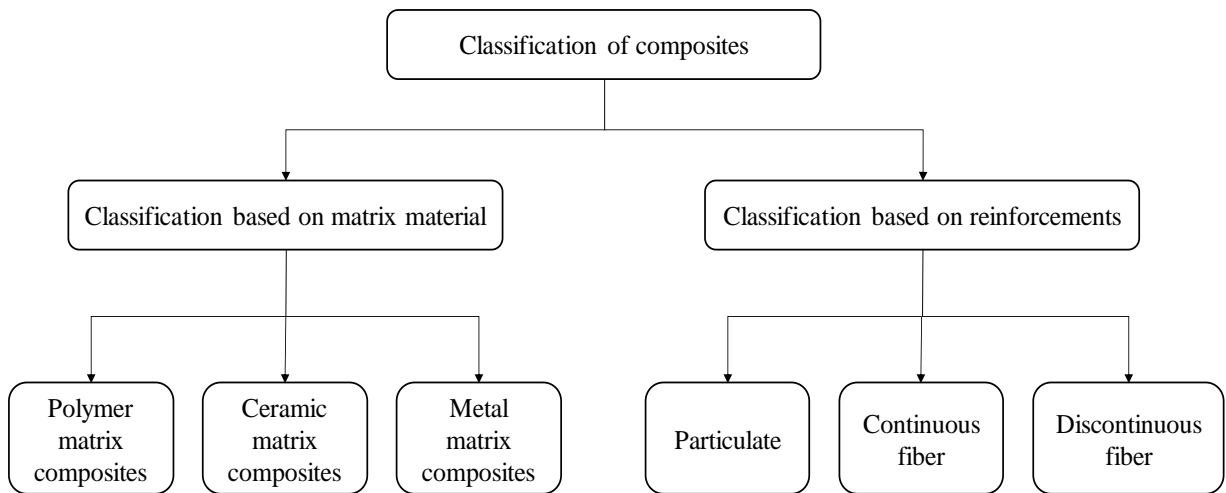


Figure 1-1: Classification of composites.

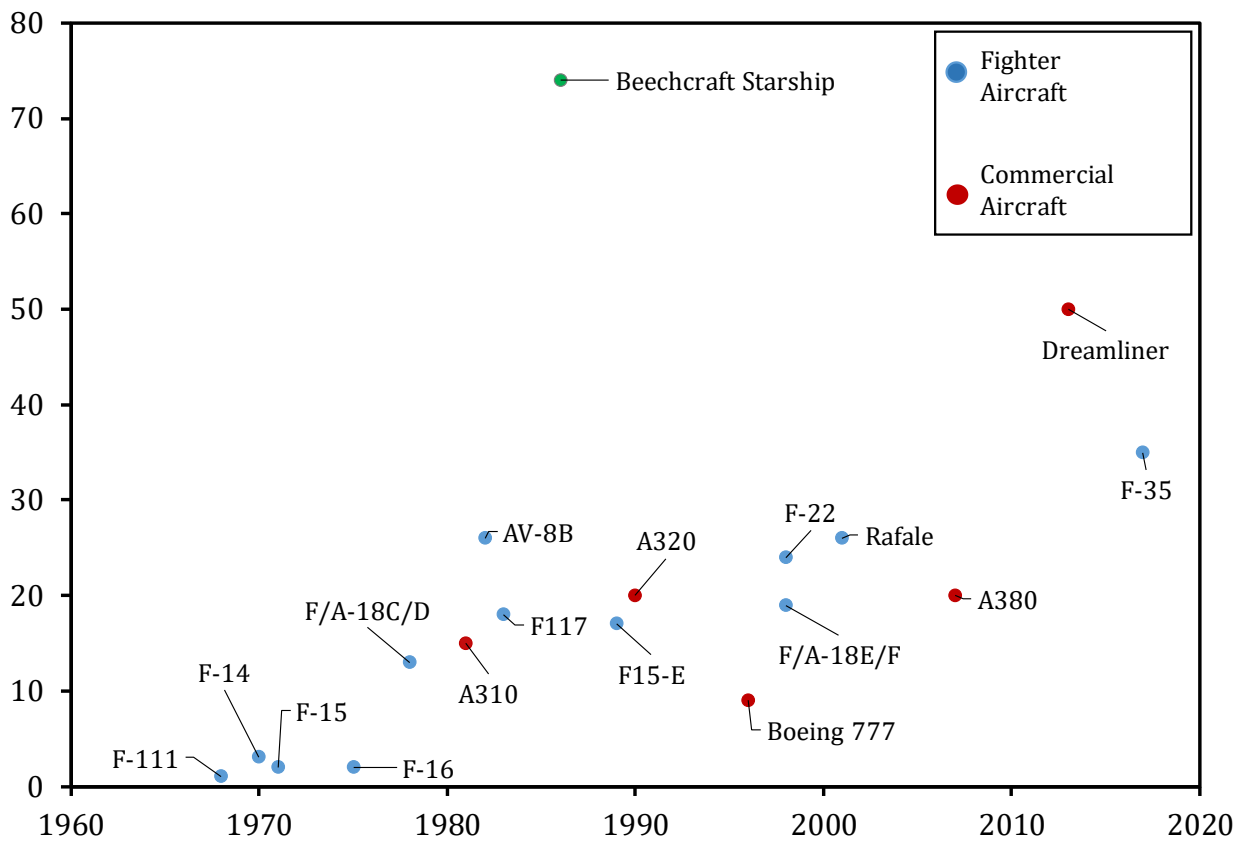


Figure 1-2: Percentage of aircraft mass built by composites material.

For a reinforcing material, the following key properties greatly influence the role of nanoparticles in the metal matrix composites such as:

- Reinforcements must have good properties (mechanical, thermal or electrical)
- It must have a high surface area and aspect ratio.
- It must be strongly bonded to matrix material after inclusions.

- It must be homogeneously dispersed within matrix material and should not agglomerate.
- It should be economical.

Composite material utilizing reinforcements such as graphene, carbon nanotube (CNT), and carbon fibres have extraordinary properties and are of great use, attracting researchers worldwide. Graphene metal matrix nanocomposites (GMMNC) could be a favourable candidate for the next generation of nanocomposites. However, the greatest challenge in developing graphene-based composites is to fabricate material having graphene dispersed with undamaged intrinsic structures. Figure 1-3, sums up the process involved in synthesising metal matrix nanocomposites.

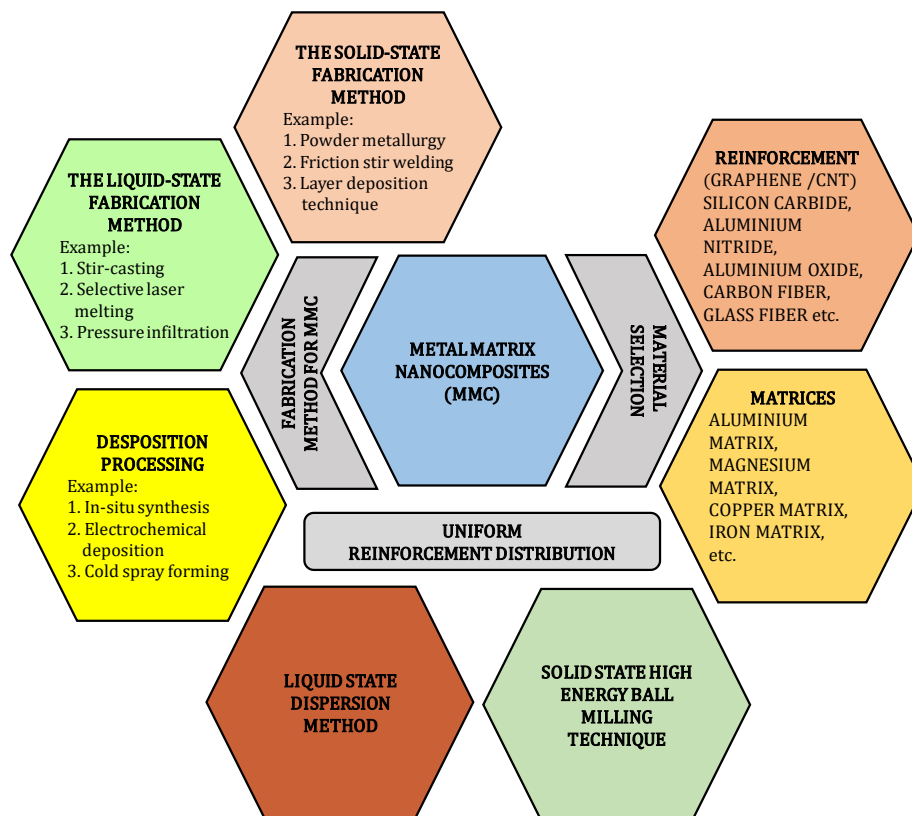


Figure 1-3: Overview of the synthesis of metal matrix nanocomposites.

1.2. A brief introduction to different carbonaceous reinforcement

1.2.1. Carbon nanotubes

In 1991, Iijima⁷ discovered carbon nanotubes (CNT). Figure 1-4 (a) shows the structure of CNT, which consists of rolled cylindrical graphite sheets (graphene) having a diameter of the order of a nanometre. Figure 4 (b) shows the total number of publications on CNT published yearly. The material has attracted great interest in research due to its

exceptional properties and ability to develop an essential class of new material used in engineering applications. The superior lubricating nature of CNT can be used as self-lubricating composites. The properties can increase efficiency, reliability, comfort of operation and safety of vehicles⁸. The composite material was based on ultra-high molecular weight polyethylene (UHMWPE), which was reinforced with multiple wall carbon nanotube (MWCNT). It was observed that with the addition of 1% of MWCNT, the ultimate strength has increased up to 4 times and yield strength by 40% in comparison with neat UHMWPE⁹. The properties attained were due to the matrix's significant load transferability to the nanotubes, and the uni-axial alignment of nanotubes in the direction of load applied. However, the difficulty in the preparation of CNT-based composites is the same as that of GNP's based composites.

Bakshi et al.¹⁰ investigated the mechanical and wear properties of CNT reinforced Al-Si composite coatings. Nanoindentation studies showed an increase in elastic modulus by 19% and 39% and yield strength by 17.5% and 27% with 5 wt. % and 10 w.% CNT. The fabrication of carbon nanotube/aluminium (CNT/Al) composites follows two steps. The first step is for the dispersion of CNT into the metal matrix for uniform distribution of the reinforcement, which can be attained by high energy ball milling^{11,12}, in-situ growth method¹³, friction stirring^{14,15} and solution coating⁹. The second step is to consolidate pre-mixed powder into bulk material which may be done by drop-casting¹⁶, spraying^{17,18}, liquid pressing¹⁹, sintering²⁰, forging and extrusion²¹. In an experiment with CNT having a concentration ranging from 0% to 6%, it was observed that composites with 2 wt. % of CNT gives higher yield and tensile strength than other concentrations²². The decrease in strength with high CNT content was because of the increase in the agglomeration of CNT, which starts functioning as a defect. Kim et al.²³ investigated the effect of milling time on the structure of CNT particles. The results have shown that as the milling time was increased to one hour, the length of CNT shortens to 1.2 microns from 5 microns. The problem of agglomeration of reinforcements was solved by a 3 D hybrid structure formed by a bridge of adjacent graphene nano platelets (GNP) with long flexible CNT, thus resulting in an increased contact area. Jiang et al.²⁴ used the flake powder method to fabricate Al/CNT composite. The method replaces spherical powder with its nanoflakes which were surface modified by polyvinyl alcohol hydrosol. The method achieved high CNT compatibility with aluminium particles, forming strong ductile composites.

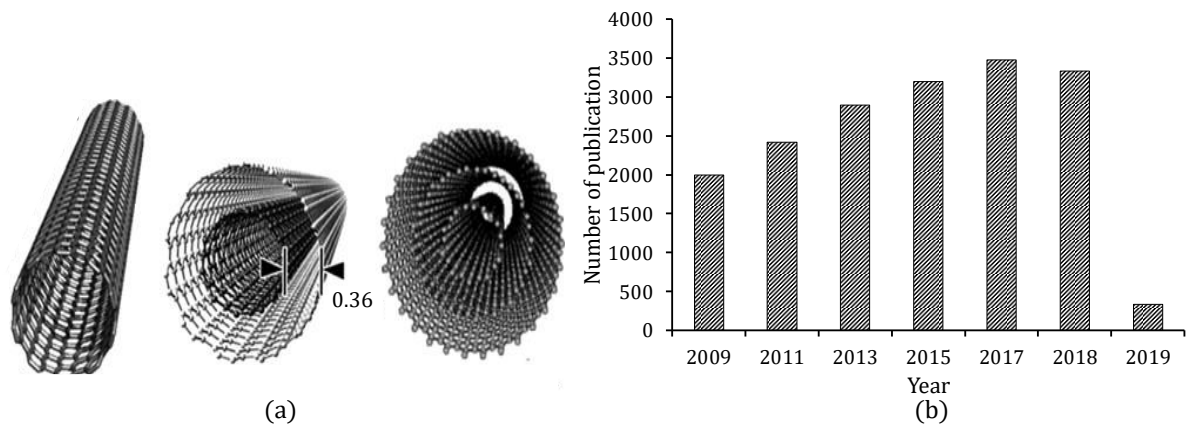


Figure 1-4: (a) Single, double and multiwall CNT, (b) Number of publications on Carbon nanotube (CNT) since 2009 (Source: web of knowledge).

1.2.2. Woven carbon fibres.

Carbon fibres (CF) were commercially available in the later 19th century by Edison and were built by carbonizing thin bamboo shoots and cotton fibres. Later they were manufactured in bulk by heating polyacrylonitrile in the air at 200–250 °C and in the inert gas atmosphere at 1200 °C. This process removed H₂, O₂ and N₂, leaving a chain of carbon atoms called CF. CF can be used in various forms, such as bundle, woven and knitted fabrics²⁵. The high fatigue resistance of CF reinforced composites is due to its high stiffness, allowing it for extremely efficient crack bridging and enhanced lower crack growth rate²⁶.

Deka et al.²⁷, in their recent study, has crafted CuO nanoparticles on the woven carbon fibre (WCF) mat. Further, GO-assisted composites were developed with a vacuum-assisted resin transfer module with unsaturated polystyrene as a matrix. Like other carbonaceous materials, the wetting of CF with molten aluminum and the formation of Al₄C₃ is the major problem associated with CF-reinforced aluminum matrix composites. The wetting ability of CF or other carbon material can be improved when the temperature of 1273 K is achieved. However, CF starts reacting with molten aluminum matrix at this temperature, creating an interfacial reaction product.

Moreover, many research articles have been published to improve CF's wetting ability with the Al matrix and are important in respect of this article. Daoud et al.²⁸ used the high-pressure gas infiltration method to fabricate CF/Al-matrix composites with high compactness. The application of pressure forces the metal to surround the fibre and improve its wetting ability. Improvement in wettability can be achieved by coating CF

with unreactive elements. Yang et al.²⁹ used copper coating on WCF using the electroplating methodology. Copper do not react with CF even at elevated temperature, thus prevents the interfacial reaction. The formation of aluminium carbide (Al_4C_3) is often accompanied by fibre degradation and deterioration of mechanical properties, leading to the earlier failure of the composite material. Abiding et al.³⁰ worked upon the coating of CF with titanium nitride by using the chemical vapour deposition technique. The coating of 30 nm to 35 nm of titanium nitride (TiN) improves the oxidation resistance of CF. The TiN deposition also improves the wetting ability and acts as a protective coating, provided the contact time with the Al-alloy melt is not too long. Zhang et al.³¹ studied the semisolid-rolling and annealing process for Ni-coated WCF composite. The result showed that at the temperature of 930 K, molten metal could not escape from the roller, and sufficient infiltration was achieved. The use of nickel as a coating material reacts with the molten Al metal upon initiation of casting. Since the fibre is at a much lower temperature than the melting temperature of the matrix, the reaction product Al_3Ni and molten metal attached to the fibre solidify instantly.

Apart from this, adding magnesium into the composite positively influences the reduction of brittle phase Al_4C_3 formation. Since magnesium and carbon have the highest negative enthalpy, so higher the negative mixing enthalpy more firmly the reaction occurs. Hence magnesium element is easily drawn into the carbon fibre, inhibiting the direct contact of Al with CF, thus reducing the formation of Al_4C_3 ³². Alhashmy et al.³³ compared liquid infiltration squeeze casting and laminate squeeze casting method (Figure 1-5). It was found that laminate squeeze casting reduces the infiltration distance to half the fibre thickness and solves most of the problems, such as premature cooling and pressure drop, thus improving wetting ability, composites homogeneity and properties.

1.2.3. Graphene nanoplatelets

Graphene-based composites have recently gained their place in aerospace, marine, automotive, electronic packaging and thermal management industries. Graphene has a broad spectrum of extraordinary properties, i.e. high electron mobility of over $2 \times 10^5 \text{ cm}^2 \text{ V}^{-1} \text{ s}^{-1}$ at electron densities of $2 \times 10^{11} \text{ cm}^{-2}$, the high thermal conductivity of $5 \times 10^3 \text{ Wm}^{-1} \text{ K}^{-1}$, impermeable to gas³⁴, ballistic transport of electrons³⁵, absorbs 2% of the white light,

has Young's modulus of 1TPa and tensile strength of 100 GPa³⁶. These are individual layers of sp² – hybridized carbon atoms arranged in two-dimensional lattices.

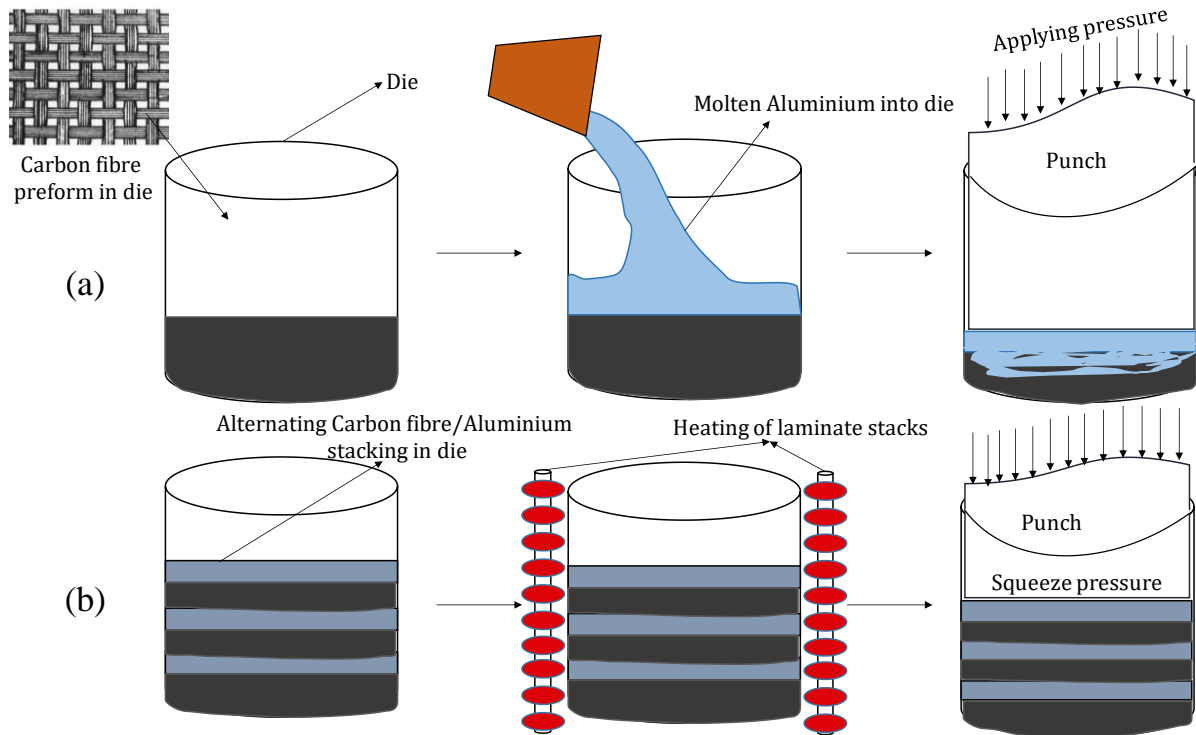


Figure 1-5: (a) Liquid infiltration squeeze casting (b) Laminate squeeze casting.

As shown in Figure 1-6(a), graphene is one atomic thickness sheet of carbon having numerous properties such as high strength and stiffness, most stretchable and thermally conductive material ever known with exceptional lower density and higher specific area³⁷. The young's modulus by various molecular dynamics simulations along the graphene plane is recorded as 1.8 TPa, compared with the diamond as 1.2 TPa, steel as 200 GPa, and copper as 100 GPa. The advantage of graphene and CNT is that they are half the density of aluminum metal and have a tensile strength of about 20 times that of high strength alloys such as annealed steel with the strength of 700 MPa^{38,39}. The advantage of graphene over CNT and graphite is its high specific surface area, leading to a higher area for interaction and high-stress transfer⁴⁰. Graphene does attract attention more than CNTs due to its three distinct features. 1) 2 D flat geometry (Crack deflecting properties), 2) high aspect ratio which allows for its interaction from both sides of the face, and 3) unique surface texture which allows it to interact with the matrix material mechanically. Graphene has been an excellent filler material when used as thermal interfacial material.

The strong coupling of graphene within the metal matrix increases the thermal conductivity of the composite material up to 2300%⁴¹. Figure 1-6(b) shows a rise in the level of research on graphene-based composites since graphene was exfoliated from graphite in 2004. Several articles were published in metal matrix composites and have increased from 11 in 2009 to 2723 in 2018. A similar trend can be noticed for the polymer matrix, which has increased from 37 to 2959 in the same period (source: www.webofknowledge.com).

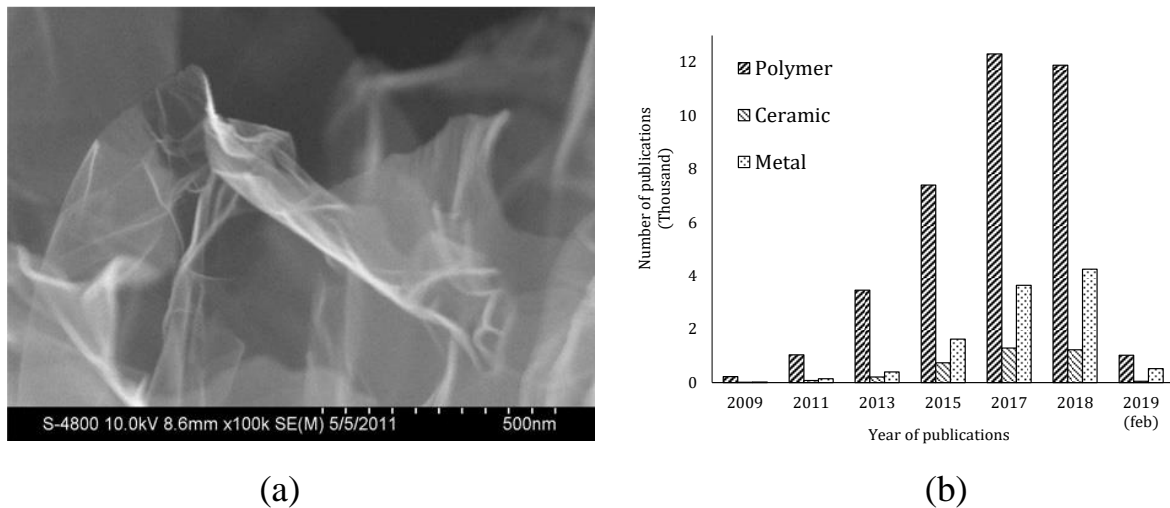


Figure 1-6: (a) Graphene nanosheet, (b) The number of publications in graphene-based composites since the year 2009 (source: web of knowledge).

1.3. Introduction to graphene-based MMC

Since 1920, Metal matrix composite (MMC) have been widely studied in various fields of science (refer Figure 1-7) because of their high technological, structural and functional application in automobile and aerospace industries⁴². The insufficient interaction between the reinforcement and matrix interface can create fragile components. Hence, it becomes an essential factor in governing the overall performance of the composites material^{43,44}. Graphene oxide (GO) has hydroxyl and epoxide functional groups and carboxyl and carbonyl groups. So in polymer matrix composites, this group acts as a strong interfacial agent that reacts with the epoxy group of the resin in polymer to form strong composite materials. GO is soluble in many organic solvents and water; hence, it becomes more comfortable to handle and disperse in matrices.

The primary difficulty with GNP's is that the weak Van der Waals force between the layer of GNP makes the material difficult to be dispersed within the matrix material⁴⁵.

Ball milling or planetary ball milling is a widely used technique for dispersion of graphene particles within a matrix material. However, due to the strong impact force, the graphene morphology is often damaged, which creates the sight for interfacial reactions and reduces the strengthening effect of graphene^{23,46-48}. However, other dispersion processes such as friction stir processing can be an excellent alternative⁴². In metal matrix composites, the lighter matrix material such as aluminum and magnesium having carbonaceous fillers are the point of attraction for current research. The demand is to create composites having low weight and strength comparable to that of other monolithic materials^{49,50}. Metal matrix composites are widely used in structural applications such as aerospace, marine, automobile and construction engineering. However, ceramic matrix composites have occupied their space in higher-temperature electronics parts, lightweight hypersonic engines etc⁵¹.

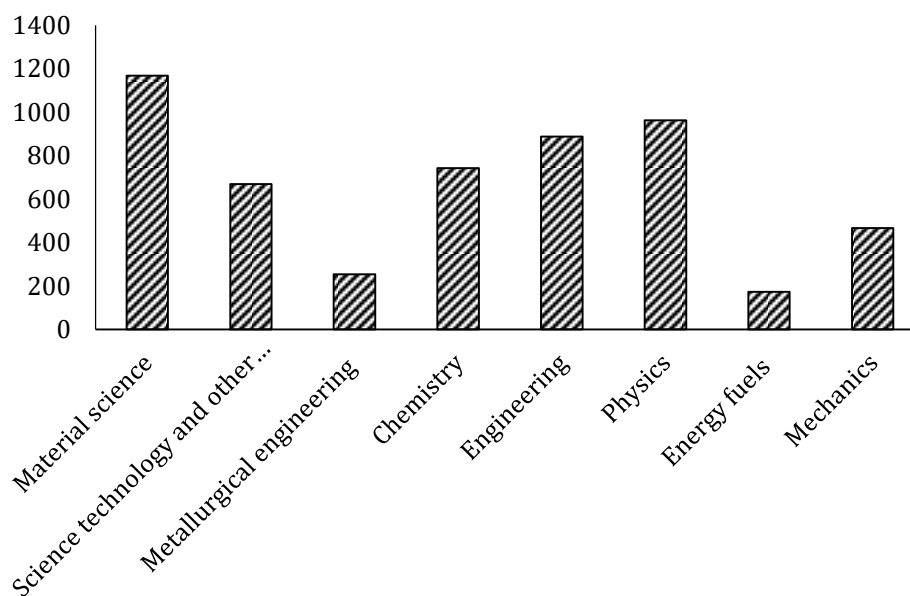


Figure 1-7: Number of publications on graphene-based MMC at various fields (2009-2019, source: web of knowledge)

1.4. Applications

1.4.1. Overview of applications of GNP/metal matrix composites

The MMC reinforced with GNP has found its place in various fields of application. So, depending upon the type of matrix material and the final use of composites formed, Table 1-1 provides a glimpse of the utility of GNP reinforcement in different matrix materials.

Table 1-1: Overview for applications of GNP/Metal matrix composites.^{14,22,59-61,25,52-58}

1.	Graphene/Al	Light weight high strength composites material for aerospace applications.
2.	Graphene/Cu	High strength, high conductivity material for electronic and other devices.
3.	Graphene/Mg	Light weight high performance composites.
4.	Graphene/Au	Bio-sensing applications.
5.	Graphene/Ag	High performance catalyst and removal of mercury from aqueous solution.
6.	Graphene/ZnO	Modified lithium storage capability and photo catalytic degradation and filtered removal of RhB dye.
7.	Graphene/Fe ₃ O ₄	Increase in performance of lithium ion battery. Enhancement in electromagnetic absorption properties.
8.	Graphene/Al/Sn/ Mg	High strength Nano filter adhesion.
9.	Graphene/Al/Pd/ Pt	Fuel cell.
10.	Graphene-Hybrid composites	Arsenic filtration, hybrid materials

1.4.2. Application of graphene

1.4.2.1. Electrical applications of graphene

Due to its attractive electrical and mechanical properties, different research has been focused on its practical applications. The mechanical, chemical and electrical characteristics of graphene can be preserved even to the atomic level of a few benzene rings. Graphene is a good material to deal with molecular scale electronics^{62,63}. For example, graphene can be employed as a semiconducting layer in barristor^{64,65}, FET (field-effect transistors)⁶⁶, and integrated circuits when the density and type of carriers in the SLG p-n junction are changed. The graphene barristor is a triode with a gate-controlled Schottky barrier and a 105 on/off ratio. Graphene can also be used as capacitors⁶⁷ and sensors⁶⁸. Furthermore, the electron flow can become a focal point when the carrier density on the n- and p-sides of a single graphene p-n junction is made equal. Graphene is also used to synthesize electronic lenses⁶⁹.

With whispering-gallery-mode as inspiration Zhao et al.⁷⁰ created a resonator to form electronic waves by building a circular p-n junction in the graphene. Due to the

vertical graphene heterostructure, a field-effect tunnelling transistor device was proposed⁷¹. This device takes advantage of graphene's low density, allowing a tiny change in V_g to result in a large rise in the value of E_f . Apart from the use of graphene in electronic devices, it can be used in photonics and optoelectronics devices which combines the optical and electronic properties⁷². Because of its low sheet resistance and excellent transparency, graphene is used as a transparent conductor in most optoelectronic devices. In inorganic⁷³, organic⁷⁴, and dye-sensitized solar cells, graphene-based transparent conducting sheets are employed as window electrodes and hole transport layers. The work function of graphene is 4.5 eV, comparable to that of indium tin oxide (ITO). Many attempts have been made to employ graphene, which will eventually replace ITO^{75,76}, in light-emitting devices and touch displays. Graphene can absorb a wide range of wavelengths, from ultraviolet to terahertz. As a result, a graphene photodetector will have a wider spectral range. Graphene functions as a transparent conductor because of its low sheet resistance and high transparency in most of its optoelectronic devices. Minimal heat loss to the substrate and low heat capacity per unit area is the minimum conditions for effective thermoacoustic sound generation⁷⁷. Monolayer graphene can meet the conditions with a minimum thickness of 0.335 nm⁷⁸. Graphene-based sound generators are capable of generating sound beyond the audible range⁷⁹. The combination of attractive mechanical and thermal properties does suggest that graphene is a suitable material for fabricating thermophones⁸⁰. Tian et al.⁸¹ were first to show that graphene-based thermophones are efficiently capable of producing audible and ultrasound sound frequencies through the thermoacoustic effect.

Good electrical and mechanical properties are obtained with laser-reduced graphene. Hence, electrochemical capacitors can have graphene as electrode material that exhibits higher energy and power density with remarkable cyclic stabilities^{82,83}. Double-layered capacitors (DLC) may have electrodes of a vertically oriented graphene nanosheet which provides decreased electronic resistance, excellent time constants for resistor-capacitor, and outstanding performance AC line-filtering. MEGO (microwave exfoliated graphene oxide) is a continuous 3D network with nanoscale pores that is produced by potassium hydroxide activation. Its design aids super capacitors which breaks the barrier of low energy storage density and increased series resistance.

1.4.2.2. Graphene resonator

Graphene resonators are the ultimate limit for 2D nanoscale resonators because of their one atomic thickness⁸⁴. Graphene-based resonators could be used as charge sensors for weak or ultra-low measurements⁸⁵ and precision measurements of mass⁸⁶. Whereas single-molecule mass detections are possible with nano electromechanical systems (NEMS) resonant sensors, graphene-based resonators have the potential for detecting a single atomic mass⁸⁷.

1.4.2.3. Graphene coating and lubrication

A coating of graphene can do protection of nano-electronic devices. Graphene, because of its 0.34 nm of thickness, can form a thin layer of transparent protective layer^{88,89} having ideal transmittance of 97.7%^{90,91}. Chen et al.⁹² has shown that graphene film grown by CVD can protect the surface of Cu and Cu-Ni alloys from oxidation in the air even after heating it to a temperature of 200°C for up to 4 hrs. Due to its exceptionally low coefficient of friction, graphene coating is the best choice for solid lubrication and for wear/scratch-resistant coatings. A few layers of graphene are used as a solid lubricant for tribo-pairs consisting of stainless steel surfaces. The coefficient of friction (COF) achieved is six times lower if graphene is used. Berman et al.⁹³ has shown that graphene-nano-diamonds are capable of showing super macroscopic lubricity than diamond-like carbon (DLC), and the resulting COF is as low as 0.004 in a dry environment.

1.4.2.4. Pressure sensor

Smith et al.⁹⁴ has manufactured a pressure sensor by suspending chemical vapour deposition (CVD) graphene on a 1.5 mm deep rectangular cavity etched with reactive-ion etching (RIE) technique. Dolleman et al.⁹⁵ used a few-layer graphene membrane as a squeeze-film pressure sensor. The device shows a strong pressure dependency on membrane resonant frequency, with a frequency shift of 4 MHz measured with no hysteresis between 8 and 1000 Mbar and the device's measured responsivity of 9000 MHz/ mbar.

1.4.2.5. Aerospace applications

Graphene along with aluminum matrix has great applications in aerospace industries. Modern aircraft utilizes more than 20 wt.% of aircraft mass as aluminum metal and around 50 wt.% of aircraft mass with composite material (laminated or carbon-carbon sandwich structure etc.). The utilization of strengthening reinforcements can further

decrease the aircraft mass by avoiding conventional materials. However, this field needs to be searched for better load transferability and high-strength materials.

1.4.2.6. Other applications

Resonant sensors- A graphene resonator with a uniform gap can be fabricated by transferring graphene onto a substrate material and then etching the oxide using a buffered hydrofluoric acid solution⁹⁶. Unlike conventional resonators, graphene has a 2D structure, and a large surface area with a high surface-to-volume ratio, which makes its interaction with external masses more convenient⁹⁷. Graphene resonators have high operating frequencies, making them more likely to be used in sensing applications⁸⁴.

Nanogenerators- Using the piezoelectric transduction property of graphene membrane, Wang et al.⁹⁸ designed a nano-generator by fabricating a hole (approx. 3 mm) on the substrate having a reactive ion etching and graphene deposition, which was prepared through exfoliation and mechanical cleaving.

Piezoelectric actuator- Rodrigues et al.⁹⁹ demonstrated the piezoelectric properties of graphene. It utilizes the SiO₂ calibration grating that has parallel rectangular grooves of 1317 ± 10 nm heights, with a periodicity of 1500 ± 10 nm as a substrate.

Ultrafiltration medium- Several theoretical¹⁰⁰ and experimental works have shown that nano-sized porosity in a graphene membrane does allow one element to pass through it, therefore performing as an ultrafiltration medium¹⁰¹. Filtration made by GO-membrane has potential application as barriers to liquid and solid which can efficiently separate the solid particle from the liquid. Graphene membrane has application in the water and gas separation filtration.

Desalination. Cohen-Tanugi et al.¹⁰², for the first time, has shown the desalination application of graphene using an MD simulation. The process utilized hydroxylated or hydrogenated nanoporous graphene membrane in the reverse osmosis process. Apart from current polyamide-based filters, water flow through graphene is easier and faster because of its thickness and large pressure withstanding abilities. Thus, desalination through graphene nanopores is potentially faster and more energy-efficient than any other process with high cost-efficiency¹⁰³.

Application Summary- The field of metal matrix reinforced composites is still a promising area of research. Powder metallurgy and roll forming techniques used in aluminum

matrix composites have built their base, but the research is still focused on the compatibility of graphene with liquid aluminum. The use of graphene in various other metal matrices has shown that the field is still open to creating new material with higher hardness, yield strength, and thermal and electrical conductivity. Food and pharmaceutical industries can apply graphene coating to keep away the water and oxygen for its longer life. Li-ion battery capacity and life cycle can be increased by using the graphene in its electrode (Al and Cu) for high charge transfer. It can be used in combination with a dielectric material to get high-performance batteries. Chemical industries have adopted the use of graphene as catalysts or solvents for its better performance. The high-performance adhesive is being made by using graphene to get properties better than with the other material available. The growth of metal oxides on the graphene particles has attracted interest in various sensors for their faster response. Lastly, graphene is a low-cost, high properties material that has opened new ways for discovering various smart material, which is of higher reliability, low cost and high performance.

1.5. Problem definition

After a comprehensive literature survey following problems have been identified in the synthesis of aluminum metal matrix composites:

- **Quality and non-uniformity in the dispersion of graphene in metal matrix:** Non-uniformity in the distribution of reinforcements creates composites with weak mechanical strength. Carbonaceous reinforcement agglomerates easily due to weak van der Waal force and affect the tensile strength of composite material.
- **Effect of alignment, volume fraction, aspect ratio and clustering of graphene in the metal matrix:** It is evident from the literature (discussed in the next chapter) that the volume fraction of graphene plays a vital role in the strengthening of composite material. The strength of composite first increases and then decreases with an increase in reinforcement percentage. The decrease is due to the clustering of graphene, limiting the maximum achievable strength of composite material.
- **Non-wettability and aluminum metal matrix attachment to 2D structured graphene:** Non-wettability refers to the ability of reinforcement to maintain contact with the matrix. Graphene has wettability issues with aluminium matrix, hindering the load

transfer between reinforcement and matrix. Non-wettability also leads to premature crack formation and propagation within the composite structure.

- **Non-wettability leads to improper interfacial bonding and weak inherent properties.**
- **The reaction between aluminum and graphene at elevated temperature leads to the formation of Al_4C_3 :** Aluminium reacts with activated carbon present in the graphene structure and forms a brittle phase of aluminium carbide. Al_4C_3 has lower strength as compared to matrix and reinforcements. Hence when it is present in composite, it causes voids and cracks formation and causes site for premature failure.

Being an excellent reinforcement, graphene lags behind its ability to enhance the performance of aluminum metal matrix composite. The issue of non-uniformity in dispersion and graphene agglomeration was addressed earlier by many researchers using the ball milling technique. However, non-wettability and formation of Al_4C_3 are still needed to be addressed. As mentioned in the literature, the reaction between graphene and aluminum matrix is based on defects formed during graphene synthesis or its processing. Therefore, care must be taken with a suitable interfacial product that can enhance wettability and minimize the possibility of carbide formation. The use of functionalized graphene could be one of the techniques to minimize defects and improve the wettability of reinforcement.

Most of the work reported on functionalized graphene is on energy storage, electronic industries and solar cells. However, there is very little or no literature (apart from GO and rGO) available on the utilization of functionalized graphene towards aluminum matrix, and it needs to be addressed.

1.6. Aim of existing project

The present research focuses on synthesizing functionalized graphene using a high energy ball milling technique and further investigating its effect on aluminum matrix to achieve high-performance composite material. To accomplish the above-mentioned objectives, task list is defined in Figure 1-8.

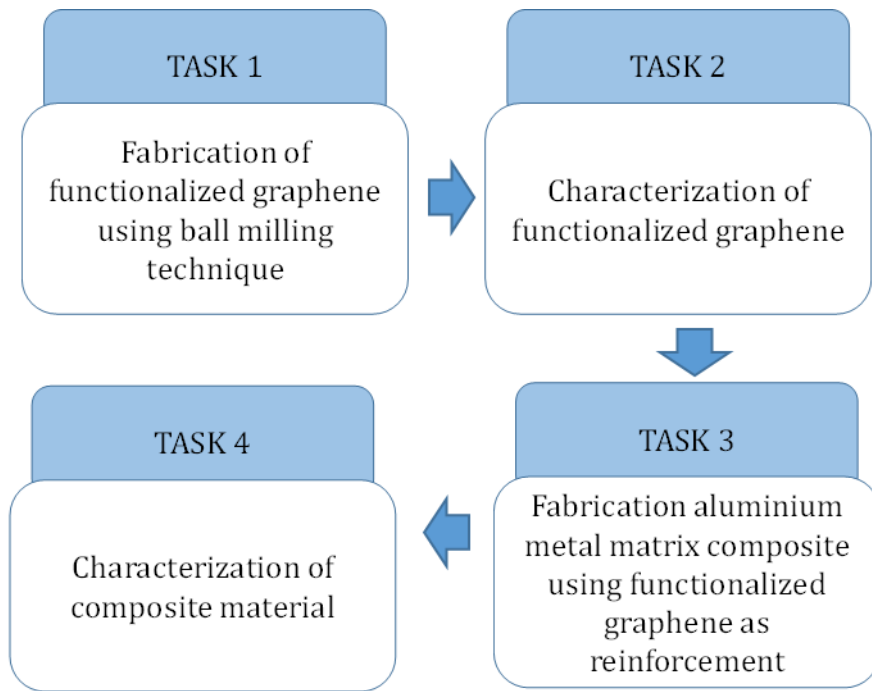


Figure 1-8: Task list

1.7. Organization of the report

Chapter 1: The first chapter of the thesis sums up the fundamental features of the research work and the merits of metal matrix composite and carbonaceous reinforcement—the chapter identifies applications of metal matrix composites and graphene in various field.

Chapter 2: The second chapter is the detailed literature survey on graphene synthesis and the merits and demerits of the processes involved. The literature elaborates the effect of graphene on various metal matrix composites and the strengthening mechanism involved for its effective load transfer.

Chapter 3: To accomplish the aim of thesis, functionalized graphene was synthesized via ball milling technique, it is very necessary to take account of the energy released during ball milling process at various milling speeds. The chapter gives an analytical approach for the release in energy at various milling speed so that graphene synthesized has lower structural defects and the process generates low heat via friction and collision at prolonged milling time.

Chapter 4: The fourth chapter sums up the methodology involved in synthesizing graphene and aluminum metal matrix composite via high energy ball milling and power metallurgy technique, respectively.

Chapter 5: The fifth chapter synthesizes nitrogen-doped graphene via high energy ball milling technique and analyses its strengthening effect on aluminum metal matrix composite. Synthesized graphene was characterized in detail using different characterization techniques. The composite synthesized has a different percentage of nitrogen doped graphene (NDG) and was characterized using different mechanical characterization techniques.

Chapter 6: The synthesis of sulfur-nitrogen co-doped graphene (S-NDG) and its strengthening effect on aluminum metal matrix composite is presented in this chapter. Sulfur doped graphene and S-NDG/Al composite were characterized by various techniques and detailed in the chapter.

Chapter 7: The synthesis of antimony doped graphene (ADG) and its effect on the mechanical performance of composite material is detailed in this chapter. Various techniques were used to characterize graphene composite material with varying ADG concentrations.

Chapter 8: This chapter includes the conclusions from the current work and identifies the future scope of the research.

CHAPTER 2: Literature review

Some essential information about metal matrix composites, graphene synthesis and functionalization techniques is reviewed to get graphene and its relevant composites with the best mechanical and interfacial properties. The literature presents the prior work done in the areas, namely, different metal matrix composites. The effect of functionalized graphene and reinforcement percentage on mechanical, chemical and thermal characteristics will be discussed.

2.1. Graphene: Preparation, processing and dispersion techniques

Most of the research work done so far has not been able to use graphene in its purest state, i.e. pristine graphene, mainly because of its limited yield from the preparation point of view. Moreover, because of its carbon-carbon, sp² hybridized double bond graphene can be easily functionalized to produce GO, rGO, Nitrogen-doped graphene¹⁰⁴ and carboxylic doped graphene¹⁰⁵ etc. These materials are commonly available and even showcase similar properties to that of graphene. From Figure 2-1, it is evident that there are several ways to produce single or few-layer graphene, such as by mechanical cleavage¹⁰⁶, epitaxial growth in high vacuum chamber¹⁰⁷, graphitization of SiC in atmospheric pressure, oxidation of graphite to produce graphite oxide^{108,109}, chemical vapour deposition (CVD) using catalyst transition metal^{110,111} and liquid phase exfoliation techniques¹¹². Among those methods, low cost and high-quality materials are only obtained from the direct liquid phase exfoliation techniques.

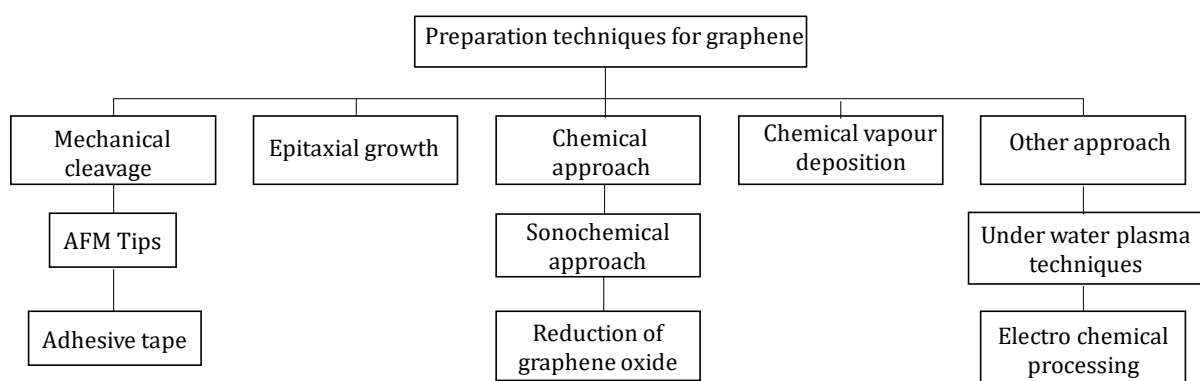


Figure 2-1: Synthesis of graphene by different techniques.

According to the literature, various processing and dispersion techniques are available for the dispersion and processing of graphene in metal matrix composites. In fact, due to similarities between GNP and CNT, various techniques adopted for the dispersion of CNTs

can be utilized to disperse GNPs. The common problem in mixing GNP is similar to that of CNT. The parallel tubes' energy interaction potentials are 500 eV/nm for single-wall CNT and 2 eV/nm² for graphene platelets^{113,114}, and is the probable reason for agglomeration. In the prevention of agglomeration, high energy is required to overcome the surface energy of graphene. However, the presence of clustering leads to the formation of cracks, pinholes and pores, leading to the premature failure of composites material. So, the interaction energy potential and the van der Waals forces must be neutralized before the graphene distribution. For this purpose, several technologies have been introduced and are being discussed in the article. However, the most significant demerits of those processes are that most of the processes are complicated and uneconomical for industrial applications. The Ball milling and ultra-sonication technique have recently emerged as the most efficient and powerful techniques for mixing GNPs into the matrix material.

2.1.1. Preparation methods

2.1.1.1. The solution made preparation techniques:

Dispersion and chemical exfoliation are some of the few techniques for the exfoliation of graphite to produce graphene. For this, the particles are dispersed in an appropriate solvent with a suitable concentration and remain dispersed for a reasonable period of time. Two main approaches are utilised to overcome the strong van der Waals force of 2 eV/nm² on the graphene surface. First, sonication of graphite in the solvent system and second, chemical functionalization or treatment of graphite to weaken its interlayer interactions¹¹⁵. However, there are a couple of problems associated with the utilization of graphene. The first is the lack of scalable synthetic routes to produce graphene required for industrial applications, and the second concern is the poor colloidal stability of graphene in most solvents⁴⁸. In the recent era, graphene production through graphite has been popularized by a sonication assisted liquid-phase exfoliation (LPE)¹¹⁶ in the presence of organic solvents¹¹⁷, ionic liquids¹¹⁸ and aqueous surfactant solution. The aqueous solution approach provides an advantage over toxic and expensive solvents. At the same time, the presence of surfactant and stabilizer molecules in dispersion minimises the free surface energy by non-covalent functionalization of graphene, which prevents the aggregation of graphene sheets¹¹⁹.

Another approach for exfoliation and dispersion of graphene is the sonochemical liquid-phase exfoliation technique¹²⁰. The process uses ultrasonication, shear exfoliation¹²¹ and micro fluidization¹²² techniques. The mechanism behind sonochemistry is the periodic compression and expansion of bubbles, which creates subsequent high and low-pressure regions inside the solution, as shown in Figure 2-2 (a-e). The activation of sonochemistry is marked by a shift in pressure that occurs before the development, expansion, and collapse of the sonic bubble. Dissolved air molecules disperse at the lower pressure cycle to create a bubble. Thus, the higher external pressure compresses the bubbles and inner matter violently. This bubble growth and compression process continues until the bubble bursts. As seen in Figure 2-2, the exploding bubbles create shock waves that accelerate undissolved solute and impurity particles to a speed of several hundred metres per second¹²³, and at this speed, collision causes a profound structural alteration that may be employed for a variety of applications. In addition to fragmentation, the process is widely used in the exfoliation of layered material to produce 2D counterpart¹²⁴. The production methods are generally characterized by dispersions with wide flake size distributions (nm- few mm) and low yielding, typically in the range of 1 to 5%. Liquid phase exfoliation techniques typically produce dispersion with low intrinsic graphene concentrations (~ 0.1 g/litre). Hence, centrifugation and re-dispersion are often required to produce graphene with industrially acceptable concentrations i.e. of (≥ 1 g/litre).

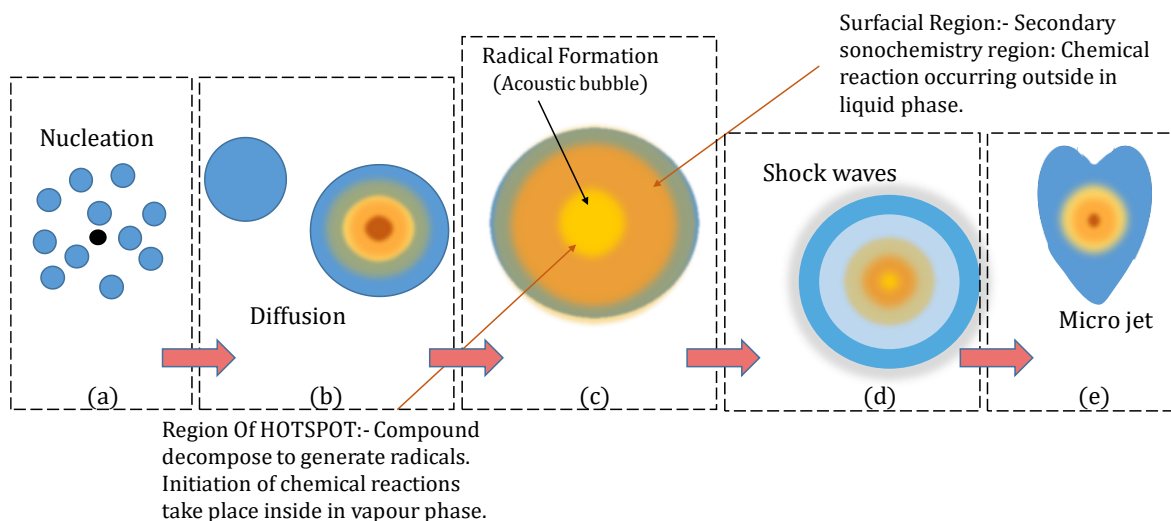


Figure 2-2: Acoustic representation of shock wave formation and different dominant inside the bubble^{125,126}.

Lei et al.¹²⁷ used the LPE technique to prepare thin Fluorographene nanosheets by interacting raw graphite fluoride (GrF) particles with N, N-dimethyl formamide molecules, followed by a short-time microwave treatment. As per AFM results, the thickness of the prepared fluorographene nanosheets ranges from ~ (1 to 4 nm). The resultant high-quality fluorographene nanosheets exhibit excellent thermal stability and remarkable lubrication behaviour in oil. The route for improving the LPE process is the utilization of different additives and the solvent for graphite dispersion. Xu et al.¹²⁸ used naphthalene as a molecular wedge for improving the yield of LPE.

An impressive dispersion with concentrations of 0.15 g/L was obtained by this method. Hadi et al.¹²⁹ used magnetic Fe₃O₄ nanoparticles as “additive wedge” to facilitate the improvement and delamination of graphite layers. The experiment showed strong shear forces resulting from the collision of Fe₃O₄ particles with graphite particles, having intense ultrasonic waves. This, led to enhanced exfoliation of graphite particles to GNP. Another route for graphene exfoliation is the electrochemical and underwater plasma technique or pulsed underwater discharge¹³⁰. The electrochemical process utilizes the intercalation of ions and electrochemical reactions from electrolytes for exfoliation. It offers a whole branch of electrochemistry to be applied for the exfoliation and functionalization of the graphite electrodes. The type of graphene materials to be produced depends greatly on the applied voltage and the electrolyte used, i.e. organic salt solution¹³¹, inorganic salt solutions¹³² etc. The disadvantage of this route is that most graphite electrodes come either as single or in continuous pieces. However, the chemical exfoliation occurs on outer layers, peeling the electrode layer by layer. In reality, the exfoliation and the ions exchange co-occur at all the graphite edges in contact with the electrolyte. Hence, it results in the production of few-layer graphene or multilayer graphite chunks¹³³. Electrohydraulic shockwaves attain the exfoliation of graphite in an underwater plasma electric discharges process. These shockwaves are formed due to the rapid formation and collapse of vapour bubbles which contain evaporated water and carbon particles¹³⁴. The process is mainly excited through a high voltage pulse of 15 kV.

However, the main disadvantage is that the shockwaves generated can erode the particle surface, thus producing much flaky debris. Segundo et al.¹³⁵ produced graphene nanosheets through underwater electrical discharge having two mediums, i.e. water and isopropyl alcohol/water solvents. The result has shown that most of the GNPs produced

were with less than 10 layers. Figure 2-3 shows that samples exfoliated in isopropyl alcohol and water solution became smaller than those treated with only water.

Challenges: Exfoliation of graphite to obtain pure graphene requires overcoming van der Waals interactions between graphite layers. The hurdle can be removed by two approaches: chemical functionalization and sonication of graphite in the presence of solvents¹³⁶. However, the technique has some ill effects because it has been observed that excessive sonication needed to break un-functionalized GNP may destroy the GNP sheet. Despite its modified processing, GO is an insulating material, and even after the chemical exfoliation, the electronic properties are quite different from the pristine GNP¹³⁷. Moreover, the use of acidic solvents complicates the process and leaves behind a problematic process for removing the functionalized link of the graphene chain.

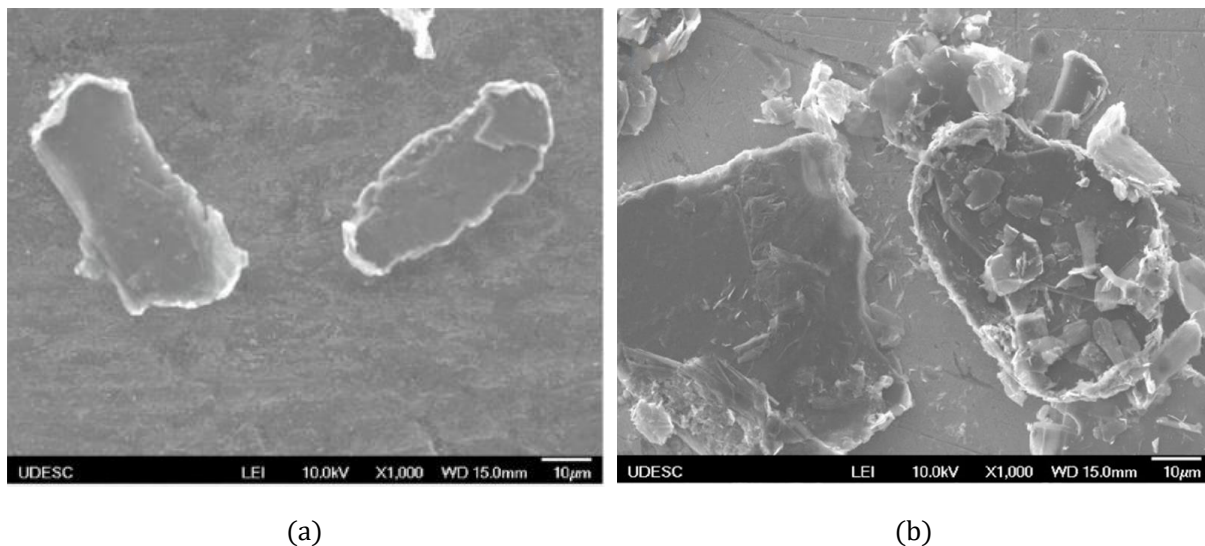


Figure 2-3: a) Graphene exfoliated in isopropyl alcohol and water solution and b) Graphene exfoliated in pure water solution¹³⁵.

2.1.1.2. Preparation by chemical vapour deposition method:

Chemical vapour deposition (CVD) (Figure 2-4, low-pressure CVD) is one of the most promising yet flexible and commonly used methods for the growth of graphitic or graphitic thin films. The process can produce large-area graphene sheets and chemically turned 2D materials, for example, substitutionally doped graphene¹³⁸, ¹³C graphene¹³⁹ and hexagonal boron nitride films^{140,141} etc. Johansson et al. successfully generated few-layer graphite in the early 1990s through this technique¹⁴². CVD has been widely used to synthesise graphene. It is a relatively low-cost and straightforward method to produce graphene of impressive size (i.e. 30 inches) and can be easily transferred to other

substrates¹⁴³. However, the large-scale synthetic graphene film produced is generally polycrystalline, consisting of various single-crystalline grains separated by grain boundaries^{144,145}.

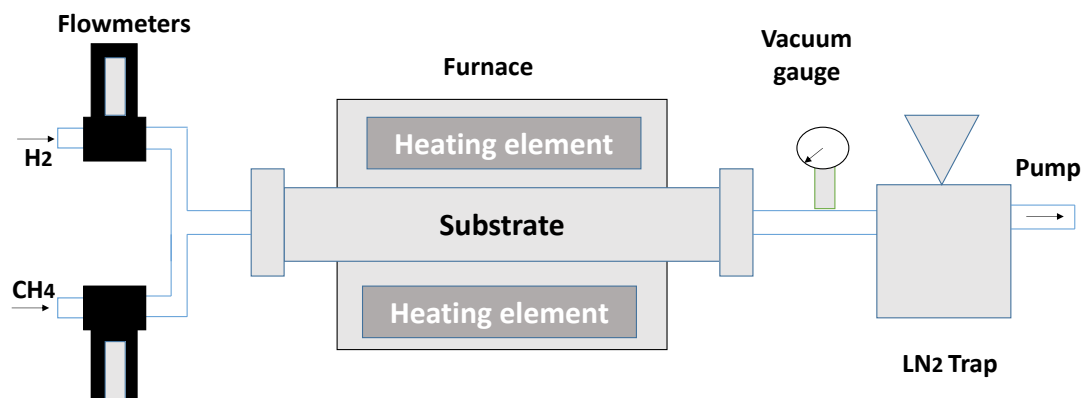


Figure 2-4: Diagram of Low-pressure CVD system for graphene synthesis¹⁴⁶.

For graphene production on metal substrates, two growth methods have been observed: 1) Carbon surface precipitation to make graphite, and 2) carbon surface adsorption. The metal surface is exposed to methane during the process, particularly $^{12}\text{CH}_4$. Methane is initially degraded on the metal substrate to produce CH_x radicals (carbon-free radicals) due to the catalytic activity of the metal surface¹⁴⁷. When the metal's carbon solubility is high, carbon atoms diffuse into the bulk of the metal until they reach their limit at the temperature of exposure or other concentrations established. Regardless of the gas precursor's dosing order, all ^{12}C and ^{13}C atoms dissolve and mix into the metal, and when the carbon in metal (such as Ni or Cu) achieves super saturation at a specific temperature, an equilibrium monolayer graphite, or graphene phase is formed on the surface. With further cooling of the metal, more dissolved carbon atoms precipitate out of metals to form multi-layered graphene, depending upon the carbon concentration and the cooling rate. In the case when the solubility of carbon percentage in the metal is very low (for Cu), the surface-adsorption growth technique dominates, where ^{12}C and ^{13}C are spatially separated across the Cu surface following the introduction of the two carbon isotopes as a function of time¹⁴⁶.

Challenges: Few challenges are associated with graphene synthesis by the CVD method. The atomic details for graphene growth are still under investigation, and a higher growth rate for single-crystal graphene is still unachieved. The maximum size achieved for single-crystal graphene is limited to a few centimetres, basically due to its slower growth rate.

The single-layer graphene still has various defects such as vacancies, wrinkling, impurities, cracks, and holes produced during the transfer process. Another big challenge for this process is controlling the stacking order and layer number for graphene growth. The growth of graphene on the target substrate is preferred (as dielectric), which eliminates the transfer process of film, avoiding various defects but degrades the quality of graphene produced. At the same time, more study and research is needed to improve GNP's quality to meet the present-day technological demand.

2.1.1.3. Preparation by reducing graphene oxide:

Graphene oxide (GO) is made up of pseudo-2D carbon layers, which is frequently made by oxidising graphite flakes. The initial motivation for GO reduction is to mass-produce graphene. Even in its disordered state, reduced graphene oxide (rGO) is proven to be a potentially beneficial material for catalytic properties^{148,149} and energy storage^{150,151}. Efficient reduction of GO into high-quality graphene should substantially enhance performance. Graphene is an excellent electrical conductor, while GO is insulating. Therefore, to restore some of graphene's favourable electrical, mechanical and thermal properties, GO is commonly reduced by thermal annealing or chemical reducing agents^{152,153}.

2.1.1.4. Chemical reduction:

The current process for graphene production is the bottom-up and top-down approaches, of which both are viable options. The bottom-up approach seeks to build graphene sheets from scratch, i.e. starting with simple carbon molecules such as ethanol and methane. The top-down approach is based upon the fundamental idea of layer by layer extraction of graphene from graphite. Both methods provide graphene of good quality and yield¹⁵⁴.

To produce rGO from GO on a large scale, chemical reduction or oxidation is an efficient and most productive technique. The procedure starts with the immersion of GO in a selected reducing agent at a particular temperature range for a particular period. The process removes a functional group such as OH and COOH. Figure 2-5 (a) and (b) depicts the chemical structure of GO and rGO. The transition of GO to graphene is frequently shown empirically by a change in the colour of the reaction mixture, i.e. from brown for GO to black for graphene and a rise in hydrophobicity aggregation. The restoration of p-conjugation may be verified by changes between GO and rGO in UV-Visible spectra, XPS (X-ray photoelectron spectroscopy) data and electrical conductivity. According to

Huckel's rule, the redshift of UV adsorption peaks suggests the extension of π - π conjugation. The appearance of the π - π satellite peak in XPS can be a good indication¹⁵⁵. The efficacy of a specific reduction process is frequently shown by a drop in elemental oxygen concentration and an increase in the current conductivity of the graphene material¹⁵⁶. Table 2-1 shows the types of reagents used for graphene oxide reduction.

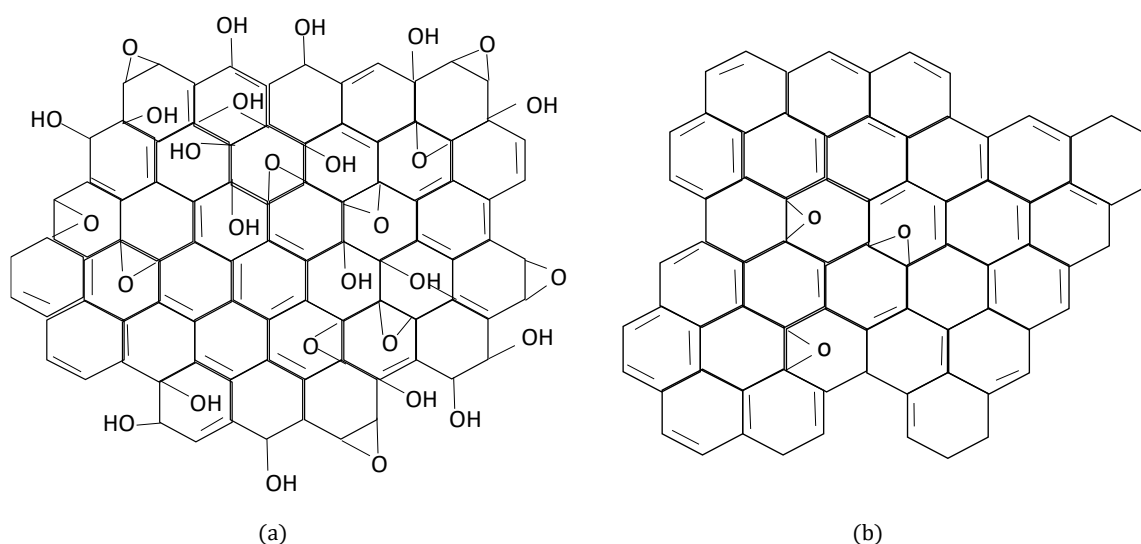


Figure 2-5: (a) Chemical structure of graphene oxide (b) Chemical structure of reduced graphene oxide¹⁵⁷.

Challenges: The use of acidic oxidants in the presence of water produces large-scaled graphene nanosheets. However, the method suffers many drawbacks, i.e. the utilization of a much tricky preparation method, complicated acid/H₂O removal technique, and low quality of product synthesized. Moreover, the involvement of various oxygen-containing groups (such as carboxyl, hydroxyl and epoxy groups) on acid-oxidized GNP's makes subsequent functionalization uncontrollable and complicated^{158,159}. The method may cause depletion in the properties of graphene, such as lower conductivity, poor mechanical and thermal stability and structural defects¹⁶⁰.

Table 2-1: List of reagent used for GO reduction^{161,162,171-177,163-170,178-186,187,188,197,198,189-}

196

Reducing agents	Conductivity	Doping	Conditions
Lithium Aluminium hydride (LiAlH ₄)	-	-	THF,12h, 66°C
Hydrohalic acid			
HI-TFA	-	-	40h, -10°C
HBr	2.3 x 10 ⁻²	Br doped	24h, 110°C
HBr-KOtBu	-	-	THF, 0.5h, 66°C
Borohydride			
NaBH ₄	17	-	1h, 80°C
	45	-	RT, 2h
	82	-	1h, 80°C
NaBH(OAc) ₃	-	-	MeOH, 2h, 70°C
NH ₃ BH ₃	19 300	B/N doped	12h, 80°C
	20 300	B/N doped	THF, 12h, 66°C
Sulphur- contained			
Thiourea dioxide-NaOH	-	-	EtOH/H ₂ O, 1h, 90°C
Thiourea dioxide-NH ₃	290	-	1h, RT
Ethanethiol-AlCl ₃	-	-	5h, 70°C
Lawesson reagent	4760	S doped	Toluene, 24h, 110°C
Nitrogen-contained			
Hydroxylamine	-	N-doped	30h, 80°C
Hydroxylamine-NH ₃	1122	-	1h, 90°C
Hydrazine	2420	N-doped	24h, 100°C
	1700	N-doped	DMF/H ₂ O,12h, 80°C
Ethylenediamine	220	N-doped	DMF, 8h, 80°C
Urea/NH ₃	43	Adsorbed	30h, 95°C
Polyamido amine	-	Covalent	1h, 90°C
Oxygen-contained			
Ethanol	1.8 x 10 ⁻⁴	-	4-5 days, 100°C
Methanol	3.2 x 10 ⁻⁴	-	4-5 days, 100°C
Benzyl alcohol	4600	-	4-5 days, 100°C
Glucose/NH ₃	-	Adsorbed	1h, 95°C
Dextran/NH ₃	1.1	Adsorbed	3h, 95°C
Isopropyl alcohol	1019	-	4-5 days, 100°C
Metallic- acids			
Fe/HCL	2300	Fe-Doped	6h, RT
Zn/H ₂ SO ₄	3416	-	2h, RT
Al/HCL	2100	-	30min, RT
Al foil/HCL	12 530	-	20min, RT
Mg/HCL	10	-	5 min, RT

2.1.1.5. Thermal annealing:

In this method, the graphene oxide is reduced under high temperatures, typically around 1000°C. The water molecule and oxygen functional group evaporate at this temperature, reducing graphene oxide as a by-product. The effectiveness of this process can be calculated by the magnitude of the carbon/ oxygen (C/O) ratio present in the graphene. Renteria et al.¹⁹⁹ analysed the annealing of freestanding graphene at a temperature of 1000°C. Due to the formation of the air pocket, there was a decrease in cross-plane thermal conductivity. However, the in-plane thermal conductivity (k) increased significantly from 2.94 W m⁻¹ K⁻¹ for the GO film to 61.8 W m⁻¹ K⁻¹ for the rGO film. Tian et al.²⁰⁰ used a rapid thermal annealing technique without using any protective environment to synthesize exfoliated graphene. The result showed that in the temperature range of 450°C to 550°C, the yield was 50%. At 600°C the C/O ratio was increased from 7.3 to 25.9 while using a two-step annealing process²⁰⁰.

Challenges: The important challenge behind the thermal annealing route is that it is not possible to remove the oxygen functional groups entirely despite various efforts. Hence, the reduced form of GO, i.e. (rGO), remains a highly disorganized material with relatively poor crystallinity and mobility with properties far inferior to graphene obtained by CVD technique^{155,201}.

2.1.2. Processing techniques

The harsh processing conditions, such as high pressure and temperature, make carbonaceous material into the metal matrix more tricky than expected. The achievement of homogenous dispersion, the attainment of high strength interfacial bonding, and the maintenance of structural stability are the primary challenges for developing MMNCs^{202,203}. The harsh processing conditions affect the structural integrity of carbonaceous material, which results in the chemical reaction between the materials occurring readily. In reality, caution must be exercised while fabricating metal matrix composites, i.e. avoiding overheating in the melting of aluminum or aluminum alloys, which can create Al₄C₃ (aluminum carbide).

The wetting ability of molten metal's on the solid surface of reinforcement plays a crucial role in processing composites to get the desired product. The wetting is related to the contact between a solid surface and liquid material, characterising a liquid's capacity to spread across a solid surface. The extent of a liquid's wetting ability is determined by

the rule of thermodynamics, which seeks to minimise the liquid droplet's surface free energy. The surface energy (surface tension) of liquid droplets on a solid surface can be expressed by the equation: -

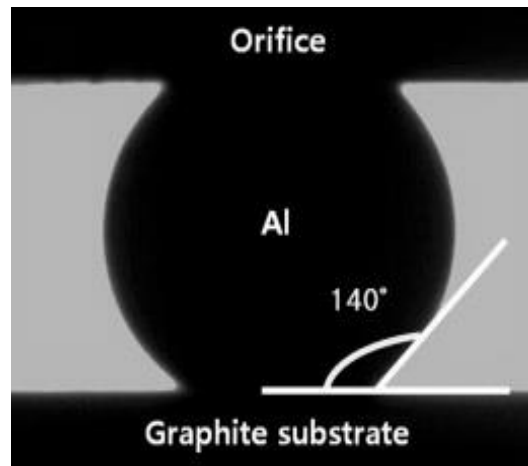
$$\gamma_{sv} = \gamma_{sl} + \gamma_{lv} \cos \varphi$$

Hence, contact angle φ can be expressed by,

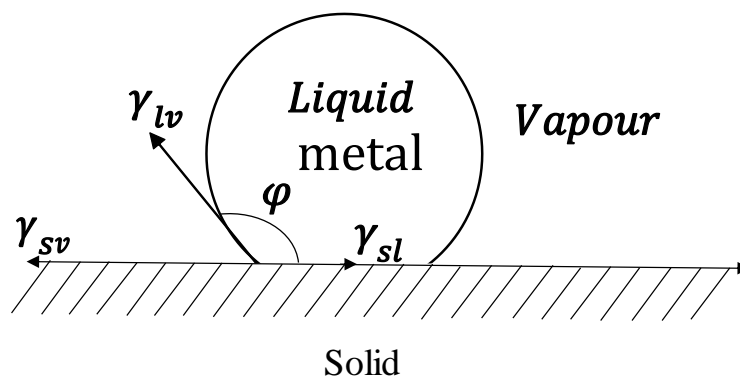
$$\cos \varphi = \frac{\gamma_{sv} - \gamma_{sl}}{\gamma_{lv}}$$

Where, γ_{sv} , γ_{sl} and γ_{lv} is the surface tension of solid-vapour, solid-liquid and liquid-vapour respectively²⁰⁴. Now, contact angle φ has greater significance since at contact angle less than 90° the droplet wets the solid surface and at angle greater than 90° it does not wet the surface.

In general, the graphite has poor wettability onto the Al and Mg surface with the angle ranging from 140 to 160° (Figure 2-6)^{205,206}. The technique applied for carbonaceous material reinforced metal matrix nano-composites is powder metallurgical process, thermal spraying, electrochemical deposition process²⁰⁷ and liquid metallurgy²⁰⁸. Each process can be classified into laser deposition, metal infiltration, and liquid metal stirrer processing for liquid metallurgy. The powder metallurgy process includes spark plasma sintering, cold compacting and sintering etc., to prepare the composite material. Thermal spraying includes plasma spraying and oxy-fuel spraying at high speed. Some other processing techniques are molecular level mixing²⁰⁹ and friction stir processing²¹⁰.



(a)



(b)

Figure 2-6: (a) The non-wetting condition of liquid Al-droplet on the graphite surface, and (b) Schematic diagram of a liquid metal droplet onto the solid surface²⁰⁵.

2.1.2.1. Spark plasma sintering:

The spark plasma sintering method (SPS), schematically illustrated in Figure 2-7, involves high pressure and temperature along with the pulsating current during the sintering process. The process leads to the formation of plasma with the help of micro discharge evolving from the impurities present on the particle surface²¹¹. The plasma enhances the heat transfer effect and produces a stronger bond by effectively cleansing the impurities present on particles. SPS techniques have many advantages over other processes, such as: quick sintering time, inhibiting the grain growth, producing the high-density product, and promoting better bonding between the composite phases. The technique has a novel application of achieving the microstructural integrity of the material by successfully closing the cracks and annealing the defects in the material. Due to compressive stress and restriction of further expansion, cracks are brought close to each other and are further bonded together by the energy of SPS technique²¹². The SPS

technique has successfully synthesised aluminum oxide and silicon nitride matrix²¹³ composites.

Inam et al.²¹⁴ investigated the effects of the SPS processing technique on the structural stability of graphene. The method used a dense Al_2O_3 sample with 3% graphene reinforcement that was treated at a dwell temperature of 1250°C - 1450°C and a pressure of 10–70 MPa. The initial GNP powder has high D- and G-peaks indicating significant defects present in the powder sample. Whereas, after the sintering process, depending on the dwell duration and temperature employed, the I_D/I_G ratio changed. The decrease in the ratio indicates minor damage when a high sintering time was utilized in combination with a higher temperature of 1450°C . The sample sintered with a low dwell time of less than 20 minutes uses the pressure of 50–70 MPa, whereas the samples sintered at 60 min dwell time use a pressure of 10 MPa. Sample sintered at lower temperature and dwell time shows the lower temperature for oxidation, indicating a high amorphous carbon²¹⁵. At the same time, the sample sintered for higher dwell time shows higher electrical conductivity indicating high content for crystalline carbon.

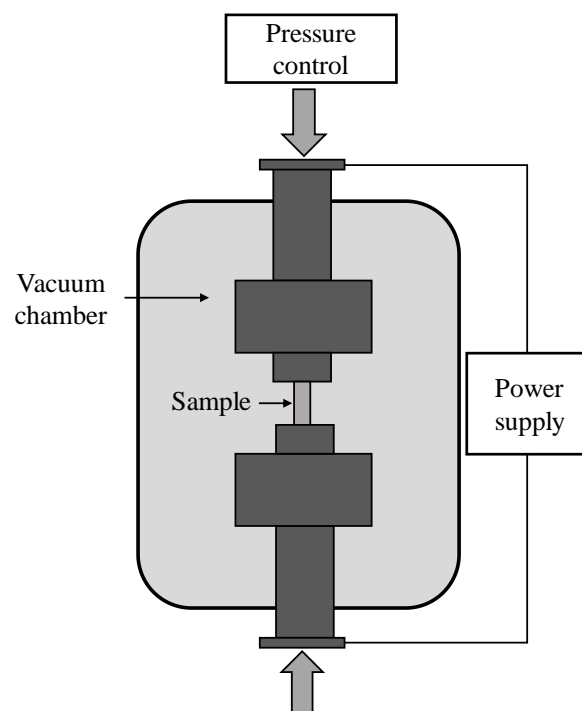


Figure 2-7: Schematic diagram of spark plasma sintering machine²¹¹.

2.1.2.2. Hot isostatic pressing:

Hot isostatic pressing (HIP) is the second most widely used technique for synthesising graphene metal matrix composites. The high pressure involved in the technique enables

complete densification of the composite material. The process utilizes metallic or ceramic powder to be fully densified by applying high uni-axial or isostatic pressure with temperature²¹⁶. The structural stability of GNP under SPS and HIP was similar when compared by Inam et al.²¹⁴. GNP's graphitisation was observed in the SPS technique when the sintering time was increased. However, the oxidation temperature and electrical conductivity were found similar when the sample was sintered under similar conditions. By employing the SPS process and sintering period of 10–20 minutes, the samples achieved complete densification with low oxidation start temperature and minimal electrical conductivity. There is less research available on HIP, and the study indicates that grain refinement was absent when this technique was utilized.

2.1.2.3. Thermal spray forming:

The thermal spraying technique involves the injection of powder particles from the spray gun to a hot jet in which they are heated and projected towards the substrate to get a surface coating. The coating layer is built by dropping the hot metal droplet on the cooler substrate and then flattening the droplet with final solidification. Thermal spray formation is subcategorized into plasma spray forming, oxyfuel high-velocity spray forming (OHVF), flame spray forming, an electric arc spray forming technique. However, plasma spray forming and OHVF are the most common method used for nanocomposite coating^{10,217}.

In plasma spray forming, arc is formed between the tungsten and copper nozzle being cathode and anode, respectively. A high-temperature plasma jet is formed when inert gas is pumped through the spark. The carrier gas feeds the material to be coated through the plasma jet, where it melts and propels the material at a stream velocity of 400-800 m/s²¹⁸. This technique is referred to as atmospheric induction plasma spraying²¹⁹. Low pressure is established at the chamber (with a vacuum or inert gas atmosphere) containing plasma guns and components to prevent the molten coating droplet from oxidising. The process can be called low-pressure plasma spraying or vacuum plasma spraying²²⁰.

Challenges with spray forming: The main problem arising from the spray forming process for developing MMC using carbonaceous material is the high processing temperature, leading to structural damage to the CNT/GNP reinforcement. Poyato et al.²²¹ reported the conversion of CNT into disordered graphite and carbon-nano onion at 1550°C. This

structural damage to the reinforcement can degrade the thermal and electrical properties. To overcome this problem, a cold spray or kinetic spray technique is used, in which the composite mixture is accelerated at a lower temperature to a high velocity of 500 to 1200 m/s. When a particle collides, its kinetic energy is transformed into plastic deformation energy. This energy ensures the excellent bonding of particles on the surface and reduces the effect of oxidation, melting, and grain coarsening effect to its minimum²²².

2.1.2.4. Metallurgical processing

The fabrication of carbonaceous material reinforced through metallurgical processing techniques is subdivided into hot rolling, hot extrusion, mechanical alloying, and solid-state friction-stir processing. As stated earlier, the significant difficulties in fabricating composites are the harsh environmental conditions implemented to consolidate metals. During this technique, the immediate attention is the survival of nano- carbonaceous material under harsh conditions.

2.1.2.5. Hot rolling:

A combination of ball milling and hot-rolling techniques was recently used to incorporate GNPs into the metal matrix during the MMNC/GNP composites fabrication. Saboori et al.²²³ studied the microstructure and thermal conductivity of Al-GNP sample by powder metallurgy and hot rolling process. The consolidation of the powder mixture was done through a duo roll-milling machine at speed of 5 RPM. As shown in Figure 2-8, the powder was first manually pressed inside the steel can and was further hot-rolled at 600 °C. The comparison result of both processes revealed that in hot-rolled samples, the thermal conductivity observed was relatively lower than that for the press sintered sample. The result was likely due to the sample's high porosity level produced by the hot rolling technique.

Moreover, one of the faults that might emerge as a result of the plastic deformation that occurs during the hot rolling process is micro void growth, as shown in Figure 2-8(d), it can cause density reduction in Al-GNP composites. The microvoids are eliminated by grain orientation during hot rolling at the Al-Al interface. However, the voids present at the Al-GNP interface are not readily removed due to GNP-GNP agglomeration; instead, get entrapped inside the agglomeration. Shin et al.²²⁴ effectively fabricated the Al/GNP composite by dispersing using ultra-sonication, ball milling, and hot-rolling techniques.

The result has shown that the composite produced with 0.7 vol.% GNP has a tensile strength of 700 MPa, which was 2-times higher than monolithic aluminum and had a maximum elongation of 4% before failure. The reason given was the higher surface area of few layer graphene (FLG), which effectively blocked the dislocation movement producing the deformation band in the composites.

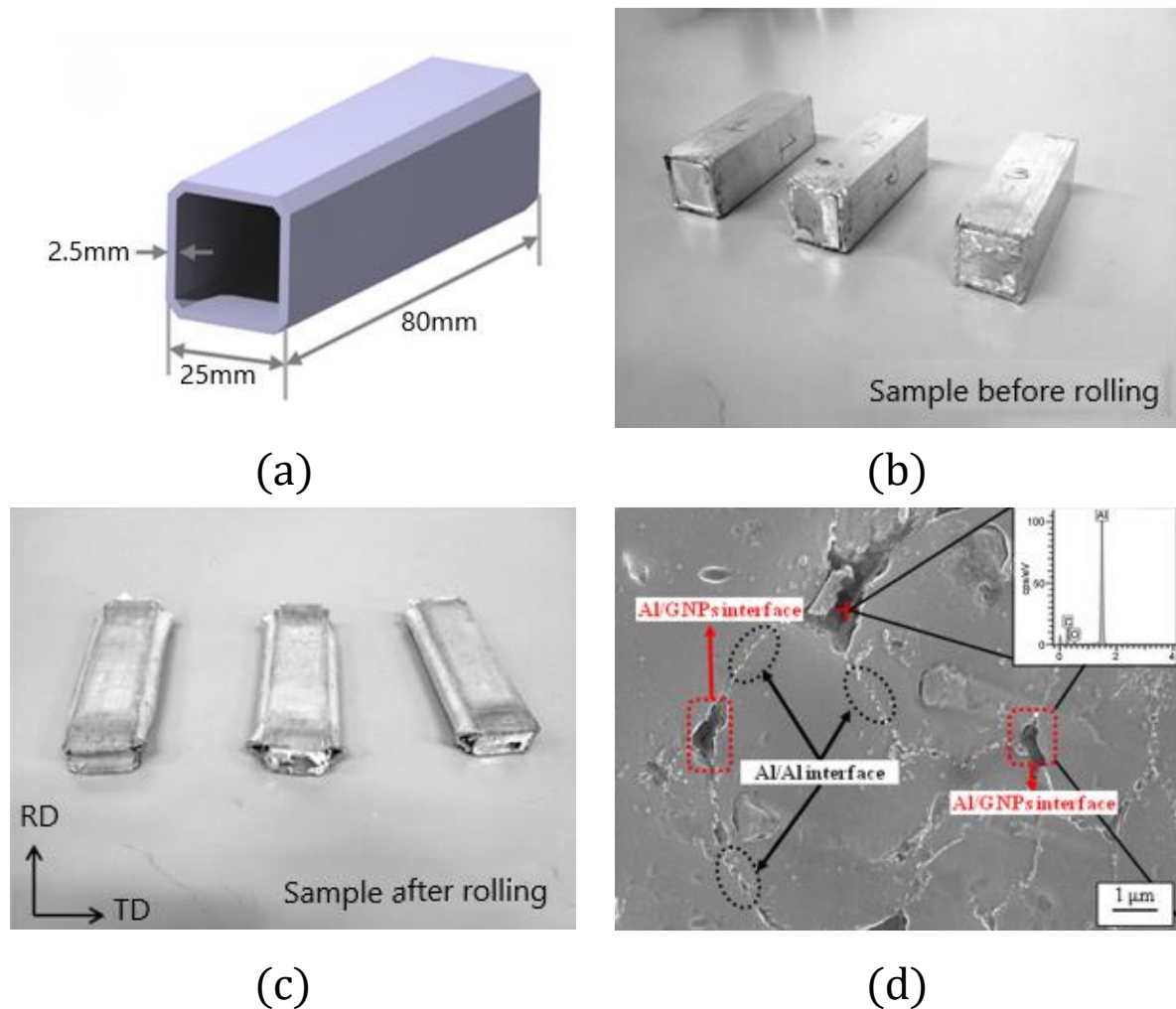


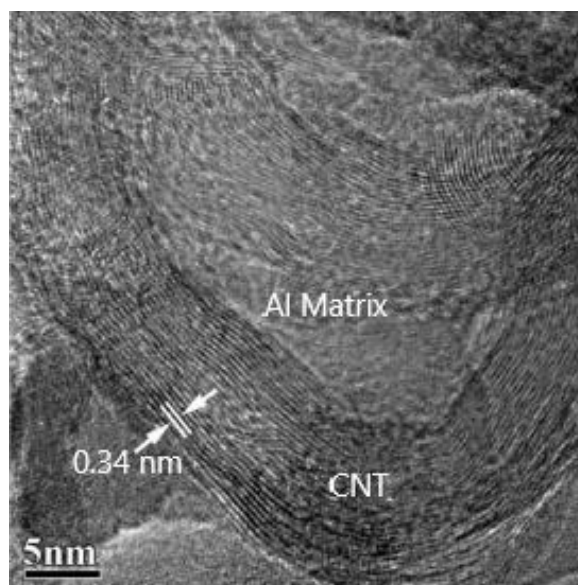
Figure 2-8: (a) Dimension of container used for consolidation, (b) & (c) sample before and after rolling process, (d) SEM image of the sample after rolling showing Al/Al and Al/GNP interface^{22,3}.

2.1.2.6. Hot extrusion:

Hot extrusion is a hot working process in which material is forced to flow through a shaped opening in a die. Since it is a hot working process hence, it inhibits work hardening. The biggest problem with graphene is the formation of carbide, and this carbide affects the strength of composites as it forms a brittle phase and does not effectively transfer load. Due to the less wetting ability of GNP with the aluminium grains,

the defects at the GNP/Al interface, such as microvoids, get elongated and produce the sight for micro-cracks to occur in future. It's worth noting that extrusion causes the billet to be in compressive and shear stress. Since no tensile force is generated, significant deformation is achievable ²²⁵.

Yang et al.²²⁶ used a new process to yield well-dispersed MWCNT with good interfacial bonding within an aluminum matrix. The procedure begins with creating Co/Al catalysts by sonicating $\text{Co}(\text{NO}_3)_2 \cdot 6\text{H}_2\text{O}$ molecules with Al powder soaked in ethanol. The resulting mixture was heated in the oven at 60°C to evaporate the ethanol, then dried for 6 hours at 80°C. In a hydrogen atmosphere, the dried mixture was heated at 250° C and 450° C, respectively. The technique produced a homogeneous coating of Co-particles on the surface of aluminum powder. MWCNTs were made by injecting a flowing mixture of C_2H_2 /argon into a reactor at 600°C with a Co/Al catalyst. The composite manufacturing starts with ball milling of prepared 2.5 wt % MWCNT/Al powder for 90 minutes at 500 RPM, followed by sintering and hot extrusion. Figure 2-9(a) shows the interfacial bonding between the Al and MWCNT, and Figure 2-9(b) illustrates that composite powder milled for 90 min has higher strength than those milled for 30 min. Rashad et al.²²⁷ studied the mechanical properties of Al/GNP composite fabricated through cold compacting, sintering and hot extrusion. The extruded composites showed an increment in hardness by 11.8%, yield strength by 14.7%, and ultimate tensile by 11.1% strength compared to the pure aluminium sample.



(a)

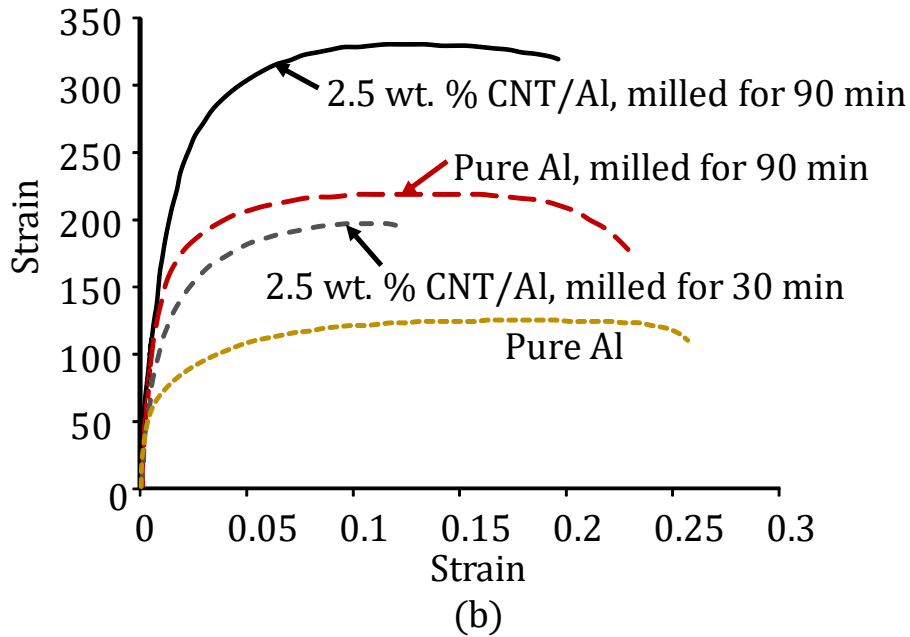


Figure 2-9: (a) HRTEM image of synthesized composites, and (b) Stress-strain diagram for composites milled for 90 min and 30 min, respectively²²⁶.

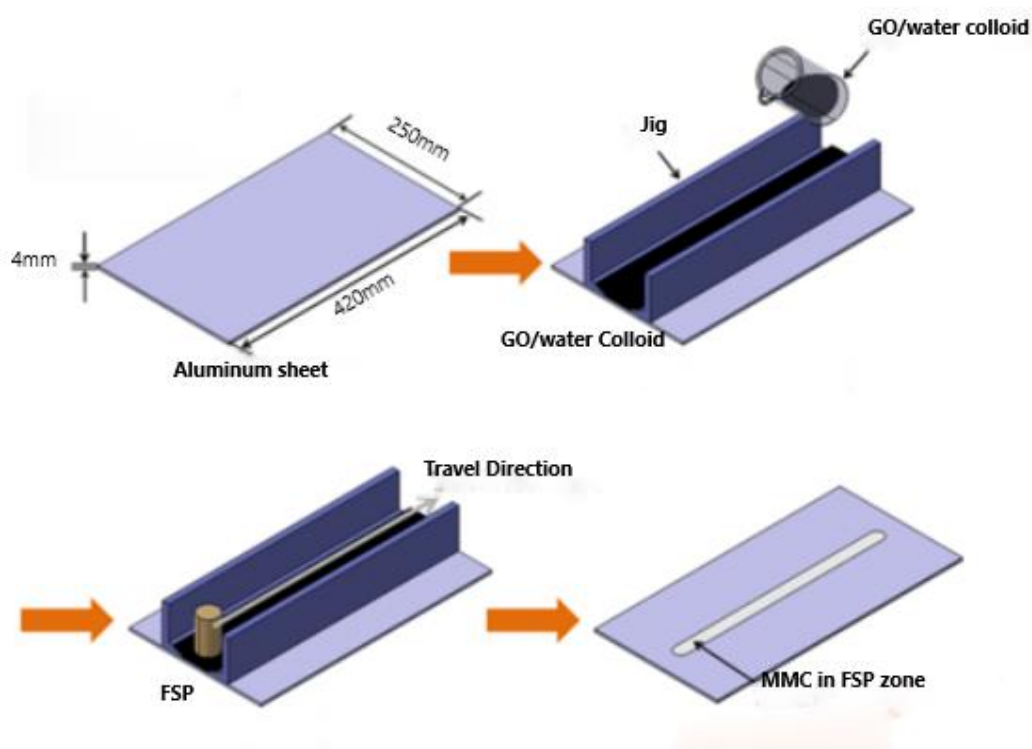
2.1.2.7. Solid-state friction-stir processing:

The friction stir processing technique (FSP) is the same approach used as in the friction stir welding process, where the non-consumable rotary tool is used to stir the material mechanically. A tool containing a shoulder and a pin provides frictional heating and mechanical mixing in the area covered by the tool. The process accompanies localised heat generation in the tool work zone, which partially heats and softens the material²²⁸. During this technique, a hole or groove is first machined on the material's surface. The groove works as a reservoir, keeping them from being swept away from the surface by the operation of quickly rotating tools. The process results in a severely plastically deformed or stir zone and leads to microstructural refinement and homogenization, resulting in extremely fine grains with nanoparticles inserted on the grooves. The transverse motion of the tool and its rotary action intermingles within the material to produce composite material. The schematic diagram of FSP is shown in *Figure 2-10*, where GO/water colloidal solution is used as reinforcement.

FSP has been developed in the broader field, covering micro-forming, superplasticity, cast modification, channelling, and powder processing²²⁹. FSP has a 'nugget' region where homogenization and microstructure refinement occurs. During the process, the temperature near the nugget region reaches up to 400–480°C²³⁰. For

nanocomposites, the nugget region is where the carbonaceous material would be placed in the sample, as shown in Figure 2-11. Since there are large deformation and strain in the material, a significant amount of mixing would occur. So, it is assumed that powder incorporated in this process would disperse thoroughly in the nugget²³¹. Despite intense plastic deformation, the solid-state FSP enables the attainment of large ductility in the product, which is because of dynamic recovery triggered by the generated frictional heat. The process consumes less time and money than that compared with powder metallurgy⁵¹. The good interfacial bonding and strength between the GNP/Al interface are due to dislocation movement restriction and load-bearing ability of graphene^{40,232}.

FSP, as compared with other metallurgical processing techniques such as extrusion and hot rolling, is not significant in the improvement of strength because the alignment of grains and nanoparticles do not occur efficiently. It is rather unsuitable for fabricating thick metal matrix components as the technique is effective only near the surface, which is in contact with the tool.



(a)

Figure 2-10: (a) Schematic of MMNC fabricated by FSP using GO/Water colloid²²⁸.

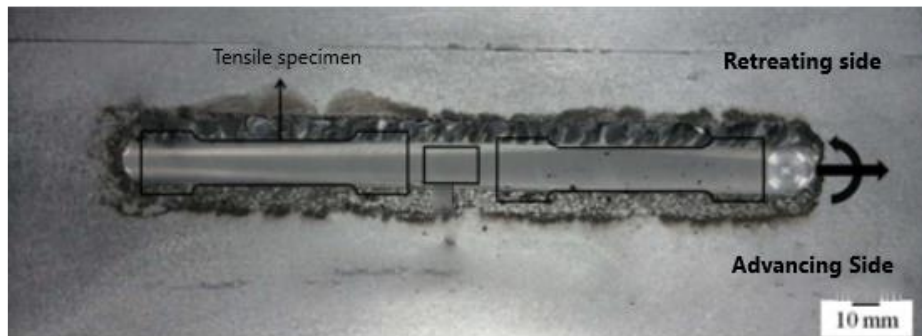
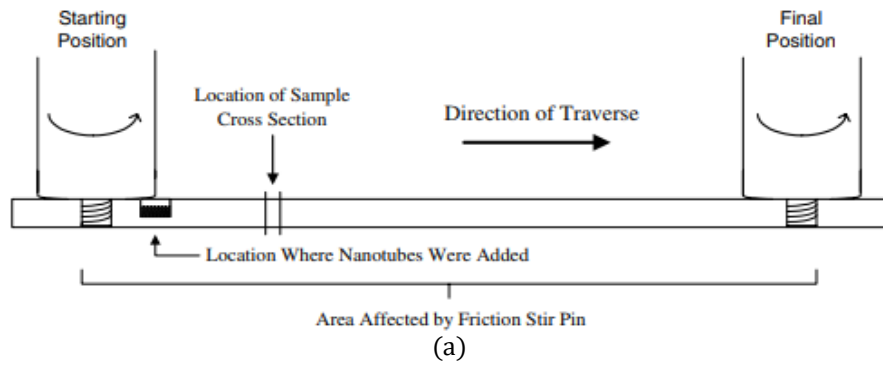


Figure 2-11: (a) Schematic showing the area affected by FSP pin, and (b) Top-view for the prepared composite sample²²⁹.

2.1.3. Recent dispersion methods and challenges

Various processing techniques have been developed to disperse carbon nanofiller into the metal matrix nanocomposites. The challenges such as structural damages to the nanofillers during the mixing/consolidation process and matrix reaction product at elevated temperatures hinder the research advances due to the sp^2 hybridized carbon atom on graphite's (001) plane. However, the interfacial reaction of metal with carbon nano reinforcements can occur via end and side contacts resulting in metal carbide formations. Though, it is well known that metal carbide formation depends mainly upon the Gibbs-free energy of metal carbide. Metals like magnesium and nickel have positive Gibbs energy, showing unwillingness for the carbide formation, whereas, titanium has negative Gibbs energy and is prone to carbide formation. Likewise, aluminum, silicon etc., are prone to carbide formation when exposed to carbon nanofillers. Aluminum and copper are the most widely used matrix material for synthesising nanocomposites because of their exceptional thermal and electrical conductivity and ability to use them in aerospace industries. Hence, proper dispersion either in solid or liquid state methods is essential for the better properties of the composite.

2.1.3.1. Solid-State dispersion technique by high energy ball milling process.

Powder metallurgy, along with ultra-sonication to a great extent, has achieved the uniform dispersion of carbonaceous material along with the good mechanical properties²³³ of synthesized composites. Mechanical alloying is one of the extensively used solid-state dispersion techniques to prepare metal alloys and MMCs because of its higher effectiveness and simplicity. The process involves the milling or refining of different powders with varying compositions and sizes for making alloys using a milling medium. The ball milling process implicates cyclic cold welding, re-fracture and re-welding of metallic powders involved resulting in grain refinement, work hardening²³⁴ and strengthening of composites/alloys to be synthesized²³⁵. The modification of the milling environment, milling time and milling methods has the most significant impact on the microstructure of composite/alloy produced to a greater end^{236,237}. Generally, dispersion is divided into three stages during ball milling of carbon fillers and metal powder. First, nano-reinforcements are distributed among spherical metal matrix powders. Second, CNT/GNP is dispersed on the surface of flake-shape metal powders by the micro-forge mechanism¹¹, and then finally trapped into the lamellar-structured powder, getting dispersed powder material.

Bastwros et al.²³⁸ successfully showed the effect of GNP dispersion by the ball milling technique. The work revealed that 10 min and 30 min ball milling times were insufficient to disperse the graphene particles into the Al6061 metal matrix uniformly. The increase in strength achieved was about 47% and 34% higher when milling time of 60 min and 90 min was used. Yu et al.²³⁷ showed an increase in tensile and electrical properties of about 22.5% and 17.4%, respectively, while using 0.3 wt% of GNP with 3 hrs of ball milling time. However, an extensive milling time of 4 hrs has resulted in the generation of a large quantity of Al₄C₃ phase and a decrease in the diameter of GNP resulting in an adverse effect on tensile properties.

2.1.3.2. Wet dispersion technique

This technique involves mixing GNP/CNT and metal matrix in an appropriate solvent followed by stirring and ultrasonication²³⁹. Ultrasonication involves sound waves to excite the powder particles, which form cavitation in the liquid solution to get uniform mixing. Sonication bath and tip sonicator are the two most commonly used devices for ultrasonication. Unlike the ball milling technique, particle size reduction and

contamination issues are absent in this method. As the uniform dispersion of GNP in the solution is attained, the matrix material is added to the dispersed solution to get the required composite composition. To achieve a homogenous solution, the composite mixture solution is ultrasonicated/stirred for a short time.

2.1.3.3. Colloidal processing

Colloidal processing is the method for generating matrix suspension by using the technique of colloidal chemistry. The technique is used to make a GNP-ceramic²⁴⁰ mixture by combining colloidal suspension of GNP and matrix powder. A similar solvent is usually preferred for mixing both materials to get a uniform medium for dispersion. The colloidal solution prepared is mixed slowly with the help of a magnetic stirrer, followed by ultrasonication to get uniformly distributed GNP in the matrix medium. Moreover, colloidal processing requires the modification of the surface for both graphene and the matrix material. The surface modification can be achieved either by functionalizing reinforcement (GNP/CNT) or by utilizing a surfactant that generates opposite charges on the mixtures. The modification, which generally involves building the opposite electric charges between the matrix particles and reinforcement, is commonly known as heterocoagulation. The heterocoagulation route is a very efficient technique for having well-dispersed CNT reinforced ceramic composites²⁴¹.

Arvanitelis et al.²⁴² investigated the 1.0 wt% carbon nanotube (CNT) in SiO₂ matrix composites using surfactant-assisted colloidal processing employing acid-treated CNTs and colloidal silica. Five systems were created by using a combination of cations and anions surfactants. The technique was to coat the CNTs with silica particles and create homogeneously dispersed CNT-ceramic composites. Grigoriev et al.²⁴³ studied the effect of graphene reinforcement on Al₂O₃ and SiC ceramic matrix composites. The composite with a small quantity of graphene, i.e. 0.5 vol.%, exhibited the highest flexural strength of (904 ± 56) MPa and fracture toughness of 10.6 ± 0.3 MPa with good dispersion of GNP in the composite by colloidal solution route.

2.1.3.4. Sol-gel processing

This method is used for making silica nanocomposites. The Sol-gel route is another method for producing GNP-glass or ceramic composites. The methods initiate with the synthesis of a precursor, which undergoes condensation to generate a green body with uniformly dispersed graphene. In this process, a stable dissolution of well-dispersed

graphene is formed in which tetramethyl orthosilicate is added. The suspension is then sonicated to get a thoroughly dispersed solution. A catalyst (acidic water) is added to initiate condensation, which initiates the hydrolysis process, and composite gels are produced²⁴⁴.

The sol-gel methodology is used to synthesise GNP reinforced composite having applications in solar cell electrode²⁴⁵, Li-ion batteries²⁴⁶, sensors²⁴⁷, microwave absorption²⁴⁸ and catalysts²⁴⁹ etc. For example, Zeng et al.²⁵⁰ employed the method to prepare SiO₂ coated GO composite to be used in electrochemical sensing of dopamine. The sol-gel process has the benefit of producing a transparent and mechanically stable film or other substantial material. Since it uses liquid precursors, it is easy to handle and utilized for making doping material.

2.2. Functionalization by ball milling technique

The functionalization of graphene nanoplatelets using a ball milling machine is a new technique that is being developed nowadays. Recently, it has been shown that solid-phase processing and the mechanical activation through the milling procedure can help synthesize different quantities of short and functionalized carbonaceous material²⁵¹. Ball milling is used to make a solution of carbonaceous material by forming a complex solution between CNT/GNP and various other substrates²⁵². The results have proven that the mechanical activation of CNT/GNP is a promising technique for the modification or functionalization of the carbonaceous material²⁵³. Noncovalent interaction, substitutional heteroatom doping of graphene, covalent C-C coupling, and hybridization with nanoparticles are a few techniques for graphene functionalization²⁵⁴. Due to the high repulsive interactions between the edge carboxylate groups, edge-carboxylate graphite (ECG) may be generated by ball-milling graphite powder (solid-state) in the presence of dry ice. In polar solvents (e.g. water), the resulting ECG can be further exfoliated into few-layer nanosheets, resulting in improved dispersability in various solvents²⁵⁵.

It was recently reported that dry ball milling graphite in an N₂ environment results in adequate direct nitrogen fixation at the boundaries of graphene nanoplatelets. Although N₂ is typically considered an inert diatomic gas, it may easily react with active carbon species produced by the mechanochemical breaking of graphitic C-C bonds. A thermodynamically favourable process, aromatization drives GNP's direct edge nitrogen fixation utilising N₂ gas²⁵⁶. Xu et al.²⁵⁷ have used a simple ball milling technique for eco-

friendly synthesis of GNP's functionalized with sulfur to get S-GNP for highly efficient lithium-sulfur batteries (LSB) cathode material. LSBs based on the S/GNP cathode material were synthesized by adding 30 wt. % of graphite and the rest of sulfur. *Figure 2-12 (a)* shows the schematic representation of S-GNP produced, and *Figure 2-12 (b) & (c)* shows the deposited sulfur particle on the surface of GNP. The material synthesized was able to show a high initial reversible capacity and was due to the excellent electrochemical performance formed by the 3D sandwich structure of the material formed.

2.3. Graphene reinforced composites

2.3.1. Graphene reinforced aluminum matrix composites

The melting and boiling points of pure aluminum (Al) are 660.4 °C and 2400 °C, respectively. It has an atomic weight of 26.98 and an atomic number of 13. It has a density of 2.7 g/cm³. It is the third most prevalent metal in the earth's crust and is a lightweight, ductile metal with a density of about one-third that of iron. Pure aluminum is an excellent heat and electrical conductor and is easy to weld. Aluminum's properties make it the best option for its application in the industrial and aerospace industries²⁵⁸. The reduced weight combined with higher mechanical properties such as high strength, stiffness and elastic modulus can make it suitable to fulfil its need in modern aerospace and automobile industries. However, the lower mechanical properties of pure aluminum do restrict its use. Aluminum-based metal matrix nano (MMNC) composites are the most commonly used MMNC in automobile and aerospace applications. Reinforcement, generally non-metallic or ceramics such as SiC, Al₂O₃, C, B, B₄C, BN etc., can be mixed efficiently and easily in molten aluminum¹.

Table 2-2 is a brief overview of graphene reinforced aluminum matrix composites with different graphene percentages as reinforcement. Boostani et al.²⁵⁹, in their study, encapsulated graphene sheets into silicon carbide (SiC) particles by the ball milling process. The process prevented the agglomeration phenomenon during the solidification of composites, leading to a lower defect on the interface.

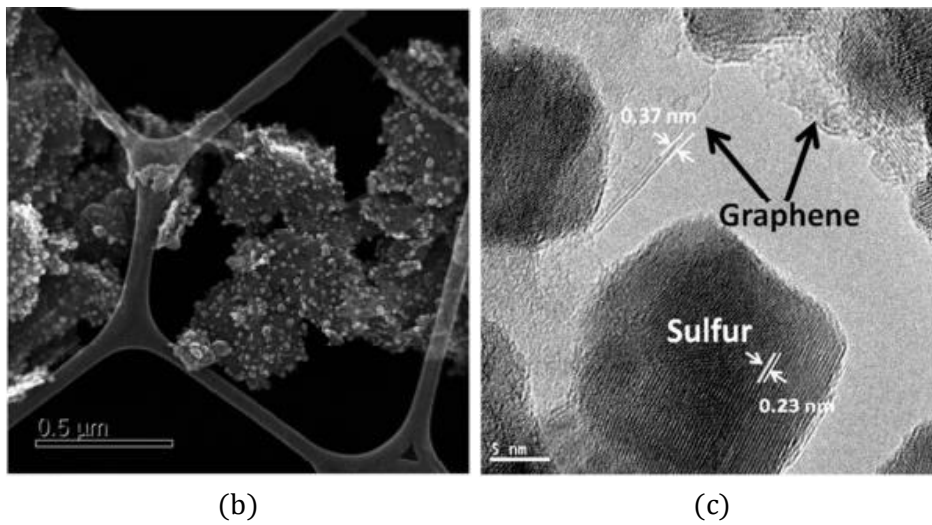
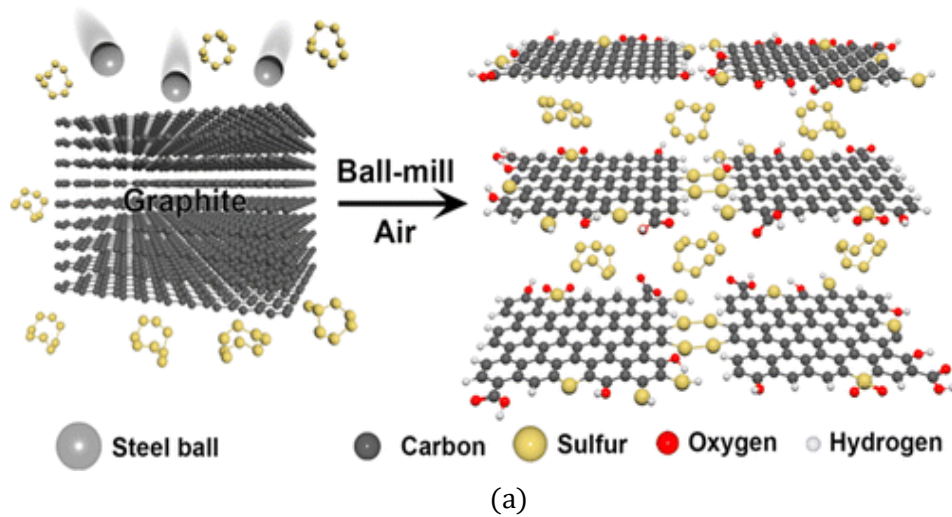


Figure 2-12: (a) Schematic representation of S-GNP's preparation, (b) & (c) The deposition of ~ 10 nm sulfur particles/amorphous sulfur into the GNP multi-layered structure²⁵⁷.

Baig et al.²⁶⁰ dispersed graphene in aluminum by colloidal processing, which combines sonication and surfactant dispersion. In his experiment, the performance of two types of surfactants, i.e. anionic-sodium didecylbenzene sulfonate (SDBS) and nonionic polymeric, ethyl cellulose (EC), was analysed. The results showed that integrating surfactant-assisted GNPs considerably enhanced Al nanocomposites' characteristics compared to pure Al. The EC based Al composite has 31% higher hardness, and a 98% lower wear rate, at 0.5 wt.% GNPs²⁶⁰. Prabhakaran et al.²⁶¹ used laser shock peening technique²⁶² to modify the surface texture and microstructure of 0.4 wt.% graphene aluminum metal matrix composite. The addition of graphene improved the ultimate tensile strength by 42% whereas laser shock peening contributes to a 10% enhancement in the strength.

Table 2-2: Overview of graphene reinforced aluminum matrix composites^{42,46,268-273,47,54,238,263-267}

Year	Reinforcement	Processing Strategy	Mechanical Properties and merits/demerits
2014	1 wt% few layers graphene	Ball milling at 10, 30, 60,90 min. Pre compacting and hot compacting	Strength increases for composites and was 47% and 34% for 60 min and 90 min milling
	GO-water collidal solution	friction stir processing	thermal conductivity 171.698 W m ⁻¹ K ⁻¹ , tensile strength 191.9 MPa, elongation 28%
	0.25, 0.50 and 1.0 wt % GNP	High energy ball mill Spex 8000M (1,3 and 5h milling time), compacting	good mechanical bonding, lack of GNP clusters, presence of aluminum carbide detected, higher hardness value obtained at 2h sintering
	0.15 and 0.5 wt% GNP	Ball Milling at 75RPM for 12h, Hot isostatic pressing	Yield strength increases from 214 MPa to 319 MPa at 0.5 wt%
	1% Mg, 1% Al, 0.18% Sn	Semi powder metallurgy	yield strength 161 MPa, tensile strength 236 MPa, fracture strain 16.7%
2015	0.5, 1.0, 1.5 and 2.0 wt% GNP	V- Blender at 17 RPM for 24h+ attritor at 180 RPM for 2h and hot extrusion	Increase in ultimate yield & strength at 1 wt. % graphene, strong, clean interface was developed
	Mg- 0.5-1.5 Al, graphene	Semi powder metallurgy	162 MPa Yield Strength, 195 MPa tensile strength, 3.7 % fracture strain
	Al + graphene	Powder metallurgy and hot rolling	262 MPa Yield Strength and 13 % Fracture Strain
2016	RGO, GNS	Cold compacting and sintering in inert atmosphere	Increase in strength with respect to pure Al was 32% and 43% respectively for the 0.3 wt.% rGO-Al and 0.15 wt.% GNS-Al composites
	GNP reinforcement, Al5083 matrix	ball milling with smaller collision energy, sintering	1.0 wt.% GNP, both the yield strength and ultimate tensile strength are enhanced by 50%
	GO reinforcement in Ni-Al matrix	Metallic plasma sprayed coating	Hardness, adhesion strength and wear resistance by 49%, 18%, and 14%, respectively.
2017	GNP 3 Vol% , Al-Mg alloy matrix	friction stir processing,	Yield strength improved by 300%, Hardness increased by 53%, some Al ₄ C ₃ phase may form at the interfaces due to solid state chemical reactions
	GNP	Surface nano composites, Electrical resistance heating and application of localized pressure	Five times increase in surface hardness was achieved; hardening effect due to graphene impregnation is more prominent in the subsurface region at a depth of 1-200 μm.
	GNP/Al composite, less than 5 wt.% GNP	Spark plasma sintering	Hardness increased by 21.4% with 1wt. % GNP. Yield and tensile increased by 84.5% and 54.8% with 1 wt. % GNP.
	multilayer graphene (0 - 10) vol.%, Aluminum nitride ceramic	Spark plasma sintering	High directionality of heat conduction obtained, thermal conductivity 80 W m ⁻¹ K ⁻¹ for the in-plane direction and nearly half for through plane. More than 5% graphene has high electrical conductivity

Cano-crespo et al.²⁷⁴ compared the behaviour of GO and CNT reinforced composites prepared by spark plasma sintering process. As a result, GO reinforced composites were systematically more creep resistant than carbon fibre reinforced composites. Since grain sliding²⁷⁵ controls creep, the grain mobility in graphene reinforced composites was substantially lower than that of the same quantity in nanofibre reinforced composites.

Apart from the role of graphene in increasing the mechanical behaviour of composites, graphene is used in self-lubricating composite to reduce wear and frictional coefficient values. A similar experiment was performed on the tribological performance of Al6061-graphene reinforced metal matrix composites with different speed, load, and graphene content values, as shown in Figure 2-13. On increasing the graphene content, wear loss and frictional coefficient value decreases and reaches an optimum value of 0.4 and 0.6% by forming a solid lubricant layer between the wearing surfaces²⁷⁶. Many researchers have proposed a different approach for the manufacturing of composites. All of the techniques are centred on the homogeneous amalgamation of graphene and eliminating the formation of aluminum carbide. Prabhakaran et al. used Graphene nanoflakes in combination with aluminum oxide as reinforcement in the aluminum alloy as matrix material. It was observed that densification increased during microwave sintering²⁷⁷ due to the increase in the diffusion rate and is found to be directly proportional to the sintering temperature. The flake morphology of graphene obstructs the particle movement during loading, leading to narrowing the distance between them and thus increasing the hardness and density. In the study of the addition of GNS in glass fibre reinforced polyamide-6 composites containing aluminum hypophosphite (AHP), it was found that AHP has successfully reduced the flammability while improving the thermal stability of the composites. In contrast, GNP improved the mechanical properties and mitigated the dipping phenomenon by improving the melt viscosity of composites²⁷⁸.

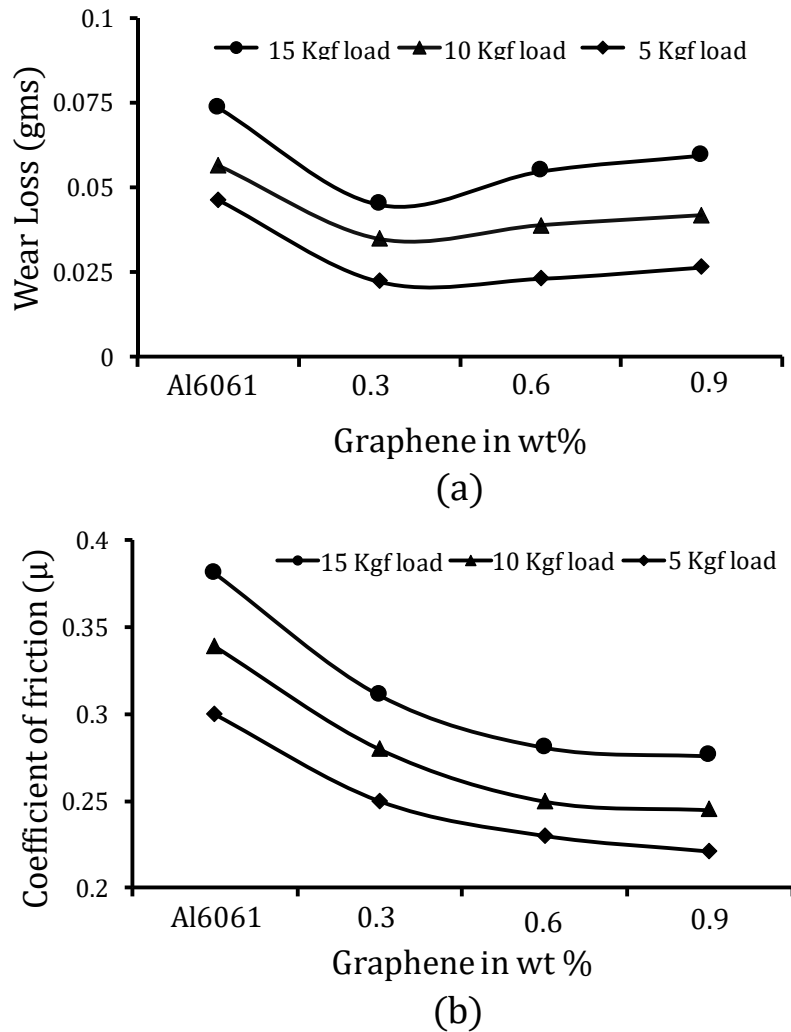


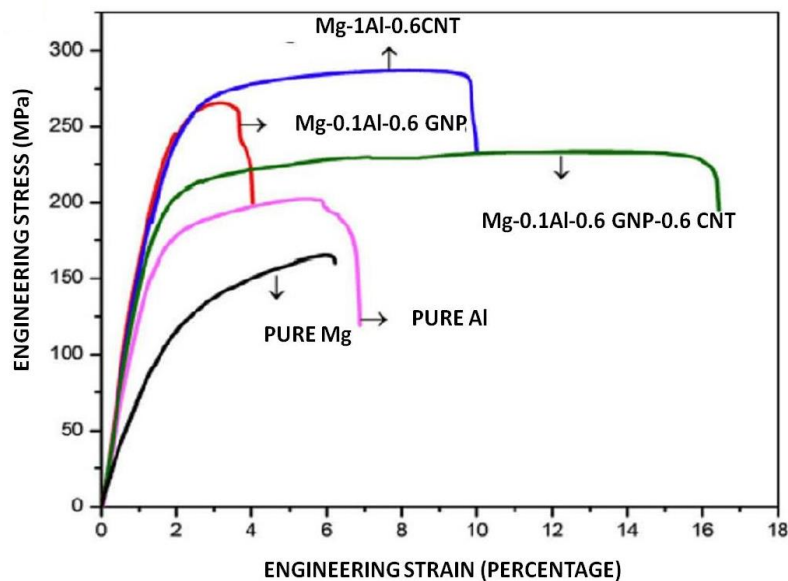
Figure 2-13: (a) Wear loss, and (b) Coefficient of friction as load function²⁷⁹.

2.3.2. Graphene reinforced magnesium matrix composite

Magnesium (Mg) is the eighth-most abundant and lightest metal on the earth crust, having a density of 1.74 g/cm³. Magnesium alloys and their composites can decrease the component weight by 35% to 75% compared to aluminum and iron-based materials, thus improving the fuel efficiency^{280,281}. However, due to its low strength, ductility and wear-resistant properties, it is not much used in structural applications when in the purest form. However, when Mg is used with other materials, it synthesises material with properties much greater than monolithic magnesium.

Table 2-3 gives a brief overview of graphene reinforced magnesium matrix composites with different graphene percentages as reinforcement. Mg-GNP^{259,282} composites were successfully manufactured by ultrasonic processing and solid-state stirring, slurry mixing, ball milling and SPS technique, etc⁵¹. Khodabakhsh et al.²⁷⁰

used the friction stir processing method to disperse and fabricate composite using glassfiber reinforced plastic (GRP) in Al-Mg alloy matrix. The resultant composite has a hardness of 84HV and an improvement of 300% in yield strength. The attained properties were due to the large coefficient of thermal expansion and the mismatch strengthening mechanism influenced by graphene's large surface area. Mg-graphene nanocomposites processed by powder metallurgy can achieve relative density up to 97-99%. The report of carbide formation for Al-GNP composites has been reported in the past, whereas in the case of Mg-GNP composite, there is no report of carbide formation till now. The inclusion of magnesium in the Al-Mg-GNP composite can hinder carbide formation, whereas this topic of research is still to be studied deeply. As shown in Figure 2-14, Mg-GNP composites exhibit greater yield strength, ultimate tensile strength, and ductility than pure Mg. More ductility was due to the less porous structure of composite than that of pure Mg. Pure Mg is brittle because of its limited-slip systems in magnesium crystal⁵⁴.



(a)

Figure 2-14: Ambient temperature tensile test for Mg-matrix composites at various reinforcement concentrations²⁸³²⁸⁴.

Rashad et al.²⁸³ studied the influence of CNT/GNP as reinforcement on the mechanical performance of Mg-matrix composites. The results have shown that with the same amount of GNP or CNT or GNP + CNT, CNT has more strengthening effect than GNP, whereas CNT + GNP has more ductility (Figure 22).

Table 2-3: Overview of graphene reinforced magnesium matrix composites^{54,283,293-300,285-292}.

Year	Reinforcement	Processing Strategy	Mechanical Properties and merits/demerits
2014	Graphene content as 0.18,0.36,0.54 % in Mg-1%Cu matrix	semi powder metallurgy	Yield and tensile strength increases from 160MPa and 240 MPa for 0.18% GNP to 226 MPa and 260 MPa for 0.54 % GNP respectively
	Mg-1Al-0.6 wt.%(CNTs + GNPs)	Powder metallurgy with extrusion	Composite reinforced with hybrid CNP+CNT has higher failure strain than that of individual.
2015	Graphene 0.3 wt % of 5-15nm thickness	sintering, compacting, extrusion	young's modulus 13.8 GPa , elongation 16.9 %
	GNP and CNT	High end ball milling, Hot sintering and extrusion	Tensile fracture strain of AZ31 magnesium alloy composite was increased by +49.6 % with 0.3wt.% GNP compared to -8.3% regression for 0.3 wt.% CNT
2017	R-GO	Powder metallurgy	Hardness improved by 64 HV, 0.3 wt% of R-GO depicts low corrosion rate of 3.57×10^{-7}
	GNP (0.1,0.25 & 0.5 %)	semi powder metallurgy	Hardness and wear behavior increases with graphene content, best wear performance was at 0.5 wt% GNP with 10N load, agglomeration becomes dominant beyond 0.5 wt% GNP
	MgO coated graphene	Casting method, chemical precipitation method	7 wt % MgO@GR, which contained 12.3 wt % GR, the thermal conductivity increased by 76%, composite exhibits good thermal conductivity and electrical insulation performance.
2018	nickel coated GNP (Mg-3 Al-1 Zn-0.5 GNPs)wt.%	Vacuum hot-press sintering process, hot extrusion.	Micro hardness increases of 0.5 wt% (GNPs+Ni)/AZ31 compared to AZ31 and 0.5 wt% GNPs/AZ31 are 34.71% and 8.2% respectively. With nickel improves interfacial binding.
	(0.05 & 0.10) wt.% GNP	Facile melt stirring and hot extrusion processes.	Less addition of GNP results in better dispersion and ultra-high strengthening efficiency of 1550 i9s obtained. With only 0.05% of GNP modifies yield strength by 62% and 79% for 0.10% GNP.
	CVD of carbon in form of Few layer graphene(FLG) on MGO powder grain	Spark plasma sintering	Electrical percolation threshold for the FLG/MgO nanocomposites is below 0.56 vol%. Strong increase in strength and micro hardness was observed.
2019	GNP in AZ91D magnesium alloy matrix.	Has applied thixomolding process for the first time to prepare graphene-reinforced nanocomposite	UTS, elongation, hardness and Porosity were 38.4%, 85.7%, 29.9%, and 33.3% higher than pure AZ91D.
	GNPs (0.1 and 0.6 wt%) in AZ80 matrix	Rheo-casting followed by hot extrusion	Studied the effect of GNP content in microstructural and mechanical properties. The tensile and compressive yield strength was enhanced by 50% and 37%.

Kavimani et al.³⁰¹ prepared composite by linear electrodeposition technique by using RGO/SiC deposition on Mg surface to investigate the corrosion behaviour of composite prepared. The corrosion result obtained from the test of electrochemical measurements in two different aqueous electrolytes of NaCl and Na₂SO₄ revealed a sharp decrease in corrosion rate for RGO/SiC composite coating. Rashad et al.³⁰² studied the corrosion behaviour of Mg/ GNP composite in NaCl solution. Experimental results showed that GNP's presence in different matrices decreases the corrosion resistance of the composite.

2.3.3. Graphene reinforced iron matrix composites

Iron is one of the essential materials in manufacturing industries because of its strength, magnetic properties, formability, and ease of casting. Though the introduction of graphene is very recent in research and its use in manufacturing sectors, the inclusion of graphene in iron or iron oxide matrix is still reported very little. Table 2-4 gives a brief overview of graphene reinforced iron-matrix composites having varying graphene percentages.

Lin et al.³⁰³ investigated the synthesis of graphene oxide reinforced iron matrix composites processed through a laser-guided sintering technique. The composite obtained had a microhardness increased by 93.5% more than the base material. Further investigation revealed that the increase in hardness value was due to the formation of cementite. Cementite is a brittle phase and has 6.67% carbon and 93.33% of iron which can harm the properties of composites. Graphene oxide composite is used excessively in electronics industries as supercapacitors with high cyclic stability. Though pseudocapacitive material has high theoretical capacitance, its use is limited to low cyclic stability. Hence, using this type of Fe₂O₃/GO composites overcomes the defect and provides high cyclic stable and thus super composites³⁰⁴.

2.3.4. Graphene in copper matrix composites

Pure copper has various applications in an electromagnet, vacuum tubes, heat sinks, welding electrodes, semiconductors, and magnetrons in the microwave. However, it suffers low structural application. Copper matrix composites have excellent properties and have vast applications in bearings, heat spreaders, and a wide range of instruments requiring a lower thermal expansion coefficient and higher electrical and thermal conductivity³⁰⁵. The mechanical and physical characteristics of graphene in the copper

matrix are considerably affected by its uniform dispersibility. However, the non-uniform distribution may affect the desired properties³⁰⁶⁻³⁰⁸.

Table 2-4: An overview of graphene reinforced iron-oxide matrix composites.^{303,309-313}

Year	Reinforcement	Processing Strategy	Mechanical Properties and merits/demerits
2014	N-doped graphene.	one-pot pyrolysis process of a Fe based metal organic framework	Material has superior electro chemical performance i.e. high discharge capacity and good capacity retention needed for Li-ion battery.
	2 wt% GO	Laser sintering	Surface micro-hardness was increased by 93.5% by laser sintering of 2 wt.% GO.
2016	(Ni/Fe)/Graphene-composite coating with graphene concentration of 3gL ⁻¹	electro-deposition technique on stainless steel substrate	The micro hardness value got increased upto 581.0HV and elastic modulus of 213.3 GPa which was 14.9% of the substrate.
	0.5, 1 and 2 vol% of GNP and CNT on FeCo alloy	Spark plasma sintering	Maximum induction (B_{sat}) of 2.39 T and 18 % increase in hardness value was observed in the 1 vol% GNP.
2017	5 wt.% of equal mixture of graphene in ferrimagnetic iron oxide	Current activated pressure assisted densification.	The thermal conductivity increased by 2.6 times without decrease in saturation magnetization
2018	Ni-Fe-Graphene composite coatings was developed with graphene concentration 0.05 g L ⁻¹ to 3 g L ⁻¹	Electro deposition process	1 g L ⁻¹ graphene concentration, Ni-Fe/Graphene composites coating exhibit the greatest hardness of 912.6 HV and good wear resistance (friction coefficient of 0.1990).
	Steel based welding surface were coated with graphene suspension.	Welding of steel plates	Graphene refined the microstructure promoting the fine acicular ferrite formation. Strength and ductility improved and hardness was found unchanged.

284,314.

Table 2-5 gives a brief overview of graphene reinforced copper matrix composites with various graphene percentages as reinforcement. Gao et al.²⁸⁴ prepared Gr/Cu composites with different graphene content by an electrostatic self-assembling process. *Figure 2-15* illustrates that the negatively charged GO and positively charged Cu powder were prepared by coating it with hexadecyl trimethyl ammonium bromide and the powder methodology process. *Figure 2-16(a)* shows the bonding between GNP and copper matrix. A high strength bonding and good wettability can be seen in the Cu/GNP composites compared with the case of Al/GNP composites. Zhang et al.³¹⁴ studied two

different reinforcements, i.e. GNP and rGO, in the Cu matrix through a molecular-level mixing process (MLM). From Figure 2-16(b), the strength of the GNP/Cu composite first increases with an increase in GNP and then decreases with a further increase in GNP. Whereas, in the rGO/Cu composite, the strength of material continually increases with an increase in rGO content from 0.05 to 1%. Better interfacial bonding and good structural integrity were the reason for composite to exhibit higher yield strength below 0.5 vol.%, whereas when the concentration increases beyond 0.5 vol. %, the GNP aggregation was predominant, which was not observed in the case of rGO. The aggregation results in high porosity by restricting metal matrix flow into GNP. The porosity causes stress concentration and ultimately decreases the strength of composite material.

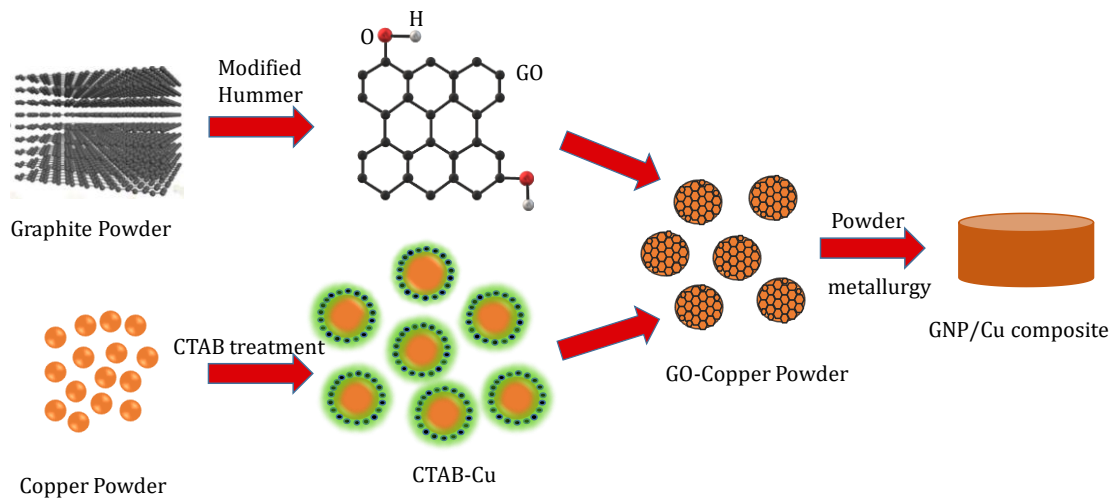


Figure 2-15: Graphical representation for GNP/Cu composites

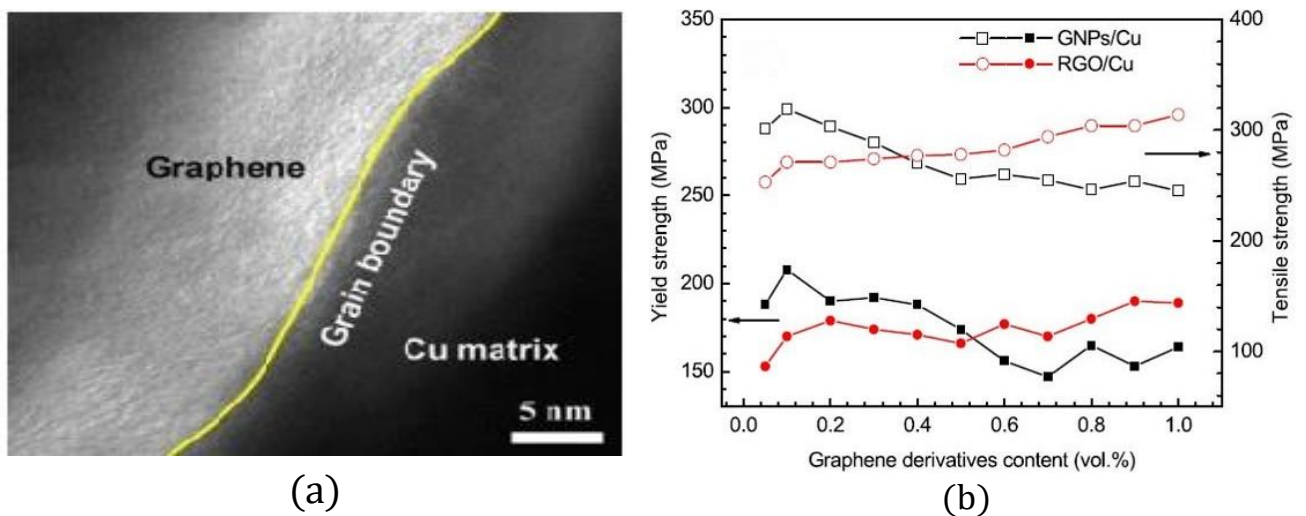


Figure 2-16: (a) HRTEM image of graphene Cu composites and (b) Yield and tensile strength of graphene/Cu composites versus graphene derived volume fraction^{284,314}.

Table 2-5: Overview of graphene reinforced Copper matrix composites^{53,235,322,323,314–321}

Year	Reinforcement	Processing strategy	Mechanical properties and merits/Demerits
2014	3,5,8 and 12 vol%	ball milling (1200 rpm for 3h), hot pressing & sintering	yield strength and young's modulus increases by 114% and 37% with 8 vol.% GNP content, defect density increases with milling
	0.5 and 1 vol%	ultrasonication and dry milling at 400 rpm at 4 h	increase in UTS and YS at 1 vol.% GNP, introduction of defects due to milling
	GO Concentration 0.5 g L ⁻¹ electrolyte	Pulse reverse electrodeposition	Hardness 2.5 GPa, Elastic modulus 137 GPa
	0.8 vol% Ni-GPL	Solution , Sonication and SPS	Tensile Strength 245MPa, elongation 9%
2015	1 and 2 wt%	ball mill for 5h, hot pressing	effective dispersion at 1 wt.% and 50 % increase in hardness with 2 vol.% GNP
	1, 2 wt%	ball milling and uniaxial hot pressing	modulus 104 GPa, 2 wt.% 2-4 nm hardness 62 HV, electrical resistivity 10 ⁻⁸ ohm- meter
	0.3 wt % single layer RGO	hot pressing, GO fill in 'brick-and-mortar'	Yield strength 233 MPa, Tensile strength 218MPa, modulus 109 GPa
2017	RGO/Cu composite coating was done	electrodeposition with [Cu ^{II} EDTA] ²⁻ and GO sheet solutions	Tribological tests with 0.27 wt. % RGO has low COF (0.24–0.26) and specific wear rate which is 35%–40% and 10–18 times of pure copper
	Sandwich model i.e. single copper film in two graphene layers (1Cu@2GNR), (2Cu@3GNR), (3Cu@4GNR), (4Cu@5GNR)	solidification of two-dimensional liquid copper confined to graphene layers using molecular dynamics simulations	2Cu@3GNR composites obtain the largest Young's modulus, tensile strength and fracture strength among all the models except fracture strain and 1Cu@2GNR has the largest fracture strain
	Graphene Nano Sheet (GNS)	powder metallurgy technique, at high pressure of 1 GPa and high temperature of 750 °C	290 MPa, 280 MPa at 2 wt.% and 1 wt.% addition of GNS which is 10 % more than pure copper
	CNT 0.2, 5, 10 SWCNT and 5, 10 MWCNT	High energy milling and SPS technique	Yield strength has increased by 2 to 3 times. MWCNT composite has lower hardness than SWCNT composite.
2018	Cu-ZnO/RGO nanocomposite photo catalyst	microwave-assisted hydrothermal method	due to copper and RGO doping leads to enhanced visible light absorption and reduced electron-hole recombination
	mesoporous SiO ₂ , 10% Cu ₂ O-graphene composite	self-assembly method by using silica precursor, Cu ₂ O-graphene content, Plutonic P123, and calcination at 550 °C	Mesoporous structure of the silica nanoparticles plays a significant role in increasing the photo degradation effect, combination of TEOS and 10% Cu ₂ O-graphene (M10) composite is much more effective.

2.3.5. Other graphene metal matrix composites

Graphene with different metals is vastly used in various other research fields to enhance their performances. For example, manufacturing of superconductors, photocatalysts in the advanced oxidation process, batteries electrode etc. Zhu et al.³²⁴ made ZnO coated with graphene using the solvothermal method. The resulting composite has a large surface area, enhanced light harvesting in the visible region, better separation efficiency, and a fast transfer rate of photo-generated carriers. Various other graphene-based MMCs are GNP/Ni composites, GNP/Au composites, GNP/Pt composites, GNP/Pb composites, GNP/Cd composites and graphene-TiO₂ composites^{55,325-329}.

Alexander et al.³³⁰ synthesised GNP-reinforced boron carbide-based composites using a hot pressing technique. The composite showed improved fracture toughness by $5.41 \pm 0.55 \text{ MPa m}^{1/2}$ with 10 vol% GNP. Mu et al.³³¹ have used the spark plasma sintering technique combined with the hot rolling process to prepare Ti-matrix composite with low graphene content. The composite formed exhibited an ultimate tensile strength of 887 MPa along the rolling direction, 54.2% higher than that of pure titanium. Nieto et al.³³² has fabricated GNP reinforced tantalum carbide composite by SPS technique. The inclusion of GNP improved the fracture toughness by 99% through toughening mechanism, i.e. GNP bending, sheet sliding, crack bridging and crack deflection. Rashad et al.³³³ reinforced magnesium with copper/GNP hybrid particles. Compared to monolithic Mg, the results showed enhanced strength and failure strain.

2.4. Strengthening methods in metal matrix composites

A large quantity of research has been done to improve the mechanical properties of metal by the intervention of nanofiller reinforcements. As a result, it's crucial to understand how reinforced metals improve the strength of a composite. Filler reinforced metal composites have two purposes: (i) primary stress-bearing material and (ii) plastic deformation or dislocation intervening material in the matrix²⁶⁶. Strengthening is influenced by various parameters, some of which are directly connected to the type of nanofillers used, and others are temperature, pressure and the conditions in which GNP's is processed^{334,335}. One of the main reasons for the variations is that the carbon nanofillers react differently depending on the conditions, such as ball milling time, ball-particle ratio, etc. To evaluate strengthening effect, the possible strengthening mechanism for the GNP-MMCs are: (i) grain refinement strengthening²³⁵, (ii) orowan

strengthening^{51,283,336-338}, (iii) efficiency of load/stress transfer from matrix to GNPs³³⁹⁻³⁴¹, and (iv) dislocation strengthening^{224,314,342,343}. Table 2-6 represents various mechanisms and equations for strengthening to evaluate metal matrix composites strength. Other strengthening mechanisms reported in the literature are as follows³⁴⁴:

- load transfer mechanism;
- dislocation interference mechanism (Orowan strengthening);
- mismatch in thermal, elastic, or geometric moduli between the metal matrix and the reinforcements;
- grain refinement strengthening;
- dispersion strengthening;
- reaction carbide transition layer strengthening;
- Strengthening by clustering reinforcements.
- Precipitation hardening strengthening.

Hence, the predicted combined strength of nanocomposites (combined yield strength) could be calculated as follows:

$$\sigma_{yc} (overall) = \Delta\sigma_{load} + \sigma_{ym} + \Delta\sigma_{Orowan} + \Delta\sigma_{Thermal + Modulus CTE} + \Delta\sigma_{GEO CTE} \dots\dots\dots (1)$$

Where σ_{yc} and σ_{ym} represents yield strength for both nanocomposites and matrix.

To effectively enhance strength by Orowan looping and strain hardening, GNPs should be uniformly distributed in grain interiors rather than at the grain boundary. As shown in Figure 2-17 (a-d), the uniformly and densely distributed GNP in the grain interior efficiently hinders the path of dislocations²³.

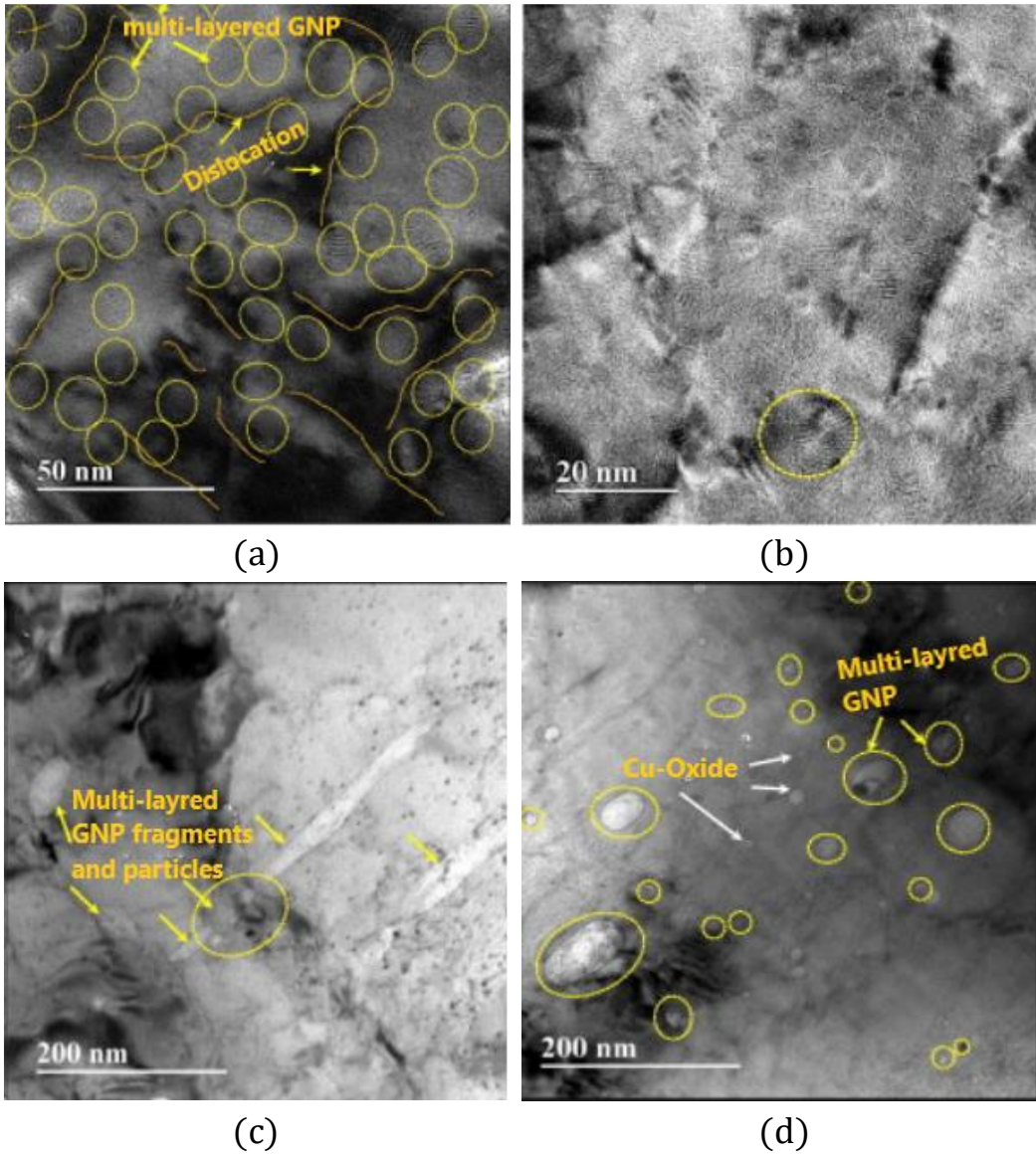


Figure 2-17: (a) & (b) HRTEM micrographs of the 1% HRDSR Cu composite showing nano-sized MLG particles in grain interiors (c) & (d) TEM micrographs of the 1% ESR Cu composites²³.

Table 2-6: Strengthening mechanism and its governing equation for MMC strength evaluation^{54,265,351-354,296,314,345-350}

S. No.	Strengthening mechanism	Equation/Model used	Equation expression/GNP
1.	Geometric mismatch	-	$\Delta\sigma_{geo} = \alpha Gb \sqrt{\frac{f_v 8\gamma}{bd_p}}$
2.	Load transfer	Shear lag model	$\sigma_c = \sigma_m \left[\frac{v_f(s+4)}{4} + (1 - v_f) \right] (\text{generalised})$ $\sigma_{LT} = \frac{f_v \sigma_m}{2} (\text{Yield strength})$ $\sigma_c = \sigma_m (1 + pV) (\text{modified shear lag})$
3.	Dislocation strengthening	Orowan effect (Orowan equation for different shape)	$\sigma_{Orowan} = \frac{0.13Gb \cdot \ln \frac{d_p}{2b}}{\lambda}$ $\lambda(\text{Spherical shape}) = d_s \left[(0.523/f_v)^{1/3} - 1 \right]$ $\lambda(\text{flake shape}) = d_f \left[(0.785/pf_v)^{1/3} - 1 \right]$
4.	Grain refinement	Hall-Petch equation	$\sigma_y = \sigma_o + Kd^{-\frac{1}{2}} \text{ (d= grain size)}$
5.	Thermal and elastic mismatch strengthening.	Taylor equation	$\rho^{EM} = \frac{6v_p}{\pi d_p^3} \varepsilon (\text{Dislocation density by elastic module mismatch})$ $\rho^{CTE} = \frac{A\Delta\alpha\Delta T v_p}{bd_p(1-v_p)} (\text{Dislocation Density by Thermal Modulus mismatch})$ $\sigma_{EM+CTE} = \sqrt{3}\beta Gb (\sqrt{\rho^{EM}} + \sqrt{\rho^{CTE}})$ <p style="text-align: center;">(Combined effect)</p>

2.4.1. Load transfer mechanism

Metal matrix composites are strengthened by load transmission from soft metal matrix to hard and stiff reinforcement particles. As proposed by Nardone and Prewo³⁵⁵, a modified shear lag model is often used to forecast the role in strengthening. The shear stress created at the interface is used to transmit the load from the matrix to the

reinforcement. As a result, the carbonaceous material's stiffness may be directly exploited. High aspect ratio reinforcements are advantageous in this model, but aspect ratios larger than 100 offer no substantial benefit. Aspect ratios of carbonaceous material play an essential role in this model. Interfacial shear stress transmission requires wetting of reinforcement, which is anticipated to be a key challenge for Al/GNP/CNT composites. CNT has a surface tension of less than 200 mN/m³⁵⁶, while Al has 865 mN/m. Hence, there is quite a difference in the values. Fortunately, K₂ZrF₆ is commonly used to manufacture carbon fibre composites to increase bonding between graphite and aluminum. Due to the structural similarity between GNP/CNT, K₂ZrF₆ can likely act as the wetting agent³⁵⁷.

The equation calculating the Young's modulus (E_c) of the composites is given as :-

$$E_c = A \cdot E_f \left(1 - \frac{\tanh(ns)}{(ns)} \right) + (1 - A)E_m \text{ ----- (2)}$$

Where,

$$n = \left[\frac{2E_m}{E_f(1 + \gamma_m) \ln \frac{1}{A}} \right]^{\frac{1}{2}}$$

E_f is the young's modulus for reinforcement and E_m is the young's modulus for matrix material. A is the volume fraction for reinforcements, "s" is its aspect ratio and γ_m is the Poisson's ratio.

2.4.2. Orowan strengthening

Orowan mechanism consists of the interaction between nano-particles and dislocation. The particle of the non-sharable reinforcement pins the crossing dislocation and forms Orowan loops, which truly are dislocations that bend around the particles³⁵⁸. This bending of the dislocations between the reinforcements produces back stress, preventing further dislocation migration, resulting in increased yield stress. In aluminum alloys reinforced by fine precipitates, the Orowan looping process is critical because the reinforcement particles in metal matrix composites are often coarse and have a high particle spacing, so the strengthening method has limited impact. Since CNT/GNP are very fine particles, i.e., fewer nanometres they can effectively strengthen the aluminum

matrix. Moreover, because of the high strength of carbonaceous particles, the shearing of those particles is of little concern³⁵⁹. Refer Table 2-6 for the Orowan equation.

Incremental shear strength for CNT/metal matrix composites can be expressed as³⁵⁷:

$$\Delta\tau = \frac{K \cdot \mu b A^{\frac{1}{2}}}{r \cdot \ln \frac{2r}{r_0}} \quad \text{----- (3)}$$

Where “r” is the radius of carbon nanotube reinforcement, constant “K” = 0.093 for edge dislocation and K = 0.14 for screw dislocation. “r₀” is the core radius, “b” is Burgers vector, and “μ” is the modulus of rigidity of matrix.

2.4.3. Thermal mismatch

During material cooling and straining, geometrically necessary dislocations (GND) are formed, resulting in a mismatch in coefficient of thermal expansion (CTE) and in elastic modulus (EM) between the two materials. The equation for GND due to CTE and EM is shown in Table 2-6. Where A is a geometric constant, “Δα” is the change in CTE and “ΔT” is the variance between test and heat treatment temperatures and “β” is a constant.

The negative coefficient of thermal expansion of graphene is 10⁻⁶ K⁻¹³⁶⁰, which is the same as graphite. Commercially available aluminum, has a coefficient of thermal expansion of 23.6 × 10⁻⁶ K⁻¹³⁶¹. As a result, there is considerable variance in CTE value in Al/GNP composites. The prismatic punch of dislocations at the interface would arise from this discrepancy, causing the matrix material to work harden. The density of dislocations produced would improve strength and is purely determined by the reinforcement surface area.

2.4.4. Hall-Petch strengthening mechanism

The grain size strongly influences material strength because the grain boundaries can resist the dislocation movement. The impediment is caused by the dislocations and inability to move on a continuous slip plane due to the difference in orientation of nearby grains and the severe lattice disorder present in the area³⁵⁸. In metal matrix composites, the particles critically influence the ultimate grain size. They interact with grain borders and serve as pinpoints for slowing or arresting the development of grains. Table 2-6

shows the hall-Petch equation where “k” is the strengthening coefficient and “d” is grain size.

2.5. The conclusion from the literature survey

2.5.1. Current issues:

- *Non-uniformity in the distribution of graphene:* Non-uniformity in the distribution of reinforcements creates composites with weak mechanical strength..
- *The agglomeration of graphene particles due to weak van-der Waals forces of attraction within layers:* Carbonaceous reinforcement agglomerates easily due to weak van der Waals force of attraction and affect the tensile strength of composite material
- *Non-feasibility of the casting process due to lower density of GNP:* Graphene has density much lower than that of molten aluminium. Lower density, agglomeration tendency and reaction between graphene and aluminium at elevated temperature makes casting process a non-feasible process for the synthesis of graphene aluminium matrix composite.
- *Non-wettability of GNP in case of aluminum matrix composites:* Non-wettability refers to the ability of reinforcement to maintain contact with the matrix. Graphene has wettability issues with aluminium matrix, hindering the load transfer between reinforcement and matrix . Non-wettability also leads to premature crack formation and propagation within the composite structure
- *Ease in the formation and propagation of cracks and voids due to non-wettability of graphene with aluminium.*
- *Formation of carbide at a temperature above 500°C in the aluminum matrix:* Damage produced in the graphene structure during its synthesis and processing creates activated carbon or unbounded carbon atoms. These activated carbon atoms easily reacts with aluminium forming aluminium carbide.

2.5.2. Scope

- The need for rectification of defects at the microscopic level, i.e. at the area of interaction of graphene with the metal matrix, is to be studied because most of the work done is towards the strength enhancement of the composite.
- The work on the development of metal matrix composites using nanofillers as reinforcement material is still in its earlier stage. It has excellent potential to produce

smart material with exclusive new thermo-physical properties having vast applications.

- GNP interacts with the matrix material in various ways. In MMNC reinforced with GNP, the orowan strengthening mechanism is only suited on the metal GNP interface. The amount of grain boundary and grain size significantly affects the boundary of grain interaction in GNP/ceramic matrix composites. Research has shown us that in the case of ceramic matrix composites, nano-sized grains provide an additional degree of freedom for GNPs. Hence, further study on optimal grain size needs to be done.
- Functionalized graphene such as GO and rGO has increased interfacial properties and needs further investigation with other functionalization groups.

2.6. Objectives

- Functionalized graphene, such as GO and rGO, has been preferable for metal matrix composites. The topic will be explored further by employing different dopants in graphene.
- Ball milling is the most appropriate technique for large-scale manufacturing of functionalized graphene without using hazardous chemicals. Hence the impact of sulfur, nitrogen, and antimony doping on aluminum metal matrix composites would be investigated.
- To evaluate the effectiveness of the ball milling method. Doped graphene will be analyzed in detail.
- The impact of functionalized graphene on the mechanical characteristics of an aluminum matrix composite will be assessed.

As noted in the chapter, the ball milling technique is used to fabric functionalized graphene and further utilized as a reinforcing material. The next chapter will mathematically formulate the optimum speed required for graphene synthesis to reduce friction and heat losses.

CHAPTER 3: Analytical approach for high energy milling process

3.1. Introduction

The chapter reports the mathematical formulation for energy released at the different rotational speeds of planetary ball mills using the different diameters of balls. It was observed that large diameter balls release more energy than smaller balls. However, when balls with different diameters were combined, the energy released was much larger than balls of individual size. The solid-state ball milling technique can successfully exfoliate the graphite into a multilayer graphene. At the same time, it introduces doping atoms on the edge of graphene sheets. From the literature, it is observed that milling time plays a crucial role in exfoliation and reduction of particles size. Hence longer the time greater would be heat generated due to friction. Further in the upcoming chapter, the particle size of 48 h milled graphene is double that of 72 h milled sample. Therefore, the chapter aims to achieve maximum energy transfer at the minimum possible speed using balls of similar or different diameters.

3.2. Motivation and approach

Graphene is a 2-dimensional, sp^2 -hybridized carbon having a thickness of a single carbon atom arrayed in a honeycomb structure. It is currently the most studied and researched material because of its extraordinary strength, stiffness and conductivity for heat and electricity. The wonderful properties of graphene make it suitable for varieties of applications such as energy storage, energy conservation³⁶² fuel cell, lithium-ion batteries³⁶³ and solar cell, and lightweight-high strength nanocomposites³⁶⁴. Initially, the production of large-area graphene with the minor defect was achieved by layer by layer graphite “peel off” method³⁶⁵. However, the technique was not suitable for mass production due to the number of ways invented. In this regard, several innovative methods have been developed for effective, low-cost and large-scale production of this material such as mechanical exfoliation³⁶⁶, reduction of graphene oxide³⁶⁷, chemical vapour deposition (CVD) and approaches such as electrochemical, in-situ and electrical discharge process¹⁰⁵. The graphene produced by these techniques differs in functional group and defects initially created by the mechanical peel-off method. For example, graphene exfoliation can be achieved by oxidation of graphite followed by reduction reaction to getting reduced graphene¹⁵². Whereas oxygen present in reduced graphene oxide is not entirely removed, limiting its utility in some essential applications.

Many scholars have previously published their findings and hypotheses in the ball milling area. In recent decades, attempts to simulate the ball mill process have been made. Burgio et al.³⁶⁸ built the foundations of a mathematical model for calculating the ball's impact velocity and the energy transmitted to the powder. Padella presented the findings of studies in which the energy transfer was carefully regulated to generate either an intermetallic compound or an amorphous phase in the Pd-Si system³⁶⁹. The present work is based on the mathematical calculation of energy released during ball milling. The work aims to achieve maximum energy to peel of graphene layers at the minimum speed possible.

3.3. Mathematical formulations

The kinetic energy of a grinding ball can be expressed as follows³⁷⁰:

$$E_b = \frac{1}{2} m_b v_b^2 \quad (1)$$

Where; m_b , is the average mass of the grinding ball and V_b , is the velocity of the ball. The velocity of ball ' V_b ' can be calculated as³⁶⁸:

$$v_b = \left[(\omega_p R_p)^2 + \omega_{jar}^2 \left(R_{jar} - \frac{d_b}{2} \right)^2 \left(1 - 2 \frac{\omega_{jar}}{\omega_p} \right) \right]^{\frac{1}{2}}$$

Where; ω_p and ω_{jar} is the angular velocity of ball mill plate and jar respectively, d_b is the average diameter of grinding ball, R_p and R_{jar} is the radius of ball mill plate and inside radius of jar respectively. For Retsch PM100 planetary ball mill, the ratio of ω_{jar} and ω_p is '-2' ³⁷¹. Hence velocity ' v_b ' becomes:

$$v_b = k_b \omega_p R_p \quad (2)$$

Where;

$$k_b = \left[1 + 20 \left(\frac{R_{jar}}{R_p} \right)^2 \right]^{\frac{1}{2}}$$

Therefore, putting values of eq. 2 into Eq. 1;

$$E_b = \frac{1}{2} m_b (k_b \omega_p R_p)^2 \quad (3)$$

The energy released from the K.E. of grinding ball in one collision event is derived from equation:

$$E_b = K_a \frac{1}{2} m_b (k_b \omega_p R_p)^2 \quad (4)$$

K_a , is the energy release ratio in the collision of wet ball milling. Where ' $K_a=0$ ' for perfectly elastic collision and ' $K_a=1$ ' for the perfectly inelastic collision [19].

Hence, total energy dissipated per ball can be calculated by:

$$\Delta E_b = K_c m_b \omega_p^2 R_p^2 \quad (\text{Joule/hit}) \quad (5)$$

Where;

$$K_c = \frac{1}{2} K_a k_b^2$$

Considering the degree of filling of the vial's [20] the Eq. 5 becomes:

$$\Delta E_b^* = \varphi_b \cdot \Delta E_b \quad (6)$$

φ_b , can be calculated by:

$$\varphi_b = (1 - n_v^e) \quad \text{where, } n_v = \frac{N_b}{N_{b,\text{total}}}$$

The value of φ_b for 1/3rd of the filled jar is '1' whereas, for 2/3rd of the filled jar is 0.667

The cracking energy [17,19] used to fracture the materials which is released and transferred from the energy ΔE_b .

$$E_{\text{transferred}} = \beta \cdot K_c m_b \omega_p^2 R_p^2 \quad (7)$$

Here, β is '0' for zero percent of energy release and '1' for 100 % energy released.

The total cracking energy per second is related to overall collision frequency [21,22].

Hence overall collision frequency is expressed as:

$$f_b = K \cdot \frac{|(\omega_p - \omega_{jar})|}{2\pi}; \quad K = 1.5 \quad (8)$$

K is the parameter related to the time required to dissipate the energy $E_{cracking}$ in the collision. Putting the value for speed ratio for PM 100 we get;

$$f_b = \frac{4.5}{2\pi} \omega_p \quad (9)$$

If the jar is filled at lower levels, the reciprocal hindering of 'N_b' number of balls is negligible, and the overall collision frequency is considered as:

$$f_f = \frac{4.5}{2\pi} \omega_p \cdot N_b \quad (10)$$

But if the jar is filled to total capacity the reciprocating hindering coefficient of N_b balls 'φ_b' is to be considered. Therefore, total K.E. transferred from the K.E. of all balls on the material in grinding time 't' is given by:

$$E_{total} = \Delta E \cdot N_b f_b \cdot t \quad (11)$$

$$E_{total} = K_c m_b \omega_p^3 R_p^2 N_b \frac{4.5}{2\pi} \cdot t \quad (12)$$

However, the total energy is transferred from the collision of two dissimilar balls, i.e. bigger and smaller balls. Applying conservation of momentum;

$$E_{total} = K_c \omega_p^3 R_p^2 N_b \frac{4.5}{2\pi} \cdot (m_{b1} N_{b1} + m_{b2} N_{b2}) \cdot t \quad (13)$$

Here m_{b1} and m_{b2} is the mass of different sized balls, and N_{b1} and N_{b2} is the number of balls used.

3.4. Mathematical calculation: The energy supplied during ball milling

Assuming perfectly inelastic collision and 100% energy is transferred during the collision of balls. For PM100 planetary ball milling machine (Figure 3-1, Table 3-1)

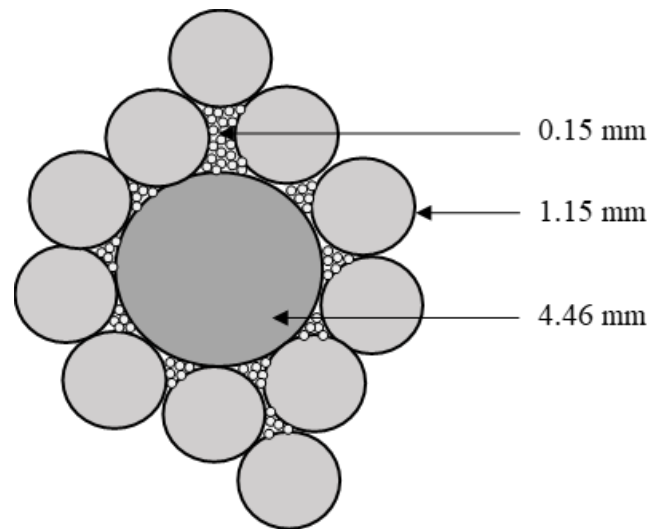


Figure 3-1: Schematic representation of milling balls during the ball milling process.

Table 3-1: Summarized input parameters to calculate the total energy

ω_p at 200 RPM	ω_p at 300 RPM	ω_p at 350 RPM	ω_p at 400 RPM
20.94 rad/s	31.41 rad/s	36.65 rad/s	41.88 rad/s
$R_p = 70.5\text{mm}$, $R_{jar} = 37\text{ mm}$ $K_a = 1$ $K_b = 2.5512$ Hence, $K_c = 3.254$			

3.4.1. Kinetic energy transfer from a collision of similar balls and dissimilar balls

Assuming that the smaller and medium-sized balls have fully surrounded the large-sized balls. The total K.E. ($E_{total, A}$) transferred from the collision of balls with avg. size of 4.46 mm, 1.15 mm and 0.15 mm is represented in Figure 3-2.

According to equations 9 and 10, the total energy transferred by the ball is directly proportional to the ball's mass. Hence, larger diameter balls (of the same material) will have a high mass and consecutively transfer more considerable energy. From Figure 3-2, the amount of energy released during the interaction of larger and smaller balls is greater than that released by the collision of similar balls. The amount of energy transferred during the collision of 4.46 mm and 1.15 mm balls is highest at the same rotation speed. The energy transferred by the collision of smaller 0.15 mm balls is minimal. With the increase in the number of smaller balls, friction force dominates, and higher heat is generated between the grinding balls, decreasing the amount of energy released.

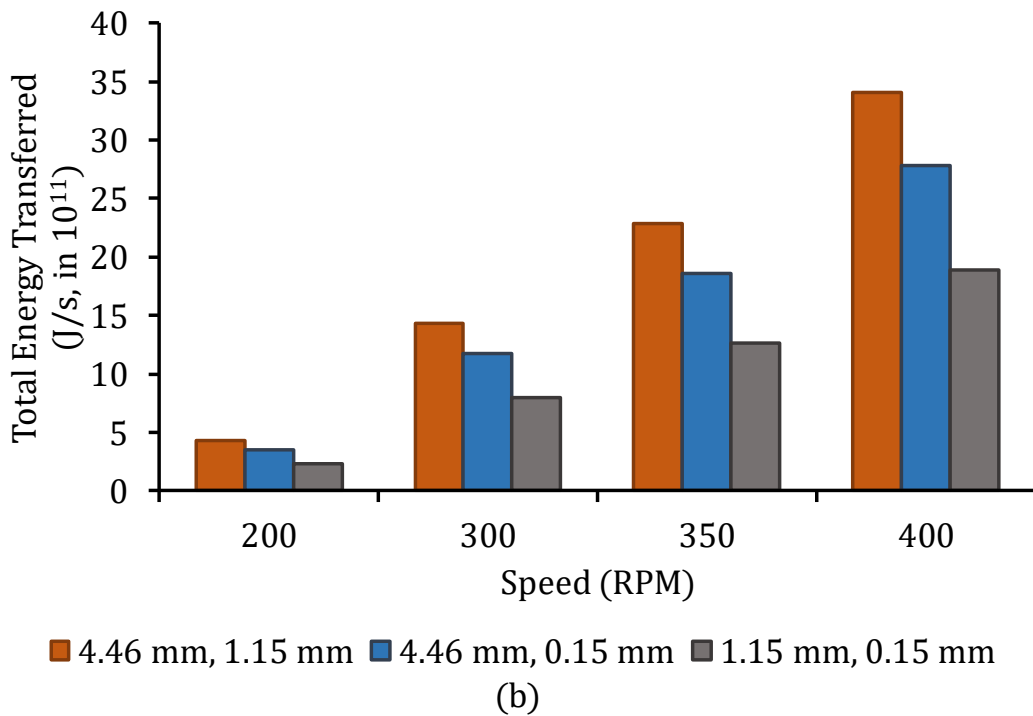
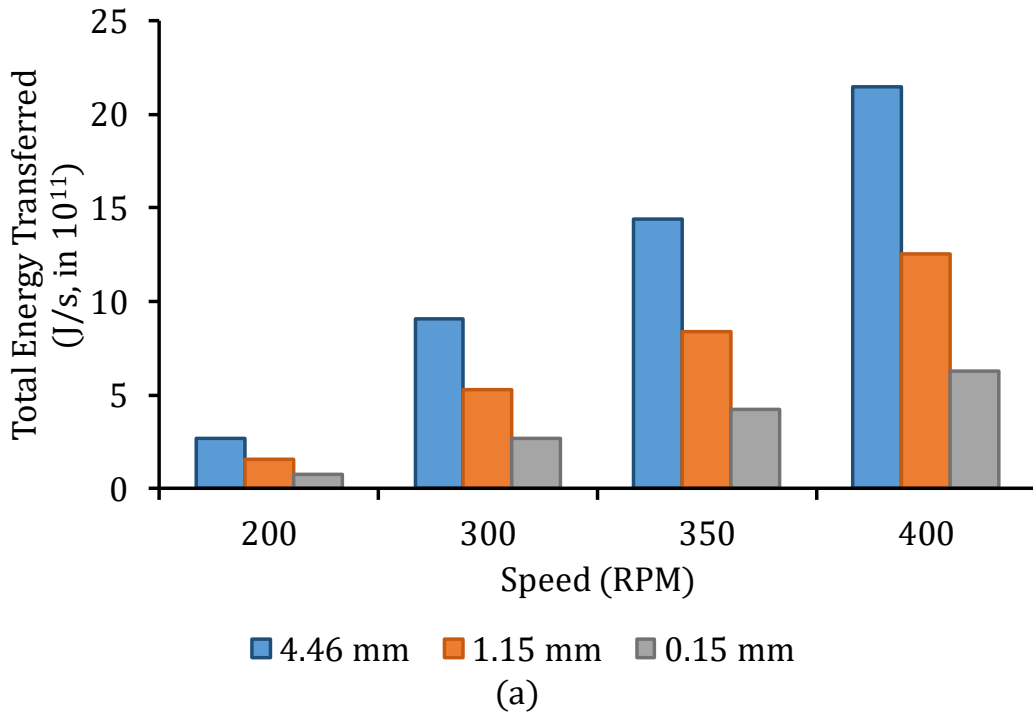


Figure 3-2: Graphical representation of total energy transferred using three different types of ball

As observed in Figure 27, when different balls are employed instead of balls of the same diameter, the slope of the curve increases with an increase in rotating speed. So by using dissimilar balls, the same amount of energy can be obtained at a lower speed than using similar balls at a higher speed of rotation.

3.5. Experimental characterization of zirconium balls

Figure 3-3 depicts the optical microscopic image of crack and fractured surface in larger ball zirconium oxide ball during the milling operation. The high impact force created during the collision of dissimilar balls with the jar's surface rotating at 350 rpm initiates fracture in the surface of beads. Due to prolonged milling time, these cracks propagate fracture into the surface of beads, which further results in breaking the balls into two parts. The cracks observed in Figure 3-3(a) was found after 48 h of milling time. Whereas fully broken beads were found after 72 h of milling time. As observed in Figure 3-2, the energy transferred during the collision of dissimilar balls, i.e. 4.46 mm and 1.15 mm, increases with increasing speed (higher slope), and at a high rotational speed, it causes a fracture in the zirconium balls. However, no fracture was observed while milling at lower speed and larger balls.

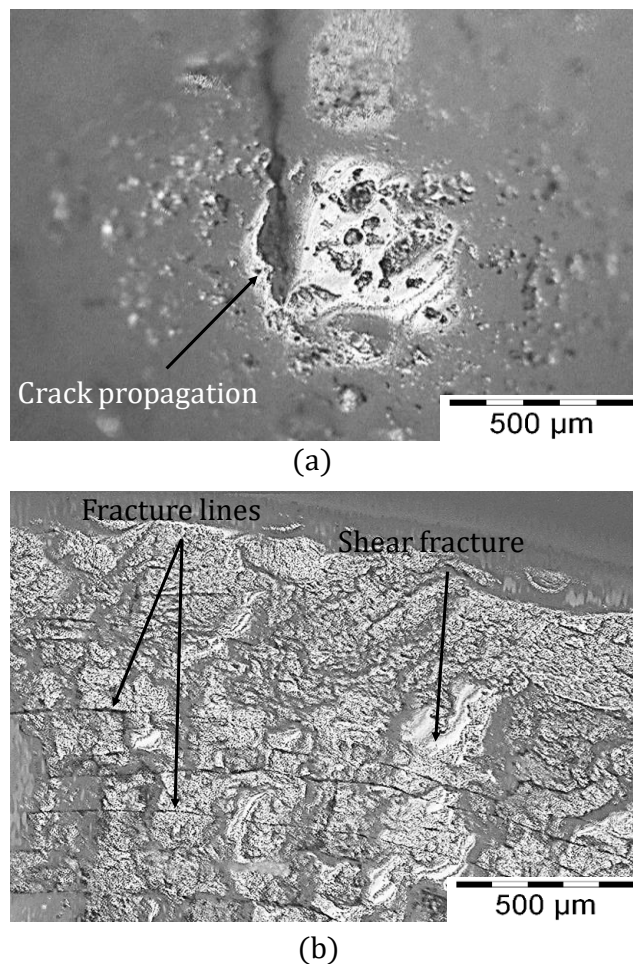


Figure 3-3: (a) Crack propagation in 4.46 mm ball and (b) Fracture surface of the ball.

3.6. Conclusion

The mathematical formulation for energy released at different rotation speeds for planetary ball milling has successfully shown that high rotational speed releases more energy for larger balls, whereas combining larger and smaller balls releases much higher energy than individual ones. Visual analysis of balls after the milling process has shown that high energy milling creates more shear fracture than the low energy milling process. Hence, a lower milling speed with a combination of balls would be more economical and reduce impurities created by ball erosion.

CHAPTER 4: Synthesis of nitrogen-doped graphene and its strengthening effect on aluminum metal matrix composite

4.1. Introduction

The mechanochemical process of solid-state dry ball milling of graphite with melamine was used to synthesise nitrogen-doped graphene nanosheets (NDG). XRD, XPS, FESEM, HRTEM, and Raman spectroscopy were used to analyse the produced NDG and was further utilised as reinforcing material in metal matrix composite. NDG was employed as a reinforcing material for the first time to improve wettability, minimise the likelihood of aluminum carbide formation, and boost strength through strong interfacial bonding. With merely 0.2 wt. % NDG, the ultimate tensile and compressive yield strengths of Al/NDG composites is enhanced by 124.05 % and 66.94 %, respectively. When the results were compared with graphene/Al composite, it was discovered that the tensile strength of the NDG/Al composite was 71.87 % higher than 0.5 wt.% graphene/Al composite. The development of strong interfacial bonding was confirmed by XRD of NDG/Al composite, which displayed a low-intensity peak of aluminum nitride (AlN) responsible for the increase in strength. The lubricating property of NDG is illustrated by the wear test of composite, which was found to be better at greater NDG concentration. Since NDG eliminates the difficulty connected with graphene and provides a special strengthening effect even at low weight percentages of reinforcement, doped graphene could be a breakthrough in the field of low weight-high strength composites.

4.2. Motivation, objective and approach

Research on metal matrix composite material (MMCM) has a long tradition. Numerous studies on the synthesis of MMCM have used a variety of reinforcements to improve performance. The homogeneous distribution of reinforcement and inappropriate interfacial bonding are the primary issues with the synthesis of MMCM^{372,373}. Carbonaceous reinforcement such as carbon nanotubes, graphene or any functionalized graphene (GO, RGO etc.) tends to agglomerate and have a devastating effect on the properties of composite material³⁷⁴. The use of a high-energy ball milling technology aids in the distribution of reinforcement in a uniform manner. However, the graphene structure is significantly tampered with during the milling process, resulting in edge defects that act as active sites for forming reaction products with part of the matrix material. Aluminum, for example, interacts with graphene at high temperatures to

generate aluminum carbide (Al_4C_3)^{375,376}, which is usually an ill-posed problem in the case of ultimate desired composite material properties³⁷⁴. There are numerous strategies for addressing these challenges; however, one strategy to solving this problem is to have a correct interfacial product that does not harm the desired properties but rather improves composite material properties.

Nitrogen doping in graphene^{377,378} has found great application in the storage, semiconductor and electronics industries. Liu et al.³⁷⁹ employed a high-energy ball milling approach to make nitrogen-doped graphene (NDG) application in Lithium-ion batteries by milling urea and graphite at 290 RPM. Chen et al.³⁸⁰ milled graphite powder at 750 RPM for 48 hours to produce boron-nitrogen-co-doped graphene in high-performance supercapacitor electrodes. After characterising the material, Chen discovered that graphene possesses an active carbon site, which reacts with nitrogen in the air to produce nitrogen-graphene carbon material.

Among other carbonaceous reinforcement, nitrogen-doped graphene (NDG) is never used as a reinforcement material. While sintering the composite at high temperatures, nitrogen present at the interstitial site of NDP may react with the aluminum to generate aluminum nitride (AlN)³⁸¹ as the interfacial product, thus reducing the odds of Al_4C_3 formation. Compared with most ceramics, AlN has high thermal conductivity, minimal thermal expansion, and superior thermal shock resistance³⁸². Compared to Al_2O_3 , it is significantly more wettable than aluminum and can improve the modulus, strength, hardness, wear resistance, and refractory nature of aluminum alloy³⁸³. As a result of these benefits, it is a particularly valuable interfacial product that will improve graphene's mechanical behaviour and wettability with an aluminum matrix.

The current study examines the synthesis and characterization of NDG and aluminum metal matrix composite material (AMMCM) with different percentages of NDG as reinforcement. High-resolution transmission electron microscopy (HRTEM), X-ray diffraction (XRD), Raman spectroscopy, X-ray photoelectron spectroscopy (XPS), and field emission scanning electron microscopy (FESEM) was used to analyse NDG. Fabricated AMMCM was mechanically characterised using tensile, compressive and wear testing methods and the fractured surface after destructive test was characterised using the FESEM technique. Every mechanical test followed ASTM guidelines and was repeated three times on three different samples to ensure consistent results

4.3. Experimental Methods

4.3.1. Material selection

Melamine (C₃H₆N₆, 99 % pure) and graphite (100 mesh, 98 % pure) were obtained from Mumbai-based research lab fine chem industries. Sisco research laboratories Pvt. Ltd. (SRL), Maharashtra, India, provided the aluminum metal powder (325 mesh, 99% pure). Synco Industries Limited has provided zirconium oxide beads (average sizes of 1.15 mm and 4.28 mm). All of the items used in the study are readily available and of commercial analytical grade, and they were used without further purification.

4.3.2. Synthesis of Nitrogen-Doped graphene (NDG)

Initially, a predetermined amount of commercial graphite and melamine powder was placed in a tungsten carbide (WC) jar containing two different sizes of zirconium balls (average dia.: 4.46 mm and 1.15mm). The jar was sealed and fixed on the planetary ball-milling machine (retsch PM100) and was agitated at 300 RPM for 72 hours. The mathematical calculations referred from the previously published article were used to determine the ball milling speed and diameter of the ball¹⁰⁴. A small amount of powder was collected after every 24-hour interval for characterization. The resulting material was rinsed multiple times in a warm water bath to dissolve any unreacted melamine and remove it from the solution. The resulting powder was ultra-sonicated for 15 minutes before being dried overnight in a vacuum oven to produce graphene powder designated as NDG.

4.3.3. Synthesis of NDG reinforced metal matrix composite material

Aluminum powder (matrix material) was mixed with 0.1, 0.2, and 0.5 % NDG and milled in a planetary ball mill for 60 minutes at 200 rpm with a ball to powder ratio of 10:1 to obtain a uniformly distributed mixture^{384,385}. The mixture was cold compacted at 450 MPa and hot sintered at 600°C in a tube furnace using an argon gas environment to get NDG reinforced metal matrix composite. The prepared composite sample was further hot extruded at 450°C (two-step extrusion) to get a 10 mm dia. cylindrical specimen.

4.4. Results and discussion

The synthesis of NDG via high energy solid-state ball milling technique using graphite and melamine is schematically illustrated in Figure 4-1. During the ball milling process, graphite particles are crushed and exfoliated into smaller, thin-layered particles generating carbon-free radicals at the edge. The nitrogen present in melamine molecules

tends to absorb and disperse on the graphite surface while interacting with carbon-free radicals to form carbon and nitrogen bond. The process weakens the Van der Waals force present between the layers producing nitrogen-doped graphene nanosheets.

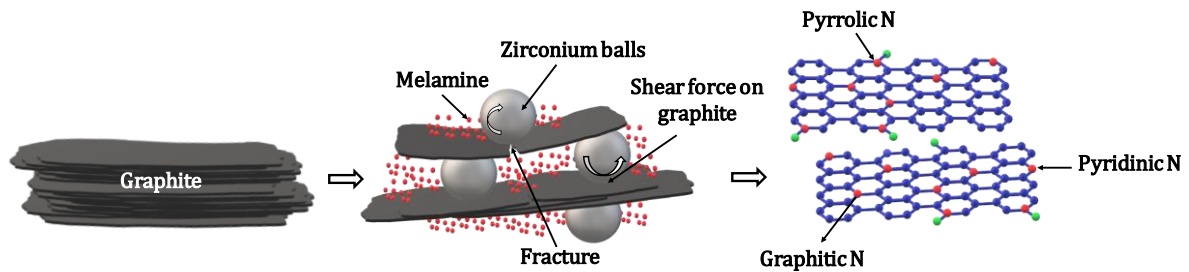


Figure 4-1: Nitrogen-doped graphene by solid-state ball-milling of graphite with melamine.

4.4.1. Physico-chemical characterization of N-doped graphene

Figure 4-2(a) represents the field emission scanning electron microscopy (FESEM) image of graphite powder before ball milling, with the average particle size distribution of tens of microns. The large shear force exerted by zirconium balls shows a significant reduction in particle size distribution from Figure 4-2(a) & (b). The tangential force exerted by the spherical balls, layer by layer, peels the graphite particle into a thin sheet of multi-layered graphene. The conversion of large chunks of graphite particles into thin sheets of multi-layered graphene is shown in Figure 4-2(c). The micrograph illustrates the successful exfoliation of graphene particles due to bonding between nitrogen and carbon which eventually weakens Van der Waals force of attraction between the layers. Figure 4-3 shows the average particle size distribution of NDG milled for 48h and 72h, respectively. The average hydrodynamic diameter for 72h milled sample is 394.2 nm, and for 48h milled sample is 601.5 nm. A significant reduction in particle size is observed in the 48h of milling time whereas, the reduction in particle size was less significant after 48h of milling time.

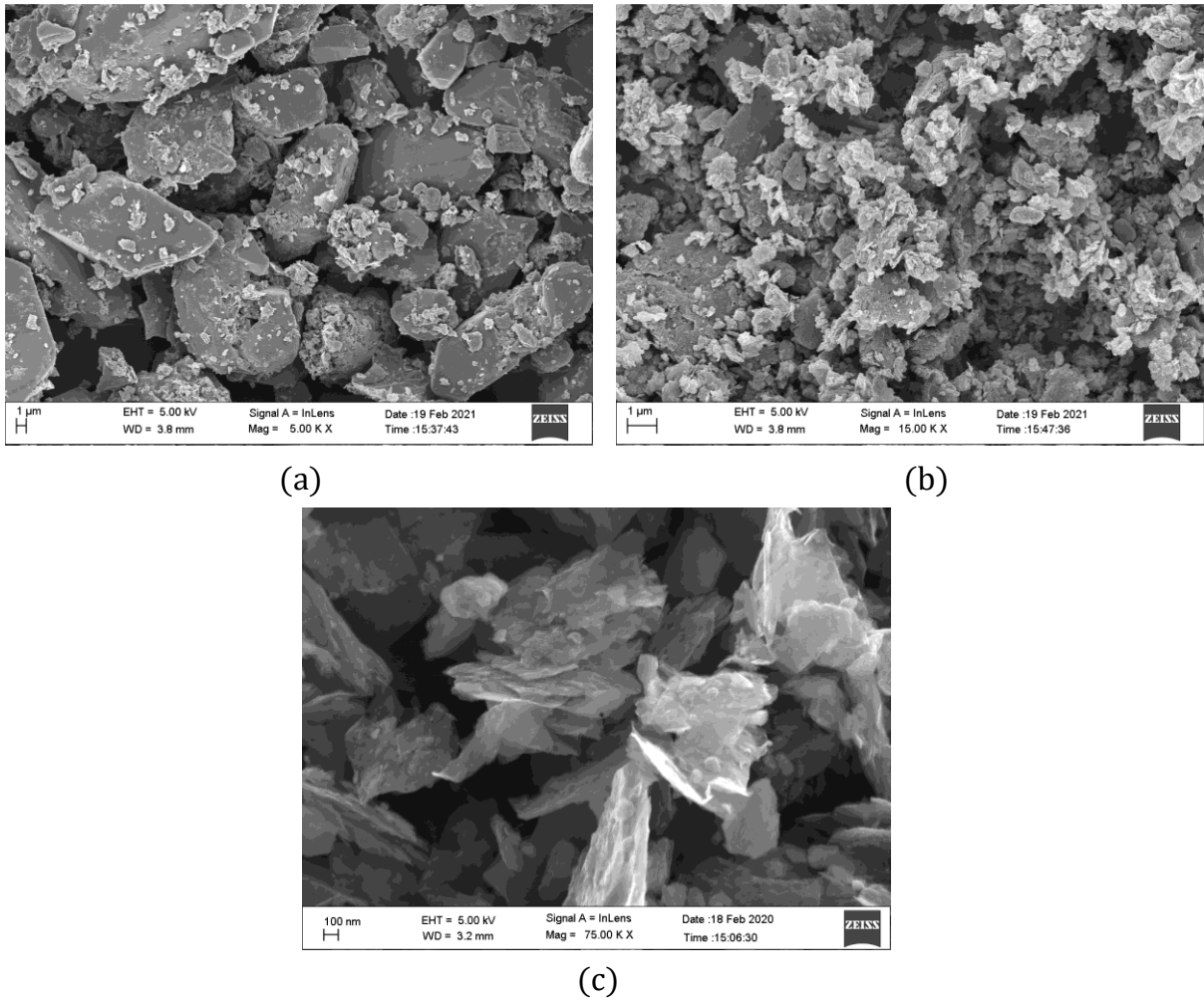


Figure 4-2: FESEM image for, (a) Graphite powder before milling, (b) &(c) N-doped graphene at different magnification.

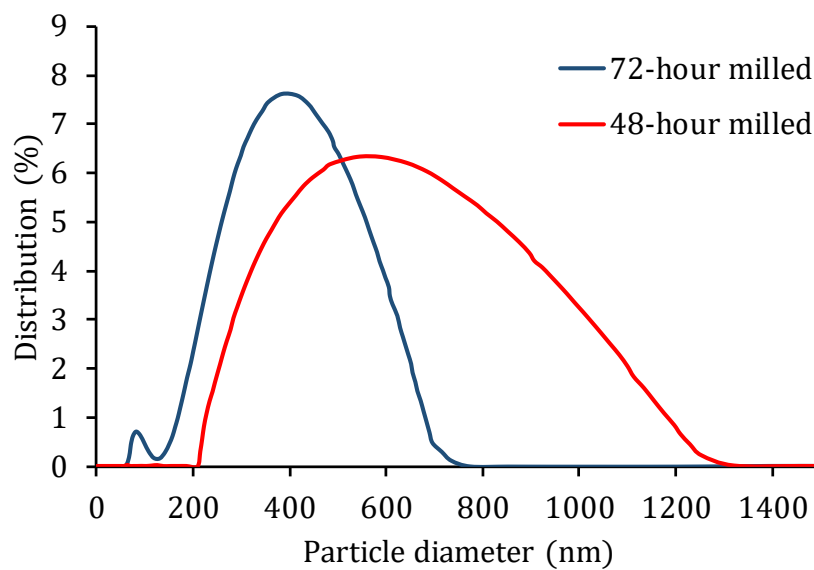


Figure 4-3: Particle size distribution for 48h and 72h-milled sample.

The HRTEM image of a single exfoliated NDG particle is given in Figure 4-4(a). The graphene particle exhibited adequate transparency and no evidence of graphite aggregation, with a flawlessly crystalline nature and unambiguous hexagonal structure, as confirmed by the SAED pattern in Figure 4-5. The NDG, due to edge hydrogen bonding and formation of hydrogen bonding between –NH groups, tends to overlap and self-assemble, which can be spotted in the image. As shown in Figure 4-4(b) & (c), the particle under higher magnification is a multi-layered graphene with a thickness of 6 to 10 layers. The estimated distance between the lattice fringes was $d = 0.21\text{ nm}$, 0.25 nm and 0.34 nm . The lattice fringe distance matched well with the in-plane lattice spacing ($d_{100} = 0.213\text{ nm}$), in-plane lattice constant ($d_{112} = 0.246\text{ nm}$) and base plane lattice spacing ($d_{002} = 0.33\text{ nm}$) of graphite structure. The hexagonal structure diffraction spots in the electron diffraction pattern of the graphene sheet (Figure 4-5) confirm the threefold symmetrical arrangement of carbon atoms. Despite integrating nitrogen-heteroatoms in hexagonal organised carbon networks, the graphene sheet has a well-ordered crystalline nature³⁸⁶.

X-ray photoelectron spectroscopy (XPS) is a proficient and most commonly used technique to confirm the nature of bonding between nitrogen and the carbon atom in graphene. The XPS comprehensive survey scan of NDG has shown the presence of carbon (C1s $\sim 284\text{ eV}$), nitrogen (N1s $\sim 400\text{ eV}$) and Oxygen (O1s $\sim 533\text{ eV}$) peaks, as shown in Figure 4-6. The XPS spectra of C1s core level, as shown in Figure 4-7(b), can be fitted into five peaks: the prominent peak at 284.8 eV corresponding to $\text{sp}^2\text{ C} - \text{sp}^2\text{ C}$ bond, peak at 284.3 eV attributes to $\text{C}=\text{C}$ bond, peak at 288.10 eV corresponds to $\text{C}=\text{O}$ bond, and two peaks at 286.00 and 286.80 corresponding to $\text{sp}^2\text{ C}-\text{N}$ bond and $\text{C}=\text{N}$ bond respectively. The deconvoluted XPS N1s spectra of NDG are shown in Figure 4-7(a). The XPS spectra of N1s core level can be divided into three peaks: The prominent peak at 400.15 eV corresponds to pyrrolic-N, peak at 401.2 eV corresponding to graphitic-N, and peak at 398.46 eV represents pyridinic-N nitrogen functionalities.

The structural evolutions and phase analysis of milled powder were examined through XRD (X-ray diffraction) tests using Rigaku-Smartlab XRD machine having X-ray source of 3 kiloWatt, Cu $\text{K}\alpha$ X-Ray radiation. The evaluated XRD data were recorded in the range of 5 to 85 degrees with a step size of 0.02 degrees and a scan speed of 4 degrees per min. The data were analysed with PANalytical X'Pert Highscore software.

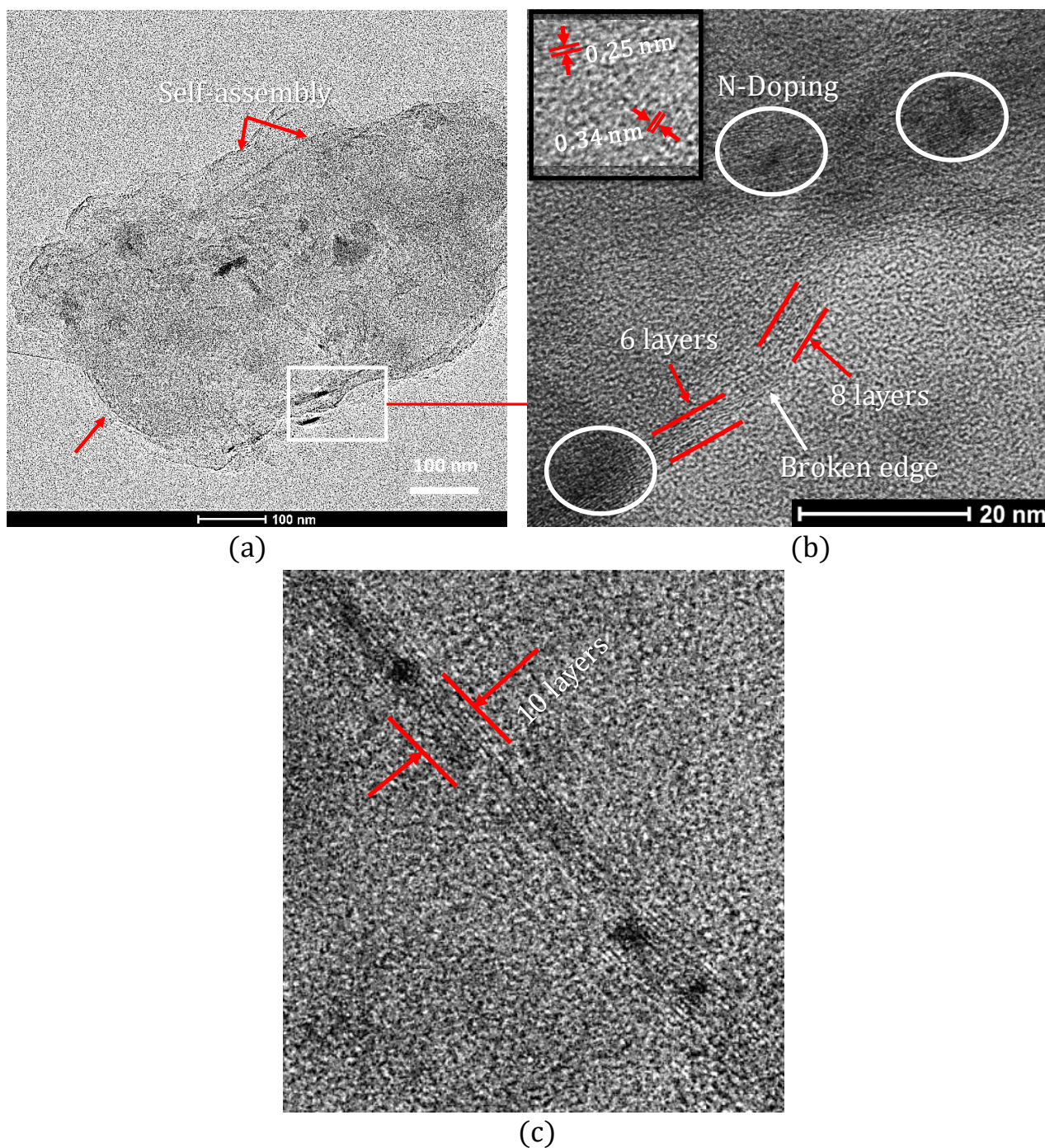


Figure 4-4: HRTEM image of N-doped graphene at (a) Lower magnification, (b) & (c) Higher magnification illustrating the number of layers of graphene and edge defects.

Figure 4-8 represents the XRD pattern of prepared samples; the XRD pattern of N-doped graphene has a strong peak at 26.175° for 72-hour milled sample and at 26.596° for 48-hour milled sample, which verifies the characteristics of crystalline graphite (002) plane. For 24-hour milled sample, multiple peaks and peak spread were not observed, as seen in 48 and 72-hour samples. The reason is that, during the first few milling hours, most

milling energy was dissipated in overcoming the van der Waal's force of attraction and peeling of graphitic layers. Due to the less availability of activated carbon atoms, the doping of graphite with nitrogen atoms was low.

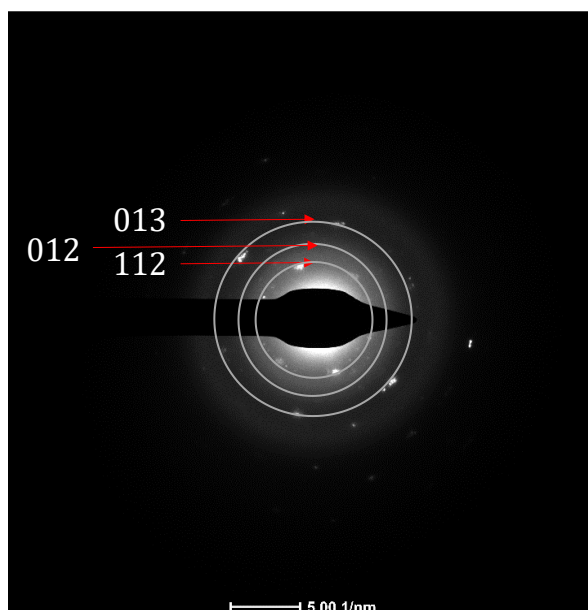


Figure 4-5: SAED diffraction of NDG.

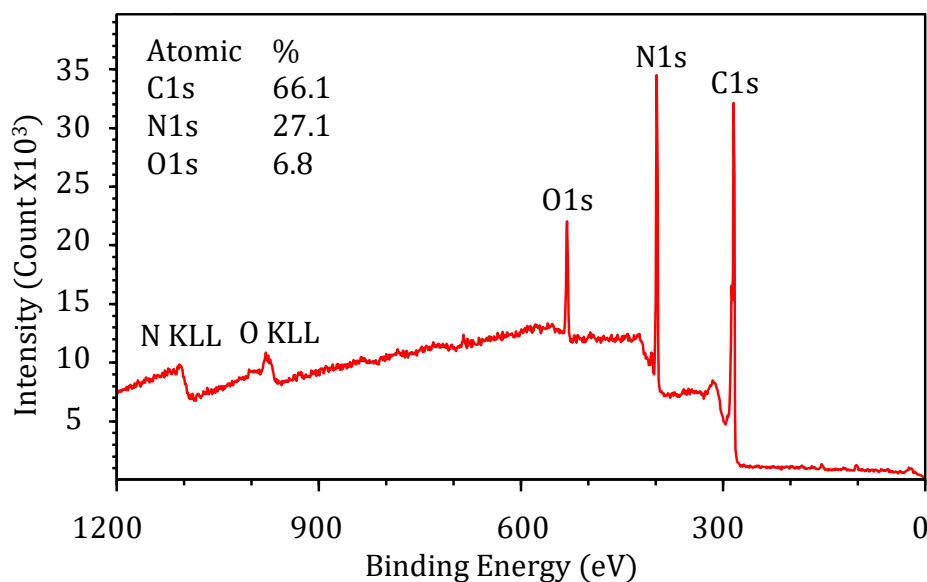


Figure 4-6: XPS survey scan for NDG.

Due to the incorporation of nitrogen atoms, the peak intensity at 17.73° , 14.94° and 21.69° for 48-hour samples and 17.66° , 21.64° and 14.87° for 72-hour samples is attributed to a nitrogen-carbon bond (ref. JCPDS card no. 96-210-3205). In addition to XRD patterns, the FWHM (full-width at half-maximum) of graphene diffraction peaks at

the (002) plane exhibits remarkable broadening from 0.067° to 0.087° for 48 to 72-hour samples. The phenomenon is often exhibited by the broadening of FWHM and can be linked to a decrease in average crystallite size³⁸⁷.

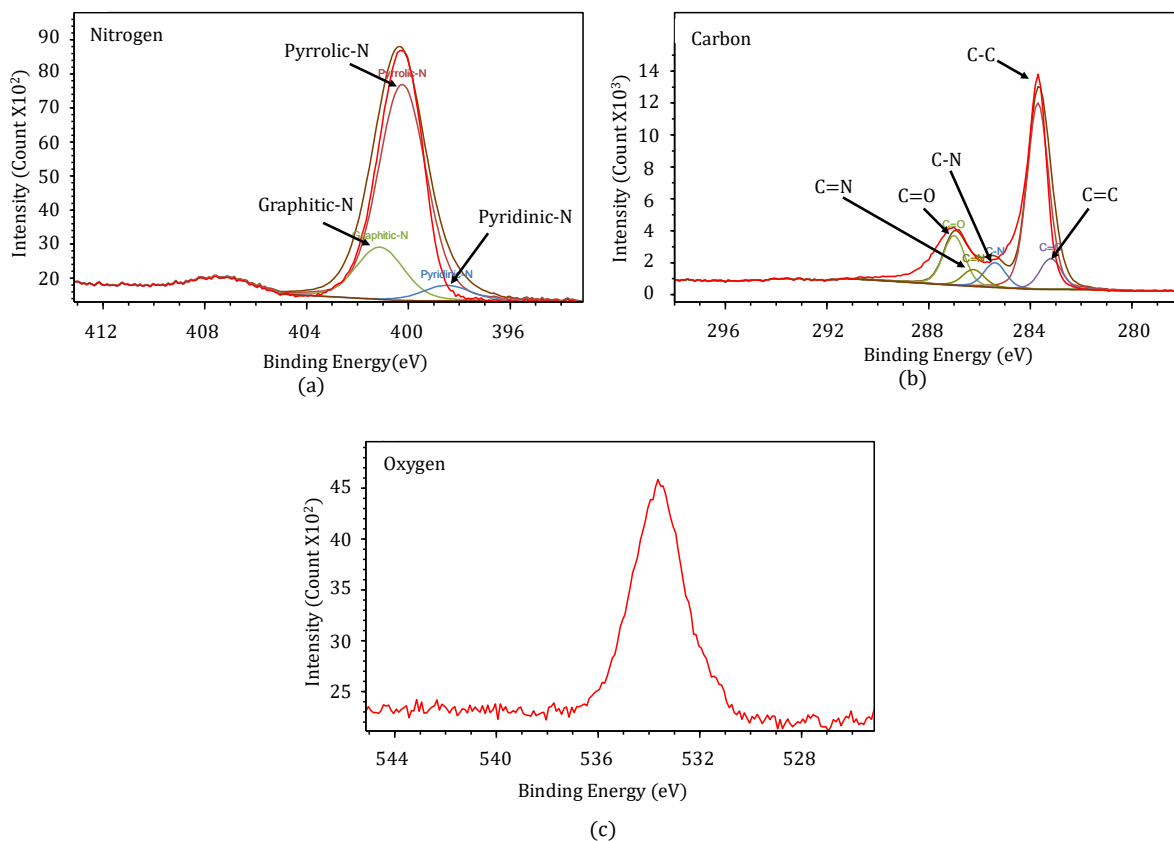


Figure 4-7: XPS high-resolution spectra of Nitrogen, (a) Carbon and (b) Oxygen.

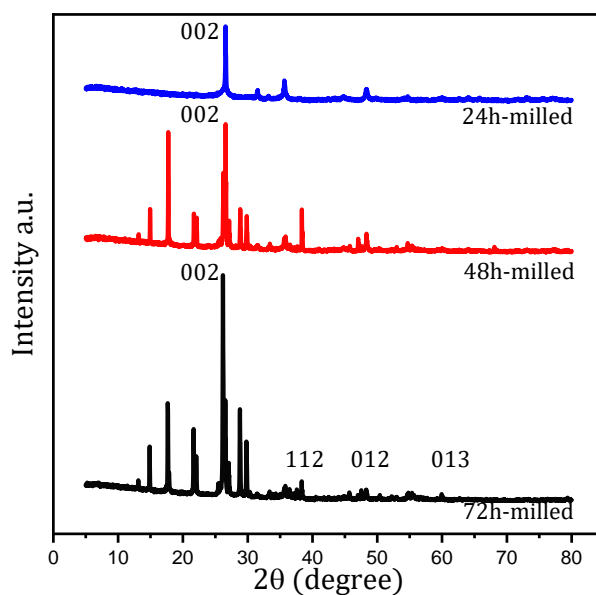


Figure 4-8: XRD of nitrogen-doped graphene milled for 24h, 48h and 72h, respectively.

The Raman Spectroscopy was performed on a "HORIBA scientific LabRAM HR-UV-Open machine" with a range of 300 to 3000 cm^{-1} and a 532 nm laser excitation wavelength. Carbon material shows its fingerprint under Raman spectroscopy by D, G and 2D peaks. The G and 2D peaks of pure exfoliated graphene are at 1580 cm^{-1} and 2710 cm^{-1} , respectively, with the absence of a D-band. Graphene exfoliated through high energy ball milling technique shows D-band peaks around 1350 cm^{-1} . It is attributed to the vibration of carbon atoms with dangling bonds in disordered graphitic planes and defects in pentagonal and hexagonal graphitic structure^{388,389}. Figure 4-9 represents the Raman spectroscopy of the as-prepared sample. The spectrum of prepared graphene shows a D-band around 1367 cm^{-1} , G band at 1610 cm^{-1} and 2D band peaks at 2710 cm^{-1} . The G band peaks occur due to the E_{2g} vibration, reflecting the structural intensity of SP²-hybridized carbon atoms. This can be seen in every sp² bond in graphitic carbon atoms. The I_D/I_G ratio of NDG of NDG in a 72-hour milling sample is 1.24; however, the increase in I_D/I_G value, as shown in Figure 4-9, could be due to more flaws in NDG due to higher nitrogen content³⁹⁰. For 24-hour and 72-hour milled samples, since the D-band intensity depends on the number of rings of hexagonal carbon atoms. The shift in the D-band peak was observed towards a lower wavelength and was due to the increase in disorder with increase in milling time and increase in doping percentage for graphene samples.³⁹¹

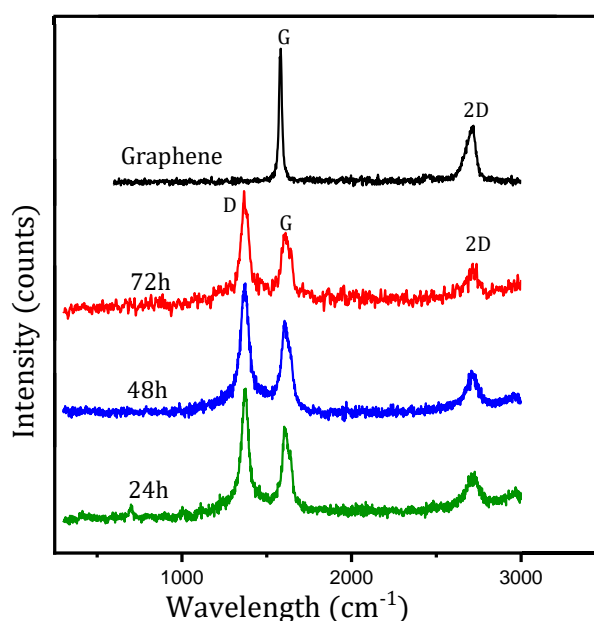


Figure 4-9: Raman spectroscopy of nitrogen-doped graphene milled for 24h, 48h and 72h, respectively.

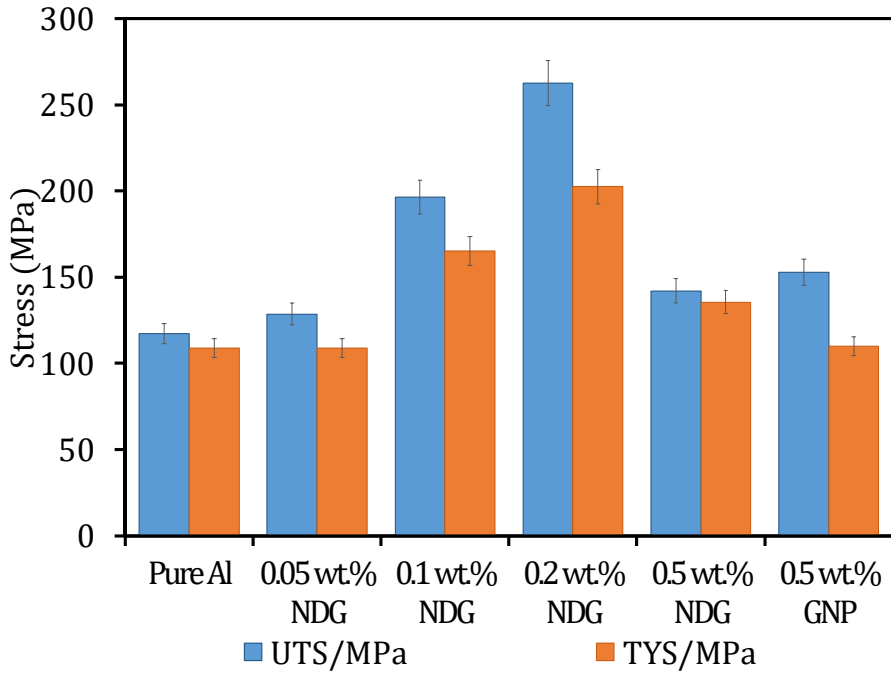
4.4.2. Mechanical Properties

The tensile, compressive, and wear test were used to investigate the mechanical properties of Al/NDG composite. Figure 4-10(a-b) illustrate the tensile and compressive stress-strain curves of Al/NDG nanocomposites with various NDG weight fractions. Figure 4-10 summarises the mechanical properties of the Al/NDG composite post tensile and compression tests. When NDG was added to an aluminum matrix, the composites strength increased significantly compared to a pure aluminum sample. The ultimate tensile and yield strength were increased by 67.56% and 51.57% for 0.1 wt. % NDG, and 124.05% and 85.82 wt.% for 0.2 wt. %NDG, however, with reinforcement of 0.5 wt.%, the composite's ultimate tensile and yield strength was found to be 152 MPa and 109.9 MPa, which is much lower than 0.1 wt. % and 0.2 wt. % NDG/Al composite. The tensile strength of NDG reinforced composite as compared to pure graphene reinforced MMCM (Graphene was purchased from M/s ACS material, 2-10nm thickness) and composite with NDG having higher melamine content (1:10, graphite: melamine) is shown in Figure 4-11(a). In contrast with 0.5 wt.% graphene/Al composite, the ultimate tensile and yield strength were improved by 71.87% and 84.30% for 0.2 wt.% NDG and 28.50% and 50.34% for 0.1 wt.% NDG. The decrease in strength of 0.5 wt. % NDG/Al composite was more dominant when composite was synthesized from NDG having a higher percentage of nitrogen doping (graphite: melamine ratio of 1:10).

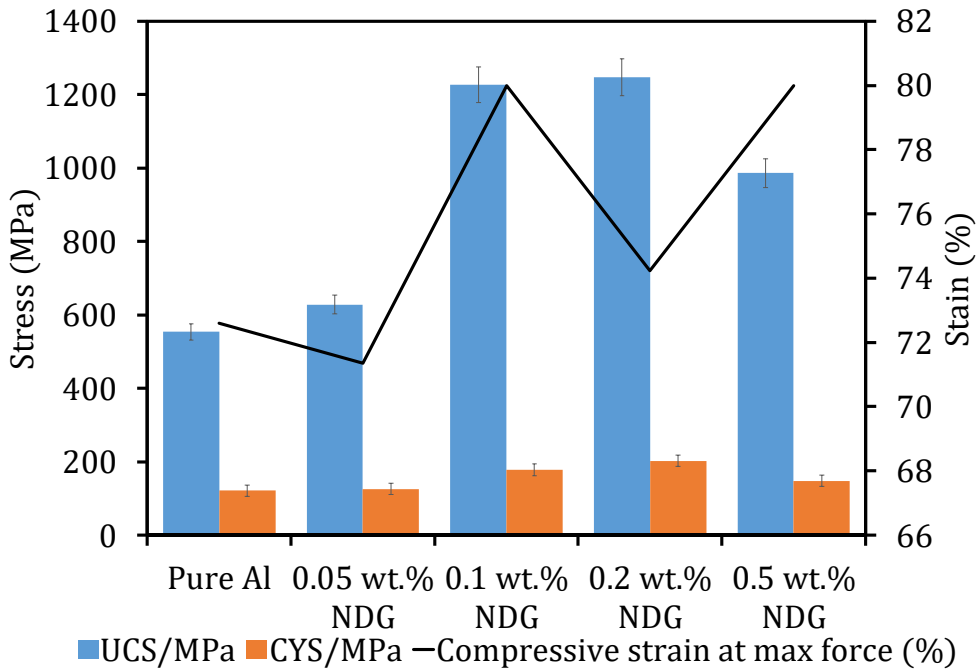
From Figure 4-10 (b), the compressive yield strength of NDG reinforced MMCM was found to be 126 MPa, 178 MPa, 202 MPa, and 148 MPa, respectively, while the ultimate compressive strength was found to be 627 MPa, 1226.76 MPa, 1247.33 MPa, and 985.96 MPa for 0.05, 0.1, 0.2, and 0.5 wt. % NDG reinforcements. For all weight percentages of NDG, compressive strength was substantially higher than compressive strength for pure aluminum. As evident from the literature discussed in chapter 2, the strength of composite increases when the reinforcement restricts the movement of dislocation. Hence, the weight percentage of NDG was increased from 0.05 to 0.5 wt. %, a finite increase in the ultimate strength of composite could be observed, however, from 0.2 to 0.5 wt. % of NDG, there is a decrease in the composite's ultimate and yield compressive strength.

The increase in NDG/Al MMCM's strength compared to pure aluminum and graphene/Al MMCM at lower NDG concentration is due to its better interfacial properties, homogenous distribution of NDG and no active carbon sites on graphene structure for aluminum carbide (Al_4C_3) formation. The presence of pyrrolic, pyridinic, and graphitic nitrogen (refer to Fig. 35) at various interstitial locations of NDG has slowed the formation of the Al_4C_3 phase and accelerated the formation of the graphene - AlN - aluminum matrix interface. AlN has an elastic modulus of 310 GPa at 1090°C³⁹² and has good wettability with aluminum metal³⁹³, so better interfacial properties are primarily responsible for the better mechanical performance of NDG reinforced Aluminum MMCM. The decrease in strength at higher reinforcement content (0.5 wt. %) can be attributed to the porosity formed due to the reaction between carbon and nitrogen at high sintering temperatures and brittleness induced within composite at higher NDG wt.%. The phenomenon creates fracture at Al/NDG interface when loaded during mechanical testing. The reaction between carbon and nitrogen produces a gaseous product, resulting in the formation of voids between the grains³⁹⁴, as evidenced by the subsequent decrease in compressive strength at 0.5 wt. % NDG concentration.

The increase and decrease in strength and ductility of composite with an increasing weight percentage of reinforcement could be explained as follows: From Figure 4-11 (a), it can be observed that tensile strength increases from 0.05 wt. % to 0.2 wt. % and then decreases after further addition of NDG, i.e. 0.5 wt. % NDG. After analysing the effect of doping percentage on composite strength, it was observed that composite strength further decreased at the same weight percentage when NDG with higher doping percentage was utilized. From Figure 4-13(section 4.4.3), it was observed that brittleness increases with an increase in NDG wt. %. Hence, it could be concluded that the inclusion of nitrogen as a doping element induces brittleness in composite, especially when the weight percentage of reinforcement is higher. However, when the reinforcement percentage was kept low, ductility within the composite was preserved and effective load transfer from matrix to reinforcement could be observed. Hence, till 0.2 wt. % of NDG effective load transfer mechanism due to the inclusion of NDG was dominant. When NDG weight percentage was increased, brittleness within the composite was dominant, and a drastic decrease in strength was observed.



(a)



(b)

Figure 4-10: (a) Tensile strength for pure Al, 0.05, 0.1, 0.2, 0.5 wt. % of NDG and 0.5 wt.% GNP and (b) Compressive stress-strain curve for NDG/Al composite.

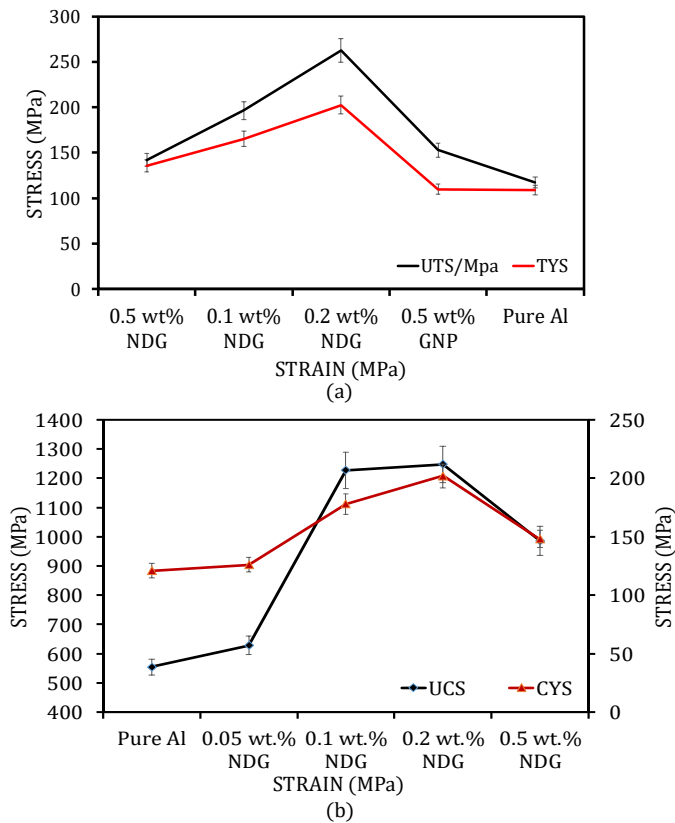


Figure 4-11: Mechanical properties of composites post, (a) Tensile and (b) Compressive test.

The pin on disc method was utilized to conduct the wear test, which was used to determine the wear rate and coefficient of friction (COF) for the Al/NDG composite material. The test was carried out in compliance with ASTM G99 specifications. The testing medium was a DUCOM wear & friction monitor machine with a die-steel disc having a Ra value of 0.23 microns and a normal load of 10 N. The wear test results for Al/NDG composites with different reinforcement percentages are shown Figure 4-12. It is evidenced from the literature that COF of graphene reinforced composite is effectively reduced through the incorporation of GNP due to its self-lubricating effects³⁹⁵. As shown in Figure 4-12(a), The coefficient of friction (COF) of NDG/Al composites decreased dramatically with increasing NDG content, such that there was a 45 % drop in COF when NDG was raised from 0.1 wt. % to 0.5 wt. %. Figure 4-12(b) depicts the wear vs time graph for the NDG/Al composite material. The proportion of NDG content significantly impacts composite material wear performance, with a 25 % reduction in wear rate when NDG was increased from 0.1 to 0.2 wt. %, and a 71 % reduction when the aluminum matrix was reinforced with 0.5 wt. % NDG. The decrease in COF and wear rate suggest

that NDG has restored its self-lubricating characteristics and have effectively bonded with the aluminum matrix material.

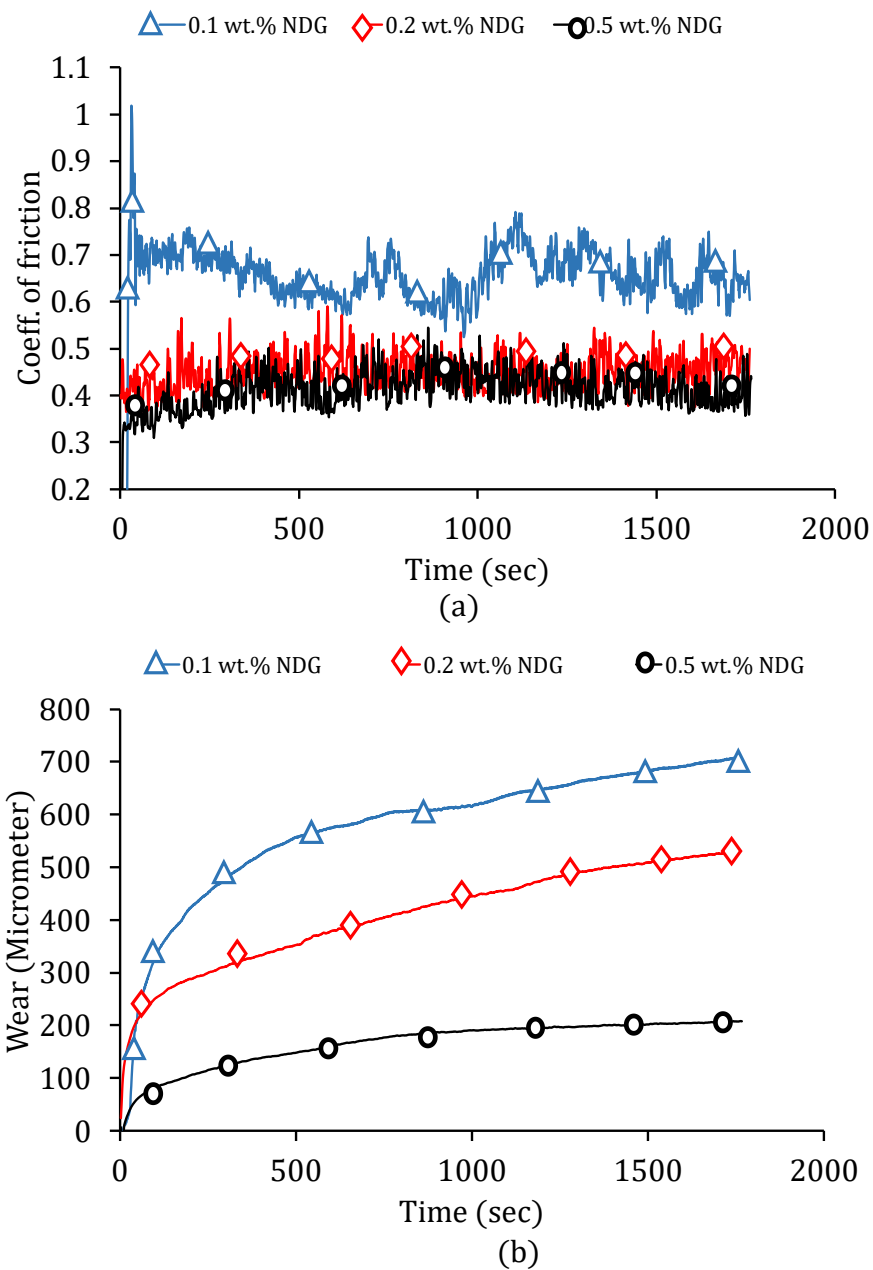


Figure 4-12: (a) Coefficient of friction (COF) and (b) Wear rate of NDG/Al composite material having different NDG concentrations

4.4.3. Characterization of composite material

The surface morphology of tensile fractured surfaces for NDG/Al composite materials with various reinforcement compositions is shown in Figure 4-13. FESEM images of the fracture surface after tensile testing with NDG weight fractions of 0.1 wt. %, 0.2 wt. %, and 0.5 wt. % is shown in Figure 4-13(a-c), as the weight fraction of NDG increased from

0.1 to 0.5 wt. %, the image clearly shows that the brittleness of the composite predominates over the ductile fracture. The creation of the ceramic interface at the aluminum-NDG grain junction at a higher sintering temperature is linked to the loss of composite ductility. The peak of carbon and oxygen caused by aluminum oxide and NDG is visible in the EDX plot of the fractured surface and is shown in Figure 4-14. Compared to the pure aluminum sample, the presence of graphene at the shattered surface must have restricted grain slippage and resulted in better composite strength.

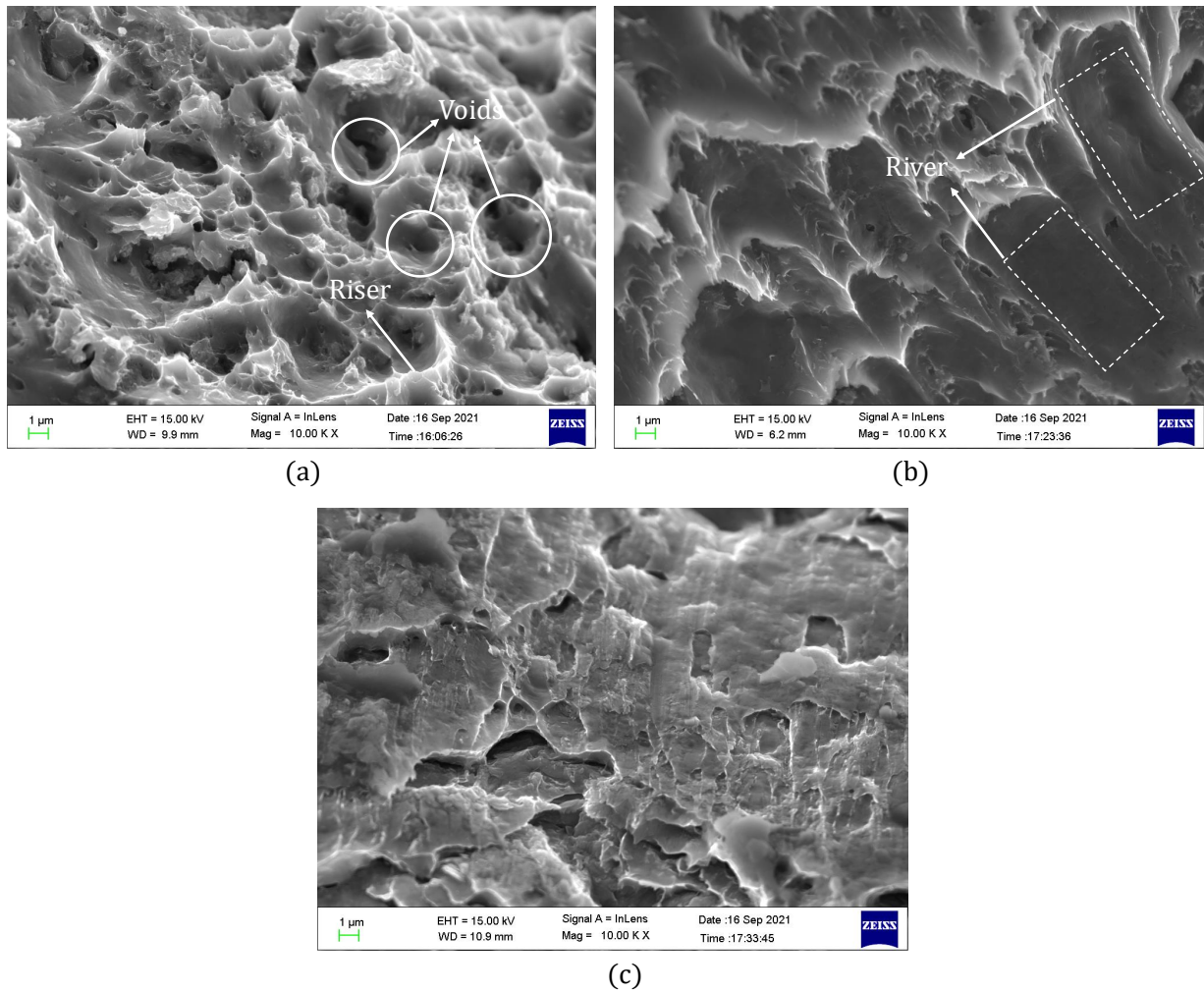
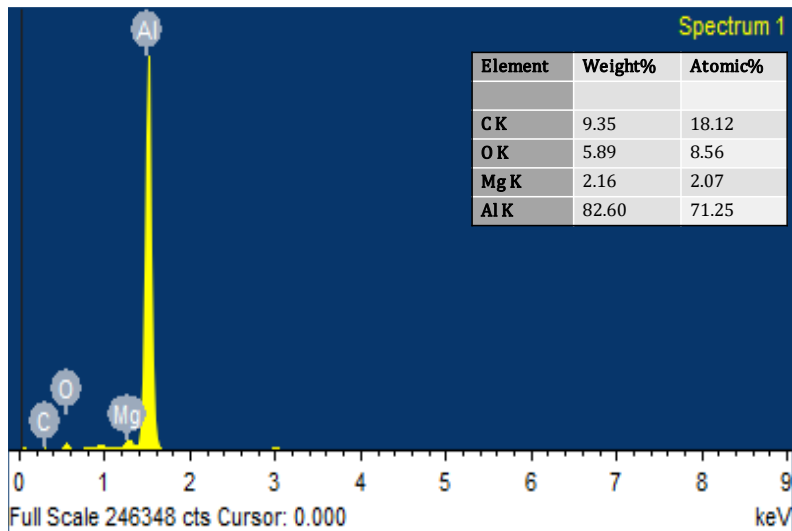
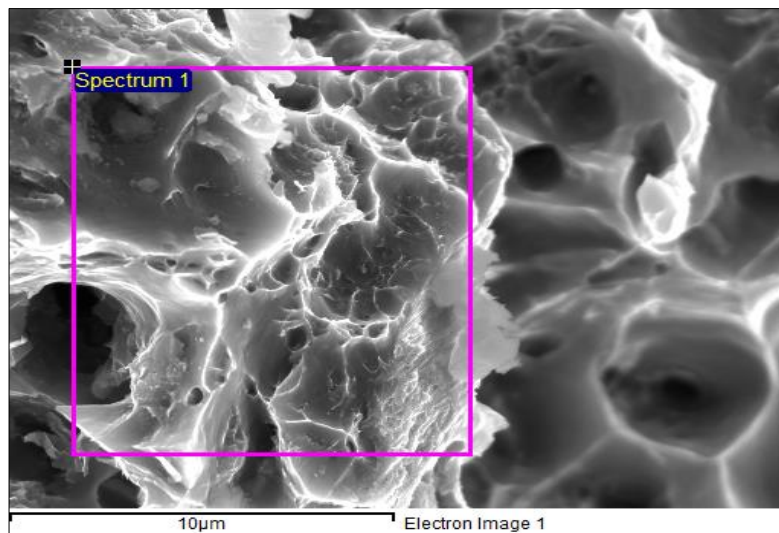


Figure 4-13: FESEM image of fractured surface after tensile test having NDG concentration of (a) 0.1 wt.% , (b) 0.2wt.% , (c) 0.5 wt.% respectively.



(a)



(b)

Figure 4-14: EDX image of the Al/NDG composite material.

The XRD plot for Al/NDG composite is shown in Figure 4-15. Peaks at 38.448° , 44.6913° , 65.025° , 78.175° and 82.365° correspond to aluminum and match well with JCPD card number 96-431-3218. A trace of aluminum nitride was found having a low-intensity Peak at 35.603° (JCPD card number 96-101-0515), indicating the formation of aluminum nitride interface at NDG/Al junction. The presence of AlN has increased the wettability and strength of composite (even more significant than Al/GNP composite; refer 42(a)). A peak at 66.97° corresponds to aluminum oxide (JCPD card number 96-100-0060). The nitrogen, carbon, and oxygen compound has a peak at 11.87° , revealing the NDG linkage (JCPD card number 96-151-9682). The low-intensity peak at 35.6036 indicates that the

aluminum nitride-aluminum-graphene interface was well-formed, resulting in improved composite strength even at a low reinforcement weight percentage.

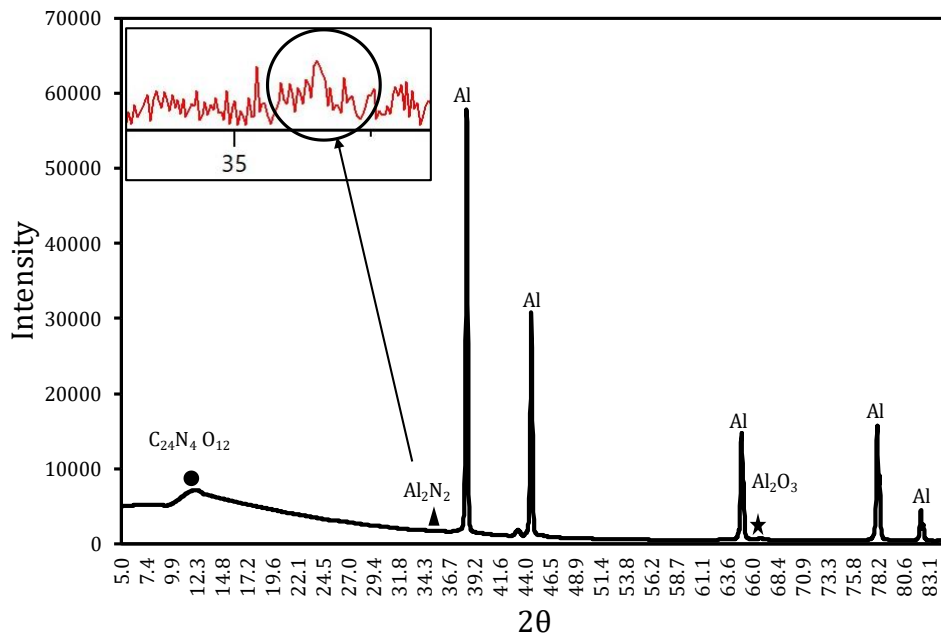


Figure 4-15: XRD of Al/NDG metal matrix composite showing peaks for ALN and Al₂O₃.

4.5. Conclusion

In summary, a high-energy ball milling approach was used to fabricate nitrogen-doped graphene (NDG) successfully and was further used as reinforcement for the synthesis of NDG/Al metal matrix composite. Various characterization techniques characterized the synthesized NDG and NDG/Al composite. XPS spectral nitrogen peaks in the synthesized NDG were at 400.15 eV, 401.2 eV, and 398.46 eV, respectively, reflecting pyrrolic-N, graphitic-N, and pyridinic-N functionalities. After experimenting with varying reinforcement percentages, it was discovered that the composite's strength was significantly higher than that of pure aluminum and graphene/Al sample. The wear properties of graphene were enhanced by adding NDG, and it was observed to rise with increasing NDG concentration, which implies that NDG reinforcement has lubrication properties. The better interfacial bonding and creation of a robust NDG/AlN/Al interface were primarily responsible for the increased strength of the NDG/Al composite. AlN has a higher wettability with aluminum, and its presence at the contact prevents Al₄C₃ production. However, creating a gaseous carbon-nitrogen product at higher sintering temperatures while utilising a substantial amount of NDG has reduced the strength of the composite.

CHAPTER 5: Synthesis of ball-milled edge-functionalized sulfur-nitrogen co-doped graphene: their influence on aluminum metal matrix composite

5.1. Introduction

Sulfur-nitrogen co-doped graphene (S-NDG) is prepared via solid-state ball milling of graphite and sulfur at 300 RPM. The prepared SDG was studied using XRD, XPS, Raman, EDAX, HRTEM and FESEM characterization techniques before being employed as reinforcement in an aluminum matrix to composites. The presence of nitrogen was discovered in the XPS and EDAX spectra of synthesised graphene, implying that nitrogen was absorbed from the atmosphere to produce sulfur-nitrogen co-doped graphene. According to elemental analysis, the nitrogen and sulfur contents were 4.7 and 2.1 atomic percentage, respectively. S-NDG has demonstrated exceptional mechanical performance by boosting tensile strength by 118.81% with just 0.5 wt.% reinforcement and 66.52% for 0.05 wt.% of S-NDG. The total strain before fracture improved when the reinforcement concentration was increased, indicating excellent wettability and stronger interfacial bonding of S-NDG with the aluminum matrix.

5.2. Motivation, objective and approach

The exceptional properties of graphene and its peculiar structure of one atomic thickness sp^2 hybridised carbon network has attracted considerable interest and have greatly improved the performances of modern appliances such as energy storage³⁹⁶, healthcare³⁹⁷, electrochemical sensing³⁹⁸ and electronic industries³⁹⁹ to that of modern composite materials⁴⁰⁰. The functionalisation of graphene⁴⁰¹ can impart the possibility of further enhancing graphene properties for specific industrial purposes. Various methods to functionalized graphene are covalent C-C coupling⁴⁰², non-covalent π - π interaction⁴⁰³, hybridisation with nanoparticles⁴⁰⁴ and substitutional heteroatom doping of graphene⁴⁰⁵. To enlarge the graphene family, heteroatom doping⁴⁰⁶ is a promising technique to tailor graphene with improved electromagnetic, physicochemical, chemical, mechanical, optical and structural properties.

The graphene's covalent functionalisation is a powerful tool for synthesising doped graphene nanoplatelets, but it can significantly destroy the π - π conjugate structure. The non-covalent functionalisation of graphene based on π - π stacking of

aromatic carbon atoms or van der Waals force of attraction can produce physically functionalized graphene with a largely preserved graphitic nature. Ball milling is one of the standard techniques primarily used in powder production industries and has proven to be a simple and efficient method to produce edge-functionalized graphene⁴⁰⁷. Recently, sulfur-doped graphene has shown several interesting electronic properties^{408,409} and has become an exciting research topic in the electronic and energy storage industries. However, sulfur-doped graphene has never been used as a reinforcement material in metal matrix composite.

The potential achievable improvement in the properties of metal matrix composite, such as improved strength, higher elastic modulus, better wear resistance, higher thermal and electrical conductivity etc., has made graphene a desirable material in aerospace and automobile industries. Aluminum-based metal matrix composites are most commonly used in automobile and aerospace applications, generally reinforced with metallic, non-metallic and ceramic reinforcements. Incorporating graphene into the aluminum matrix has attracted the focus of many active researchers. However, its low wettability, agglomeration tendency and formation of aluminum carbide (Al_4C_3) is still a primary challenge⁴¹⁰. Bustamante et al.⁴¹¹ have shown the formation of Al_4C_3 in the synthesis of CNT/Al composite. The carbide formation depended on the composite material's processing temperature (above 500°C). Al_4C_3 is energetically the most favourable stoichiometry during the processing of composite and is potentially harmful to the mechanical properties of the composite. However, a highly stable defect-free graphitic plane on graphene or CNT do not react with aluminum even at very high temperature⁴¹². Carbide formation is predominantly promoted at the defect site within graphene and is most commonly formed during the ball milling process. Functionalized graphene with suitable dopant can eventually solve many problems associated with graphene, such as (1) stabilise graphene by adding itself at the location of edge defect⁴¹³, (2) improving wettability with aluminum by forming proper interfacial product⁴¹⁴ and (3) enhancing other properties of graphene to get high-performance composite material³⁷⁴. The use of functionalized graphene is strictly limited in composite material, and it must be utilized to get high strength, high-performance modern composite materials.

We have recently incorporated nitrogen atoms into the graphite material to get nitrogen-doped graphene via dry high energy ball-milling technique using melamine as a

doping material. The graphene obtained has Pyrrolic-N, pyridinic-N and graphitic-N, functional groups attached at the interstitial sites of the carbon atom. In the current work, we have investigated the synthesis of nitrogen-sulfur co-doped graphene by ball-milling technique and the strengthening effect of sulfur-doped graphene when used as reinforcement in aluminum metal matrix composite. The work aims to enhance composite material performance by creating the proper interfacial product. Since sulfur has more electron affinity than carbon and aluminum, hence the formation of aluminum carbide would be less.

5.3. Experimental

5.3.1. Material Selection

Graphite (100 mesh, 98% pure) is purchased from research lab fine chem industries, Mumbai. The sulfur powder was purchased from finar chemicals, Gujarat. Aluminum metal powder (325 mesh, 99% pure) was purchased from Sisco research laboratories Pvt. Ltd., Maharashtra. Carbon disulphide (99% pure) was purchased from Loba Chemie PVT. Ltd., Maharashtra. Zirconium oxide beads (having an average size of 1.15mm and 4.46mm) were purchased from synco industries limited, Rajasthan. All products used in this study are commercially available and of commercial analytical grade, which was utilised without further purification.

5.3.2. Preparation of Sulfur-doped graphene

Graphite powder, weighing 5 grams, was mixed with sulfur powder in the ratio of 1:5 and was poured into the tungsten carbide (WC) jar of 250 ml capacity. To achieve the maximum energy transfer (refer, ¹⁰⁴) jar was filled with zirconium beads of size 4.46 mm and 1.15 mm up to 2/3rd of the jar volume. The jar was sealed airtight and dry milled in the Retsch planetary ball-milling machine at 300 RPM for 72 hours. After every 24 hours, a small quantity of samples was collected for analytical purposes. The collected sample was washed with carbon disulphide several times in the centrifuge to remove extra unreacted sulfur present in the mixture. The prepared sample was dispersed and dried to get sulfur-doped graphene.

5.3.3. Preparation of metal matrix composite material

Aluminum powder (matrix material) was mixed with 0.05 wt. %, 0.1 wt. %, 0.2 wt. % and 0.5 wt. % of sulfur-doped graphene, the mixture was milled for 60 min in a planetary ball milling machine to get the uniformly mixed mixture. Four samples obtained were cold

compacted at 450 MPa and hot sintered at 600°C in a tube furnace using an argon gas environment to get a sulfur-doped graphene metal matrix composite. The prepared composite sample (25mm diameter) was further hot extruded at 450°C to get a 10mm diameter sample. The composite sample with four different reinforcement concentrations was mechanically tested and repeated to check the repeatability of the results.

5.4. Result and discussion

Schematics for the synthesis of nitrogen-sulfur co-doped graphene via dry ball milling technique is represented in Figure 5-1. During the ball milling process, the strong shear force generated between high speed rotating balls crushes and exfoliates the graphite particle creating mechanochemical fracture of graphitic C-C bond resulting in smaller and thin layered particles, generating carbon-free radicals. The broken edge of graphitic framework or active carbon free radicals leads to the spontaneous incorporation of functional group/sulfur heteroatoms with subsequent generation/exfoliation of graphene nanoplatelets. Typically, graphene material synthesised by high energy ball-milling technique possesses a particle size fewer than 1 μm .

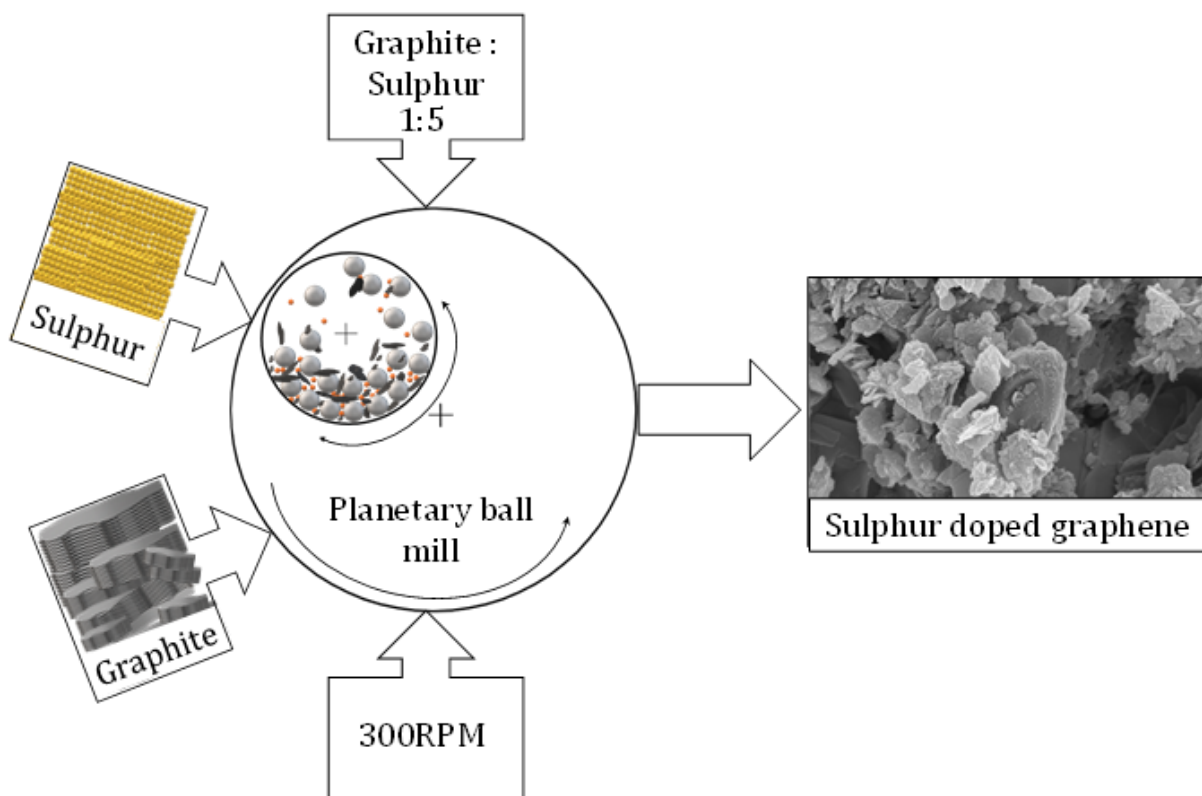


Figure 5-1: Schematic diagram for the synthesis of sulfur-nitrogen co-doped graphene.

5.4.1. Physicochemical characterization of sulfur-doped graphene

Figure 5-2 shows the FESEM image of nitrogen-sulfur co-doped graphene (SDG). The mechanism behind graphene synthesis through high energy ball milling technique is the sizeable tangential shear force exerted by zirconium balls, significantly layer by layer peels of the graphite particle into thin sheets of multi-layered graphene. The conversion of large-sized graphite particles into a thin sheet of multi-layered graphene is shown in Figure 5-2. During the milling process, graphite particles are crushed into smaller, thin layered particles generating carbon-free radicals. The sulfur particle tends to absorb and disperse on the graphite surface while interacting with carbon-free radicals to form a carbon and sulfur bond. Figure 5-2(c) shows the fractured surface of graphite particle milled for 24 hours. The S-NDG particle synthesised through the ball milling technique exhibits a co-deposition of sulfur nanoparticles on the surface of the graphene sheet, as marked by the red arrow in Figure 5-2(b). The sulfur nanoparticle was found to be deposited all over the surface of S-NDG sheets (marked with a white arrow), and its size was observed in the range of 15 to 25 nm, indicating a robust molecular bonding between the sulfur and graphene sheets. The EDAX spectrum of synthesised S-NDG milled for 72 hours is shown in Figure 5-3. A strong EDAX peak confirms the presence of co-deposited sulfur particles on the surface of S-NDG sheets. However, along with the presence of carbon and sulfur in the EDAX spectrum, a low-intensity nitrogen peak was observed, suggesting that nitrogen present in the air has interacted with the carbon-free radicals producing S, N co-doped graphene. The presence of nitrogen is acceptable because it will not allow any vacant sites to react to active carbon and aluminum at an elevated temperature during the synthesis of composite material, thus producing strong interfacial bonding.

X-ray photoelectron spectroscopy (XPS) is a powerful and most commonly used technique to evaluate the nature of bonding between carbon, sulfur and nitrogen (since nitrogen were present in the EDAX spectrum) atoms in graphene. The XPS comprehensive survey scan illustrated in Figure 5-4 shows the presence of carbon at 284 eV, sulfur at 163.80 eV, nitrogen at 399.5 eV and oxygen at 532 eV. Figure 5-5(a) represents XPS spectra of C1s core level having the main peak at 284.50 eV corresponds to sp^2 -hybridized C-C bond. The sample produced a small peak at 287.6 eV and 288.9 eV corresponding to carbonyls (C=O) and carboxylate (O-C=O) bonds. The C1s spectrum

can be fitted with small intensity peaks at 286.0 eV, 286.7 eV, and 285.2 eV corresponding to C-N, C=N, and C-S bonding.

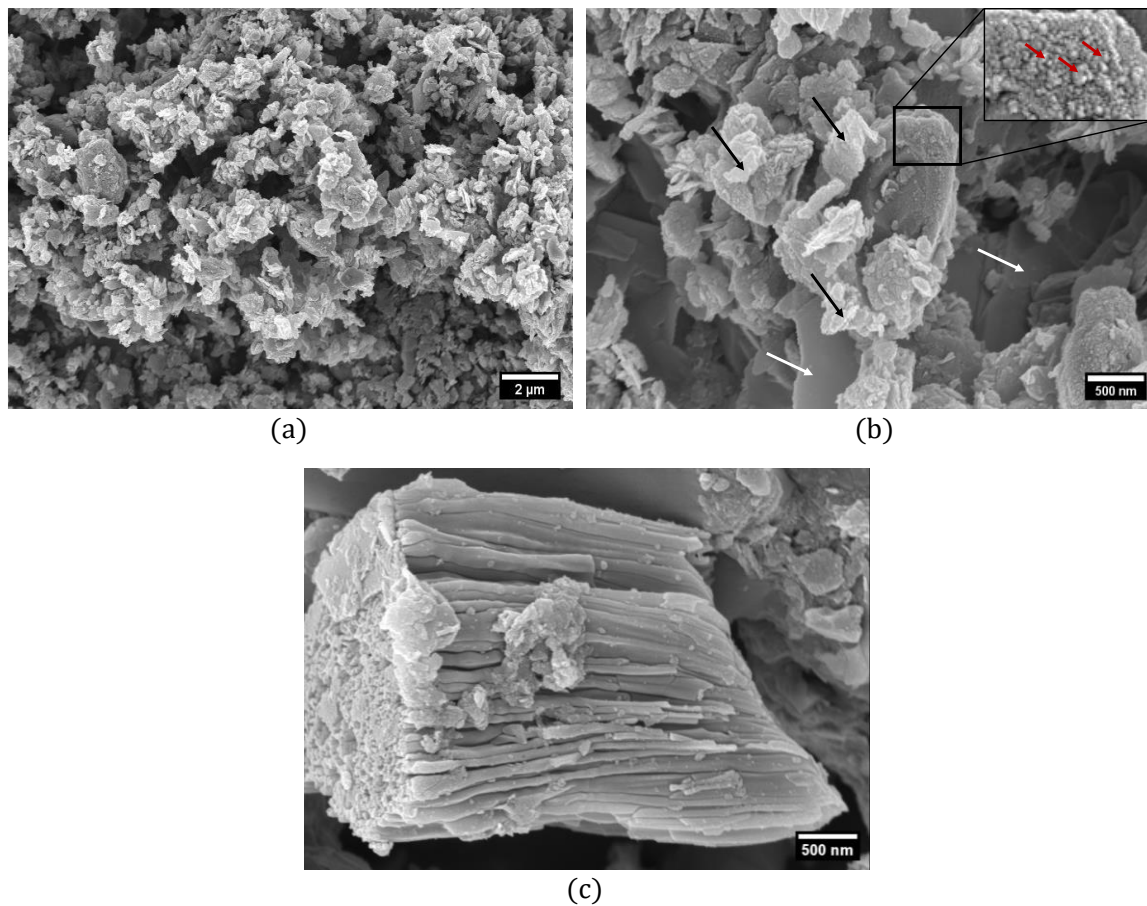


Figure 5-2: FESEM image of sulfur-nitrogen co-doped graphene (a) Milled for 72h, (b) sulfur nanoparticles deposited on all over the graphene sheet, (c) Fractured graphite surface after 24h milling.

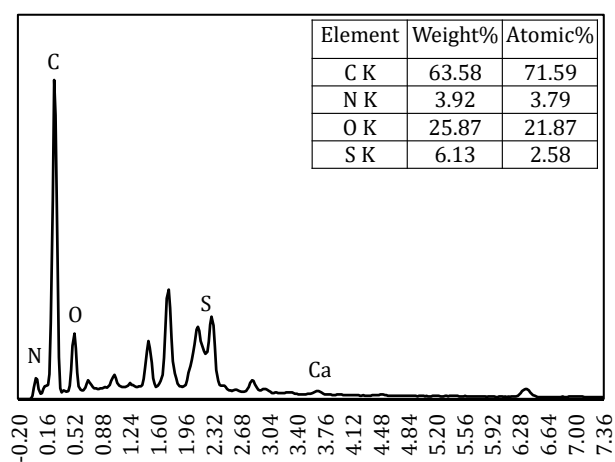


Figure 5-3: EDAX spectrum of sulfur-nitrogen co-doped graphene showing S, C, O and N peaks.

The deconvoluted XPS N1s spectra of SDG is shown in Figure 5-5(b). The high-resolution N1s spectra can be decomposed into three different peaks, which are assigned to pyridinic-N (398.7 eV), Pyrrolic-N (400.15 eV) and graphitic-N (401.2 eV). This result suggests that S or N atoms are a covalently bonded graphene network. The high-resolution S 2p XPS spectra, as shown in Figure 5-5(c), corresponding to the peak at 163.8 eV and 168.4 eV can be attributed to C-S-C and C-SO₂ bond, respectively, SP₂ peaks at 165 eV (S 2p_{1/2}) and 163.8 eV (S P_{3/2}) can also be attributed C-S/S-S bonding. According to the analysis, the sulfur content of SDG was 2.1 atomic %, and nitrogen was 4.7 atomic %. The XPS spectrum reveals that nitrogen and sulfur are structurally integrated into an extended carbon network.

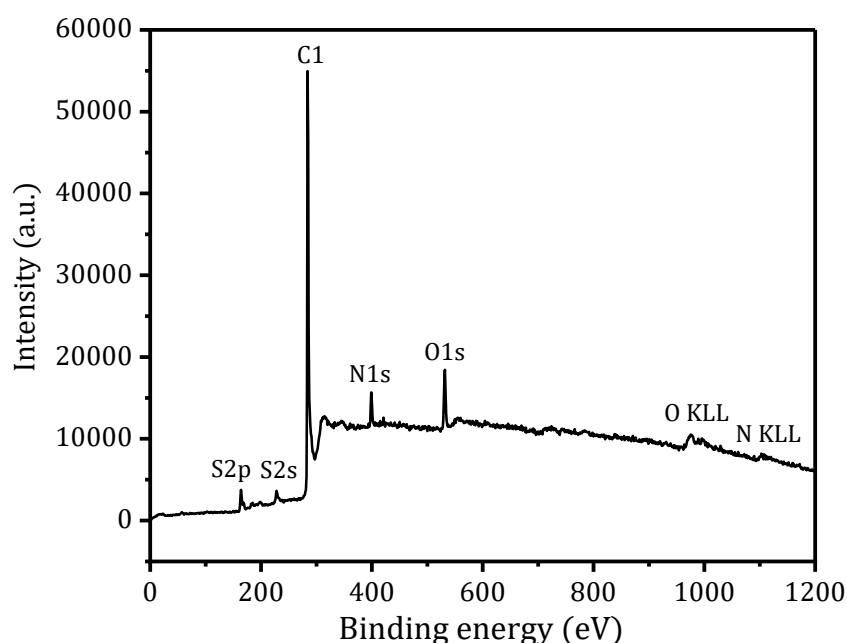


Figure 5-4: XPS high-resolution XPS survey scan of S-NDG

The HRTEM image of exfoliated S-NDG particle is illustrated in Figure 5-6. The low magnification HRTEM image, as shown in Figure 5-6(a), shows the presence of sulfur particles at various locations and is found to be uniformly distributed along the graphene surface, which was confirmed by TEM bright-field surface mapping and is illustrated in Figure 5-7(d). The graphene formed has proper transparency and no evidence of graphite agglomeration with a perfectly polycrystalline nature, as confirmed by the SAED pattern in Figure 5-6(b). The particle under higher magnification is multi-layered graphene with a thickness of 7 layers (average) and inner layer spacing of 0.32 nm. The surface mapping of S-NDG with oxygen, carbon and sulfur on S-NDG surface is shown in Figure 5-7.

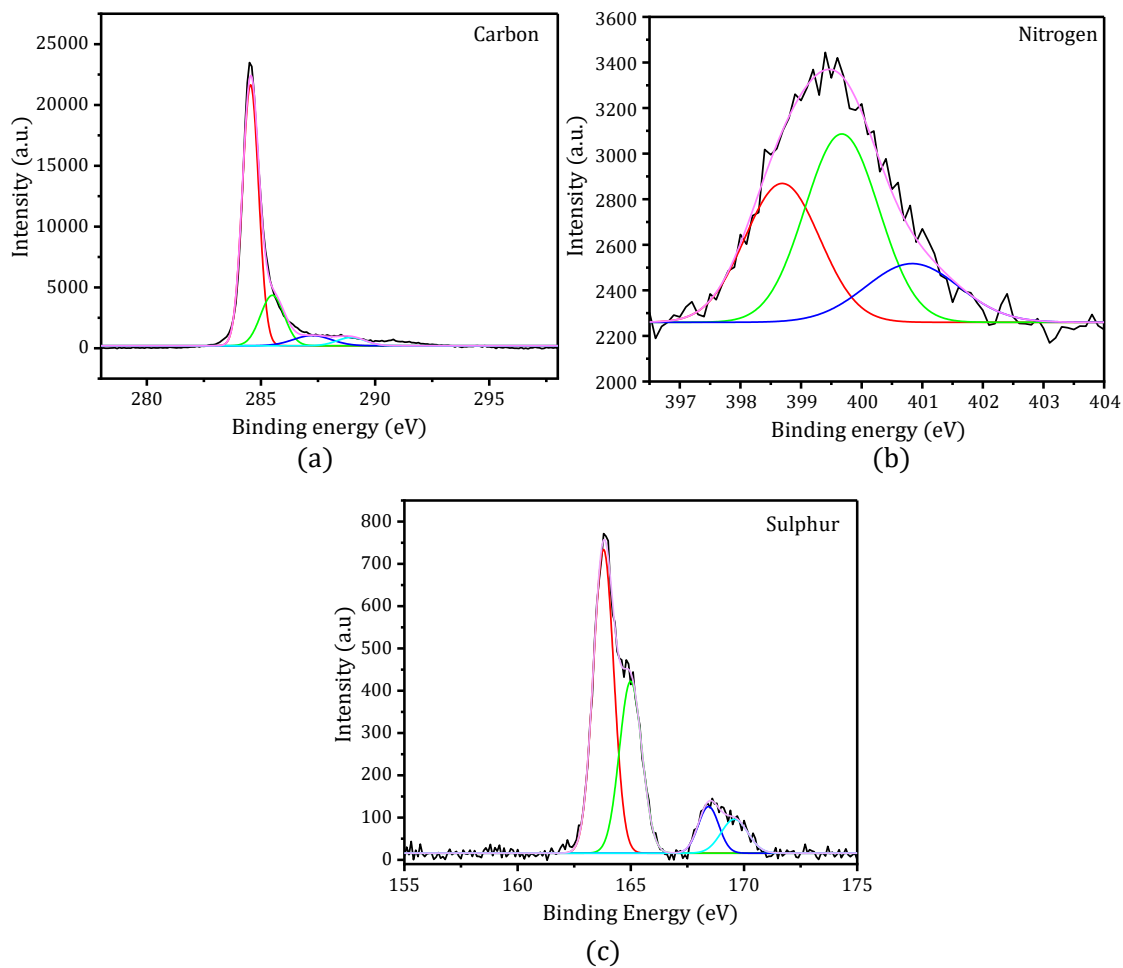


Figure 5-5: : High-resolution XPS spectra of sulfur-nitrogen co-doped graphene (SDG) (a) XPS high-resolution spectra of C 1s, (b) N 1s and (c) S 2p

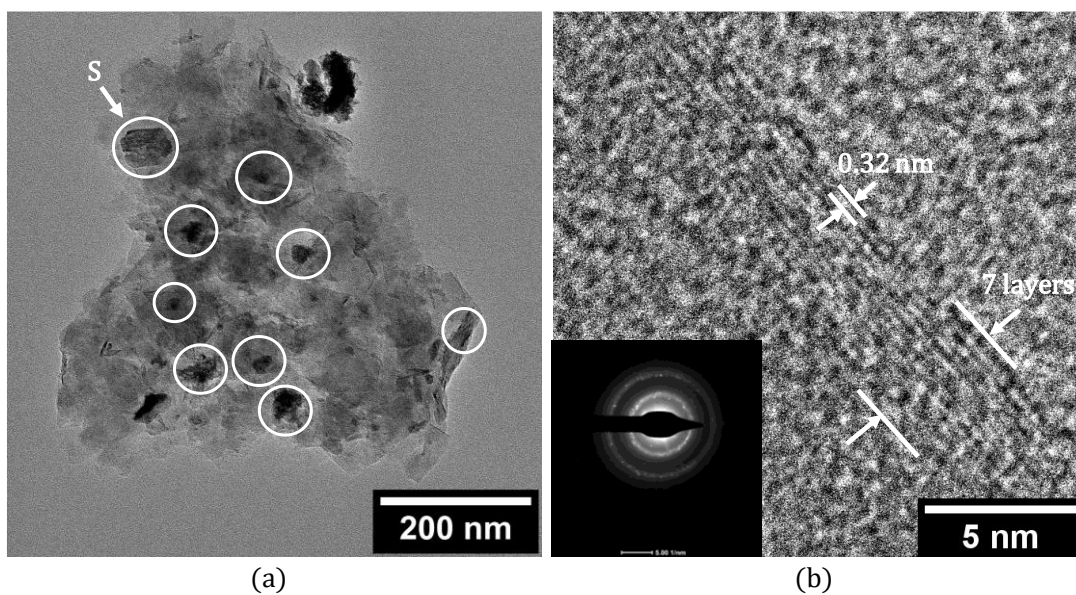


Figure 5-6: HRTEM image of sulfur-nitrogen co-doped graphene of (a) lower magnification (b) Higher magnification image with SAED diffraction.

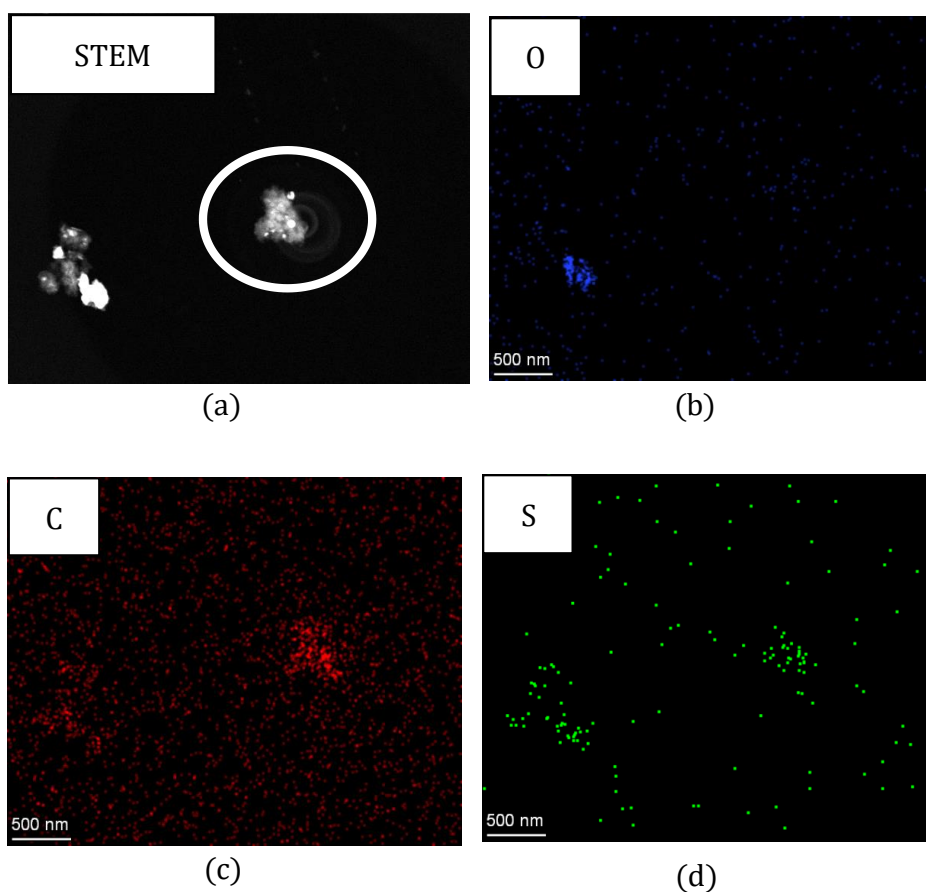


Figure 5-7: (a) STEM image at lower magnification with, (b) TEM surface mapping of oxygen, (c) Carbon and (d) Sulfur.

Raman spectroscopy of S-NDG milled for 24h and 72h is illustrated in Figure 5-8. The analysis was conducted using “HORIBA scientific LabRAM HR-UV-open, France” with a range of 300 to 3000 cm^{-1} and wavelength of 532 nm. Carbonaceous material shows its fingerprint under this technique by D, 2D and G peaks. Pristine graphene shows G and 2D peaks at 1580 cm^{-1} and 2710 cm^{-1} without a D peak. The G-band peak occurs due to E_{2g} vibration and reflects the structural integrity of SP₂-hybridised carbon atom and is observed in every SP₂ bonded graphitic carbon atom. Most of the graphene exfoliated through high energy ball milling technique shows D-band peaks at 1350 cm^{-1} and is attributed to the vibration of carbon atoms with dangling bonds in the disordered graphitic plane and the presence of defects in the pentagonal and hexagonal graphitic structure. The Raman spectroscopy of the prepared sample shows D-band, G-band and 2D band peaks at 1350 cm^{-1} , 1582 cm^{-1} and 2694 cm^{-1} for the 24-hour milled sample and 1334 cm^{-1} , 1566 cm^{-1} and 2682 cm^{-1} for 72-hour milled sample. The shift in Raman peaks towards lower wavenumber for extended milling time is because of an increase in bond

length caused by adding heteroatoms at interstitial sites of graphitic structure⁴¹⁵. The I_D/I_G ratio of the 24h milled sample was found to be 0.96, and for the 72h milled sample was observed to be 0.88, corresponding to the lattice size of 20.03 nm and 21.85 nm, respectively. The presence of a near symmetrical 2D band and a high-intensity G band suggests the successful exfoliation of graphite down to fewer layers of graphene. At the same time, a lower I_D/I_G ratio indicates lower structural defects⁴¹⁶. The drop in I_D/I_G ratio from 24h milled to 72h milled sample is due to the formation of some nano-sized S-NDG particles during the extended milling time and could be responsible for less disordered structure in the milled graphite³⁹¹.

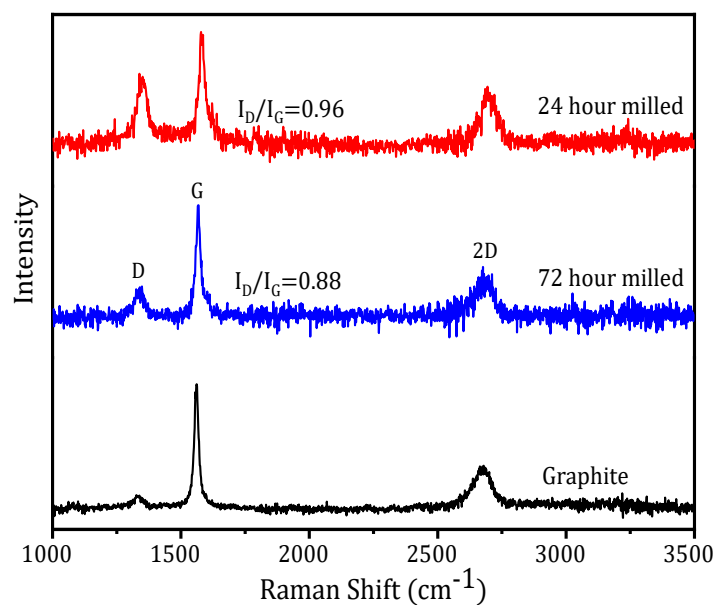


Figure 5-8: Raman spectroscopy of pure graphite and S-NDG milled for 24h and 72 hours.

5.4.2. Mechanical Characterization of Al/S-NDG composite

Mechanical properties of S-NDG reinforced MMCM is studied with the help of tensile and compression test, respectively. The test specimen was fabricated using ASTM standards, having a gauge diameter of 6 mm and a gauge length of 30 mm for the tensile test and an L/D ratio of 2 for the compressive test. Figure 5-9 illustrates the tensile and compressive stress-strain curve for Al/S-NDG composite with various S-NDG weight fractions. The tensile stress at maximum force and tensile stress at yield for a composite having 0.05 wt. % S-NDG was found to be 179.32 MPa and 109.89 MPa, respectively and for 0.5 wt. % S-NDG was found to be 256.71 MPa and 195.37 MPa, respectively. Al/S-NDG composite, even with a tiny percentage of S-NDG (0.05 wt. %), significantly improves the tensile

strength by 66.52% and with 0.5 wt. % S-NDG, the percentage increase in tensile strength was 118.81%, compared to pure aluminum (standard value).

The composite material based on carbonaceous reinforcements often suffers certain demerits, i.e. non-wettability of carbonaceous reinforcement with aluminum matrix leading to the porosity within grains and development of brittle phase Al_4C_3 at higher sintering temperature. The phenomenon decreases strength at a higher reinforcement weight percentage and often decreases the total strain percentage at the breakpoint⁴¹⁷⁻⁴²⁰. The inclusion of reinforcement generally hinders the movement of dislocation when strained, increases yield strength, and decreases ductility. Tensile strain before fracture decreases from 0.05 wt. % to 0.2 wt. % S-NDG and is evident in every particle reinforced composites. The decrease in the strain at failure with increasing reinforcement is because reinforcement generally hinders dislocation movement when strained, thus improving strength and barring the further movement of grains. Due to this phenomenon yield and ultimate strength of Al/S-NDG composite increase and strain decreases. However, the fall in the strain at failure in S-NDG/Al composite is less than NDG/Al composite even in the case of 0.5 wt. % S-NDG suggesting better wettability of S-NDG. The compressive stress-strain curve for Al/S-NDG composite with various S-NDG weight percentages is illustrated in Figure 5-9(b). The compressive strength value for 0.05, 0.1, 0.2 and 0.5 wt. % S-NDG and was found to vary between 596.53 MPa to 738.20 MPa. However, the compressive strength of pure aluminum is 554.16 MPa. The increase in compressive strength was 33.21% for 0.5 wt. % and 7.64 % for 0.05 wt. % S-NDG.

Figure 5-10 shows the FESEM image of the fractured surface for the tensile specimen. From the nature of the stress-strain graph, it is evident that the composite exhibits ductile behaviour. The fractographic study of the composite after a tensile fracture, as shown in Figure 5-10 has a ductile failure. Ductile failure shows the presence of voids^{421,422}, cleavage (Riser)⁴²³ and dimples at the fractured surface⁴²⁴. When ductile failure occurs by mechanical instability of the test specimen, the fracture surface exhibits partial or total slanging, resulting in shear failure and is evidenced by rivers on failure parts⁴²⁵. The surface under higher magnification has shown that failure has started initially along the grain boundaries by forming small voids under higher loading conditions. As the load increases, the void elongates, resulting in the removal of grain and the formation of risers and dimples. Risers or cleavage preferentially occurs over the

dense atomic plane⁴²⁶. In most composite materials, dimples or larger voids sometimes occur at reinforcement particles where the bond strength is weaker than the bonding between matrix materials. A thin sheet of graphene pullover is also marked in the image. The EDAX spectrum of the fractured surface Figure 5-11 shows the presence of carbon uniformly mixed along with the composite matrix material.

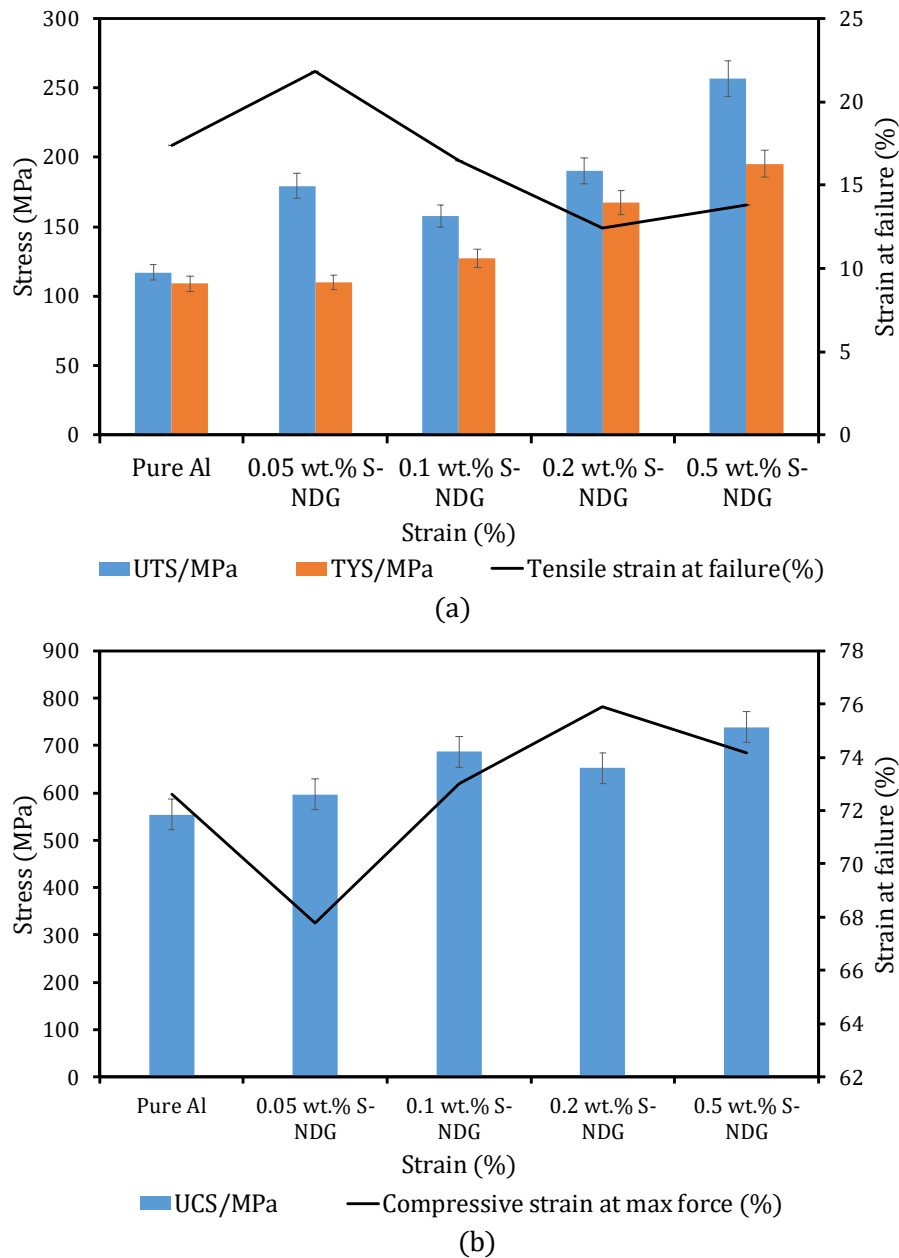


Figure 5-9: Stress-strain graphs of the composite after (a) Tensile test and (b) Compressive test.

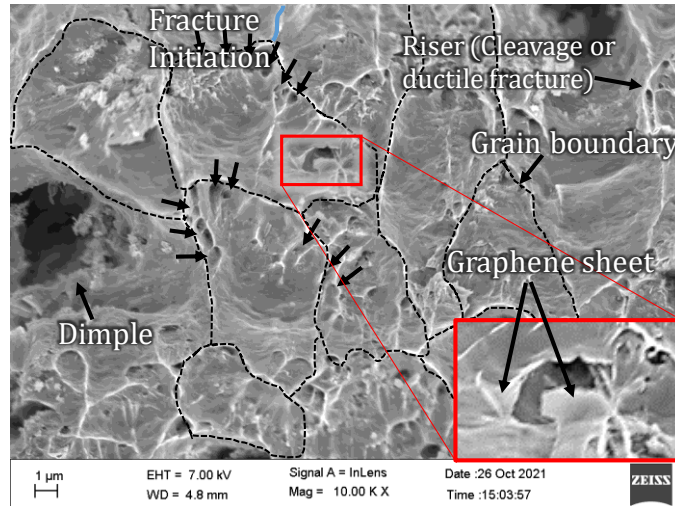


Figure 5-10: FESEM image after tensile fractured.

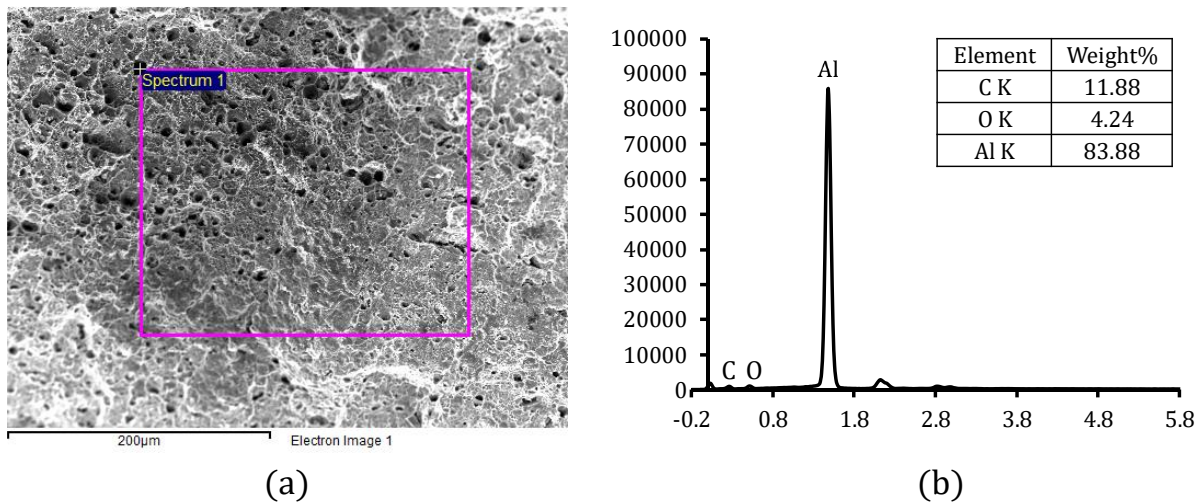


Figure 5-11: EDX spectrum of S-NDG fractured surface

5.5. Conclusion

In summary, a high energy ball milling technique is used to fabricate sulfur-nitrogen co-doped graphene (S-NDG) successfully. The S-NDG was further used as a reinforcement material to synthesise Al/S-NDG composite material. The XPS analysis of graphene has shown that synthesised graphene has 2.1 atomic % of sulfur and 4.7 atomic % of nitrogen, indicating nitrogen was absorbed from the air, forming sulfur-nitrogen co-doped graphene. The graphene synthesised through the ball milling technique is multi-layered graphene and was confirmed by a high-resolution HRTEM image. The composite was fabricated using different percentages of S-NDG and has shown a 118.81% increase in tensile strength with 0.5 wt.% S-NDG as compared with the pure Al sample. At a higher S-NDG weight %, the composite has increased value of total strain before fracture which

suggests increased wettability, regained ductility, and robust bonding with the aluminum matrix. S-NDG as reinforcement has eliminated the demerits of non-wettability and aluminum carbide formation present in pristine graphene aluminum composites.

CHAPTER 6: Synthesis of ball-milled edge-functionalized Antimony-doped graphene and its influence on aluminum metal matrix composite

6.1. Introduction

Antimony doped graphene (ADG) is synthesized via high energy solid-state ball milling technique by milling graphite and antimony powder at 300 RPM. The synthesized ADG was analysed using XPS, Raman, EDX, HRTEM and FESEM techniques and was further employed as reinforcing material in aluminum metal matrix composite. XPS spectrum of ADG has shown that antimony has Sb^{3+} and Sb^{5+} oxidation states present on the graphitic structure. Raman spectroscopy of ADG after 72h of milling has illustrated a sharp G-band peak with increasing I_D/I_G ratio resulting from an increase in disorder by adding larger Sb atoms to the graphitic structure. The composite tensile test has shown a remarkable increase in strength with increasing ADG concentration.

6.2. Motivation, objective and approach

Graphene is a two dimensional, sp^2 hybridised, honeycomb structured carbon-based material having impressive properties that include large surface area, the high electron mobility of $2 \times 10^5 \text{ cm}^2 \text{ V}^{-1} \text{ s}^{-1}$ at electron densities of $2 \times 10^{11} \text{ cm}^{-2}$, high thermal conductivity of $5 \times 10^3 \text{ Wm}^{-1} \text{ K}^{-1}$, young's modulus of 1TPa and tensile strength of 100 GPa. The impressive properties of graphene have various literature available on different fields of application such as solar cells, resonators, pressure sensors and fuel cells. There have been various reports on functionalized graphene with different heteroatoms as doping material such as sulfur, nitrogen, selenium, boron etc. The doping of heteroatoms provides some exceptional abilities to graphene. It can be achieved by many different approaches, such as chemical vapour deposition and graphite oxides, but the process is complex and non-economical. Ball milling has proven to be the most economical, mass production and efficient process for the functionalisation of graphene.

The mechanochemical approach to synthesise edge-functionalized graphene has various advantages over other processes. One of the essential advantages is the minimal damage on the graphitic basal plane induced by the kinetic energy of milling balls. The grinding balls travelling at high speed deliver kinetic energy to graphitic layers that are large enough to unzip carbon C-C bonds. The unzipping of graphitic bonds generates

carbon-free radicals that are active enough to start a corresponding reaction. The process thus includes unzipping, edge functionalisation, and delamination simultaneously.

Metal matrix composite has a vast literature, primarily due to its advantages and properties. The vast application of low weight and high strength composite has focused on aluminum and magnesium as matrix materials. Hard ceramic materials such as SiC, CNT, TiC, Al₂O₃ and B₄C are introduced as reinforcement to increase strength, stiffness, thermal conductivity, temperature resistance, and wear resistance properties. However, using these types of reinforcement has certain disadvantages on microscopic levels, such as graphene can react with aluminum at elevated temperature to produce Al₄C₃ phase and has less wettability to the aluminum matrix. Different approaches have been made to overcome the difficulty, such as using a small percentage of magnesium in the matrix because of its chemical compatibility with graphene and SiC (refer section 1.2.2 & 2.3.2). The demand for lightweight, high strength material with excellent electrical and thermal properties has led to the search for new reinforcing materials. Pure graphene as reinforcement produces carbide with aluminum upon high sintering temperature, thus decreasing the strength and strain before fracture. Hence measures must be taken to improve the wettability and limit the formation of carbides at the matrix reinforcement interface. Doped graphene has proven its utility in vast application areas but has limited research towards metal matrix composites. Thus, for the first time, with the motive to increase the wettability and strength of composite and to harness the capability of graphene, antimony doped graphene (ADG) is used as reinforcement material.

Antimony doped graphene was synthesised using high energy ball milling technique and characterised by Raman spectroscopy, X-ray Photoemission Spectroscopy (XPS), Field Emission Scanning Electron Microscope (FESEM), High-Resolution Transmission Electron Microscope (HRTEM). The fabricated doped graphene was further utilised as reinforcement material in the aluminum matrix to synthesise Al/ADG composite material. The mechanical properties of the composite were characterised using tensile and compressive tests, respectively.

6.3. Experimental Methods

6.3.1. Material

This research selects pure Al-powder (325 mesh, 99 % pure, purchased from Synco Industries Limited, Rajasthan) as a base matrix material to develop Al/ADG composite.

Aluminum can produce composites with better strength to weight ratio with good ductility and hence can find applications in aerospace, mechanical and structural components. Graphite (100 mesh, 98 % pure, purchased from research lab fine chem industries, Mumbai) was used to synthesise graphene by mixing Pure antimony powder in the ratio of 1:5 by weight. After the milling process, concentrated HCl was used as a solvent to remove excess antimony. Zirconium oxide balls (Synco Industries Limited, Rajasthan) with an average size of 4.28mm and 1.15mm were used in a tungsten carbide jar to synthesise doped graphene.

6.3.2. Preparation of functionalized Graphene

Ball milling is a simple yet efficient process to synthesise edge-functionalized graphene nanoplatelets. In the particular experiment, graphite powder was mixed with antimony powder (ratio 1:5) in a sealed jar with a capacity of 250 ml having ball to powder ratio of 18:1. The mixture was dry-milled for 72 hours in the planetary ball milling machine at 300 RPM to get ADG powder. The mechanism behind the graphene synthesis is that the strong shear force produced between the rotating balls creates mechanochemical fracture of C-C bonds in the graphitic structure and simultaneously cracks the Sb crystals, generating Sb species and active carbon, respectively. The process incorporates a functional group at the broken edge of the graphitic framework with the subsequent exfoliation of graphene nanoplatelets, schematically illustrated in Figure 6-1. Before the graphene characterization, a careful procedure is to be followed to remove free-standing antimony. To dissolve excess Sb present in the sample, the powder was dispersed in concentrated HCl by sonicating it for 30 minutes and centrifuged at 10000 RPM to receive pure antimony doped graphene.

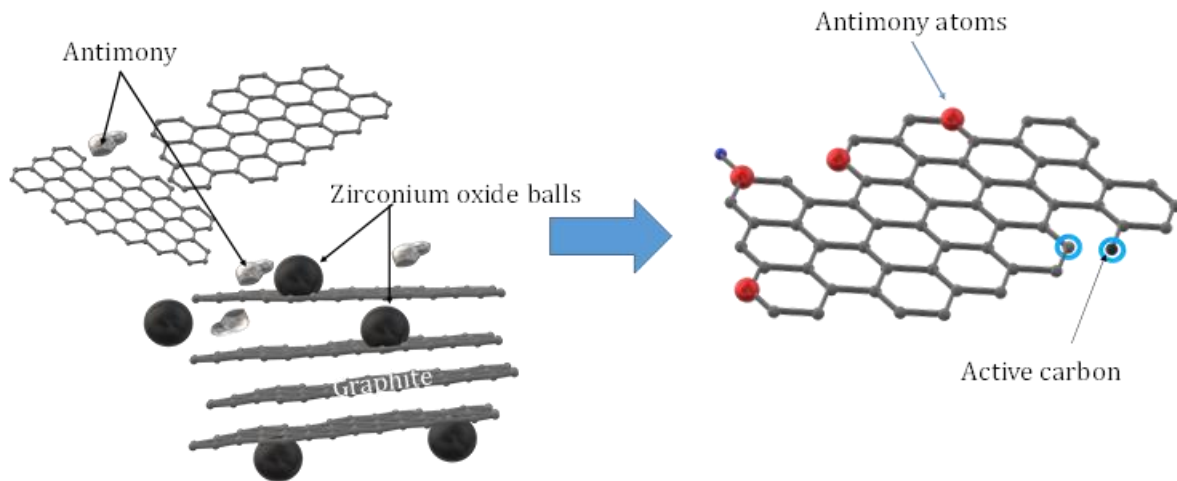


Figure 6-1: Schematics for the mechanochemical synthesis of antimony doped graphene.

6.3.3. Preparation of ADG reinforced metal matrix composite

The composite material was synthesised through the powder metallurgy route by mixing 0.05 wt. %, 0.1 wt.%, 0.2 wt. % and 0.5 wt.% of ADG in the pure aluminum matrix. The mixture was further poured into the “Retsch PM100” ball milling machine and milled at 150 rpm for another 15 min to get homogeneously mixed powder samples. The processed powdered sample was poured into stainless steel die having a bore diameter of 20 mm and is cold compacted at a pressure of 220 MPa to receive the solid cylindrical sample. The sample was then sintered using a tube furnace at 600 °C for a couple of hours in argon gas environment to get ADG/Al composite. The composite was further hot extruded at 350 °C and with a pressure of 500 MPa to get a 10 mm diameter composite rod. For the mechanical characterization of composite, the sample was prepared according to ASTM standard (B557 standard for tensile and ASTM E9 for compression test) and is illustrated in Figure 6-2.

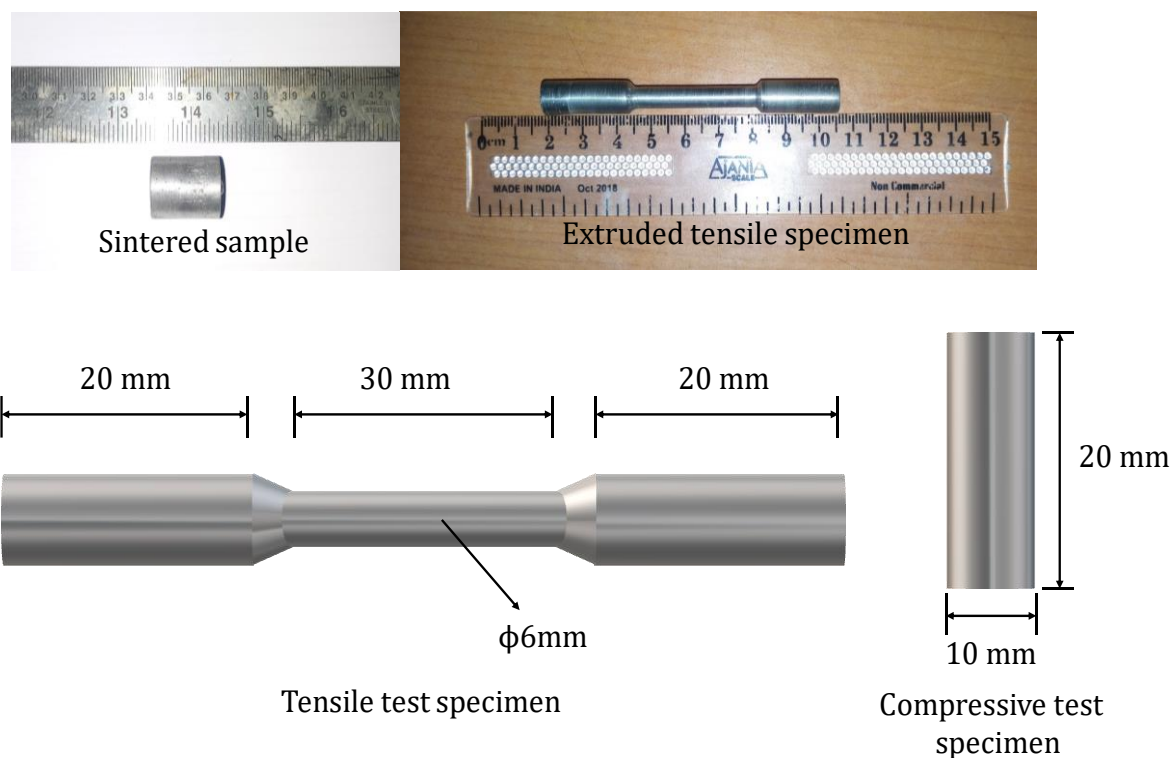
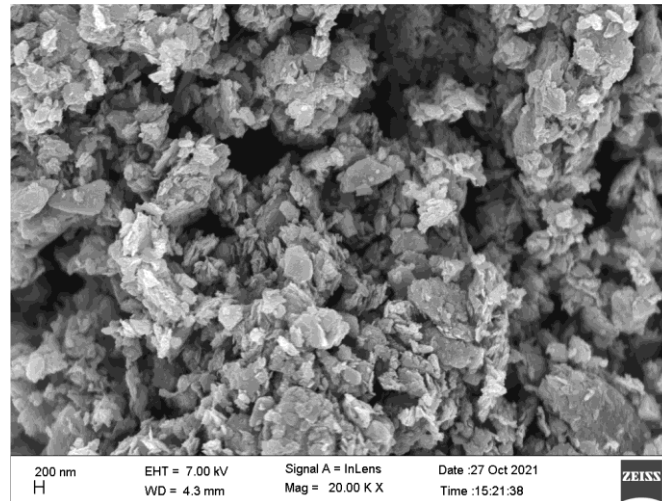


Figure 6-2: Tensile and compressive test specimen

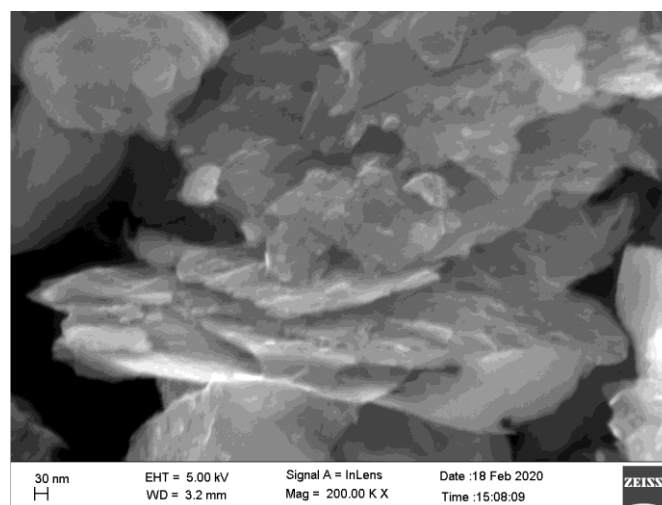
6.4. Result and discussion

6.4.1. Characterization of synthesized ADG

The schematic representation for the synthesis of edge selective antimony doped graphene is illustrated in Figure 6-1. The field emission scanning electron microscopic image of ADG is illustrated in Figure 6-3. The graphite particles with a size greater than 200 microns were crushed into ADG with less than 1microns. However, it is well-known fact that graphene synthesized through the ball milling technique is multi-layered graphene with a small crystal size. Figure 6-3(a) shows the particle size of ADG after 72 hours of milling time. Milling time always plays a crucial role in synthesizing graphene, and in this case, the average particle size is less than 1 micron. Figure 6-3(b) is the high-resolution image of ADG particles, and it clearly illustrates that ball milling has successfully exfoliated the graphite particle into a thin sheet of graphene. The heavy size reduction of graphite structure under high milling energy creates de-bonding of carbon atoms, resulting in carbon-free radicals and Sb species, which further combine to form a C-Sb bond at the edge of the graphene structure.



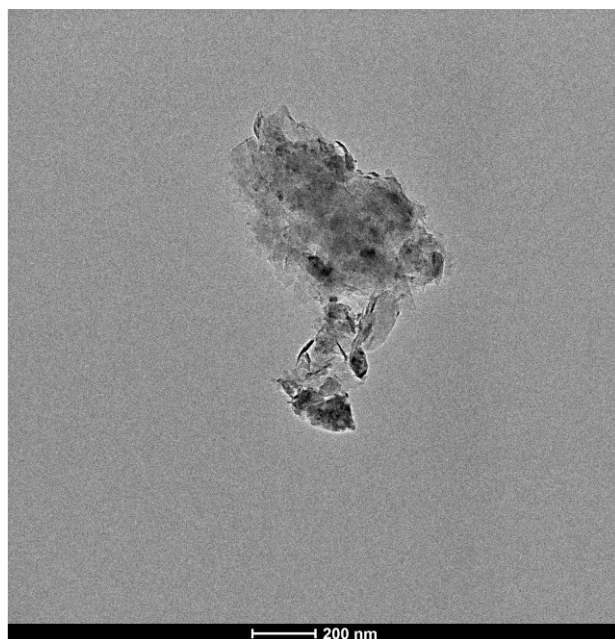
(a)



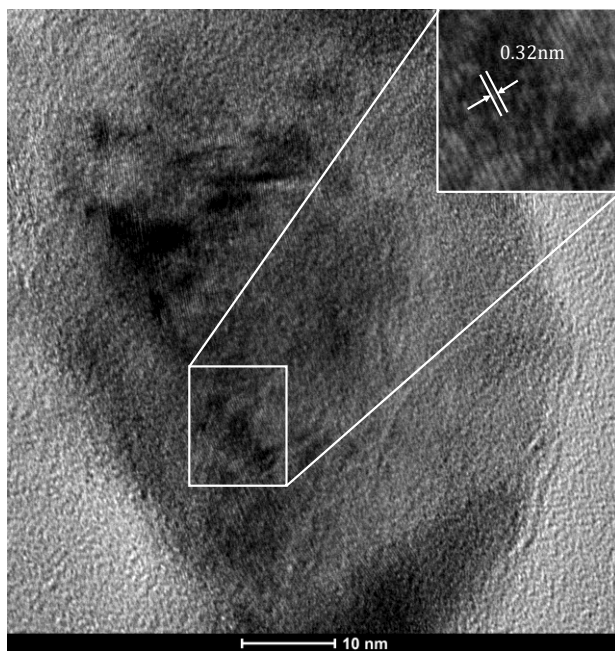
(b)

Figure 6-3: FESEM image of; (a) ADG shown average particle size, and (b) Particle under higher magnification.

The HRTEM image of exfoliated ADG is shown in Figure 6-4. The Sb atoms with a dark background are visible in the figure. The distance between the fringes of ADG particles is 0.32 nm which is also the interatomic distance between graphene atoms. The HRTEM image illustrates that the ball milling technique has successfully exfoliated graphene with selective doping of Sb atoms along the broken edge of the graphene sheet.



(a)



(b)

Figure 6-4: HRTEM image showing (a) Exfoliated ADG particle and (b) High magnification image of ADG.

The XPS analysis illustrated in Figure 6-5 shows the presence of carbon at 284 eV and antimony, Sb_{3d_5} at 529.5 eV and Sb_{3d_3} at 538 eV, respectively. The atomic percentage of carbon, oxygen, Sb_{3d_5} and N was 72.4%, 24.0%, 2.9% and 0.7%, respectively. The presence of a minimal amount of nitrogen illustrates that the nitrogen trace may be absorbed from the atmosphere and bonded into the carbon atom.

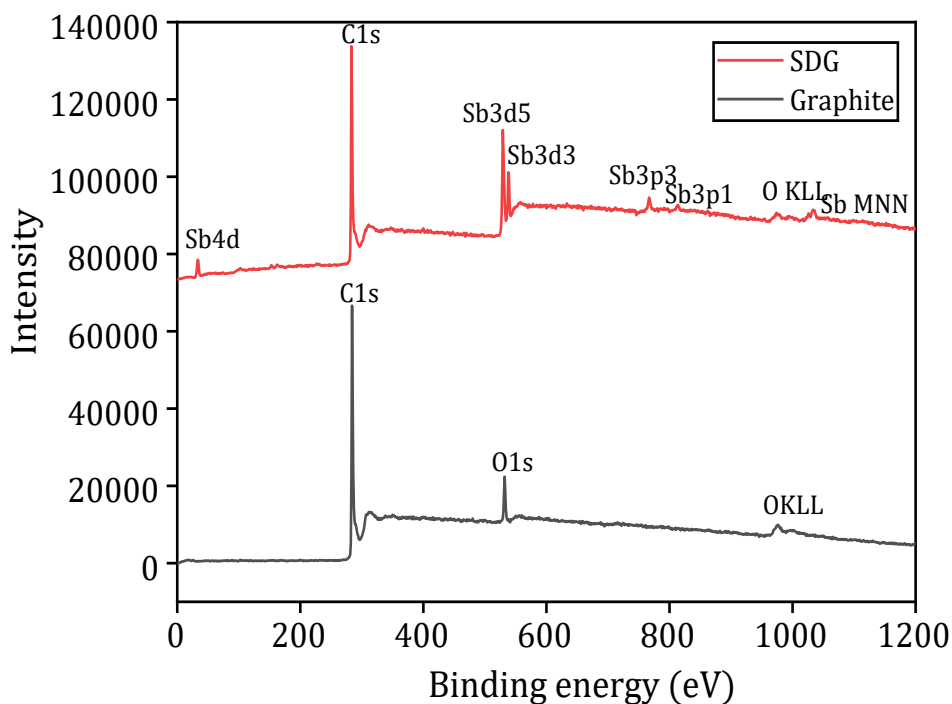


Figure 6-5: XPS high-resolution survey scan for ADG.

The high-resolution XPS spectrum for carbon and antimony is illustrated in Figure 6-6. The curves fitting of C1s carbon have peaks of C=O bond at 289 eV, C-C at 283 eV, C-O at 284.15 eV and C-Sb at 282.13 eV. For the curve fitting of antimony, the Sb3d peak can be divided into Sb3d5 at 539.5 eV and Sb3d3 at 538 eV. In addition, the Sb3d3 peak can be fitted with two separate contributions, i.e. 537.87 eV and 538.92 eV corresponding to antimony with a Sb³⁺ and Sb⁵⁺ oxidation states, respectively. Sb has a sizeable atomic size, and it may accommodate a more stable structural chemical bond for the most stable structure. However, the doping of smaller atoms such as nitrogen cannot. Hence, a larger-sized atom is highly susceptible to the highest oxidation state. Sb⁵⁺ is the most suitable form of structure present in ADG structure rather than Sb³⁺ structural form. The structure of antimony doped graphene was further analysed using Raman spectroscopy and is illustrated in Figure 6-7. The carbonaceous material such as graphene or CNT shows their fingerprint under this characterization technique.

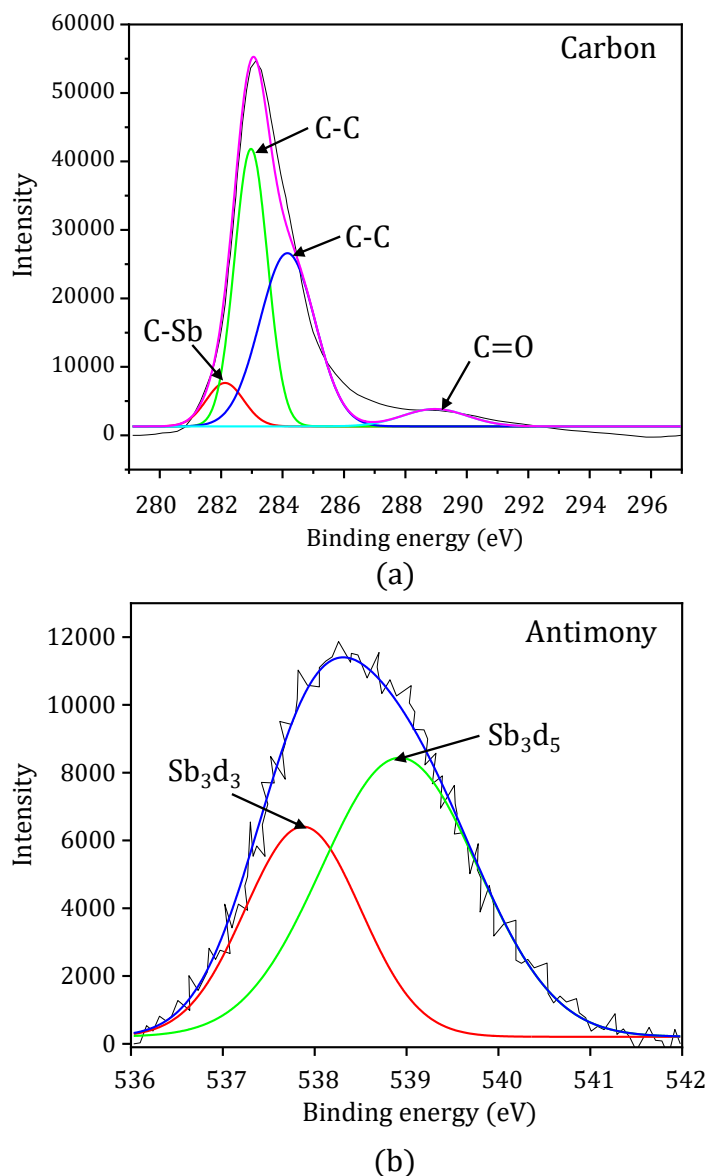


Figure 6-6: XPS high-resolution spectrum for (a) Carbon and (b) Antimony (Sb).

Pristine graphene has the absence of D-peak with G and 2D peaks at 1580 cm^{-1} and 2710 cm^{-1} , where D-peaks occurs due to the presence of carbon atoms with dangling bonds in the graphitic structure. D-peaks are observed in every graphene synthesized through rough methods such as high energy ball milling. G-band peaks reflect the structural integrity of SP_2 -hybridized carbon atoms and are due to the E_{2g} vibrating bonding. The D, G and 2D peaks for 72 h samples were found at 1342 cm^{-1} , 1571 cm^{-1} and 2685.74 cm^{-1} , respectively and the I_D/I_G ratio of 24h, 48h, and 72h milled samples are found to be 0.25, 0.35 and 0.74 respectively. The increase in the ratio was observed due to the presence of larger Sb bonds attached at the edge of graphene.

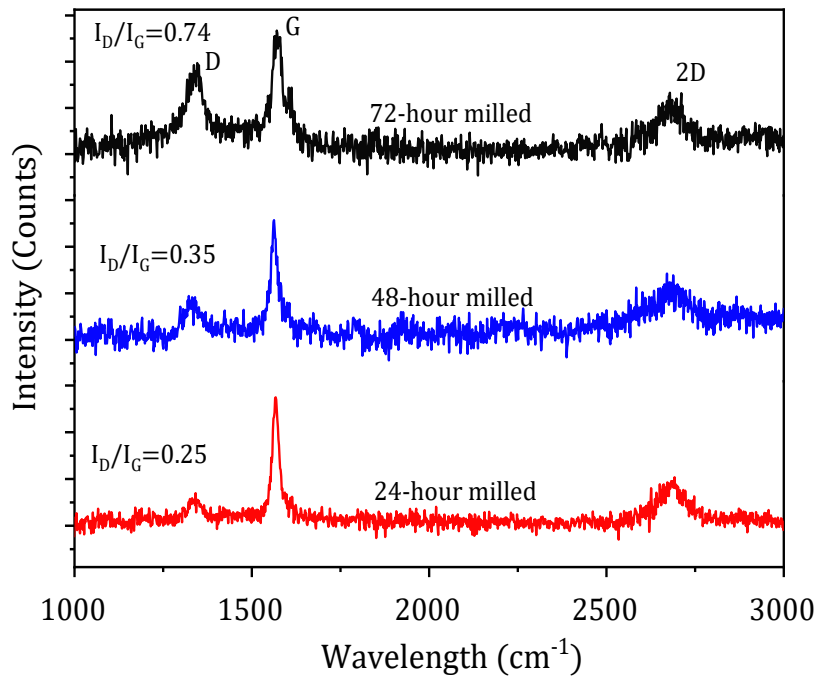


Figure 6-7: Raman spectroscopy of ADG.

6.4.2. Mechanical characterization of Al/ADG composites

The mechanical properties of ADG reinforced composite are studied with the help of tensile and compressive testing techniques. The test specimen was fabricated using ASTM standard and is given in Figure 6-2, illustrated earlier in the article. Figure 6-8 (a) & (b) shows the tensile and compressive test curve for ADG/Al composite material with 0.05 wt. %, 0.1 wt. %, 0.2 wt. % and 0.5 wt. % respectively. The tensile stress at maximum force for 0.5 wt. %, 0.2 wt.%, 0.1 wt.% and 0.05 wt.% ADG/Al composite was found to be 274.69 MPa, 212.28 MPa, 226.23 MPa and 221.32 MPa, respectively. The tensile strength of the composite has increased remarkably with the addition of ADG. The percentage increase in tensile strength for 0.5 wt. % ADG was found to be 134.7%, and the percentage increase in tensile strength for 0.05 wt. % ADG is 39.45% as compared with pure Al. However, there was a decrease in total strain before fracture for 0.5 wt. % ADG and maybe because of increased brittleness within the sample. The increase in tensile strength for ADG/Al composite is due to the load transfer mechanism of ADG within aluminium matrix and better wettability of reinforcement and matrix material. Compressive strength of composite decreases with increasing ADG % and is because of increased brittleness within the composite material. The compressive strength of the composite was found to be much higher than that of the pure Al sample (shown in the previous chapter)

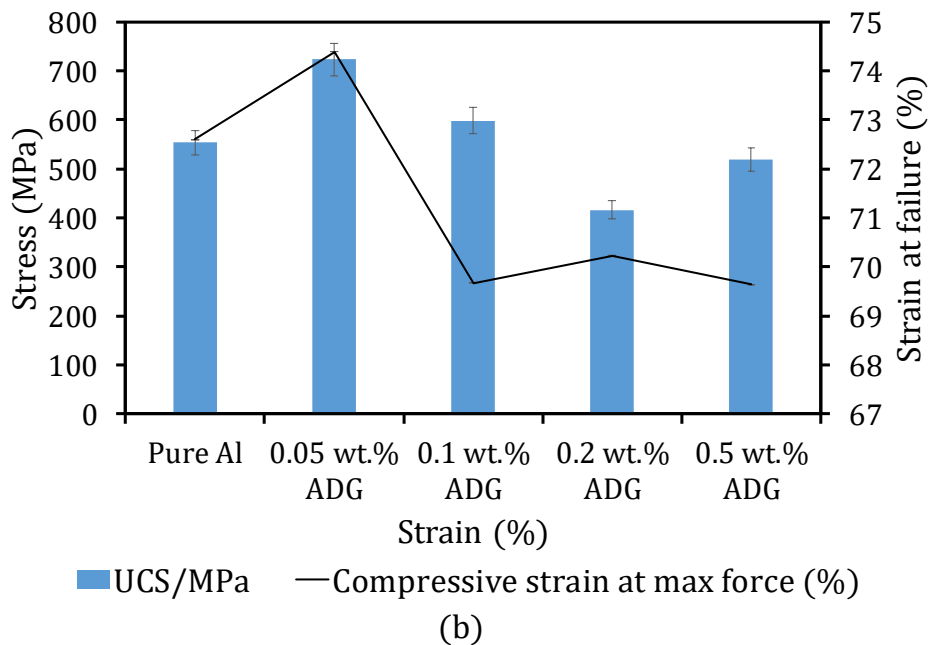
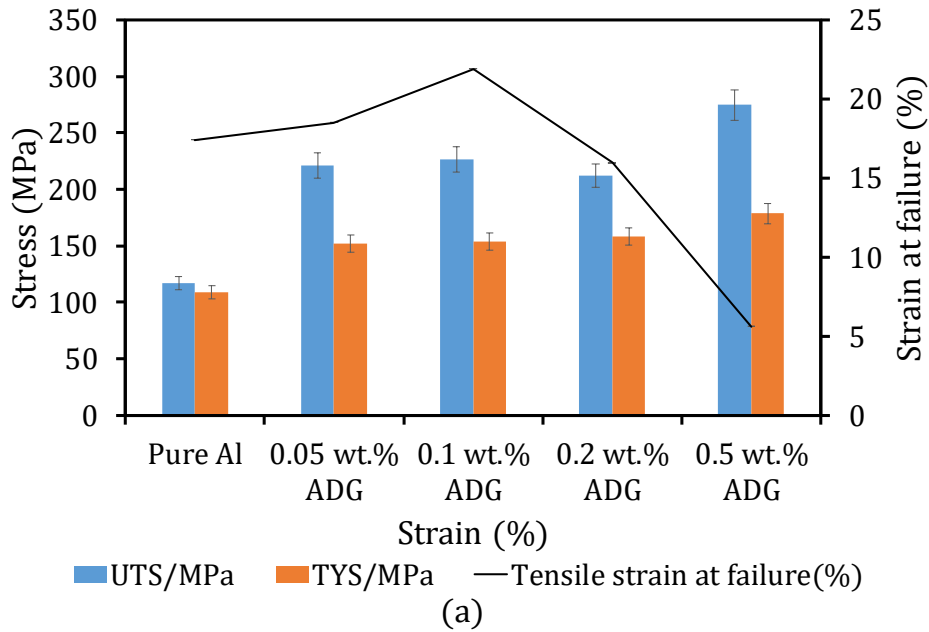
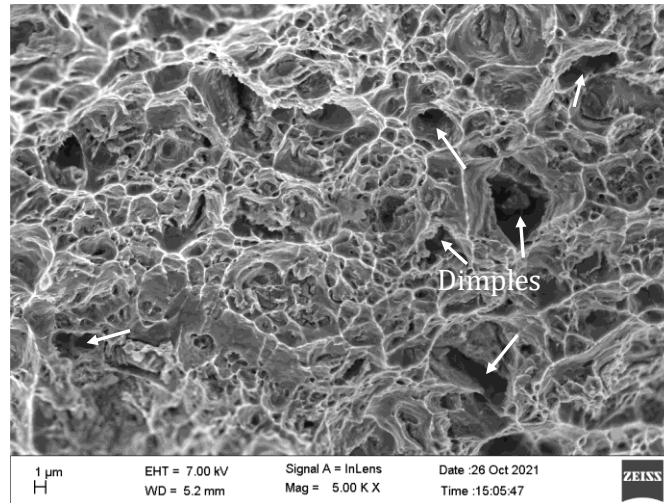


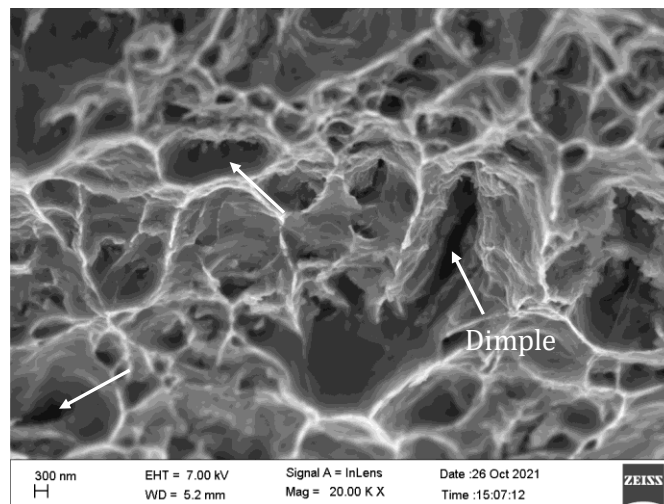
Figure 6-8: Stress-strain curve for (a) Tensile test and (b) Compressive test.

6.4.3. Morphological analysis of composite material

The surface morphology of the composite is shown in Figure 6-9. The composite showed a ductile fracture. Figure 6-9(a) shows the FESEM image after tensile fracture for 0.5 wt.% ADG/Al composite material. The ductile fracture of composite occurs by mechanical instability of the test specimen by showing the presence of voids and dimple, marked with arrow. The image shows many cracks, depicting that the antimony may have reacted and oxidized at higher sintering temperatures creating pores and decreasing the total strain before fracture.



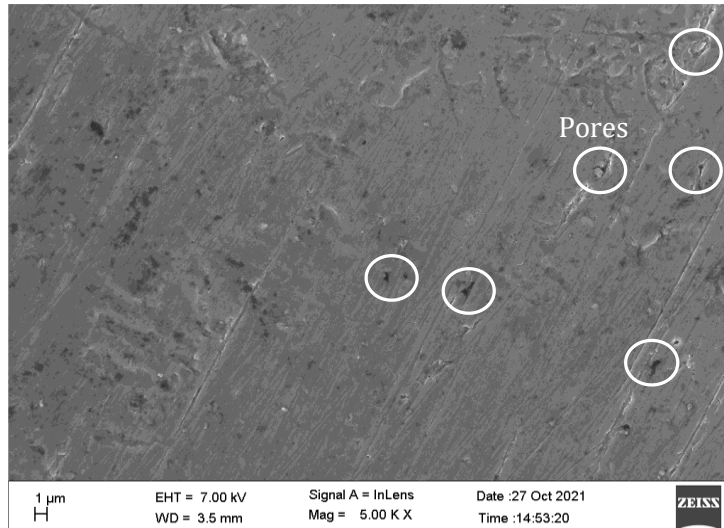
(a)



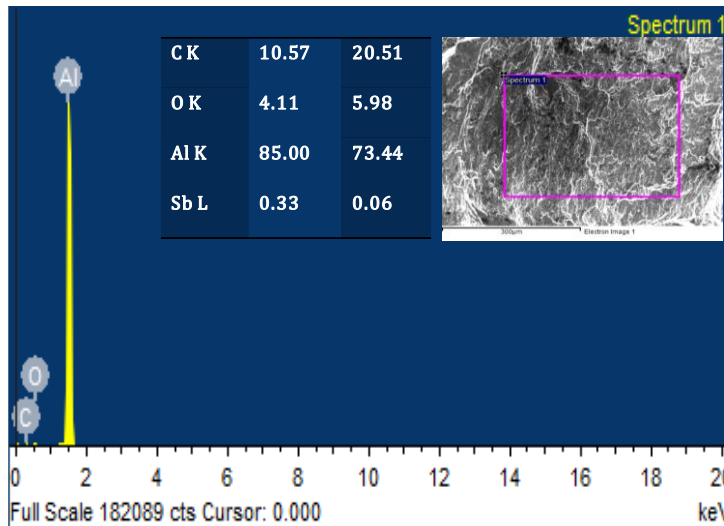
(b)

Figure 6-9: FESEM image after tensile fracture for 0.5 wt. % composite material.

Figure 6-10 (a) shows the surface morphology of the ADG/Al composite. The surface contains pores due to the lower wettability of reinforcement caused due to the reaction between antimony, aluminum and oxygen, creating antimony trioxide and aluminum oxide. The reaction at a higher sintering temperature may have decreased the wettability and is visible by the formation of pores on the composite surface. Figure 6-10(b) is the EDAX spectroscopy of Al/ADG composite showing the peak of Sb and carbon. The presence of Sb in EDAX spectrum illustrates that though antimony may have reacted with aluminum but is still bonded with SDG graphitic structure.



(a)



(b)

Figure 6-10: (a) Surface morphology of 0.5 wt. % ADG/Al composite and (b) Corresponding EDAX.

6.5. Conclusion

This chapter illustrates the strengthening effect of antimony doped graphene (ADG), when used as reinforcement in aluminium metal matrix composite. ADG was synthesized using a high energy ball milling technique by milling antimony and graphite for 72 hours at 300 rpm. The XPS spectroscopy of ADG has shown that antimony has Sb^{3+} and Sb^{5+} oxidation states present on the graphitic structure. Raman spectroscopy of the ADG powder after 24h, 48h and 72h milling time illustrates the sharp G-peak and increasing I_D/I_G ratio because of increasing distortion and the addition of large Sb atoms to the graphitic plane. The tensile strength of composite increases with increasing ADG

concentration. The percentage increase in tensile strength for 0.5 wt. % was found to be 134.7%. Total strain before fracture at a higher ADG weight percentage decreases and would be due to the formation of oxides at higher sintering temperatures creating pores and thus decreasing the strength of the composite.

CHAPTER 7: Conclusion and Future Scope

Aluminum has one-third the density of iron and is a ductile and electrically conductive material. Although the density of aluminum is low, its strength and hardness can be improved considerably by alloying or adding reinforcements. Aluminum is used widely in automobile, marine, aerospace, and manufacturing industries. Graphene, a carbonaceous reinforcement, is used as a reinforcing material for a decade and has proven to increase strength up to 90% of the strength of pure aluminum with just 0.5 wt. %. However, due to the pure graphene non-wettability with aluminum and reaction product formation, the results of strength enhancement are much lower than its actual capability. Functionalized graphene such as graphene oxide(GO) and reduced graphene oxide(rGO) have proven to eliminate aluminum carbide formation by attaching oxygen at activated carbon sites, thus eliminating one of the problems associated with graphene. However, functionalized graphene has been widely used in the electrical and electronic industries. Despite its capability, it has shown limited or no attention (other than GO and rGO) towards its utility in metal matrix composites. A perfect doping material on graphene structure has lots of capability and can be a better substitute for graphene for enhancing properties (electrical, thermal or mechanical). So, this chapter summarizes the thesis's outcome and suggests the area to be further investigated.

7.1. Key conclusions:

7.1.1. Analytical approach to the high energy milling process

The effect of milling energy plays a crucial role in graphite's exfoliation to graphene. The following conclusion can be drawn from the analytical modelling of high energy milling process:

- The milling speed of the planetary ball mill plays a vital role in the total energy released during the process.
- The total energy released for different sized balls shows that large diameter balls released more energy at the same speed.
- The total energy released for different milling balls illustrates that energy released for the combination of balls is higher than using individual-sized balls.
- Milling at a higher speed contributes more damage to balls and will add impurities during graphene synthesis.

7.1.2. Characterization of NDG and its effect on aluminum matrix composite

7.1.2.1. Characterization of NDG

NDG was synthesized using a high energy ball milling technique by milling graphite and melamine at 300 RPM for 72 hours. The synthesized NDG was characterized using XPS, XRD, Raman spectroscopy and HRTEM technique. Following conclusions can be drawn from the experimental study:

- Prolonged milling time has shown a significant reduction in particle size. The average particle size of the 48-hour milled sample was 601.5 nm, and for the 72-hour milled sample was 394.2 nm.
- HRTEM image illustrates that graphene obtained is multi-layered graphene with an average layer thickness of 6 to 10 layers with a lattice spacing of 0.34nm, 0.25nm and 0.21nm.
- XRD of 72 hours milled graphene has a peak at 17.66°, 14.87° and 21.64°, attributing to the presence of nitrogen-carbon bonding.
- XPS spectroscopy has shown the presence of carbon, nitrogen and oxygen peaks, and nitrogen from melamine is attached to graphene, forming pyrrolic-N, graphitic-N and pyridinic-N functionalities.
- Raman spectrum of graphene has a higher D-band peak with increasing I_D/I_G ratio illustrating high disorder in graphitic plane due to the presence of significant nitrogen content.

7.1.2.2. Characterization of NDG/Al composites

- Composite's ultimate tensile and yield strength increased by 124.05% and 85.82%, respectively, with just 0.2 wt. % of NDG.
- Compressive yield strength of NDG/Al composite is 126 MPa, 178 MPa, 202 MPa and 148 MPa with 0.05, 0.1, 0.2 and 0.5 wt. % NDG, respectively.
- The coefficient of friction (COF) of NDG/Al composites decreased dramatically with increasing NDG content, such that there was a 45% decrease in COF when NDG was raised from 0.1 wt. % to 0.5 wt. %.
- With increase of NDG from 0.1 to 0.2 wt. % the wear rate decreased by 25%, and there was a 71% reduction when NDG content was 0.5 wt. %.
- Surface morphology of tensile fractured surface illustrated a decrease in ductility with increasing NDG wt. %.

- EDX of 0.5. wt.% NDG/AL composite showed a small peak of AlN.

7.1.3. Characterization of S-NDG and its effect in aluminum matrix composite

7.1.3.1. *Characterization of S-NDG*

S-NDG was synthesized using a high energy ball milling technique by milling graphite and sulfur powder at 300 rpm for 72 hours. The synthesized S-NDG was characterized using XPS, XRD, HRTEM and Raman spectroscopy techniques. The following conclusion is drawn from the experimental investigation of S-NDG:

- After prolonged milling time, sulfur particles are deposited all over the graphene sheets, having sizes of 15 to 25 nm.
- EDX spectrum confirmed the presence of sulfur nanoparticles on graphene nanosheets with a presence of nitrogen peak.
- XPS comprehensive survey scan has shown the peaks of carbon, sulfur, nitrogen and oxygen with atomic % of 86.9%, 2.1%, 4.7% and 6.3%, respectively.
- XPS curve fitting for C1s has shown peaks of C=O, O-C=O, C-N, C=N and C-S bonding.
- XPS curve fitting for N1s spectra can be fitted to pyrrolic-N, graphitic-N and pyridinic-N functionalities.
- XPS curve fitting for S2p is fitted with C-S-C, C-SO₂, and C-S/S-S bonding.
- HRTEM image illustrates the uniform distribution of sulfur particles on the graphene surface having a perfectly polycrystalline nature.
- Raman spectroscopy of 72-hour and 24-hour milled samples has shown a Raman peak shift towards lower intensity, indicating an increase in bond length caused by adding heteroatoms.

7.1.3.2. *Characterization of S-NDG/Al composites*

- Tensile stress at maximum force and tensile stress at yield for a composite having 0.05 wt. % S-NDG was found to be 179.32 MPa and 109.89 MPa, respectively and for 0.5 wt. % S-NDG was observed to be 256.71 MPa and 195.37 MPa, respectively.
- An increase in total strain value before fracture with higher S-NDG weight per cent is because of increased wettability of S-NDG with aluminum matrix.
- The compressive strength for 0.05 wt. % to 0.5 wt.% S-NDG was found to be between 596.53 MPa to 738.20 MPa, respectively.

- After tensile failure, the fractographic study of the composites exhibits ductile behaviour and evidence of graphene pullover from the composite surface.
- EDX spectrum of composite exhibits peaks of aluminum, carbon and oxygen

7.1.4. Characterization of ADG and its effect in aluminum matrix composite

7.1.4.1. *Characterization of ADG*

ADG was synthesized using a high energy ball milling technique by ball-milling graphite and antimony powder at 300 RPM for 72 hours. The synthesized ADG was characterized using FESEM, HRTEM, XPS, and Raman spectroscopy. The following conclusion can be drawn from the experimental investigation of ADG:

- FESEM image of synthesized ADG illustrates that graphene has an average size of less than 1 micron.
- HRTEM image of ADG illustrates that the distance between fringes is 0.32 nm and is the interatomic distance between graphite particles.
- XPS survey scan of ADG has indicated the presence of carbon at 284 eV and antimony (Sb_{3d_5} at 529.5 eV and Sb_{3d_3} at 538 eV).
- Atomic percentage of Carbon, oxygen Sb_{3d_5} and nitrogen was 72.4%, 24.0%, 2.9% and 0.7% respectively.
- XPS curves fitting of C1s carbon have peaks of C=O bond at 289 eV, C-C at 283 eV, C-O at 284.15 eV and C-Sb at 282.13 eV.
- For the curve fitting of antimony, the Sb_{3d} peak can be divided into Sb_{3d_5} at 529.5 eV and Sb_{3d_3} at 538 eV. The Sb_{3d_3} peak can be fitted with two separate contributions, i.e. 537.87 eV and 538.92 eV corresponding to antimony with an Sb^{3+} and Sb^{5+} oxidation state.
- D, G and 2D peaks for 72 h samples were found at 1342 cm^{-1} , 1571 cm^{-1} and 2685.74 cm^{-1} , respectively.
- The I_D/I_G ratio of 24h, 48h and 72h milled samples are found to be 0.25, 0.35 and 0.74, respectively.

7.1.4.2. *Characterization of ADG/Al composite*

- The tensile stress at maximum force for 0.5 wt. %, 0.2 wt. %, 0.1 wt. % and 0.05 wt. % ADG/Al composite was found to be 274.69 MPa, 212.28 MPa, 226.23 MPa and 221.32 MPa, respectively.

- The compressive strength of composite has shown a similar trend and is much higher than pure aluminum samples.
- Surface morphology of fractured surface and the polished surface has shown the presence of voids, indicating the decrease in strain before fracture.
- The EDX spectrum of composite shows the peak of carbon, oxygen, aluminum and antimony, illustrating that antimony doping has played an essential role in increasing the strength of composite at a higher ADG weight percentage.

7.2. Contributions

The major contribution of the work is as follows:

- The idea is that strengthening properties of graphene can be harnessed more when functionalized graphene is used instead of pure graphene. The functionalized graphenes have better load transfer mechanism, reduces the probability of Al_4C_3 formation and improves the wettability of graphene with aluminum.
- Analytical approach to the ball milling process.
- Sulfur-nitrogen co-doped graphene doping has proven to increase wettability (clearly indicated by the increase in total strain before fracture) at higher weight % of reinforcement.
- Defects in graphene structure (formed during synthesis or probably during the ball milling process) can be eliminated by doping with a suitable dopant.
- Sulfur-nitrogen co-doped graphene nanosheet contains sub nano particles of sulfur all around its surface and may be the reason for increased wettability.
- Small atomic size nitrogen dopant, sulfur dopant and antimony dopant have contributed much towards strength enhancement and were much more significant than pure graphene reinforced composites.
- Strength can be significantly enhanced if graphene were used as reinforcement with aluminium with alloying elements (such as magnesium etc.)

7.3. Future Scope

The following work can be investigated for future research:

- Functionalized graphene has genuinely shown to be a more effective alternative for pure graphene and can be investigated for other dopant materials.

- The effect of functionalized graphene is limited to strength enhancement and can be used for other applications areas.
- The controlled utilization of the anisotropic properties will lead towards developing appliances with directional dependent properties, such as in the heat sink. The use of anisotropy will lead us to form a gradient structure that will show much increase in strength and ductility.

List of Publications

- Ranjan, R. et al. (2018) “Metal matrix nano composites using graphene nanoplatelets indented on copper particles in aluminum matrix,” *Advanced materials letters*, 9(9), pp. 652–655. doi: 10.5185/amlett.2018.2078
- Ranjan, R. and Bajpai, V. (2021) “Graphene-based metal matrix nanocomposites: Recent development and challenges,” *Journal of composite materials*, 55(17), pp. 2369–2413. doi: 10.1177/0021998320988566. SCIE, impact factor: 2.591 (JCR)
- Ranjan, R., Rai, R. S. and Bajpai, V. (2020) “A novel approach to synthesize nitrogen-doped graphene in aspects of milling energy,” *Diamond and related materials*, 110(108116), p. 108116. doi: 10.1016/j.diamond.2020.108116. SCIE, impact factor: 3.315 (JCR)

Under Review

- Synthesis of nitrogen-doped graphene and its effect on aluminum matrix composite material
- Synthesis of sulfur-nitrogen co-doped graphene and its effect on aluminum matrix composite material
- Synthesis of antimony-doped graphene and its effect on aluminum matrix composite material

References

- (1) Haghshenas, M. Metal–Matrix Composites. In *Reference Module in Materials Science and Materials Engineering*; 2016. <https://doi.org/10.1016/b978-0-12-803581-8.03950-3>.
- (2) R. H. Holley. The great test tube in the sky <http://arch5541.wordpress.com/2013/01/08/the-great-metal-tube-in-the-sky/> (accessed Apr 20, 2017).
- (3) Boeing. Boeing: 787 By Design: By Design: Advanced Composite Use <https://www.boeing.com/commercial/787/by-design/#/advanced-composite-use> (accessed Feb 9, 2019).
- (4) IMAMURA, T.; YAMAGUCHI, Y. Composite Materials for Aircraft Structures. In *Journal of the Japan Society for Aeronautical and Space Sciences*; 1995; Vol. 43, pp 213–223. <https://doi.org/10.2322/jjsass1969.43.213>.
- (5) Slayton, R.; Spinardi, G. Radical Innovation in Scaling up: Boeing’s Dreamliner and the Challenge of Socio-Technical Transitions. *Technovation* **2016**, *47*, 47–58. <https://doi.org/10.1016/j.technovation.2015.08.004>.
- (6) Dursun, T.; Soutis, C. Recent Developments in Advanced Aircraft Aluminium Alloys. *Materials and Design*. 2014, pp 862–871. <https://doi.org/10.1016/j.matdes.2013.12.002>.
- (7) Iijima, S. Helical Microtubules of Graphitic Carbon. *Nature* **1991**, *354* (6348), 56–58. <https://doi.org/10.1038/354056a0>.
- (8) Moghadam, A. D.; Schultz, B. F.; Ferguson, J. B.; Omrani, E.; Rohatgi, P. K.; Gupta, N. Functional Metal Matrix Composites: Self-Lubricating, Self-Healing, and Nanocomposites-an Outlook. *Jom* **2014**, *66* (6), 872–881. <https://doi.org/10.1007/s11837-014-0948-5>.
- (9) Maksimkin, A. V.; Kaloshkin, S. D.; Kaloshkina, M. S.; Gorshenkov, M. V.; Tcherdyntsev, V. V.; Ergin, K. S.; Shchetinin, I. V. Ultra-High Molecular Weight Polyethylene Reinforced with Multi-Walled Carbon Nanotubes: Fabrication Method and Properties. *J. Alloys Compd.* **2012**, *536* (SUPPL.1), S538–S540.

<https://doi.org/10.1016/j.jallcom.2012.01.151>.

- (10) Bakshi, S. R.; Keshri, A. K.; Agarwal, A. A Comparison of Mechanical and Wear Properties of Plasma Sprayed Carbon Nanotube Reinforced Aluminum Composites at Nano and Macro Scale. *Mater. Sci. Eng. A* **2011**, *528* (9), 3375–3384. <https://doi.org/10.1016/j.msea.2011.01.061>.
- (11) Xu, R.; Tan, Z.; Xiong, D.; Fan, G.; Guo, Q.; Zhang, J.; Su, Y.; Li, Z.; Zhang, D. Balanced Strength and Ductility in CNT/Al Composites Achieved by Flake Powder Metallurgy via Shift-Speed Ball Milling. *Compos. Part A Appl. Sci. Manuf.* **2017**, *96*, 57–66. <https://doi.org/10.1016/j.compositesa.2017.02.017>.
- (12) Esawi, A. M. K.; Morsi, K.; Sayed, A.; Gawad, A. A.; Borah, P. Fabrication and Properties of Dispersed Carbon Nanotube-Aluminum Composites. *Mater. Sci. Eng. A* **2009**, *508* (1–2), 167–173. <https://doi.org/10.1016/j.msea.2009.01.002>.
- (13) Yang, X.; Zou, T.; Shi, C.; Liu, E.; He, C.; Zhao, N. Effect of Carbon Nanotube (CNT) Content on the Properties of in-Situ Synthesis CNT Reinforced Al Composites. *Mater. Sci. Eng. A* **2016**, *660*, 11–18. <https://doi.org/10.1016/j.msea.2016.02.062>.
- (14) Hosseini, S. A.; Ranjbar, K.; Dehmlaei, R.; Amirani, A. R. Fabrication of Al5083 Surface Composites Reinforced by CNTs and Cerium Oxide Nano Particles via Friction Stir Processing. *J. Alloys Compd.* **2015**, *622*, 725–733. <https://doi.org/10.1016/j.jallcom.2014.10.158>.
- (15) Du, Z.; Tan, M. J.; Guo, J. F.; Bi, G.; Wei, J. Fabrication of a New Al-Al₂O₃-CNTs Composite Using Friction Stir Processing (FSP). *Mater. Sci. Eng. A* **2016**, *667*, 125–131. <https://doi.org/10.1016/j.msea.2016.04.094>.
- (16) Hu, Q.; Zhao, H.; Li, F. Microstructures and Properties of SiC Particles Reinforced Aluminum-Matrix Composites Fabricated by Vacuum-Assisted High Pressure Die Casting. *Mater. Sci. Eng. A* **2017**, *680*, 270–277. <https://doi.org/10.1016/j.msea.2016.10.090>.
- (17) Eshraghi, N.; Caes, S.; Mahmoud, A.; Cloots, R.; Vertruyen, B.; Boschini, F. Sodium Vanadium (III) Fluorophosphate/Carbon Nanotubes Composite (NVPF/CNT) Prepared by Spray-Drying: Good Electrochemical Performance Thanks to Well-Dispersed CNT Network within NVPF Particles. *Electrochim. Acta* **2017**, *228*, 319–

324. <https://doi.org/10.1016/j.electacta.2017.01.026>.
- (18) Pialago, E. J. T.; Kwon, O. K.; Kim, M.-S.; Park, C. W. Ternary Cu–CNT–AlN Composite Coatings Consolidated by Cold Spray Deposition of Mechanically Alloyed Powders. *J. Alloys Compd.* **2015**, *650*, 199–209. <https://doi.org/10.1016/j.jallcom.2015.08.007>.
- (19) Jo, I.; Cho, S.; Kim, H.; Jung, B. M.; Lee, S.-K.; Lee, S.-B. Titanium Dioxide Coated Carbon Nanofibers as a Promising Reinforcement in Aluminum Matrix Composites Fabricated by Liquid Pressing Process. *Scr. Mater.* **2016**, *112*, 87–91. <https://doi.org/10.1016/j.scriptamat.2015.09.019>.
- (20) Najimi, A. A.; Shahverdi, H. R. Effect of Milling Methods on Microstructures and Mechanical Properties of Al6061-CNT Composite Fabricated by Spark Plasma Sintering. *Mater. Sci. Eng. A* **2017**, *702*, 87–95. <https://doi.org/10.1016/j.msea.2017.04.041>.
- (21) Chen, B.; Shen, J.; Ye, X.; Imai, H.; Umeda, J.; Takahashi, M.; Kondoh, K. Solid-State Interfacial Reaction and Load Transfer Efficiency in Carbon Nanotubes (CNTs)-Reinforced Aluminum Matrix Composites. *Carbon N. Y.* **2016**, *114*, 198–208. <https://doi.org/10.1016/j.carbon.2016.12.013>.
- (22) Carvalho, O.; Miranda, G.; Soares, D.; Silva, F. S. CNT-Reinforced Aluminum Composites: Processing and Mechanical Properties. *Cienc. e Tecnol. dos Mater.* **2013**, *25* (2), 75–78. <https://doi.org/10.1016/j.ctmat.2014.03.002>.
- (23) Kim, W. J.; Lee, T. J.; Han, S. H. Multi-Layer Graphene/Copper Composites: Preparation Using High-Ratio Differential Speed Rolling, Microstructure and Mechanical Properties. *Carbon N. Y.* **2014**, *69*, 55–65. <https://doi.org/10.1016/j.carbon.2013.11.058>.
- (24) Jiang, L.; Li, Z.; Fan, G.; Cao, L.; Zhang, D. The Use of Flake Powder Metallurgy to Produce Carbon Nanotube (CNT)/Aluminum Composites with a Homogenous CNT Distribution. *Carbon N. Y.* **2012**, *50* (5), 1993–1998. <https://doi.org/10.1016/j.carbon.2011.12.057>.
- (25) Yazdanie, N.; Mahood, M. Carbon Fiber Acrylic Resin Composite: An Investigation of Transverse Strength. *J. Prosthet. Dent.* **1985**, *54* (4), 543–547.

[https://doi.org/10.1016/0022-3913\(85\)90431-7](https://doi.org/10.1016/0022-3913(85)90431-7).

- (26) Liu, H. T.; Yang, L. W.; Sun, X.; Cheng, H. F.; Wang, C. Y.; Mao, W. G.; Molina-Aldareguia, J. M. Enhancing the Fracture Resistance of Carbon Fiber Reinforced SiC Matrix Composites by Interface Modification through a Simple Fiber Heat-Treatment Process. *Carbon N. Y.* **2016**, *109*, 435–443. <https://doi.org/10.1016/j.carbon.2016.08.047>.
- (27) Deka, B. K.; Hazarika, A.; Kong, K.; Kim, D.; Park, Y. Bin; Park, H. W. Interfacial Resistive Heating and Mechanical Properties of Graphene Oxide Assisted CuO Nanoparticles in Woven Carbon Fiber/Polyester Composite. *Compos. Part A Appl. Sci. Manuf.* **2016**, *80*, 159–170. <https://doi.org/10.1016/j.compositesa.2015.10.023>.
- (28) Daoud, A. Microstructure and Tensile Properties of 2014 Al Alloy Reinforced with Continuous Carbon Fibers Manufactured by Gas Pressure Infiltration. *Mater. Sci. Eng. A* **2005**, *391* (1), 114–120. <https://doi.org/10.1016/j.msea.2004.08.075>.
- (29) Yang, Q.; Liu, J.; Li, S.; Wang, F.; Wu, T. Fabrication and Mechanical Properties of Cu-Coated woven Carbon Fibers Reinforced Aluminum Alloy Composite. *Mater. Des.* **2014**, *57*, 442–448. <https://doi.org/10.1016/j.matdes.2013.12.064>.
- (30) Abidin, A. Z.; Kozera, R.; Höhn, M.; Endler, I.; Knaut, M.; Boczkowska, A.; Czulak, A.; Malczyk, P.; Sobczak, N.; Michaelis, A. Preparation and Characterization of CVD-TiN-Coated Carbon Fibers for Applications in Metal Matrix Composites. *Thin Solid Films* **2015**, *589*, 479–486. <https://doi.org/10.1016/j.tsf.2015.06.022>.
- (31) Zhang, J.; Liu, S.; Lu, Y.; Jiang, L.; Zhang, Y.; Li, T. Semisolid-Rolling and Annealing Process of Woven Carbon Fibers Reinforced Al-Matrix Composites. *J. Mater. Sci. Technol.* **2017**, *33* (7), 623–629. <https://doi.org/10.1016/j.jmst.2017.01.002>.
- (32) Zhang, J.; Liu, S.; Zhang, Y.; Dong, Y.; Lu, Y.; Li, T. Fabrication of Woven Carbon Fibers Reinforced Al-Mg (95–5wt%) Matrix Composites by an Electromagnetic Casting Process. *J. Mater. Process. Technol.* **2015**, *226*, 78–84. <https://doi.org/10.1016/j.jmatprotec.2015.06.040>.
- (33) Alhashmy, H. A.; Nganbe, M. Laminate Squeeze Casting of Carbon Fiber Reinforced Aluminum Matrix Composites. *Mater. Des.* **2015**, *67*, 154–158.

- <https://doi.org/10.1016/j.matdes.2014.11.034>.
- (34) Berry, V. Impermeability of Graphene and Its Applications. *Carbon N. Y.* **2013**, *62*, 1–10. <https://doi.org/10.1016/J.CARBON.2013.05.052>.
- (35) Moradi, O.; Gupta, V. K.; Agarwal, S.; Tyagi, I.; Asif, M.; Makhlof, A. S. H.; Sadegh, H.; Shahryari-ghoshekandi, R. Characteristics and Electrical Conductivity of Graphene and Graphene Oxide for Adsorption of Cationic Dyes from Liquids: Kinetic and Thermodynamic Study. *J. Ind. Eng. Chem.* **2015**, *28*, 294–301. <https://doi.org/10.1016/j.jiec.2015.03.005>.
- (36) Mazilova, T. I.; Sadanov, E. V.; Mikhailovskij, I. M. Tensile Strength of Graphene Nanoribbons: An Experimental Approach. *Mater. Lett.* **2019**, *242*, 17–19. <https://doi.org/10.1016/j.matlet.2019.01.051>.
- (37) Prashantha Kumar, H. G.; Anthony Xavier, M. Graphene Reinforced Metal Matrix Composite (GRMMC): A Review. In *Procedia Engineering*; 2014; Vol. 97, pp 1033–1040. <https://doi.org/10.1016/j.proeng.2014.12.381>.
- (38) Warner, J. H.; Schä, F.; Bachmatiuk, A.; Rü, M. H. *Front Matter*; Elsevier, 2013. <https://doi.org/http://dx.doi.org/10.1016/B978-0-12-385870-2.00054-8>.
- (39) Lee, C.; Wei, X.; Kysar, J. W.; Hone, J. Measurement of the Elastic Properties and Intrinsic Strength of Monolayer Graphene. *Science (80-.)*. **2008**, *321* (5887), 385–388. <https://doi.org/10.1126/science.1157996>.
- (40) Soldano, C.; Mahmood, A.; Dujardin, E. Production, Properties and Potential of Graphene. *Carbon N. Y.* **2010**, *48* (8), 2127–2150. <https://doi.org/10.1016/j.carbon.2010.01.058>.
- (41) Shahil, K. M. F.; Balandin, A. A. Graphene-Multilayer Graphene Nanocomposites as Highly Efficient Thermal Interface Materials. *Nano Lett.* **2012**, *12* (2), 861–867. <https://doi.org/10.1021/nl203906r>.
- (42) Liu, J.; Khan, U.; Coleman, J.; Fernandez, B.; Rodriguez, P.; Naher, S.; Brabazon, D. Graphene Oxide and Graphene Nanosheet Reinforced Aluminium Matrix Composites: Powder Synthesis and Prepared Composite Characteristics. *Mater. Des.* **2016**, *94*, 87–94. <https://doi.org/10.1016/j.matdes.2016.01.031>.

- (43) Peng, Q.; Li, Y.; He, X.; Lv, H.; Hu, P.; Shang, Y.; Wang, C.; Wang, R.; Sritharan, T.; Du, S. Interfacial Enhancement of Carbon Fiber Composites by Poly(Amido Amine) Functionalization. *Compos. Sci. Technol.* **2013**, *74*, 37–42. <https://doi.org/10.1016/j.compscitech.2012.10.005>.
- (44) He, H.; Wang, J.; Li, K.; Wang, J.; Gu, J. Mixed Resin and Carbon Fibres Surface Treatment for Preparation of Carbon Fibres Composites with Good Interfacial Bonding Strength. *Mater. Des.* **2010**, *31* (10), 4631–4637. <https://doi.org/10.1016/j.matdes.2010.05.031>.
- (45) Li, B.; Zhong, W. H. Review on Polymer/Graphite Nanoplatelet Nanocomposites. *J. Mater. Sci.* **2011**, *46* (17), 5595–5614. <https://doi.org/10.1007/s10853-011-5572-y>.
- (46) Yan, S. J. J.; Dai, S. L. L.; Zhang, X. Y. Y.; Yang, C.; Hong, Q. H. H.; Chen, J. Z. Z.; Lin, Z. M. M. Investigating Aluminum Alloy Reinforced by Graphene Nanoflakes. *Mater. Sci. Eng. A* **2014**, *612*, 440–444. <https://doi.org/10.1016/j.msea.2014.06.077>.
- (47) Li, J. L.; Xiong, Y. C.; Wang, X. D.; Yan, S. J.; Yang, C.; He, W. W.; Chen, J. Z.; Wang, S. Q.; Zhang, X. Y.; Dai, S. L. Microstructure and Tensile Properties of Bulk Nanostructured Aluminum/Graphene Composites Prepared via Cryomilling. *Mater. Sci. Eng. A* **2015**, *626*, 400–405. <https://doi.org/10.1016/j.msea.2014.12.102>.
- (48) Gao, X.; Yue, H.; Guo, E.; Zhang, H.; Lin, X.; Yao, L.; Wang, B. Preparation and Tensile Properties of Homogeneously Dispersed Graphene Reinforced Aluminum Matrix Composites. *Mater. Des.* **2016**, *94*, 54–60. <https://doi.org/10.1016/j.matdes.2016.01.034>.
- (49) Schiøtz, J.; Di Tolla, F. D.; Jacobsen, K. W. Softening of Nanocrystalline Metals at Very Small Grain Sizes. *Nature* **1998**, *391* (6667), 561–563. <https://doi.org/10.1038/35328>.
- (50) Varol, T.; Canakci, A. Synthesis and Characterization of Nanocrystalline Al 2024–B₄ C Composite Powders by Mechanical Alloying. *Philos. Mag. Lett.* **2013**, *93* (6), 339–345. <https://doi.org/10.1080/09500839.2013.779758>.
- (51) Nieto, A.; Bisht, A.; Lahiri, D.; Zhang, C.; Agarwal, A. Graphene Reinforced Metal and Ceramic Matrix Composites: A Review. *Int. Mater. Rev.* **2017**, *62* (5), 241–302.

<https://doi.org/10.1080/09506608.2016.1219481>.

- (52) Dorri Moghadam, A.; Omrani, E.; Menezes, P. L.; Rohatgi, P. K. Mechanical and Tribological Properties of Self-Lubricating Metal Matrix Nanocomposites Reinforced by Carbon Nanotubes (CNTs) and Graphene - A Review. *Compos. Part B Eng.* **2015**, *77*, 402–420. <https://doi.org/10.1016/j.compositesb.2015.03.014>.
- (53) Dutkiewicz, J.; Ozga, P.; Maziarz, W.; Pstruś, J.; Kania, B.; Bobrowski, P.; Stolarska, J. Microstructure and Properties of Bulk Copper Matrix Composites Strengthened with Various Kinds of Graphene Nanoplatelets. *Mater. Sci. Eng. A* **2015**, *628*, 124–134. <https://doi.org/10.1016/j.msea.2015.01.018>.
- (54) Rashad, M.; Pan, F.; Asif, M.; Tang, A. Powder Metallurgy of Mg-1%Al-1%Sn Alloy Reinforced with Low Content of Graphene Nanoplatelets (GNPs). *J. Ind. Eng. Chem.* **2014**, *20* (6), 4250–4255. <https://doi.org/10.1016/j.jiec.2014.01.028>.
- (55) Gao, L.; Yue, W.; Tao, S.; Fan, L. Novel Strategy for Preparation of Graphene-Pd, Pt Composite, and Its Enhanced Electrocatalytic Activity for Alcohol Oxidation. *Langmuir* **2013**, *29* (3), 957–964. <https://doi.org/10.1021/la303663x>.
- (56) Dixit, S.; Mahata, A.; Mahapatra, D. R.; Kailas, S. V.; Chattopadhyay, K. Multi-Layer Graphene Reinforced Aluminum – Manufacturing of High Strength Composite by Friction Stir Alloying. *Compos. Part B Eng.* **2018**, *136*, 63–71. <https://doi.org/10.1016/j.compositesb.2017.10.028>.
- (57) Rashad, M.; Pan, F.; Tang, A.; Asif, M.; She, J.; Gou, J.; Mao, J.; Hu, H. Development of Magnesium-Graphene Nanoplatelets Composite. *J. Compos. Mater.* **2015**, *49* (3), 285–293. <https://doi.org/10.1177/0021998313518360>.
- (58) Lou, X.; Pan, H.; Zhu, S.; Zhu, C.; Liao, Y.; Li, Y.; Zhang, D.; Chen, Z. Synthesis of Silver Nanoprisms on Reduced Graphene Oxide for High-Performance Catalyst. *Catal. Commun.* **2015**, *69*, 43–47. <https://doi.org/10.1016/j.catcom.2015.05.021>.
- (59) Yu, M.; Shao, D.; Lu, F.; Sun, X.; Sun, H.; Hu, T.; Wang, G.; Sawyer, S.; Qiu, H.; Lian, J. ZnO/Graphene Nanocomposite Fabricated by High Energy Ball Milling with Greatly Enhanced Lithium Storage Capability. *Electrochem. commun.* **2013**, *34*, 312–315. <https://doi.org/10.1016/j.elecom.2013.07.013>.

- (60) Huang, Y.; Wang, L.; Sun, X. Sandwich-Structured Graphene@Fe₃O₄@carbon Nanocomposites with Enhanced Electromagnetic Absorption Properties. *Mater. Lett.* **2015**, *144*, 26–29. <https://doi.org/10.1016/j.matlet.2015.01.015>.
- (61) Li, X.; Zheng, X.; Shao, J.; Gao, T.; Shi, Q.; Qu, Q. Synergistic Ternary Composite (Carbon/Fe₃O₄@Graphene) with Hollow Microspherical and Robust Structure for Li-Ion Storage. *Chem. - A Eur. J.* **2016**, *22* (1), 376–381. <https://doi.org/10.1002/chem.201504035>.
- (62) Ponomarenko, L. A.; Schedin, F.; Katsnelson, M. I.; Yang, R.; Hill, E. W.; Novoselov, K. S.; Geim, A. K. Chaotic Dirac Billiard in Graphene Quantum Dots. *Science (80-.)*. **2008**, *320* (5874), 356–358. <https://doi.org/10.1126/science.1154663>.
- (63) Bao, R.; Huang, L.; Lai, Y. C.; Grebogi, C. Conductance Fluctuations in Chaotic Bilayer Graphene Quantum Dots. *Phys. Rev. E - Stat. Nonlinear, Soft Matter Phys.* **2015**, *92* (1). <https://doi.org/10.1103/PhysRevE.92.012918>.
- (64) Shim, J.; Kim, Y.-H.; Park, J.-H. Theoretical Analysis and Experimental Optimization of Graphene/TMD Heterojunction Barristors. In *ECS Transactions*; 2016; Vol. 75, pp 43–48. <https://doi.org/10.1149/07513.0043ecst>.
- (65) Hammam, A. M. M.; Schmidt, M. E.; Muruganathan, M.; Mizuta, H. Sharp Switching Behaviour in Graphene Nanoribbon P-n Junction. *Carbon N. Y.* **2017**, *121*, 399–407. <https://doi.org/10.1016/j.carbon.2017.05.097>.
- (66) Mao, S. Graphene Field-Effect Transistor Sensors. In *Graphene Bioelectronics*; 2018; pp 113–132. <https://doi.org/10.1016/B978-0-12-813349-1.00005-6>.
- (67) Kakaei, K.; Esrafil, M. D.; Ehsani, A. Graphene-Based Electrochemical Supercapacitors. In *Interface Science and Technology*; 2019; Vol. 27, pp 339–386. <https://doi.org/10.1016/B978-0-12-814523-4.00009-5>.
- (68) Choi, W.; Alwarappan, S. Graphene-Based Biosensors and Gas Sensors. In *Graphene*; 2018; pp 248–277. <https://doi.org/10.1201/b11259-11>.
- (69) Cheianov, V. V.; Fal'ko, V. I.; Altshuler, B. L. Veselago Lens for Electrons: Focusing and Caustics in Graphene p-n Junctions. *Science (80-.)*. **2007**, *315*, 1252. <https://doi.org/10.1126/science.1138020>.

- (70) Zhao, Y.; Wyrick, J.; Natterer, F. D.; Rodriguez-Nieva, J. F.; Lewandowski, C.; Watanabe, K.; Taniguchi, T.; Levitov, L. S.; Zhitenev, N. B.; Strosio, J. A. Creating and Probing Electron Whispering-Gallery Modes in Graphene. *Science (80-.)*. **2015**, *348* (6235), 672–675. <https://doi.org/10.1126/science.aaa7469>.
- (71) Reddy, D.; Register, L. F.; Banerjee, S. K. Bilayer Graphene Vertical Tunneling Field Effect Transistor. In *Device Research Conference - Conference Digest, DRC*; 2012; pp 73–74. <https://doi.org/10.1109/DRC.2012.6256932>.
- (72) Nanjunda, S. B.; Hoh, H. Y.; Sophia, J.; Xue, Y.; Yuan, J.; Yu, W.; Mu, H.; Chen, Y.; Baoa, Q. *Introduction*; 2017. <https://doi.org/10.1201/9781315196671>.
- (73) Li, X.; Zhu, H.; Wang, K.; Cao, A.; Wei, J.; Li, C.; Jia, Y.; Li, Z.; Li, X.; Wu, D. Graphene-on-Silicon Schottky Junction Solar Cells. *Adv. Mater.* **2010**, *22* (25), 2743–2748. <https://doi.org/10.1002/adma.200904383>.
- (74) Chen, S.; Yu, X.; Zhang, M.; Cao, J.; Li, Y.; Ding, L.; Shi, G. A Graphene Oxide/Oxygen Deficient Molybdenum Oxide Nanosheet Bilayer as a Hole Transport Layer for Efficient Polymer Solar Cells. *J. Mater. Chem. A* **2015**, *3* (36), 18380–18383. <https://doi.org/10.1039/c5ta04823k>.
- (75) Koh, W. S.; Gan, C. H.; Phua, W. K.; Akimov, Y. A.; Bai, P. The Potential of Graphene as an ITO Replacement in Organic Solar Cells: An Optical Perspective. *IEEE J. Sel. Top. Quantum Electron.* **2014**, *20* (1). <https://doi.org/10.1109/JSTQE.2013.2247976>.
- (76) Yan, L.; Zhang, Y.; Zhang, X.; Zhao, J.; Wang, Y.; Zhang, T.; Jiang, Y.; Gao, W.; Yin, J.; Zhao, J.; et al. Single Layer Graphene Electrodes for Quantum Dot-Light Emitting Diodes. *Nanotechnology* **2015**, *26* (13). <https://doi.org/10.1088/0957-4484/26/13/135201>.
- (77) Suk, J. W.; Kirk, K.; Hao, Y.; Hall, N. A.; Ruoff, R. S. Thermoacoustic Sound Generation from Monolayer Graphene for Transparent and Flexible Sound Sources. *Adv. Mater.* **2012**, *24* (47), 6342–6347. <https://doi.org/10.1002/adma.201201782>.
- (78) Tian, H.; Xie, D.; Yang, Y.; Ren, T. L.; Wang, Y. F.; Zhou, C. J.; Peng, P. G.; Wang, L. G.; Liu, L. T. Single-Layer Graphene Sound-Emitting Devices: Experiments and Modeling. *Nanoscale* **2012**, *4* (7), 2272–2277.

<https://doi.org/10.1039/c2nr11572g>.

- (79) Tao, L. Q.; Sun, H.; Liu, Y.; Ju, Z. Y.; Yang, Y.; Ren, T. L. Flexible Graphene Sound Device Based on Laser Reduced Graphene. *Appl. Phys. Lett.* **2017**, *111* (10). <https://doi.org/10.1063/1.5002113>.
- (80) Lee, K. R.; Jang, S. H.; Jung, I. Acoustic Performance of Dual-Electrode Electrostatic Sound Generators Based on CVD Graphene on Polyimide Film. *Nanotechnology* **2018**, *29* (32). <https://doi.org/10.1088/1361-6528/aac6ae>.
- (81) Tian, H.; Ren, T. L.; Xie, D.; Wang, Y. F.; Zhou, C. J.; Feng, T. T.; Fu, D.; Yang, Y.; Peng, P. G.; Wang, L. G.; et al. Graphene-on-Paper Sound Source Devices. *ACS Nano* **2011**, *5* (6), 4878–4885. <https://doi.org/10.1021/nn2009535>.
- (82) Chen, Y.; Xu, J.; Yang, Y.; Zhao, Y.; Yang, W.; He, X.; Li, S.; Jia, C. Enhanced Electrochemical Performance of Laser Scribed Graphene Films Decorated with Manganese Dioxide Nanoparticles. *J. Mater. Sci. Mater. Electron.* **2016**, *27* (3), 2564–2573. <https://doi.org/10.1007/s10854-015-4059-z>.
- (83) El-Kady, M. F.; Strong, V.; Dubin, S.; Kaner, R. B. Laser Scribing of High-Performance and Flexible Graphene-Based Electrochemical Capacitors. *Science (80-.)*. **2012**, *335* (6074), 1326–1330. <https://doi.org/10.1126/science.1216744>.
- (84) Bunch, J. S.; Van Der Zande, A. M.; Verbridge, S. S.; Frank, I. W.; Tanenbaum, D. M.; Parpia, J. M.; Craighead, H. G.; McEuen, P. L. Electromechanical Resonators from Graphene Sheets. *Science (80-.)*. **2007**, *315* (5811), 490–493. <https://doi.org/10.1126/science.1136836>.
- (85) Eichler, A.; Moser, J.; Chaste, J.; Zdrojek, M.; Wilson-Rae, I.; Bachtold, A. Nonlinear Damping in Mechanical Resonators Made from Carbon Nanotubes and Graphene. *Nat. Nanotechnol.* **2011**, *6* (6), 339–342. <https://doi.org/10.1038/nnano.2011.71>.
- (86) Adhikari, S.; Chowdhury, R. Zeptogram Sensing from Gigahertz Vibration: Graphene Based Nanosensor. *Phys. E Low-Dimensional Syst. Nanostructures* **2012**, *44* (7–8), 1528–1534. <https://doi.org/10.1016/j.physe.2012.03.021>.
- (87) Singh, V.; Sengupta, S.; Solanki, H. S.; Dhall, R.; Allain, A.; Dhara, S.; Pant, P.; Deshmukh, M. M. Probing Thermal Expansion of Graphene and Modal Dispersion

- at Low-Temperature Using Graphene Nanoelectromechanical Systems Resonators. *Nanotechnology* **2010**, *21* (16). <https://doi.org/10.1088/0957-4484/21/16/165204>.
- (88) Sun, Y.; Sun, M.; Xie, D. Graphene Electronic Devices. In *Graphene*; 2018; pp 103–155. <https://doi.org/10.1016/B978-0-12-812651-6.00005-7>.
- (89) Du, D.; Li, P.; Ouyang, J. Graphene Coated Nonwoven Fabrics as Wearable Sensors. *J. Mater. Chem. C* **2016**, *4* (15), 3224–3230. <https://doi.org/10.1039/c6tc00350h>.
- (90) Nair, R. R.; Blake, P.; Grigorenko, A. N.; Novoselov, K. S.; Booth, T. J.; Stauber, T.; Peres, N. M. R.; Geim, A. K. Fine Structure Constant Defines Visual Transparency of Graphene. *Science* (80-.). **2008**, *320* (5881), 1308. <https://doi.org/10.1126/science.1156965>.
- (91) Chae, S.; Jang, S.; Choi, W. J.; Kim, Y. S.; Chang, H.; Lee, T. Il; Lee, J. O. Lattice Transparency of Graphene. *Nano Lett.* **2017**, *17* (3), 1711–1718. <https://doi.org/10.1021/acs.nanolett.6b04989>.
- (92) Chen, S.; Brown, L.; Levendorf, M.; Cai, W.; Ju, S. Y.; Edgeworth, J.; Li, X.; Magnuson, C. W.; Velamakanni, A.; Piner, R. D.; et al. Oxidation Resistance of Graphene-Coated Cu and Cu/Ni Alloy. *ACS Nano* **2011**, *5* (2), 1321–1327. <https://doi.org/10.1021/nn103028d>.
- (93) Berman, D.; Deshmukh, S. A.; Sankaranarayanan, S. K. R. S.; Erdemir, A.; Sumant, A. V. Macroscale Superlubricity Enabled by Graphene Nanoscroll Formation. *Science* (80-.). **2015**, *348* (6239), 1118–1122. <https://doi.org/10.1126/science.1262024>.
- (94) Smith, A. D.; Vaziri, S.; Niklaus, F.; Fischer, A. C.; Sterner, M.; Delin, A.; Östling, M.; Lemme, M. C. Pressure Sensors Based on Suspended Graphene Membranes. *Solid State Electron.* **2013**, *88*, 89–94. <https://doi.org/10.1016/j.sse.2013.04.019>.
- (95) Dolleman, R. J.; Davidovikj, D.; Cartamil-Bueno, S. J.; Van Der Zant, H. S. J.; Steeneken, P. G. Graphene Squeeze-Film Pressure Sensors. *Nano Lett.* **2016**, *16* (1), 568–571. <https://doi.org/10.1021/acs.nanolett.5b04251>.
- (96) Wang, Q.; Arash, B. A Review on Applications of Carbon Nanotubes and Graphenes as Nano-Resonator Sensors. *Comput. Mater. Sci.* **2014**, *82*, 350–360.

<https://doi.org/10.1016/j.commatsci.2013.10.010>.

- (97) Verbridge, S. S.; Craighead, H. G.; Parpia, J. M. A Megahertz Nanomechanical Resonator with Room Temperature Quality Factor over a Million. *Appl. Phys. Lett.* **2008**, *92* (1). <https://doi.org/10.1063/1.2822406>.
- (98) Wang, X.; Tian, H.; Xie, W.; Shu, Y.; Mi, W. T.; Mohammad, M. A.; Xie, Q. Y.; Yang, Y.; Xu, J. Bin; Ren, T. L. Observation of a Giant Two-Dimensional Band-Piezoelectric Effect on Biaxial-Strained Graphene. *NPG Asia Mater.* **2015**, *7* (1), e154. <https://doi.org/10.1038/am.2014.124>.
- (99) Da Cunha Rodrigues, G.; Zelenovskiy, P.; Romanyuk, K.; Luchkin, S.; Kopelevich, Y.; Kholkin, A. Strong Piezoelectricity in Single-Layer Graphene Deposited on SiO₂ Grating Substrates. *Nat. Commun.* **2015**, *6*. <https://doi.org/10.1038/ncomms8572>.
- (100) Sun, C.; Boutilier, M. S. H.; Au, H.; Poesio, P.; Bai, B.; Karnik, R.; Hadjiconstantinou, N. G. Mechanisms of Molecular Permeation through Nanoporous Graphene Membranes. *Langmuir* **2014**, *30* (2), 675–682. <https://doi.org/10.1021/la403969g>.
- (101) Wang, X.; Guo, X.; Shao, H.; Zhou, Q.; Hu, W.; Song, X. Methods, Performances and Mechanisms of Separation Membrane Modified by Graphene and Graphene Oxide. *Prog. Chem.* **2015**, *27*(10). <https://doi.org/10.7536/PC150321>.
- (102) Cohen-Tanugi, D.; Grossman, J. C. Water Desalination across Nanoporous Graphene. *Nano Lett.* **2012**, *12* (7), 3602–3608. <https://doi.org/10.1021/nl3012853>.
- (103) Cohen-Tanugi, D.; Grossman, J. C. Nanoporous Graphene as a Reverse Osmosis Membrane: Recent Insights from Theory and Simulation. *Desalination* **2015**, *366*, 59–70. <https://doi.org/10.1016/j.desal.2014.12.046>.
- (104) Ranjan, R.; Rai, R. S.; Bajpai, V. A Novel Approach to Synthesize Nitrogen-Doped Graphene in Aspects of Milling Energy. *Diam. Relat. Mater.* **2020**, *110*. <https://doi.org/10.1016/j.diamond.2020.108116>.
- (105) Mohan, V. B.; Lau, K. tak; Hui, D.; Bhattacharyya, D. Graphene-Based Materials and Their Composites: A Review on Production, Applications and Product Limitations.

- Compos. Part B Eng.* **2018**, *142*, 200–220.
<https://doi.org/10.1016/j.compositesb.2018.01.013>.
- (106) Iniewski, K.; Morris, J. *Graphene, Carbon Nanotubes, and Nanostructures: Techniques and Applications*; 2016.
- (107) Alwarappan, S.; Kumar, A. *Graphene-Based materials: Science and Technology*; CRC Press, 2013. <https://doi.org/10.1201/b15545>.
- (108) Muzyka, R.; Kwoka, M.; Smędowski, Ł.; Díez, N.; Gryglewicz, G. Oxidation of Graphite by Different Modified Hummers Methods. *New Carbon Mater.* **2017**, *32* (1), 15–20. [https://doi.org/10.1016/S1872-5805\(17\)60102-1](https://doi.org/10.1016/S1872-5805(17)60102-1).
- (109) Rathnayake, R. M. N. M.; Wijayasinghe, H. W. M. A. C.; Pitawala, H. M. T. G. A.; Yoshimura, M.; Huang, H. H. Synthesis of Graphene Oxide and Reduced Graphene Oxide by Needle Platy Natural Vein Graphite. *Appl. Surf. Sci.* **2017**, *393*, 309–315. <https://doi.org/10.1016/j.apsusc.2016.10.008>.
- (110) Wei, D.; Liu, Y.; Wang, Y.; Zhang, H.; Huang, L.; Yu, G. Synthesis of N-Doped Graphene by Chemical Vapor Deposition and Its Electrical Properties. *Nano Lett.* **2009**, *9*(5), 1752–1758. <https://doi.org/10.1021/nl803279t>.
- (111) Reina, A.; Jia, X.; Ho, J.; Nezich, D.; Son, H.; Bulovic, V.; Dresselhaus, M. S.; Jing, K. Large Area, Few-Layer Graphene Films on Arbitrary Substrates by Chemical Vapor Deposition. *Nano Lett.* **2009**, *9*(1), 30–35. <https://doi.org/10.1021/nl801827v>.
- (112) Mori, F.; Kubouchi, M.; Arao, Y. Effect of Graphite Structures on the Productivity and Quality of Few-Layer Graphene in Liquid-Phase Exfoliation. *J. Mater. Sci.* **2018**, *53*(18), 12807–12815. <https://doi.org/10.1007/s10853-018-2538-3>.
- (113) Frank, I. W.; Tanenbaum, D. M.; van der Zande, A. M.; McEuen, P. L. Mechanical Properties of Suspended Graphene Sheets. *J. Vac. Sci. Technol. B Microelectron. Nanom. Struct.* **2007**, *25*(6), 2558. <https://doi.org/10.1116/1.2789446>.
- (114) Dawidczyk, T. J.; Kong, H.; Katz, H. E. Organic Semiconductors (OSCs) for Electronic Chemical Sensors. In *Handbook of Organic Materials for Optical and (Opto)Electronic Devices: Properties and Applications*; 2013; pp 577–596. <https://doi.org/10.1533/9780857098764.3.577>.

- (115) Green, A. A.; Hersam, M. C. Emerging Methods for Producing Monodisperse Graphene Dispersions. *J. Phys. Chem. Lett.* **2010**, *1* (2), 544–549. <https://doi.org/10.1021/jz900235f>.
- (116) Ciesielski, A.; Samorì, P. Graphene via Sonication Assisted Liquid-Phase Exfoliation. *Chem. Soc. Rev.* **2014**, *43* (1), 381–398. <https://doi.org/10.1039/c3cs60217f>.
- (117) Wei, Y.; Sun, Z. Liquid-Phase Exfoliation of Graphite for Mass Production of Pristine Few-Layer Graphene. *Curr. Opin. Colloid Interface Sci.* **2015**, *20* (5–6), 311–321. <https://doi.org/10.1016/j.cocis.2015.10.010>.
- (118) Ravula, S.; Baker, S. N.; Kamath, G.; Baker, G. A. Ionic Liquid-Assisted Exfoliation and Dispersion: Stripping Graphene and Its Two-Dimensional Layered Inorganic Counterparts of Their Inhibitions. *Nanoscale* **2015**, *7* (10), 4338–4353. <https://doi.org/10.1039/c4nr01524j>.
- (119) Lotya, M.; Hernandez, Y.; King, P. J.; Smith, R. J.; Nicolosi, V.; Karlsson, L. S.; Blighe, F. M.; De, S.; Wang, Z.; McGovern, I. T.; et al. Liquid Phase Production of Graphene by Exfoliation of Graphite in Surfactant/Water Solutions. *J. Am. Chem. Soc.* **2009**, *131* (10), 3611–3620. <https://doi.org/10.1021/ja807449u>.
- (120) Gong, P.; Wang, Z.; Wang, J.; Wang, H.; Li, Z.; Fan, Z.; Xu, Y.; Han, X.; Yang, S. One-Pot Sonochemical Preparation of Fluorographene and Selective Tuning of Its Fluorine Coverage. *J. Mater. Chem.* **2012**, *22* (33), 16950–16956. <https://doi.org/10.1039/c2jm32294c>.
- (121) King, P.; Crossley, A.; Backes, C.; Barwich, S.; May, P.; Pettersson, H.; Paton, K. R.; Istrate, O. M.; Duesberg, G. S.; O'Neill, A.; et al. Scalable Production of Large Quantities of Defect-Free Few-Layer Graphene by Shear Exfoliation in Liquids. *Nat. Mater.* **2014**, *13* (6), 624–630. <https://doi.org/10.1038/nmat3944>.
- (122) Karagiannidis, P. G.; Hodge, S. A.; Lombardi, L.; Tomarchio, F.; Decorde, N.; Milana, S.; Goykhman, I.; Su, Y.; Mesite, S. V.; Johnstone, D. N.; et al. Microfluidization of Graphite and Formulation of Graphene-Based Conductive Inks. *ACS Nano* **2017**, *11* (3), 2742–2755. <https://doi.org/10.1021/acsnano.6b07735>.
- (123) Doktycz, S. J.; Suslick, K. S. Interparticle Collisions Driven by Ultrasound. *Science*

- (80-). **1990**, *247*(4946), 1067–1069. <https://doi.org/10.1126/science.2309118>.
- (124) Pokhrel, N.; Vabbina, P. K.; Pala, N. Sonochemistry: Science and Engineering. *Ultrason. Sonochem.* **2016**, *29*, 104–128. <https://doi.org/10.1016/j.ULTSONCH.2015.07.023>.
- (125) Plesset, M. S.; Prosperetti, A. Bubble Dynamics and Cavitation. *Annu. Rev. Fluid Mech.* **2003**, *9* (1), 145–185. <https://doi.org/10.1146/annurev.fl.09.010177.001045>.
- (126) Leighton, T. G.; Apfel, R. E. The Acoustic Bubble. *J. Acoust. Soc. Am.* **2005**, *96* (4), 2616–2616. <https://doi.org/10.1121/1.410082>.
- (127) Lei, F.; Yang, M.; Jiang, F.; Zhang, H.; Zhang, Z.; Sun, D. Microwave-Assisted Liquid Phase Exfoliation of Graphite Fluoride into Fluorographene. *Chem. Eng. J.* **2019**, *360*, 673–679. <https://doi.org/10.1016/j.cej.2018.12.044>.
- (128) Xu, J.; Dang, D. K.; Tran, V. T.; Liu, X.; Chung, J. S.; Hur, S. H.; Choi, W. M.; Kim, E. J.; Kohl, P. A. Liquid-Phase Exfoliation of Graphene in Organic Solvents with Addition of Naphthalene. *J. Colloid Interface Sci.* **2014**, *418*, 37–42. <https://doi.org/10.1016/j.jcis.2013.12.009>.
- (129) Hadi, A.; Zahirifar, J.; Karimi-Sabet, J.; Dastbaz, A. Graphene Nanosheets Preparation Using Magnetic Nanoparticle Assisted Liquid Phase Exfoliation of Graphite: The Coupled Effect of Ultrasound and Wedging Nanoparticles. *Ultrason. Sonochem.* **2018**, *44*, 204–214. <https://doi.org/10.1016/j.ultsonch.2018.02.028>.
- (130) Lee, H.; Bratescu, M. A.; Ueno, T.; Saito, N. Solution Plasma Exfoliation of Graphene Flakes from Graphite Electrodes. *RSC Adv.* **2014**, *4* (93), 51758–51765. <https://doi.org/10.1039/c4ra03253e>.
- (131) Parvez, K.; Li, R.; Puniredd, S. R.; Hernandez, Y.; Hinkel, F.; Wang, S.; Feng, X.; Müllen, K. Electrochemically Exfoliated Graphene as Solution-Processable, Highly Conductive Electrodes for Organic Electronics. *ACS Nano* **2013**, *7*(4), 3598–3606. <https://doi.org/10.1021/nn400576v>.
- (132) Parvez, K.; Wu, Z. S.; Li, R.; Liu, X.; Graf, R.; Feng, X.; Müllen, K. Exfoliation of Graphite into Graphene in Aqueous Solutions of Inorganic Salts. *J. Am. Chem. Soc.*

- 2014, *136* (16), 6083–6091. <https://doi.org/10.1021/ja5017156>.
- (133) Zhong, Y. L.; Tian, Z.; Simon, G. P.; Li, D. Scalable Production of Graphene via Wet Chemistry: Progress and Challenges. *Mater. Today* **2015**, *18* (2), 73–78. <https://doi.org/10.1016/j.mattod.2014.08.019>.
- (134) Jiang, F.; Yu, Y.; Wang, Y.; Feng, A.; Song, L. A Novel Synthesis Route of Graphene via Microwave Assisted Intercalation-Exfoliation of Graphite. *Mater. Lett.* **2017**, *200*, 39–42. <https://doi.org/10.1016/J.MATLET.2017.04.048>.
- (135) Segundo, E. H.; Fontana, L. C.; Recco, A. A. C.; Scholtz, J. S.; Nespolo Vomstein, M. A.; Becker, D. Graphene Nanosheets Obtained through Graphite Powder Exfoliation in Pulsed Underwater Electrical Discharge. *Mater. Chem. Phys.* **2018**, *217*, 1–4. <https://doi.org/10.1016/j.matchemphys.2018.06.036>.
- (136) Hernandez, Y.; Nicolosi, V.; Lotya, M.; Blighe, F. M.; Sun, Z.; De, S.; McGovern, I. T.; Holland, B.; Byrne, M.; Gun'ko, Y. K.; et al. High-Yield Production of Graphene by Liquid-Phase Exfoliation of Graphite. *Nat. Nanotechnol.* **2008**, *3* (9), 563–568. <https://doi.org/10.1038/nnano.2008.215>.
- (137) Bagri, A.; Mattevi, C.; Acik, M.; Chabal, Y. J.; Chhowalla, M.; Shenoy, V. B. Structural Evolution during the Reduction of Chemically Derived Graphene Oxide. *Nat. Chem.* **2010**, *2* (7), 581–587. <https://doi.org/10.1038/nchem.686>.
- (138) Ito, Y.; Christodoulou, C.; Nardi, M. V.; Koch, N.; Sachdev, H.; Müllen, K. Chemical Vapor Deposition of N-Doped Graphene and Carbon Films: The Role of Precursors and Gas Phase. *ACS Nano* **2014**, *8* (4), 3337–3346. <https://doi.org/10.1021/nn405661b>.
- (139) Koltai, J.; Kuzmany, H.; Pichler, T.; Simon, F. Arrayed Arrangement Of ^{13}C Isotopes During the Growth of Inner Single-Walled Carbon Nanotubes. *Phys. Status Solidi Basic Res.* **2017**, *254* (11). <https://doi.org/10.1002/pssb.201700217>.
- (140) Chang, R. J.; Wang, X.; Wang, S.; Sheng, Y.; Porter, B.; Bhaskaran, H.; Warner, J. H. Growth of Large Single-Crystalline Monolayer Hexagonal Boron Nitride by Oxide-Assisted Chemical Vapor Deposition. *Chem. Mater.* **2017**, *29* (15), 6252–6260. <https://doi.org/10.1021/acs.chemmater.7b01285>.

- (141) Wang, M.; Jang, S. K.; Jang, W. J.; Kim, M.; Park, S. Y.; Kim, S. W.; Kahng, S. J.; Choi, J. Y.; Ruoff, R. S.; Song, Y. J.; et al. A Platform for Large-Scale Graphene Electronics - CVD Growth of Single-Layer Graphene on CVD-Grown Hexagonal Boron Nitride. *Adv. Mater.* **2013**, *25* (19), 2746–2752. <https://doi.org/10.1002/adma.201204904>.
- (142) Johansson, A.-S.; Lu, J.; Carlsson, J.-O. TEM Investigation of CVD Graphite on Nickel. *Thin Solid Films* **1994**, *252* (1), 19–25. [https://doi.org/10.1016/0040-6090\(94\)90819-2](https://doi.org/10.1016/0040-6090(94)90819-2).
- (143) Chen, M.; Yan, Y.; Zhang, X. F.; Liu, W. M.; Zhou, C.; Guo, Z. Q.; Wang, Y. L.; Li, L.; Zhang, G. L. Advances in Large-Area Graphene Film Transfer Techniques. *Hangkong Cailiao Xuebao/Journal Aeronaut. Mater.* **2015**, *35* (2), 1–11. <https://doi.org/10.11868/j.issn.1005-5053.2015.2.001>.
- (144) Yu, W. J.; Huang, Y.; Wang, Y.; Cheng, R.; Huang, X.; Liu, Y.; Chen, Y.; Zhou, H.; Duan, X.; Liu, L. Chemical Vapour Deposition Growth of Large Single Crystals of Monolayer and Bilayer Graphene. *Nat. Commun.* **2013**, *4* (1), 1–8. <https://doi.org/10.1038/ncomms3096>.
- (145) Chang, S. J.; Hyun, M. S.; Myung, S.; Kang, M. A.; Yoo, J. H.; Lee, K. G.; Choi, B. G.; Cho, Y.; Lee, G.; Park, T. J. Graphene Growth from Reduced Graphene Oxide by Chemical Vapour Deposition: Seeded Growth Accompanied by Restoration. *Sci. Rep.* **2016**, *6*. <https://doi.org/10.1038/srep22653>.
- (146) Li, X.; Colombo, L.; Ruoff, R. S. Synthesis of Graphene Films on Copper Foils by Chemical Vapor Deposition. *Adv. Mater.* **2016**, *28* (29), 6247–6252. <https://doi.org/10.1002/adma.201504760>.
- (147) Zhang, R.; Duan, T.; Ling, L.; Wang, B. CH₄dehydrogenation on Cu(1 1 1), Cu@Cu(1 1 1), Rh@Cu(1 1 1) and RhCu(1 1 1) Surfaces: A Comparison Studies of Catalytic Activity. *Appl. Surf. Sci.* **2015**, *341*, 100–108. <https://doi.org/10.1016/j.apsusc.2015.03.013>.
- (148) Li, J. Sen; Wang, Y.; Liu, C. H.; Li, S. L.; Wang, Y. G.; Dong, L. Z.; Dai, Z. H.; Li, Y. F.; Lan, Y. Q. Coupled Molybdenum Carbide and Reduced Graphene Oxide Electrocatalysts for Efficient Hydrogen Evolution. *Nat. Commun.* **2016**, *7* (1), 11204.

<https://doi.org/10.1038/ncomms11204>.

- (149) Lv, J. J.; Wang, A. J.; Ma, X.; Xiang, R. Y.; Chen, J. R.; Feng, J. J. One-Pot Synthesis of Porous Pt-Au Nanodendrites Supported on Reduced Graphene Oxide Nanosheets toward Catalytic Reduction of 4-Nitrophenol. *J. Mater. Chem. A* **2015**, *3* (1), 290–296. <https://doi.org/10.1039/c4ta05034g>.
- (150) Kuila, T.; Mishra, A. K.; Khanra, P.; Kim, N. H.; Lee, J. H. Recent Advances in the Efficient Reduction of Graphene Oxide and Its Application as Energy Storage Electrode Materials. *Nanoscale* **2013**, *5* (1), 52–71. <https://doi.org/10.1039/C2NR32703A>.
- (151) Sun, H.; Mei, L.; Liang, J.; Zhao, Z.; Lee, C.; Fei, H.; Ding, M.; Lau, J.; Li, M.; Wang, C.; et al. Three-Dimensional Holey-Graphene/Niobia Composite Architectures for Ultrahigh-Rate Energy Storage. *Science* **2017**, *356* (6338), 599–604. <https://doi.org/10.1126/science.aam5852>.
- (152) De Silva, K. K. H.; Huang, H. H.; Joshi, R. K.; Yoshimura, M. Chemical Reduction of Graphene Oxide Using Green Reductants. *Carbon*. 2017, pp 190–199. <https://doi.org/10.1016/j.carbon.2017.04.025>.
- (153) Tortello, M.; Colonna, S.; Bernal, M.; Gomez, J.; Pavese, M.; Novara, C.; Giorgis, F.; Maggio, M.; Guerra, G.; Saracco, G.; et al. Effect of Thermal Annealing on the Heat Transfer Properties of Reduced Graphite Oxide Flakes: A Nanoscale Characterization via Scanning Thermal Microscopy. *Carbon N. Y.* **2016**, *109*, 390–401. <https://doi.org/10.1016/j.carbon.2016.08.017>.
- (154) Tour, J. M. Top-down versus Bottom-up Fabrication of Graphene-Based Electronics. *Chem. Mater.* **2014**, *26* (1), 163–171. <https://doi.org/10.1021/cm402179h>.
- (155) Gao, W. The Chemistry of Graphene Oxide. In *Graphene Oxide: Reduction Recipes, Spectroscopy, and Applications*; 2015; pp 61–95. https://doi.org/10.1007/978-3-319-15500-5_3.
- (156) Chua, C. K.; Pumera, M. Chemical Reduction of Graphene Oxide: A Synthetic Chemistry Viewpoint. *Chem. Soc. Rev.* **2014**, *43* (1), 291–312. <https://doi.org/10.1039/c3cs60303b>.

- (157) Gao, X.; Jang, J.; Nagase, S. Hydrazine and Thermal Reduction of Graphene Oxide: Reaction Mechanisms, Product Structures, and Reaction Design. *J. Phys. Chem. C* **2010**, *114* (2), 832–842. <https://doi.org/10.1021/jp909284g>.
- (158) Muszynski, R.; Seger, B.; Kamat, P. V. Decorating Graphene Sheets with Gold Nanoparticles. *J. Phys. Chem. C* **2008**, *112* (14), 5263–5266. <https://doi.org/10.1021/jp800977b>.
- (159) Stankovich, S.; Piner, R. D.; Nguyen, S. B. T.; Ruoff, R. S. Synthesis and Exfoliation of Isocyanate-Treated Graphene Oxide Nanoplatelets. *Carbon N. Y.* **2006**, *44* (15), 3342–3347. <https://doi.org/10.1016/j.carbon.2006.06.004>.
- (160) Yan, L.; Lin, M.; Zeng, C.; Chen, Z.; Zhang, S.; Zhao, X.; Wu, A.; Wang, Y.; Dai, L.; Qu, J.; et al. Electroactive and Biocompatible Hydroxyl- Functionalized Graphene by Ball Milling. *J. Mater. Chem.* **2012**, *22* (17), 8367–8371. <https://doi.org/10.1039/c2jm30961k>.
- (161) An Wong, C. H.; Pumera, M. Highly Conductive Graphene Nanoribbons from the Reduction of Graphene Oxide Nanoribbons with Lithium Aluminium Hydride. *J. Mater. Chem. C* **2014**, *2* (5), 856–863. <https://doi.org/10.1039/c3tc31688b>.
- (162) Cui, P.; Lee, J.; Hwang, E.; Lee, H. (1) Cui, P.; Lee, J.; Hwang, E.; Lee, H. Chem. Commun. 2011, 47 (45), 12370. One-Pot Reduction of Graphene Oxide at Subzero Temperatures. *Chem. Commun.* **2011**, *47* (45), 12370. <https://doi.org/10.1039/c1cc15569e>.
- (163) Mohan, V. B.; Brown, R.; Jayaraman, K.; Bhattacharyya, D. Characterisation of Reduced Graphene Oxide: Effects of Reduction Variables on Electrical Conductivity. *Mater. Sci. Eng. B Solid-State Mater. Adv. Technol.* **2015**, *193* (C), 49–60. <https://doi.org/10.1016/j.mseb.2014.11.002>.
- (164) Chua, C. K.; Pumera, M. Renewal of Sp² Bonds in Graphene Oxides via Dehydrobromination. *J. Mater. Chem.* **2012**, *22* (43), 23227–23231. <https://doi.org/10.1039/c2jm34358d>.
- (165) Arifin, N. F. T.; Aziz, M. Effect of Reduction Time on Optical Properties of Reduced Graphene Oxide. *J. Teknol.* **2017**, *79* (1–2), 25–28. <https://doi.org/10.11113/jt.v79.10432>.

- (166) Hou, Z.; Zhou, Y.; Li, G.; Wang, S.; Wang, M.; Hu, X.; Li, S. Reduction of Graphene Oxide and Its Effect on Square Resistance of Reduced Graphene Oxide Films. *Bull. Korean Chem. Soc.* **2015**, *36*(6), 1681–1687. <https://doi.org/10.1002/bkcs.10323>.
- (167) Gao, W. Graphite Oxide: Structure, Reduction and Applications. *Mater. Manuf. Process.* **2012**, *4* (March 2012), 6–10.
- (168) Chua, C. K.; Pumera, M. Reduction of Graphene Oxide with Substituted Borohydrides. *J. Mater. Chem. A* **2013**, *1* (5), 1892–1898. <https://doi.org/10.1039/c2ta00665k>.
- (169) Zhuo, Q.; Zhang, Y.; Du, Q.; Yan, C. Facile Reduction of Graphene Oxide at Room Temperature by Ammonia Borane via Salting out Effect. *J. Colloid Interface Sci.* **2015**, *457*, 243–247. <https://doi.org/10.1016/j.jcis.2015.07.029>.
- (170) Pham, V. H.; Hur, S. H.; Kim, E. J.; Kim, B. S.; Chung, J. S. Highly Efficient Reduction of Graphene Oxide Using Ammonia Borane. *Chem. Commun.* **2013**, *49*(59), 6665–6667. <https://doi.org/10.1039/c3cc43503b>.
- (171) Chua, C. K.; Ambrosi, A.; Pumera, M. Graphene Oxide Reduction by Standard Industrial Reducing Agent: Thiourea Dioxide. *J. Mater. Chem.* **2012**, *22* (22), 11054–11061. <https://doi.org/10.1039/c2jm16054d>.
- (172) Dong, L. long; Chen, W. ge; Deng, N.; Zheng, C. hao. A Novel Fabrication of Graphene by Chemical Reaction with a Green Reductant. *Chem. Eng. J.* **2016**, *306*, 754–762. <https://doi.org/10.1016/j.cej.2016.08.027>.
- (173) Ma, Q.; Song, J.; Jin, C.; Li, Z.; Liu, J.; Meng, S.; Zhao, J.; Guo, Y. A Rapid and Easy Approach for the Reduction of Graphene Oxide by Formamidinesulfinic Acid. *Carbon N. Y.* **2013**, *54*, 36–41. <https://doi.org/10.1016/j.carbon.2012.10.067>.
- (174) Chua, C. K.; Pumera, M. Selective Removal of Hydroxyl Groups from Graphene Oxide. *Chem. - A Eur. J.* **2013**, *19* (6), 2005–2011. <https://doi.org/10.1002/chem.201204002>.
- (175) Liu, H.; Zhang, L.; Guo, Y.; Cheng, C.; Yang, L.; Jiang, L.; Yu, G.; Hu, W.; Liu, Y.; Zhu, D. Reduction of Graphene Oxide to Highly Conductive Graphene by Lawesson's Reagent and Its Electrical Applications. *J. Mater. Chem. C* **2013**, *1* (18), 3104–3109.

<https://doi.org/10.1039/c3tc00067b>.

- (176) Mohammadi, S. Z.; Beitollahi, H.; Mousavi, M. Determination of Hydroxylamine Using a Carbon Paste Electrode Modified with Graphene Oxide Nano Sheets. *Russ. J. Electrochem.* **2017**, *53* (4), 374–379. <https://doi.org/10.1134/s1023193517040097>.
- (177) Zhou, X.; Zheng, J.; Wu, H.; Yang, H.; Zhang, J.; Guo, S. Reducing Graphene Oxide via Hydroxylamine: A Simple and Efficient Route to Graphene. *J. Phys. Chem. C* **2011**, *115* (24), 11957–11961. <https://doi.org/10.1021/jp202575j>.
- (178) Ruoff, R. S.; Piner, R. D.; Stankovich, S.; Nguyen, S. T.; Wu, Y.; Jia, Y.; Kohlhaas, K. A.; Dikin, D. A.; Kleinhammes, A. Synthesis of Graphene-Based Nanosheets via Chemical Reduction of Exfoliated Graphite Oxide. *Carbon*. 2007, pp 1558–1565. <https://doi.org/10.1016/j.carbon.2007.02.034>.
- (179) Ccorahua, R.; Troncoso, O. P.; Rodriguez, S.; Lopez, D.; Torres, F. G. Hydrazine Treatment Improves Conductivity of Bacterial Cellulose/Graphene Nanocomposites Obtained by a Novel Processing Method. *Carbohydr. Polym.* **2017**, *171*, 68–76. <https://doi.org/10.1016/j.carbpol.2017.05.005>.
- (180) Kim, N. H.; Kuila, T.; Lee, J. H. Simultaneous Reduction, Functionalization and Stitching of Graphene Oxide with Ethylenediamine for Composites Application. *J. Mater. Chem. A* **2013**, *1* (4), 1349–1358. <https://doi.org/10.1039/c2ta00853j>.
- (181) Zhang, J.; Wang, C.; Zhou, J. Ethylenediamine-Functionalized Reduced Graphene Oxide for Enhanced Methylene Blue Removal. *Environ. Eng. Sci.* **2017**, *34* (6), 394–400. <https://doi.org/10.1089/ees.2016.0262>.
- (182) Lei, Z.; Lu, L.; Zhao, X. S. The Electrocapacitive Properties of Graphene Oxide Reduced by Urea. *Energy Environ. Sci.* **2012**, *5* (4), 6391–6399. <https://doi.org/10.1039/c1ee02478g>.
- (183) Khojasteh, H.; Salavati-Niasari, M.; Safajou, H.; Safardoust-Hojaghan, H. Facile Reduction of Graphene Using Urea in Solid Phase and Surface Modification by N-Doped Graphene Quantum Dots for Adsorption of Organic Dyes. *Diam. Relat. Mater.* **2017**, *79*, 133–144. <https://doi.org/10.1016/j.diamond.2017.09.011>.

- (184) Liu, M.; Hou, Z.; Huang, B.; Gou, L.; Zhang, P. The Preparation, Characterization, and Properties of Silver Nanoparticle Reinforced Reduced Graphene Oxide–Poly(Amidoamine) Nanocomposites. *J. Appl. Polym. Sci.* **2017**, *134* (32). <https://doi.org/10.1002/app.45172>.
- (185) Yuan, Y.; Zhang, G.; Li, Y.; Zhang, G.; Zhang, F.; Fan, X. Poly(Amidoamine) Modified Graphene Oxide as an Efficient Adsorbent for Heavy Metal Ions. *Polym. Chem.* **2013**, *4* (6), 2164–2167. <https://doi.org/10.1039/c3py21128b>.
- (186) He, J.; Fang, L. Controllable Synthesis of Reduced Graphene Oxide. *Curr. Appl. Phys.* **2016**, *16* (9), 1152–1158. <https://doi.org/10.1016/j.cap.2016.06.011>.
- (187) Dreyer, D. R.; Murali, S.; Zhu, Y.; Ruoff, R. S.; Bielawski, C. W. Reduction of Graphite Oxide Using Alcohols. *J. Mater. Chem.* **2011**, *21* (10), 3443–3447. <https://doi.org/10.1039/c0jm02704a>.
- (188) Pousa Soares, C. P.; Lacerda Baptista, R. de; Cesar, D. V. Solvothermal Reduction of Graphite Oxide Using Alcohols. *Mater. Res.* **2018**, *21* (1). <https://doi.org/10.1590/1980-5373-MR-2017-0726>.
- (189) Zhu, C.; Guo, S.; Fang, Y.; Dong, S. Reducing Sugar: New Functional Molecules for the Green Synthesis of Graphene Nanosheets. *ACS Nano* **2010**, *4* (4), 2429–2437. <https://doi.org/10.1021/nn1002387>.
- (190) Kamisan, A. I.; Zainuddin, L. W.; Kamisan, A. S.; Tunku Kudin, T. I. A. I.; Hassan, O. H.; Abdul Halim, N.; Yahya, M. Z. A. Ultrasonic Assisted Synthesis of Reduced Graphene Oxide in Glucose Solution. *Key Eng. Mater.* **2016**, *708*, 25–29. <https://doi.org/10.4028/www.scientific.net/KEM.708.25>.
- (191) Hu, Y.; Sun, D.; Ding, J.; Chen, L.; Chen, X. Decorated Reduced Graphene Oxide for Photo-Chemotherapy. *J. Mater. Chem. B* **2016**, *4* (5), 929–937. <https://doi.org/10.1039/c5tb02359a>.
- (192) Bo, Z.; Shuai, X.; Mao, S.; Yang, H.; Qian, J.; Chen, J.; Yan, J.; Cen, K. Green Preparation of Reduced Graphene Oxide for Sensing and Energy Storage Applications. *Sci. Rep.* **2014**, *4*. <https://doi.org/10.1038/srep04684>.
- (193) Lee, J. Y.; Kim, N. Y.; Shin, D. Y.; Park, H. Y.; Lee, S. S.; Joon Kwon, S.; Lim, D. H.; Bong,

- K. W.; Son, J. G.; Kim, J. Y. Nitrogen-Doped Graphene-Wrapped Iron Nanofragments for High-Performance Oxygen Reduction Electrocatalysts. *J. Nanoparticle Res.* **2017**, *19* (3). <https://doi.org/10.1007/s11051-017-3793-y>.
- (194) Fan, Z. J.; Kai, W.; Yan, J.; Wei, T.; Zhi, L. J.; Feng, J.; Ren, Y. M.; Song, L. P.; Wei, F. Facile Synthesis of Graphene Nanosheets via Fe Reduction of Exfoliated Graphite Oxide. *ACS Nano* **2011**, *5* (1), 191–198. <https://doi.org/10.1021/nn102339t>.
- (195) Fan, Z.; Wang, K.; Wei, T.; Yan, J.; Song, L.; Shao, B. An Environmentally Friendly and Efficient Route for the Reduction of Graphene Oxide by Aluminum Powder. *Carbon*. 2010, pp 1686–1689. <https://doi.org/10.1016/j.carbon.2009.12.063>.
- (196) Jankovský, O.; Šimek, P.; Nováček, M.; Luxa, J.; Sedmidubský, D.; Pumera, M.; Macková, A.; Mikšová, R.; Sofer, Z. Use of Deuterium Labelling - Evidence of Graphene Hydrogenation by Reduction of Graphite Oxide Using Aluminium in Sodium Hydroxide. *RSC Adv.* **2015**, *5* (24), 18733–18739. <https://doi.org/10.1039/c4ra16794e>.
- (197) Domingues, S. H.; Kholmanov, I. N.; Kim, T.; Kim, J.; Tan, C.; Chou, H.; Alieva, Z. A.; Piner, R.; Zarbin, A. J. G.; Ruoff, R. S. Reduction of Graphene Oxide Films on Al Foil for Hybrid Transparent Conductive Film Applications. *Carbon N. Y.* **2013**, *63*, 454–459. <https://doi.org/10.1016/j.carbon.2013.07.007>.
- (198) Sohn, M.; Park, E.; Yoo, B. M.; Han, T. H.; Park, H. B.; Kim, H. Metal-Assisted Mechanochemical Reduction of Graphene Oxide. *Carbon N. Y.* **2016**, *110*, 79–86. <https://doi.org/10.1016/j.carbon.2016.08.045>.
- (199) Renteria, J. D.; Ramirez, S.; Malekpour, H.; Alonso, B.; Centeno, A.; Zurutuza, A.; Cocemasov, A. I.; Nika, D. L.; Balandin, A. A. Strongly Anisotropic Thermal Conductivity of Free-Standing Reduced Graphene Oxide Films Annealed at High Temperature. *Adv. Funct. Mater.* **2015**, *25* (29), 4664–4672. <https://doi.org/10.1002/adfm.201501429>.
- (200) Tian, S.; Sun, J.; Yang, S.; He, P.; Ding, S.; Ding, G.; Xie, X. Facile Thermal Annealing of Graphite Oxide in Air for Graphene with a Higher C/O Ratio. *RSC Adv.* **2015**, *5* (85), 69854–69860. <https://doi.org/10.1039/c5ra09388k>.
- (201) Voiry, D.; Yang, J.; Kupferberg, J.; Fullon, R.; Lee, C.; Jeong, H. Y.; Shin, H. S.;

- Chhowalla, M. High-Quality Graphene via Microwave Reduction of Solution-Exfoliated Graphene Oxide. *Science (80-.)*. **2016**, *353* (6306), 1413–1416. <https://doi.org/10.1126/science.aah3398>.
- (202) Neubauer, E.; Kitzmantel, M.; Hulman, M.; Angerer, P. Potential and Challenges of Metal-Matrix-Composites Reinforced with Carbon Nanofibers and Carbon Nanotubes. *Compos. Sci. Technol.* **2010**, *70* (16), 2228–2236. <https://doi.org/10.1016/j.compscitech.2010.09.003>.
- (203) Wang, F.; Chu, K.; Li, Y. biao; Wang, X. hu. Enhanced Interfacial Bonding and Mechanical Properties of Graphene/Cu Composites: A Matrix-Alloying Method. *Phys. Status Solidi Appl. Mater. Sci.* **2018**, *215* (18). <https://doi.org/10.1002/pssa.201800104>.
- (204) Schrader, M. E. Young-Dupre Revisited. *Langmuir* **1995**, *11* (9), 3585–3589. <https://doi.org/10.1021/la00009a049>.
- (205) Oh, S. Il; Lim, J. Y.; Kim, Y. C.; Yoon, J.; Kim, G. H.; Lee, J.; Sung, Y. M.; Han, J. H. Fabrication of Carbon Nanofiber Reinforced Aluminum Alloy Nanocomposites by a Liquid Process. *J. Alloys Compd.* **2012**, *542*, 111–117. <https://doi.org/10.1016/j.jallcom.2012.07.029>.
- (206) Rocher, J. P.; Quenisset, J. M.; Naslain, R. Wetting Improvement of Carbon or Silicon Carbide by Aluminium Alloys Based on a K2ZrF6 surface Treatment: Application to Composite Material Casting. *J. Mater. Sci.* **1989**, *24* (8), 2697–2703. <https://doi.org/10.1007/BF02385613>.
- (207) Ashraf, P. M.; Thomas, S. N.; Edwin, L. Development of Graphene–Nanometre-Sized Cerium Oxide-Incorporated Aluminium and Its Electrochemical Evaluation. *Appl. Nanosci.* **2016**, *6* (2), 149–158. <https://doi.org/10.1007/s13204-015-0438-2>.
- (208) Zhang, C.; Zhang, J.; Lin, K.; Huang, Y. Laser-Assisted Chemical Vapor Deposition Setup for Fast Synthesis of Graphene Patterns. *Rev. Sci. Instrum.* **2017**, *88* (5). <https://doi.org/10.1063/1.4984004>.
- (209) Cha, S. I.; Kim, K. T.; Arshad, S. N.; Mo, C. B.; Hong, S. H. Extraordinary Strengthening Effect of Carbon Nanotubes in Metal-Matrix Nanocomposites Processed by Molecular-Level Mixing. *Adv. Mater.* **2005**, *17* (11), 1377–1381.

<https://doi.org/10.1002/adma.200401933>.

- (210) Tjong, S. C. Recent Progress in the Development and Properties of Novel Metal Matrix Nanocomposites Reinforced with Carbon Nanotubes and Graphene Nanosheets. *Materials Science and Engineering R: Reports*. 2013, pp 281–350. <https://doi.org/10.1016/j.mser.2013.08.001>.
- (211) Nieto, A.; Lahiri, D.; Agarwal, A. Synthesis and Properties of Bulk Graphene Nanoplatelets Consolidated by Spark Plasma Sintering. *Carbon N. Y.* **2012**, *50* (11), 4068–4077. <https://doi.org/10.1016/j.carbon.2012.04.054>.
- (212) Parameswaran, P.; Ezhilarasi, T.; Bakshi, S. R.; Thomas Paul, V.; Mohandas, E. Spark Plasma Sintering Process as a Tool for Achieving Microstructural Integrity. In *Advances in Structural Integrity*, 2018. https://doi.org/10.1007/978-981-10-7197-3_54.
- (213) Bahrami, S.; Zakeri, M.; Faeghinia, A.; Rahimpour, M. R. Spark Plasma Sintering of Silicon Nitride/Barium Aluminum Silicate Composite. *Ceram. Int.* **2017**, *43* (12), 9153–9157. <https://doi.org/10.1016/j.ceramint.2017.04.065>.
- (214) Inam, F.; Vo, T.; Bhat, B. R. Structural Stability Studies of Graphene in Sintered Ceramic Nanocomposites. *Ceram. Int.* **2014**, *40* (PB), 16227–16233. <https://doi.org/10.1016/j.ceramint.2014.07.058>.
- (215) Singh, D. K.; Iyer, P. K.; Giri, P. K. Diameter Dependence of Oxidative Stability in Multiwalled Carbon Nanotubes: Role of Defects and Effect of Vacuum Annealing. *J. Appl. Phys.* **2010**, *108* (8). <https://doi.org/10.1063/1.3491022>.
- (216) Barre, C. Hot Isostatic Pressing. *Adv. Mater. Process.* **1999**, *155* (3), 47–48. [https://doi.org/10.1016/0261-3069\(85\)90012-3](https://doi.org/10.1016/0261-3069(85)90012-3).
- (217) Jambagi, S. C.; Bandyopadhyay, P. P. Plasma Sprayed Carbon Nanotube Reinforced Splats and Coatings. *J. Eur. Ceram. Soc.* **2017**, *37* (5), 2235–2244. <https://doi.org/10.1016/j.jeurceramsoc.2017.01.028>.
- (218) Viswanathan, V.; Laha, T.; Balani, K.; Agarwal, A.; Seal, S. Challenges and Advances in Nanocomposite Processing Techniques. *Materials Science and Engineering R: Reports*. 2006, pp 121–285. <https://doi.org/10.1016/j.mser.2006.11.002>.

- (219) Nutsch, G. Atmospheric Induction Plasma Spraying. *High Temp. Mater. Process. (An Int. Q. High-Technology Plasma Process.* **2014**, *6* (3), 8. <https://doi.org/10.1615/hightempmatproc.v6.i3.80>.
- (220) Azarmi, F. Vacuum Plasma Spraying. *Adv. Mater. Process.* **2005**, *163* (8), 37–39.
- (221) Poyato, R.; Vasiliev, A. L.; Padture, N. P.; Tanaka, H.; Nishimura, T. Aqueous Colloidal Processing of Single-Wall Carbon Nanotubes and Their Composites with Ceramics. *Nanotechnology* **2006**, *17* (6), 1770–1777. <https://doi.org/10.1088/0957-4484/17/6/038>.
- (222) Kang, K.; Bae, G.; Won, J.; Lee, C. Mechanical Property Enhancement of Kinetic Sprayed Al Coatings Reinforced by Multi-Walled Carbon Nanotubes. *Acta Mater.* **2012**, *60* (13–14), 5031–5039. <https://doi.org/10.1016/j.actamat.2012.05.034>.
- (223) Saboori, A.; Pavese, M.; Badini, C.; Fino, P. Microstructure and Thermal Conductivity of Al-Graphene Composites Fabricated by Powder Metallurgy and Hot Rolling Techniques. *Acta Metall. Sin. (English Lett.* **2017**, *30* (7), 675–687. <https://doi.org/10.1007/s40195-017-0579-2>.
- (224) Shin, S. E.; Bae, D. H. Deformation Behavior of Aluminum Alloy Matrix Composites Reinforced with Few-Layer Graphene. *Compos. Part A Appl. Sci. Manuf.* **2015**, *78*, 42–47. <https://doi.org/10.1016/j.compositesa.2015.08.001>.
- (225) Ab Rahim, S. N.; Lajis, M. A.; Ariffin, S. A Review on Recycling Aluminum Chips by Hot Extrusion Process. In *Procedia CIRP*, 2015; Vol. 26, pp 761–766. <https://doi.org/10.1016/j.procir.2015.01.013>.
- (226) Yang, X.; Liu, E.; Shi, C.; He, C.; Li, J.; Zhao, N.; Kondoh, K. Fabrication of Carbon Nanotube Reinforced Al Composites with Well-Balanced Strength and Ductility. *J. Alloys Compd.* **2013**, *563*, 216–220. <https://doi.org/10.1016/j.jallcom.2013.02.066>.
- (227) Rashad, M.; Pan, F.; Tang, A.; Asif, M. Effect of Graphene Nanoplatelets Addition on Mechanical Properties of Pure Aluminum Using a Semi-Powder Method. *Prog. Nat. Sci. Mater. Int.* **2014**, *24* (2), 101–108. <https://doi.org/10.1016/j.pnsc.2014.03.012>.

- (228) Jeon, C. H.; Jeong, Y. H.; Seo, J. J.; Tien, H. N.; Hong, S. T.; Yum, Y. J.; Hur, S. H.; Lee, K. J. Material Properties of Graphene/Aluminum Metal Matrix Composites Fabricated by Friction Stir Processing. *Int. J. Precis. Eng. Manuf.* **2014**, *15* (6), 1235–1239. <https://doi.org/10.1007/s12541-014-0462-2>.
- (229) Johannes, L. B.; Yowell, L. L.; Sosa, E.; Arepalli, S.; Mishra, R. S. Survivability of Single-Walled Carbon Nanotubes during Friction Stir Processing. *Nanotechnology* **2006**, *17*(12), 3081–3084. <https://doi.org/10.1088/0957-4484/17/12/044>.
- (230) Jata, K. V.; Mahoney, M. W.; Mishra, R. S.; Lienert, T. J. Friction Stir Welding and Processing III. In *Friction Stir Welding and Processing III*; 2010; Vol. 29, p 298. <https://doi.org/10.1002/9781118062302>.
- (231) Mishra, R. S.; Ma, Z. Y.; Charit, I. Friction Stir Processing: A Novel Technique for Fabrication of Surface Composite. *Mater. Sci. Eng. A* **2003**, *341* (1–2), 307–310. [https://doi.org/10.1016/S0921-5093\(02\)00199-5](https://doi.org/10.1016/S0921-5093(02)00199-5).
- (232) Chen, L. Y.; Konishi, H.; Fehrenbacher, A.; Ma, C.; Xu, J. Q.; Choi, H.; Xu, H. F.; Pfefferkorn, F. E.; Li, X. C. Novel Nanoprocessing Route for Bulk Graphene Nanoplatelets Reinforced Metal Matrix Nanocomposites. *Scr. Mater.* **2012**, *67* (1), 29–32. <https://doi.org/10.1016/j.scriptamat.2012.03.013>.
- (233) Luo, H.; Sui, Y.; Qi, J.; Meng, Q.; Wei, F.; He, Y. Copper Matrix Composites Enhanced by Silver/Reduced Graphene Oxide Hybrids. *Mater. Lett.* **2017**, *196*, 354–357. <https://doi.org/10.1016/j.matlet.2017.03.084>.
- (234) Pérez-Bustamante, R.; Bolaños-Morales, D.; Bonilla-Martínez, J.; Estrada-Guel, I.; Martínez-Sánchez, R. Microstructural and Hardness Behavior of Graphene-Nanoplatelets/Aluminum Composites Synthesized by Mechanical Alloying. *J. Alloys Compd.* **2015**, *615* (S1), S578–S582. <https://doi.org/10.1016/j.jallcom.2014.01.225>.
- (235) Chu, K.; Jia, C. Enhanced Strength in Bulk Graphene-Copper Composites. *Phys. Status Solidi Appl. Mater. Sci.* **2014**, *211* (1), 184–190. <https://doi.org/10.1002/pssa.201330051>.
- (236) El-Eskandarany, M. S. Reactive Ball Milling for Fabrication of Metal Nitride Nanocrystalline Powders. In *Mechanical Alloying*; 2015; pp 182–201.

<https://doi.org/10.1016/B978-1-4557-7752-5.00008-5>.

- (237) Yu, Z.; Yang, W.; Zhou, C.; Zhang, N.; Chao, Z.; Liu, H.; Cao, Y.; Sun, Y.; Shao, P.; Wu, G. Effect of Ball Milling Time on Graphene Nanosheets Reinforced Al6063 Composite Fabricated by Pressure Infiltration Method. *Carbon N. Y.* **2019**, *141*, 25–39. <https://doi.org/10.1016/j.carbon.2018.09.041>.
- (238) Bastwros, M.; Kim, G. Y.; Zhu, C.; Zhang, K.; Wang, S.; Tang, X.; Wang, X. Effect of Ball Milling on Graphene Reinforced Al6061 Composite Fabricated by Semi-Solid Sintering. *Compos. Part B Eng.* **2014**, *60*, 111–118. <https://doi.org/10.1016/j.compositesb.2013.12.043>.
- (239) Prashantha Kumar, H. G.; Anthony Xavier, M. Encapsulation and Microwave Hybrid Processing of Al 6061–Graphene–SiC Composites. *Mater. Manuf. Process.* **2018**, *33* (1), 19–25. <https://doi.org/10.1080/10426914.2017.1279320>.
- (240) Lewis, J. A. Colloidal Processing of Ceramics. *J. Am. Ceram. Soc.* **2000**, *83* (10), 2341–2359. <https://doi.org/10.1111/j.1151-2916.2000.tb01560.x>.
- (241) Jambagi, S. C.; Sarkar, N.; Bandyopadhyay, P. P. Preparation of Carbon Nanotube Doped Ceramic Powders for Plasma Spraying using Heterocoagulation Method. *J. Eur. Ceram. Soc.* **2015**, *35* (3), 989–1000. <https://doi.org/10.1016/j.jeurceramsoc.2014.10.017>.
- (242) Arvanitelis, C.; Jayaseelan, D. D.; Cho, J.; Boccaccini, A. R. Carbon, Nanotube-SiO₂ Composites by Colloidal Processing. *Adv. Appl. Ceram.* **2008**, *107* (3). <https://doi.org/10.1179/174367608X263412>.
- (243) Grigoriev, S.; Peretyagin, P.; Smirnov, A.; Solís, W.; Díaz, L. A.; Fernández, A.; Torrecillas, R. Effect of Graphene Addition on the Mechanical and Electrical Properties of Al₂O₃-SiC_w Ceramics. *J. Eur. Ceram. Soc.* **2017**, *37* (6), 2473–2479. <https://doi.org/10.1016/j.jeurceramsoc.2017.01.027>.
- (244) Zheng, C.; Feng, M.; Zhen, X.; Huang, J.; Zhan, H. Materials Investigation of Multi-Walled Carbon Nanotubes Doped Silica Gel Glass Composites. *J. Non. Cryst. Solids* **2008**, *354* (12–13), 1327–1330. <https://doi.org/10.1016/j.jnoncrysol.2007.02.089>.

- (245) Mao, J.; Iocozzia, J.; Huang, J.; Meng, K.; Lai, Y.; Lin, Z. Graphene Aerogels for Efficient Energy Storage and Conversion. *Energy and Environmental Science*. 2018, pp 772–799. <https://doi.org/10.1039/c7ee03031b>.
- (246) Etacheri, V. Sol-Gel Processed Cathode Materials for Lithium-Ion Batteries. In *Adv.Sol-Gel Deriv. Materials Technol.*; 2017.
- (247) Hu, Y. C.; Hsu, W. L.; Wang, Y. T.; Ho, C. T.; Chang, P. Z. Enhance the Pyroelectricity of Polyvinylidene Fluoride by Graphene-Oxide Doping. *Sensors (Switzerland)* **2014**, *14* (4), 6877–6890. <https://doi.org/10.3390/s140406877>.
- (248) Jiang, Y.; Chen, Y.; Liu, Y. J.; Sui, G. X. Lightweight Spongy Bone-like Graphene@SiC Aerogel Composites for High-Performance Microwave Absorption. *Chem. Eng. J.* **2018**, *337*, 522–531. <https://doi.org/10.1016/j.cej.2017.12.131>.
- (249) Cauqui, M. A.; Rodríguez-Izquierdo, J. M. Application of the Sol-Gel Methods to Catalyst Preparation. *J. Non. Cryst. Solids* **1992**, *147–148* (C), 724–738. [https://doi.org/10.1016/S0022-3093\(05\)80707-0](https://doi.org/10.1016/S0022-3093(05)80707-0).
- (250) Zeng, Y.; Zhou, Y.; Kong, L.; Zhou, T.; Shi, G. A Novel Composite of SiO₂-Coated Graphene Oxide and Molecularly Imprinted Polymers for Electrochemical Sensing Dopamine. *Biosens. Bioelectron.* **2013**, *45* (1), 25–33. <https://doi.org/10.1016/j.bios.2013.01.036>.
- (251) Jeon, I. Y.; Bae, S. Y.; Seo, J. M.; Baek, J. B. Scalable Production of Edge-Functionalized Graphene Nanoplatelets via Mechanochemical Ball-Milling. *Adv. Funct. Mater.* **2015**, *25* (45), 6961–6975. <https://doi.org/10.1002/adfm.201502214>.
- (252) Ikeda, A.; Nobusawa, K.; Hamano, T.; Kikuchi, J. I. Single-Walled Carbon Nanotubes Template the One-Dimensional Ordering of a Polythiophene Derivative. *Org. Lett.* **2006**, *8* (24), 5489–5492. <https://doi.org/10.1021/ol062187q>.
- (253) León, V.; Quintana, M.; Herrero, M. A.; Fierro, J. L. G.; Hoz, A. D. La; Prato, M.; Vázquez, E. Few-Layer Graphenes from Ball-Milling of Graphite with Melamine. *Chem. Commun.* **2011**, *47* (39), 10936–10938. <https://doi.org/10.1039/c1cc14595a>.

- (254) Cha, J.; Jun, G. H.; Park, J. K.; Kim, J. C.; Ryu, H. J.; Hong, S. H. Improvement of Modulus, Strength and Fracture Toughness of CNT/Epoxy Nanocomposites through the Functionalization of Carbon Nanotubes. *Compos. Part B Eng.* **2017**, *129*, 169–179. <https://doi.org/10.1016/j.compositesb.2017.07.070>.
- (255) Jeon, I. Y.; Shin, Y. R.; Sohn, G. J.; Choi, H. J.; Bae, S. Y.; Mahmood, J.; Jung, S. M.; Seo, J. M.; Kim, M. J.; Chang, D. W.; et al. Edge-Carboxylated Graphene Nanosheets via Ball Milling. *Proc. Natl. Acad. Sci. U. S. A.* **2012**, *109* (15), 5588–5593. <https://doi.org/10.1073/pnas.1116897109>.
- (256) Fan, X.; Chang, D. W.; Chen, X.; Baek, J.-B. B.; Dai, L. Functionalized Graphene Nanoplatelets from Ball Milling for Energy Applications. *Curr. Opin. Chem. Eng.* **2016**, *11*, 52–58. <https://doi.org/10.1016/j.coche.2016.01.003>.
- (257) Xu, J.; Shui, J.; Wang, J.; Wang, M.; Liu, H. K.; Dou, S. X.; Jeon, I. Y.; Seo, J. M.; Baek, J. B.; Dai, L. Sulfur-Graphene Nanostructured Cathodes via Ball-Milling for High-Performance Lithium-Sulfur Batteries. *ACS Nano* **2014**, *8* (10), 10920–10930. <https://doi.org/10.1021/nn5047585>.
- (258) Sjögren, B.; Iregren, A.; Montelius, J.; Yokel, R. A. *Aluminum*, Fourth Edi.; Elsevier, 2015; Vol. 1. <https://doi.org/10.1016/B978-0-444-59453-2.00026-3>.
- (259) Fadavi Boostani, A.; Tahamtan, S.; Jiang, Z. Y.; Wei, D.; Yazdani, S.; Azari Khosroshahi, R.; Taherzadeh Mousavian, R.; Xu, J.; Zhang, X.; Gong, D. Enhanced Tensile Properties of Aluminium Matrix Composites Reinforced with Graphene Encapsulated SiC Nanoparticles. *Compos. Part A Appl. Sci. Manuf.* **2015**, *68*, 155–163. <https://doi.org/10.1016/j.compositesa.2014.10.010>.
- (260) Baig, Z.; Mamat, O.; Mustapha, M.; Sarfraz, M. Influence of Surfactant Type on the Dispersion State and Properties of Graphene Nanoplatelets Reinforced Aluminium Matrix Nanocomposites. *Fullerenes Nanotub. Carbon Nanostructures* **2017**, *25* (9), 545–557. <https://doi.org/10.1080/1536383X.2017.1362396>.
- (261) Prabhakaran, S.; Kumar, H. G. P.; Kalainathan, S.; Vasudevan, V. K.; Shukla, P.; Lin, D. Laser Shock Peening Modified Surface Texturing, Microstructure and Mechanical Properties of Graphene Dispersion Strengthened Aluminium Nanocomposites. *Surfaces and Interfaces* **2019**, *14*, 127–137.

<https://doi.org/10.1016/j.surfin.2018.12.003>.

- (262) Prashantha, P. K.; S, P.; M, A. X.; S, K.; Lin, D.; Shukla, P.; Vasudevan, V. K. Enhanced Surface and Mechanical Properties of Bioinspired Nanolaminate Graphene-Aluminum Alloy Nanocomposites through Laser Shock Processing for Engineering Applications. *Mater. Today Commun.* **2018**, *16*, 81–89. <https://doi.org/10.1016/j.mtcomm.2018.04.010>.
- (263) Hu, Z.; Tong, G.; Lin, D.; Chen, C.; Guo, H.; Xu, J.; Zhou, L. Graphene-Reinforced Metal Matrix Nanocomposites - A Review. *Mater. Sci. Technol. (United Kingdom)* **2016**, *32* (9), 930–953. <https://doi.org/10.1080/02670836.2015.1104018>.
- (264) Rashad, M.; Pan, F.; Asif, M.; Hussain, S.; Saleem, M. Improving Properties of Mg with Al-Cu Additions. *Mater. Charact.* **2014**, *95*, 140–147. <https://doi.org/10.1016/j.matchar.2014.06.020>.
- (265) Rashad, M.; Pan, F.; Tang, A.; Asif, M.; Hussain, S.; Gou, J.; Mao, J. Improved Strength and Ductility of Magnesium with Addition of Aluminum and Graphene Nanoplatelets (Al+GNPs) Using Semi Powder Metallurgy Method. *J. Ind. Eng. Chem.* **2015**, *23*, 243–250. <https://doi.org/10.1016/j.jiec.2014.08.024>.
- (266) Shin, S. E.; Choi, H. J.; Shin, J. H.; Bae, D. H. Strengthening Behavior of Few-Layered Graphene/Aluminum Composites. *Carbon N. Y.* **2015**, *82* (C), 143–151. <https://doi.org/10.1016/j.carbon.2014.10.044>.
- (267) Zhang, H.; Xu, C.; Xiao, W.; Ameyama, K.; Ma, C. Enhanced Mechanical Properties of Al5083 Alloy with Graphene Nanoplates Prepared by Ball Milling and Hot Extrusion. *Mater. Sci. Eng. A* **2016**, *658*, 8–15. <https://doi.org/10.1016/j.msea.2016.01.076>.
- (268) Ward, D.; Gupta, A.; Saraf, S.; Zhang, C.; Sakthivel, T. S.; Barkam, S.; Agarwal, A.; Seal, S. Functional NiAl-Graphene Oxide Composite as a Model Coating for Aerospace Component Repair. *Carbon N. Y.* **2016**, *105*, 529–543. <https://doi.org/10.1016/j.carbon.2016.04.025>.
- (269) Kumar, H. G. P.; Xavior, M. A. Fatigue and Wear Behavior of Al6061–Graphene Composites Synthesized by Powder Metallurgy. *Trans. Indian Inst. Met.* **2016**, *69* (2), 415–419. <https://doi.org/10.1007/s12666-015-0780-9>.

- (270) Khodabakhshi, F.; Arab, S. M.; Švec, P.; Gerlich, A. P. Fabrication of a New Al-Mg/Graphene Nanocomposite by Multi-Pass Friction-Stir Processing: Dispersion, Microstructure, Stability, and Strengthening. *Mater. Charact.* **2017**, *132*, 92–107. <https://doi.org/10.1016/j.matchar.2017.08.009>.
- (271) Sahoo, B.; Joseph, J.; Sharma, A.; Paul, J. Surface Modification of Aluminium by Graphene Impregnation. *Mater. Des.* **2017**, *116*, 51–64. <https://doi.org/10.1016/j.matdes.2016.11.075>.
- (272) Bisht, A.; Srivastava, M.; Kumar, R. M.; Lahiri, I.; Lahiri, D. Strengthening Mechanism in Graphene Nanoplatelets Reinforced Aluminum Composite Fabricated through Spark Plasma Sintering. *Mater. Sci. Eng. A* **2017**, *695* (April), 20–28. <https://doi.org/10.1016/j.msea.2017.04.009>.
- (273) Simsek, I. N. G.; Nistal, A.; García, E.; Pérez-Coll, D.; Miranzo, P.; Osendi, M. I. The Effect of Graphene Nanoplatelets on the Thermal and Electrical Properties of Aluminum Nitride Ceramics. *J. Eur. Ceram. Soc.* **2017**, *37* (12), 3721–3729. <https://doi.org/10.1016/j.jeurceramsoc.2016.12.044>.
- (274) Cano-Crespo, R.; Malmal Moshtaghioun, B.; Gómez-García, D.; Domínguez-Rodríguez, A.; Moreno, R. High-Temperature Creep of Carbon Nanofiber-Reinforced and Graphene Oxide-Reinforced Alumina Composites Sintered by Spark Plasma Sintering. *Ceram. Int.* **2017**, *43* (9), 7136–7141. <https://doi.org/10.1016/j.ceramint.2017.02.146>.
- (275) Turan, M. E.; Rashad, M.; Zengin, H.; Topcu, I.; Sun, Y.; Asif, M. Effect of Multiwalled Carbon Nanotubes on Elevated Temperature Tensile and Wear Behavior of Al2024 Matrix Composites Fabricated by Stir Casting and Hot Extrusion. *J. Mater. Eng. Perform.* **2020**, *29* (8), 5227–5237. <https://doi.org/10.1007/s11665-020-05032-0>.
- (276) Prashantha Kumar, H. G.; Anthony Xavier, M. Effect of Graphene Addition and Tribological Performance of Al 6061/Graphene Flake Composite. *Tribol. - Mater. Surfaces Interfaces* **2017**, *11* (2), 88–97. <https://doi.org/10.1080/17515831.2017.1329920>.
- (277) Prashantha Kumar, H. G.; Anthony Xavier, M. Effect of Graphene Addition on

- Flexural Properties of Al 6061 Nanocomposites. In *Materials Today: Proceedings*, 2017; Vol. 4, pp 8127–8133. <https://doi.org/10.1016/j.matpr.2017.07.153>.
- (278) Pan, Y.; Hong, N.; Zhan, J.; Wang, B.; Song, L.; Hu, Y. Effect of Graphene on the Fire and Mechanical Performances of Glass Fiber-Reinforced Polyamide 6 Composites Containing Aluminum Hypophosphite. *Polym. - Plast. Technol. Eng.* **2014**, *53* (14), 1467–1475. <https://doi.org/10.1080/03602559.2014.909483>.
- (279) Prashantha Kumar, H. G.; Anthony Xavier, M. Effect of Graphene Addition and Tribological Performance of Al 6061/Graphene Flake Composite. *Tribol. - Mater. Surfaces Interfaces* **2017**, *11* (2), 88–97. <https://doi.org/10.1080/17515831.2017.1329920>.
- (280) Chen, J.; Song, Y.; Shan, D.; Han, E. H. Modifications of the Hydrotalcite Film on AZ31 Mg Alloy by Phytic Acid: The Effects on Morphology, Composition and Corrosion Resistance. *Corros. Sci.* **2013**, *74*, 130–138. <https://doi.org/10.1016/j.corsci.2013.04.034>.
- (281) Wilke, B. M.; Zhang, L.; Li, W.; Ning, C.; Chen, C. F.; Gu, Y. Corrosion Performance of MAO Coatings on AZ31 Mg Alloy in Simulated Body Fluid vs. Earle's Balance Salt Solution. *Appl. Surf. Sci.* **2016**, *363*, 328–337. <https://doi.org/10.1016/j.apsusc.2015.12.026>.
- (282) Rashad, M.; Pan, F.; Tang, A.; Lu, Y.; Asif, M.; Hussain, S.; She, J.; Gou, J.; Mao, J. Effect of Graphene Nanoplatelets (GNPs) Addition on Strength and Ductility of Magnesium-Titanium Alloys. *J. Magnes. Alloy.* **2013**, *1* (3), 242–248. <https://doi.org/10.1016/j.jma.2013.09.004>.
- (283) Rashad, M.; Pan, F.; Tang, A.; Asif, M.; Aamir, M. Synergetic Effect of Graphene Nanoplatelets (GNPs) and Multi-Walled Carbon Nanotube (MW-CNTs) on Mechanical Properties of Pure Magnesium. *J. Alloys Compd.* **2014**, *603*, 111–118. <https://doi.org/10.1016/j.jallcom.2014.03.038>.
- (284) Gao, X.; Yue, H.; Guo, E.; Zhang, H.; Lin, X.; Yao, L.; Wang, B. Mechanical Properties and Thermal Conductivity of Graphene Reinforced Copper Matrix Composites. *Powder Technol.* **2016**, *301*, 601–607. <https://doi.org/10.1016/j.powtec.2016.06.045>.

- (285) Rashad, M.; Pan, F.; Liu, Y.; Chen, X.; Lin, H.; Pan, R.; Asif, M.; She, J. High Temperature Formability of Graphene Nanoplatelets-AZ31 Composites Fabricated by Stir-Casting Method. *J. Magnes. Alloy.* **2016**, *4* (4), 270–277. <https://doi.org/10.1016/j.jma.2016.11.003>.
- (286) Rashad, M.; Pan, F.; Asif, M.; Li, L. Enhanced Ductility of Mg-3Al-1Zn Alloy Reinforced with Short Length Multi-Walled Carbon Nanotubes Using a Powder Metallurgy Method. *Prog. Nat. Sci. Mater. Int.* **2015**, *25* (4), 276–281. <https://doi.org/10.1016/j.pnsc.2015.08.002>.
- (287) Rashad, M.; Pan, F.; Yu, Z.; Asif, M.; Lin, H.; Pan, R. Investigation on Microstructural, Mechanical and Electrochemical Properties of Aluminum Composites Reinforced with Graphene Nanoplatelets. *Prog. Nat. Sci. Mater. Int.* **2015**, *25* (5), 460–470. <https://doi.org/10.1016/j.pnsc.2015.09.005>.
- (288) Rashad, M.; Pan, F.; Asif, M. Magnesium Matrix Composites Reinforced with Graphene Nanoplatelets. In *Graphene Materials: Fundamentals and Emerging Applications*; 2015; pp 151–189. <https://doi.org/10.1002/9781119131816.ch5>.
- (289) Rashad, M.; Pan, F.; Zhang, J.; Asif, M. Use of High Energy Ball Milling to Study the Role of Graphene Nanoplatelets and Carbon Nanotubes Reinforced Magnesium Alloy. *J. Alloys Compd.* **2015**, *646*, 223–232. <https://doi.org/10.1016/j.jallcom.2015.06.051>.
- (290) Rashad, M.; Pan, F.; Asif, M. Exploring Mechanical Behavior of Mg-6Zn Alloy Reinforced with Graphene Nanoplatelets. *Mater. Sci. Eng. A* **2016**, *649*, 263–269. <https://doi.org/10.1016/j.msea.2015.10.009>.
- (291) Rashad, M.; Pan, F.; Lin, D.; Asif, M. High Temperature Mechanical Behavior of AZ61 Magnesium Alloy Reinforced with Graphene Nanoplatelets. *Mater. Des.* **2016**, *89*, 1242–1250. <https://doi.org/10.1016/j.matdes.2015.10.101>.
- (292) Kavimani, V.; Soorya Prakash, K.; Arun Pandian, M. Influence of R-GO Addition on Enhancement of Corrosion and Wear Behavior of AZ31 MMC. *Appl. Phys. A* **2017**, *123* (8), 514. <https://doi.org/10.1007/s00339-017-1118-8>.
- (293) Turan, M. E.; Sun, Y.; Akgul, Y.; Turen, Y.; Ahlatci, H. The Effect of GNPs on Wear and Corrosion Behaviors of Pure Magnesium. *J. Alloys Compd.* **2017**, *724*, 14–23.

<https://doi.org/10.1016/j.jallcom.2017.07.022>.

- (294) Du, F. P.; Yang, W.; Zhang, F.; Tang, C. Y.; Liu, S. P.; Yin, L.; Law, W. C. Enhancing the Heat Transfer Efficiency in Graphene-Epoxy Nanocomposites Using a Magnesium Oxide-Graphene Hybrid Structure. *ACS Appl. Mater. Interfaces* **2015**, *7* (26), 14397–14403. <https://doi.org/10.1021/acsami.5b03196>.
- (295) Wu, L.; Wu, R.; Hou, L.; Zhang, J.; Zhang, M. Microstructure, Mechanical Properties and Wear Performance of AZ31 Matrix Composites Reinforced by Graphene Nanoplatelets(GNPs). *J. Alloys Compd.* **2018**, *750*, 530–536. <https://doi.org/10.1016/j.jallcom.2018.04.035>.
- (296) Du, X.; Du, W.; Wang, Z.; Liu, K.; Li, S. Ultra-High Strengthening Efficiency of Graphene Nanoplatelets Reinforced Magnesium Matrix Composites. *Mater. Sci. Eng. A* **2018**, *711*, 633–642. <https://doi.org/10.1016/j.msea.2017.11.040>.
- (297) Weibel, A.; Mesguich, D.; Chevallier, G.; Flahaut, E.; Laurent, C. Fast and Easy Preparation of Few-Layered-Graphene/Magnesia Powders for Strong, Hard and Electrically Conducting Composites. *Carbon N. Y.* **2018**, *136*, 270–279. <https://doi.org/10.1016/j.carbon.2018.04.085>.
- (298) Chen, L.; Zhao, Y.; Hou, H.; Zhang, T.; Liang, J.; Li, M.; Li, J. Development of AZ91D Magnesium Alloy-Graphene Nanoplatelets Composites Using Thixomolding Process. *J. Alloys Compd.* **2019**, *778*, 359–374. <https://doi.org/10.1016/j.jallcom.2018.11.148>.
- (299) Torabi Parizi, M.; Ebrahimi, G. R.; Ezatpour, H. R. Effect of Graphene Nanoplatelets Content on the Microstructural and Mechanical Properties of AZ80 Magnesium Alloy. *Mater. Sci. Eng. A* **2019**, *742*, 373–389. <https://doi.org/10.1016/j.msea.2018.11.025>.
- (300) Kumar, P.; Mallick, A.; Kujur, M. S.; Tun, K. S.; Gupta, M. Effects of Graphene Nanoplatelets on the Tribological, Mechanical, and Thermal Properties of Mg-3Al Alloy Nanocomposites. *Int. J. Mater. Res.* **2019**. <https://doi.org/10.3139/146.111777>.
- (301) V., K.; Prakash, S.; Rajesh, R.; Rammasamy, D.; Selvaraj, N. B.; Yang, T.; Prabakaran, B.; Jothi, S.; Prakash, K. S.; Rajesh, R.; et al. Electro Deposition of R-GO/SiC Nano-

- Composites on Magnesium and Its Corrosion Behavior in Aqueous Electrolyte. *Appl. Surf. Sci.* **2017**, *424*, 63–71. <https://doi.org/10.1016/j.apsusc.2017.02.082>.
- (302) Rashad, M.; Pan, F.; Asif, M.; Chen, X. Corrosion Behavior of Magnesium-Graphene Composites in Sodium Chloride Solutions. *J. Magnes. Alloy.* **2017**, *5* (3), 271–276. <https://doi.org/10.1016/j.jma.2017.06.003>.
- (303) Lin, D.; Richard Liu, C.; Cheng, G. J. Single-Layer Graphene Oxide Reinforced Metal Matrix Composites by Laser Sintering: Microstructure and Mechanical Property Enhancement. *Acta Mater.* **2014**, *80*, 183–193. <https://doi.org/10.1016/j.actamat.2014.07.038>.
- (304) Moysowicz, A.; Śliwak, A.; Miniach, E.; Gryglewicz, G. Polypyrrole/Iron Oxide/Reduced Graphene Oxide Ternary Composite as a Binderless Electrode Material with High Cyclic Stability for Supercapacitors. *Compos. Part B Eng.* **2017**, *109*, 23–29. <https://doi.org/10.1016/j.compositesb.2016.10.036>.
- (305) Ayyappadas, C.; Muthuchamy, A.; Raja Annamalai, A.; Agrawal, D. K. An Investigation on the Effect of Sintering Mode on Various Properties of Copper-Graphene Metal Matrix Composite. *Adv. Powder Technol.* **2017**, *28*(7), 1760–1768. <https://doi.org/10.1016/j.apt.2017.04.013>.
- (306) Rajkovic, V.; Bozic, D.; Stasic, J.; Wang, H.; Jovanovic, M. T. Processing, Characterization and Properties of Copper-Based Composites Strengthened by Low Amount of Alumina Particles. *Powder Technol.* **2014**, *268*, 392–400. <https://doi.org/10.1016/j.powtec.2014.08.051>.
- (307) Li, J.; Yu, S.; Zhou, Y.; Ge, M.; Qian, Y.; Zhang, W. Phase Separation in Pre-Ceramic Polymers Blends and Its Influence on the Microstructure of ZrC/SiC Ceramic Derivatives. *Mater. Lett.* **2015**, *156*, 72–75. <https://doi.org/10.1016/j.matlet.2015.04.118>.
- (308) Leon, C. A.; Rodriguez-Ortiz, G.; Nanko, M.; Aguilar, E. A. Pulsed Electric Current Sintering of Cu Matrix Composites Reinforced with Plain and Coated Alumina Powders. *Powder Technol.* **2014**, *252*, 1–7. <https://doi.org/10.1016/j.powtec.2013.10.025>.
- (309) Tan, Y.; Zhu, K.; Li, D.; Bai, F.; Wei, Y.; Zhang, P. N-Doped Graphene/Fe-Fe₃C Nano-

- Composite Synthesized by a Fe-Based Metal Organic Framework and Its Anode Performance in Lithium Ion Batteries. *Chem. Eng. J.* **2014**, *258*, 93–100. <https://doi.org/10.1016/j.cej.2014.07.066>.
- (310) Zhang, L.; Li, N.; Xia, H.; Zhang, J.; Zhang, P.; Xu, M.; Ma, H. Preparation and Mechanical Properties of (Ni–Fe)–Graphene Composite Coating. *Adv. Eng. Mater.* **2016**, *18*(10), 1716–1719. <https://doi.org/10.1002/adem.201600357>.
- (311) Albaaji, A. J.; Castle, E. G.; Reece, M. J.; Hall, J. P.; Evans, S. L. Synthesis and Properties of Graphene and Graphene/Carbon Nanotube-Reinforced Soft Magnetic FeCo Alloy Composites by Spark Plasma Sintering. *J. Mater. Sci.* **2016**, *51*(16), 7624–7635. <https://doi.org/10.1007/s10853-016-0041-2>.
- (312) Ramirez, S.; Chan, K.; Hernandez, R.; Recinos, E.; Hernandez, E.; Salgado, R.; Khitun, A. G.; Garay, J. E.; Balandin, A. A. Thermal and Magnetic Properties of Nanostructured Densified Ferrimagnetic Composites with Graphene - Graphite Fillers. *Mater. Des.* **2017**, *118*, 75–80. <https://doi.org/10.1016/j.matdes.2017.01.018>.
- (313) Li, N.; Zhang, L.; Zhu, Y.; Xu, M.; Xu, Y.; Ruan, X.; Ma, H. The Effect of Graphene on the Deposition and Mechanical Property of Ni-Fe-Graphene Composite Coating. *J. Electrochem. Soc.* **2018**, *165*(5), D215–D222. <https://doi.org/10.1149/2.1061805jes>.
- (314) Zhang, D.; Zhan, Z. Strengthening Effect of Graphene Derivatives in Copper Matrix Composites. *J. Alloys Compd.* **2016**, *654*, 226–233. <https://doi.org/10.1016/j.jallcom.2015.09.013>.
- (315) Pavithra, C. L. P.; Sarada, B. V.; Rajulapati, K. V.; Rao, T. N.; Sundararajan, G. A New Electrochemical Approach for the Synthesis of Copper-Graphene Nanocomposite Foils with High Hardness. *Sci. Rep.* **2014**, *4*. <https://doi.org/10.1038/srep04049>.
- (316) Li, M.; Che, H.; Liu, X.; Liang, S.; Xie, H. Highly Enhanced Mechanical Properties in Cu Matrix Composites Reinforced with Graphene Decorated Metallic Nanoparticles. *J. Mater. Sci.* **2014**, *49*(10), 3725–3731. <https://doi.org/10.1007/s10853-014-8082-x>.
- (317) Xiong, D. B.; Cao, M.; Guo, Q.; Tan, Z.; Fan, G.; Li, Z.; Zhang, D. Graphene-and-Copper

- Artificial Nacre Fabricated by a Preform Impregnation Process: Bioinspired Strategy for Strengthening-Toughening of Metal Matrix Composite. *ACS Nano* **2015**, *9*(7), 6934–6943. <https://doi.org/10.1021/acsnano.5b01067>.
- (318) Mai, Y. J.; Zhou, M. P.; Ling, H. J.; Chen, F. X.; Lian, W. Q.; Jie, X. H. Surfactant-Free Electrodeposition of Reduced Graphene Oxide/Copper Composite Coatings with Enhanced Wear Resistance. *Appl. Surf. Sci.* **2017**. <https://doi.org/10.1016/j.apsusc.2017.10.014>.
- (319) He, Y.; Huang, F.; Li, H.; Sui, Y.; Wei, F.; Meng, Q.; Yang, W.; Qi, J. Tensile Mechanical Properties of Nano-Layered Copper/Graphene Composite. *Phys. E Low-Dimensional Syst. Nanostructures* **2017**, *87*, 233–236. <https://doi.org/10.1016/j.physe.2016.10.044>.
- (320) Ponraj, N. V.; Azhagurajan, A.; Vettivel, S. C.; Sahaya Shajan, X.; Nabhiraj, P. Y.; Sivapragash, M. Graphene Nanosheet as Reinforcement Agent in Copper Matrix Composite by Using Powder Metallurgy Method. *Surfaces and Interfaces* **2017**, *6*, 190–196. <https://doi.org/10.1016/j.surfin.2017.01.010>.
- (321) Nayan, N.; Shukla, A. K.; Chandran, P.; Bakshi, S. R.; Murty, S. V. S. N.; Pant, B.; Venkitakrishnan, P. V. Processing and Characterization of Spark Plasma Sintered Copper/Carbon Nanotube Composites. *Mater. Sci. Eng. A* **2017**. <https://doi.org/10.1016/j.msea.2016.10.114>.
- (322) Hsieh, S.-H.; Ting, J.-M. Characterization and Photocatalytic Performance of Ternary Cu-Doped ZnO/Graphene Materials. *Appl. Surf. Sci.* **2018**, *427*, 465–475. <https://doi.org/10.1016/j.apsusc.2017.06.176>.
- (323) Nguyen, D. C. T.; Oh, W. C. Ternary Self-Assembly Method of Mesoporous Silica and Cu₂O Combined Graphene Composite by Nonionic Surfactant and Photocatalytic Degradation of Cationic-Anionic Dye Pollutants. *Sep. Purif. Technol.* **2018**, *190*, 77–89. <https://doi.org/10.1016/j.seppur.2017.08.054>.
- (324) Zhu, L.; Liu, Z.; Xia, P.; Li, H.; Xie, Y. Synthesis of Hierarchical ZnO&Graphene Composites with Enhanced Photocatalytic Activity. *Ceram. Int.* **2017**, *44* (1), 849–856. <https://doi.org/10.1016/j.ceramint.2017.10.009>.
- (325) Fu, X.; Jiang, T.; Zhao, Q.; Yin, H. A Facile Synthesis of Graphene-Metal (Pb, Zn, Cd,

- Mn) Sulfide Composites. *J. Mater. Sci.* **2012**, *47* (2), 1026–1032. <https://doi.org/10.1007/s10853-011-5890-0>.
- (326) Chen, C.; Cai, W.; Long, M.; Zhou, B.; Wu, Y.; Wu, D.; Feng, Y. Synthesis of Visible-Light Responsive Graphene Oxide/TiO₂ Composites with p/n Heterojunction. *ACS Nano* **2010**, *4* (11), 6425–6432. <https://doi.org/10.1021/nn102130m>.
- (327) Zhao, G.; Ren, X.; Gao, X.; Tan, X.; Li, J.; Chen, C.; Huang, Y.; Wang, X. Removal of Pb(II) Ions from Aqueous Solutions on Few-Layered Graphene Oxide Nanosheets. *Dalt. Trans.* **2011**, *40* (41), 10945. <https://doi.org/10.1039/c1dt11005e>.
- (328) Wang, Y.; Liang, S.; Chen, B.; Guo, F.; Yu, S.; Tang, Y. Synergistic Removal of Pb(II), Cd(II) and Humic Acid by Fe₃O₄@Mesoporous Silica-Graphene Oxide Composites. *PLoS One* **2013**, *8* (6). <https://doi.org/10.1371/journal.pone.0065634>.
- (329) Bao, Q.; Zhang, D.; Qi, P. Synthesis and Characterization of Silver Nanoparticle and Graphene Oxide Nanosheet Composites as a Bactericidal Agent for Water Disinfection. *J. Colloid Interface Sci.* **2011**, *360* (2), 463–470. <https://doi.org/10.1016/j.jcis.2011.05.009>.
- (330) Alexander, R.; Murthy, T. S. R. C.; Ravikanth, K. V.; Prakash, J.; Mahata, T.; Bakshi, S. R.; Krishnan, M.; Dasgupta, K. Effect of Graphene Nano-Platelet Reinforcement on the Mechanical Properties of Hot Pressed Boron Carbide Based Composite. *Ceram. Int.* **2018**. <https://doi.org/10.1016/j.ceramint.2018.02.225>.
- (331) Mu, X. N.; Zhang, H. M.; Cai, H. N.; Fan, Q. B.; Zhang, Z. H.; Wu, Y.; Fu, Z. J.; Yu, D. H. Microstructure Evolution and Superior Tensile Properties of Low Content Graphene Nanoplatelets Reinforced Pure Ti Matrix Composites. *Mater. Sci. Eng. A* **2017**, *687* (January), 164–174. <https://doi.org/10.1016/j.msea.2017.01.072>.
- (332) Nieto, A.; Lahiri, D.; Agarwal, A. Graphene NanoPlatelets Reinforced Tantalum Carbide Consolidated by Spark Plasma Sintering. *Mater. Sci. Eng. A* **2013**. <https://doi.org/10.1016/j.msea.2013.06.006>.
- (333) Rashad, M.; Pan, F. S.; Asif, M.; Ullah, A. Improved Mechanical Properties of Magnesium-Graphene Composites with Copper-Graphene Hybrids. *Mater. Sci. Technol. (United Kingdom)* **2015**, *31* (12), 1452–1461.

<https://doi.org/10.1179/1743284714Y.0000000726>.

- (334) Xiang, J.; Xie, L.; Meguid, S. A.; Pang, S.; Yi, J.; Zhang, Y.; Liang, R. An Atomic-Level Understanding of the Strengthening Mechanism of Aluminum Matrix Composites Reinforced by Aligned Carbon Nanotubes. *Comput. Mater. Sci.* **2017**, *128*, 359–372. <https://doi.org/10.1016/j.commatsci.2016.11.032>.
- (335) Sun, G.; Liang, R.; Lu, Z.; Zhang, J.; Li, Z. Mechanism of Cement/Carbon Nanotube Composites with Enhanced Mechanical Properties Achieved by Interfacial Strengthening. *Constr. Build. Mater.* **2016**, *115*, 87–92. <https://doi.org/10.1016/j.conbuildmat.2016.04.034>.
- (336) Tang, X. C.; Meng, L. Y.; Zhan, J. M.; Jian, W. R.; Li, W. H.; Yao, X. H.; Han, Y. L. Strengthening Effects of Encapsulating Graphene in SiC Particle-Reinforced Al-Matrix Composites. *Comput. Mater. Sci.* **2018**, *153*, 275–281. <https://doi.org/10.1016/j.commatsci.2018.07.003>.
- (337) Chen, X.; Tao, J.; Yi, J.; Liu, Y.; Li, C.; Bao, R. Strengthening Behavior of Carbon Nanotube-Graphene Hybrids in Copper Matrix Composites. *Mater. Sci. Eng. A* **2018**, *718*, 427–436. <https://doi.org/10.1016/j.msea.2018.02.006>.
- (338) Zhang, Z.; Chen, D. L. Contribution of Orowan Strengthening Effect in Particulate-Reinforced Metal Matrix Nanocomposites. *Mater. Sci. Eng. A* **2008**, *483–484* (1-2 C), 148–152. <https://doi.org/10.1016/j.msea.2006.10.184>.
- (339) Zhang, Y.; Zhuang, X.; Muthu, J.; Mabrouki, T.; Fontaine, M.; Gong, Y.; Rabczuk, T. Load Transfer of Graphene/Carbon Nanotube/Polyethylene Hybrid Nanocomposite by Molecular Dynamics Simulation. *Compos. Part B Eng.* **2014**, *63*, 27–33. <https://doi.org/10.1016/j.compositesb.2014.03.009>.
- (340) Anagnostopoulos, G.; Pappas, P. N.; Li, Z.; Kinloch, I. A.; Young, R. J.; Novoselov, K. S.; Lu, C. Y.; Pugno, N.; Parthenios, J.; Galiotis, C.; et al. Mechanical Stability of Flexible Graphene-Based Displays. *ACS Appl. Mater. Interfaces* **2016**, *8* (34), 22605–22614. <https://doi.org/10.1021/acsami.6b05227>.
- (341) Zare, Y.; Fasihi, M.; Rhee, K. Y. Efficiency of Stress Transfer between Polymer Matrix and Nanoplatelets in Clay/Polymer Nanocomposites. *Appl. Clay Sci.* **2017**, *143*, 265–272. <https://doi.org/10.1016/j.clay.2017.03.043>.

- (342) Fadavi Boostani, A.; Yazdani, S.; Taherzadeh Mousavian, R.; Tahamtan, S.; Azari Khosroshahi, R.; Wei, D.; Brabazon, D.; Xu, J. Z.; Zhang, X. M.; Jiang, Z. Y. Strengthening Mechanisms of Graphene Sheets in Aluminium Matrix Nanocomposites. *Mater. Des.* **2015**, *88*, 983–989. <https://doi.org/10.1016/j.matdes.2015.09.063>.
- (343) Lin, D.; Motlag, M.; Saei, M.; Jin, S.; Rahimi, R. M.; Bahr, D.; Cheng, G. J. Shock Engineering the Additive Manufactured Graphene-Metal Nanocomposite with High Density Nanotwins and Dislocations for Ultra-Stable Mechanical Properties. *Acta Mater.* **2018**, *150*, 360–372. <https://doi.org/10.1016/j.actamat.2018.03.013>.
- (344) Baig, Z.; Mamat, O.; Mustapha, M. Recent Progress on the Dispersion and the Strengthening Effect of Carbon Nanotubes and Graphene-Reinforced Metal Nanocomposites: A Review. *Critical Reviews in Solid State and Materials Sciences.* 2018, pp 1–46. <https://doi.org/10.1080/10408436.2016.1243089>.
- (345) Fleck, N. A.; Ashby, M. F.; Hutchinson, J. W. The Role of Geometrically Necessary Dislocations in Giving Material Strengthening. *Scripta Materialia.* 2003, pp 179–183. [https://doi.org/10.1016/S1359-6462\(02\)00338-X](https://doi.org/10.1016/S1359-6462(02)00338-X).
- (346) Dong, S.; Zhou, J.; Hui, D.; Wang, Y.; Zhang, S. Size Dependent Strengthening Mechanisms in Carbon Nanotube Reinforced Metal Matrix Composites. *Compos. Part A Appl. Sci. Manuf.* **2015**, *68*, 356–364. <https://doi.org/10.1016/j.compositesa.2014.10.018>.
- (347) Ang, K. K.; Ahmed, K. S. An Improved Shear-Lag Model for Carbon Nanotube Reinforced Polymer Composites. *Compos. Part B Eng.* **2013**, *50*, 7–14. <https://doi.org/10.1016/j.compositesb.2013.01.016>.
- (348) Kurita, H.; Estili, M.; Kwon, H.; Miyazaki, T.; Zhou, W.; Silvain, J. F.; Kawasaki, A. Load-Bearing Contribution of Multi-Walled Carbon Nanotubes on Tensile Response of Aluminum. *Compos. Part A Appl. Sci. Manuf.* **2015**, *68*, 133–139. <https://doi.org/10.1016/j.compositesa.2014.09.014>.
- (349) Hansen, N. Hall-Petch Relation and Boundary Strengthening. *Scr. Mater.* **2004**, *51* (8 SPEC. ISS.), 801–806. <https://doi.org/10.1016/j.scriptamat.2004.06.002>.
- (350) Li, C. L.; Mei, Q. S.; Li, J. Y.; Chen, F.; Ma, Y.; Mei, X. M. Hall-Petch Relations and

- Strengthening of Al-ZnO Composites in View of Grain Size Relative to Interparticle Spacing. *Scr. Mater.* **2018**, *153*, 27–30. <https://doi.org/10.1016/j.scriptamat.2018.04.042>.
- (351) Baig, Z.; Mamat, O.; Mustapha, M. Recent Progress on the Dispersion and the Strengthening Effect of Carbon Nanotubes and Graphene-Reinforced Metal Nanocomposites: A Review. *Crit. Rev. Solid State Mater. Sci.* **2016**, *8436* (December), 1–46. <https://doi.org/10.1080/10408436.2016.1243089>.
- (352) Smallman, R. E.; Ngan, A. H. W. *Physical Metallurgy and Advanced Materials*; 2007. <https://doi.org/10.1016/B978-0-7506-6906-1.X5000-8>.
- (353) Arsenault, R. J.; Shi, N. Dislocation Generation Due to Differences between the Coefficients of Thermal Expansion. *Mater. Sci. Eng.* **1986**, *81* (C), 175–187. [https://doi.org/10.1016/0025-5416\(86\)90261-2](https://doi.org/10.1016/0025-5416(86)90261-2).
- (354) Rashad, M.; Pan, F.; Tang, A.; Asif, M. Effect of Graphene Nanoplatelets Addition on Mechanical Properties of Pure Aluminum Using a Semi-Powder Method. *Prog. Nat. Sci. Mater. Int.* **2014**, *24* (2), 101–108. <https://doi.org/10.1016/j.pnsc.2014.03.012>.
- (355) Nardone, V. C.; Prewo, K. M. On the Strength of Discontinuous Silicon Carbide Reinforced Aluminum Composites. *Scr. Metall.* **1986**, *20* (1), 43–48. [https://doi.org/10.1016/0036-9748\(86\)90210-3](https://doi.org/10.1016/0036-9748(86)90210-3).
- (356) Dujardin, E.; Ebbesen, T. W.; Hiura, H.; Tanigaki, K. Capillarity and Wetting of Carbon Nanotubes. *Science (80-.)*. **1994**, *265* (5180), 1850–1852. <https://doi.org/10.1126/science.265.5180.1850>.
- (357) George, R.; Kashyap, K. T.; Rahul, R.; Yamdagni, S. Strengthening in Carbon Nanotube/Aluminium (CNT/Al) Composites. *Scr. Mater.* **2005**, *53* (10), 1159–1163. <https://doi.org/10.1016/j.scriptamat.2005.07.022>.
- (358) Hull, D.; Bacon, D. J. *Introduction to Dislocations*; 2011. <https://doi.org/10.1016/C2009-0-64358-0>.
- (359) Orowan, E. Zur Kristallplastizität. III - Über Den Mechanismus Des Gleitvorganges. *Zeitschrift für Phys.* **1934**, *89* (9–10), 634–659.

<https://doi.org/10.1007/BF01341480>.

- (360) Shaina, P. R.; George, L.; Yadav, V.; Jaiswal, M. Estimating the Thermal Expansion Coefficient of Graphene: The Role of Graphene-Substrate Interactions. *J. Phys. Condens. Matter* **2016**, *28* (8). <https://doi.org/10.1088/0953-8984/28/8/085301>.
- (361) Wilson, A. J. C. The Thermal Expansion of Aluminium from 0° to 650°C. *Proc. Phys. Soc.* **1941**, *53* (3), 235–244. <https://doi.org/10.1088/0959-5309/53/3/305>.
- (362) Zhang, L.; Chen, Z.; Zheng, S.; Qin, S.; Wang, J.; Chen, C.; Liu, D.; Wang, L.; Yang, G.; Su, Y.; et al. Shape-Tailorable High-Energy Asymmetric Micro-Supercapacitors Based on Plasma Reduced and Nitrogen-Doped Graphene Oxide and MoO₂ Nanoparticles. *J. Mater. Chem. A* **2019**. <https://doi.org/10.1039/c9ta03620b>.
- (363) Fan, Y.; Yang, Z.; Hua, W.; Liu, D.; Tao, T.; Rahman, M. M.; Lei, W.; Huang, S.; Chen, Y. Functionalized Boron Nitride Nanosheets/Graphene Interlayer for Fast and Long-Life Lithium–Sulfur Batteries. *Adv. Energy Mater.* **2017**. <https://doi.org/10.1002/aenm.201602380>.
- (364) Papageorgiou, D. G.; Kinloch, I. A.; Young, R. J. Mechanical Properties of Graphene and Graphene-Based Nanocomposites. *Progress in Materials Science*. 2017, pp 75–127. <https://doi.org/10.1016/j.pmatsci.2017.07.004>.
- (365) Yang, J.; Kumar, S.; Kim, M.; Hong, H.; Akhtar, I.; Rehman, M. A.; Lee, N.; Park, J. Y.; Kim, K. B.; Seo, Y. Studies on Directly Grown Few Layer Graphene Processed Using Tape-Peeling Method. *Carbon N. Y.* **2020**, *158*, 749–755. <https://doi.org/10.1016/j.carbon.2019.11.049>.
- (366) Liu, D.; Lei, W.; Portehault, D.; Qin, S.; Chen, Y. High N-Content Holey Few-Layered Graphene Electrocatalysts: Scalable Solvent-Less Production. *J. Mater. Chem. A* **2015**, *3* (4), 1682–1687. <https://doi.org/10.1039/c4ta05008h>.
- (367) Zhang, J.; Lei, W.; Liu, D.; Wang, X. Synergistic Influence from the Hybridization of Boron Nitride and Graphene Oxide Nanosheets on the Thermal Conductivity and Mechanical Properties of Polymer Nanocomposites. *Compos. Sci. Technol.* **2017**. <https://doi.org/10.1016/j.compscitech.2017.08.033>.

- (368) Burgio, N.; Iasonna, A.; Magini, M.; Martelli, S.; Padella, F. Mechanical Alloying of the Fe-Zr System. Correlation between Input Energy and End Products. *Nuovo Cim. D* **1991**, *13* (4), 459–476. <https://doi.org/10.1007/BF02452130>.
- (369) Kho, H. X.; Bae, S.; Bae, S.; Kim, B.-W.; Kim, J. S. Planetary Ball Mill Process in Aspect of Milling Energy. *J. Korean Powder Metall. Inst.* **2014**, *21* (2), 155–164. <https://doi.org/10.4150/kpmi.2014.21.2.155>.
- (370) Abdellaoui, M.; Gaffet, E. Mechanical Alloying in a Planetary Ball Mill: Kinematic Description. *J. Phys. IV JP* **1994**, *4* (3), 291–296. <https://doi.org/10.1051/jp4:1994340>.
- (371) RETSCH. Planetary Ball Mill PM 100 - RETSCH - highest fineness <https://www.retsch.com/products/milling/ball-mills/planetary-ball-mill-pm-100/function-features/> (accessed Mar 5, 2020).
- (372) Zhao, Z.; Bai, P.; Du, W.; Liu, B.; Pan, D.; Das, R.; Liu, C.; Guo, Z. An Overview of Graphene and Its Derivatives Reinforced Metal Matrix Composites: Preparation, Properties and Applications. *Carbon*. **2020**, pp 302–326. <https://doi.org/10.1016/j.carbon.2020.08.040>.
- (373) Ghodrati, H.; Ghomashchi, R. Effect of Graphene Dispersion and Interfacial Bonding on the Mechanical Properties of Metal Matrix Composites: An Overview. *FlatChem*. **2019**. <https://doi.org/10.1016/j.flatc.2019.100113>.
- (374) Ranjan, R.; Bajpai, V. Graphene-Based Metal Matrix Nanocomposites: Recent Development and Challenges. *J. Compos. Mater.* **2021**, *55* (17), 2369–2413. <https://doi.org/10.1177/0021998320988566>.
- (375) Alfonso, I.; Navarro, O.; Vargas, J.; Beltrán, A.; Aguilar, C.; González, G.; Figueroa, I. A. FEA Evaluation of the Al₄C₃ Formation Effect on the Young's Modulus of Carbon Nanotube Reinforced Aluminum Matrix Composites. *Compos. Struct.* **2015**, *127*, 420–425. <https://doi.org/10.1016/j.compstruct.2015.03.032>.
- (376) Arik, H.; Aydin, M.; Kurt, A.; Turker, M. Weldability of Al₄C₃-Al Composites via Diffusion Welding Technique. *Mater. Des.* **2005**, *26* (6), 555–560. <https://doi.org/10.1016/j.matdes.2004.07.017>.

- (377) Wang, H.; Xie, M.; Thia, L.; Fisher, A.; Wang, X. Strategies on the Design of Nitrogen-Doped Graphene. *J. Phys. Chem. Lett.* **2014**, *5* (1), 119–125. <https://doi.org/10.1021/jz402416a>.
- (378) Sibul, R.; Kibena-Pöldsepp, E.; Ratso, S.; Kook, M.; Käärrik, M.; Merisalu, M.; Paiste, P.; Leis, J.; Sammelselg, V.; Tammeveski, K. Nitrogen-Doped Carbon-Based Electrocatalysts Synthesised by Ball-Milling. *Electrochem. commun.* **2018**, *93*, 39–43. <https://doi.org/10.1016/j.elecom.2018.05.027>.
- (379) Liu, C.; Liu, X.; Tan, J.; Wang, Q.; Wen, H.; Zhang, C. Nitrogen-Doped Graphene by All-Solid-State Ball-Milling Graphite with Urea as a High-Power Lithium Ion Battery Anode. *J. Power Sources* **2017**, *342*, 157–164. <https://doi.org/10.1016/j.jpowsour.2016.11.110>.
- (380) Chen, Z.; Hou, L.; Cao, Y.; Tang, Y.; Li, Y. Gram-Scale Production of B, N Co-Doped Graphene-like Carbon for High Performance Supercapacitor Electrodes. *Appl. Surf. Sci.* **2018**, *435*, 937–944. <https://doi.org/10.1016/j.apsusc.2017.11.159>.
- (381) Liu, Z.; Li, D.; Wei, S.; Wang, W.; Tian, F.; Bao, K.; Duan, D.; Yu, H.; Liu, B.; Cui, T. Bonding Properties of Aluminum Nitride at High Pressure. *Inorg. Chem.* **2017**, *56* (13), 7494–7500. <https://doi.org/10.1021/acs.inorgchem.7b00980>.
- (382) Taylor, K. M.; Lenie, C. Some Properties of Aluminum Nitride. *J. Electrochem. Soc.* **1960**, *107*(4), 308. <https://doi.org/10.1149/1.2427686>.
- (383) Hou, Q.; Mutharasan, R.; Koczak, M. Feasibility of Aluminium Nitride Formation in Aluminum Alloys. *Mater. Sci. Eng. A* **1995**, *195* (C), 121–129. [https://doi.org/10.1016/0921-5093\(94\)06511-X](https://doi.org/10.1016/0921-5093(94)06511-X).
- (384) Abu-Oqail, A.; Wagih, A.; Fathy, A.; Elkady, O.; Kabeel, A. M. Effect of High Energy Ball Milling on Strengthening of Cu-ZrO₂ Nanocomposites. *Ceram. Int.* **2019**, *45*(5), 5866–5875. <https://doi.org/10.1016/j.ceramint.2018.12.053>.
- (385) Zhang, L.; Huang, Z.; Liu, Y.; Shen, Y.; Li, K.; Cao, Z.; Ren, Z.; Jian, Y. Effects of Mechanical Ball Milling Time on the Microstructure and Mechanical Properties of Mo₂NiB₂-Ni Cermets. *Materials (Basel)*. **2019**, *12* (12). <https://doi.org/10.3390/ma12121926>.

- (386) Dai, G. P.; Zhang, J. M.; Deng, S. Synthesis and Characterization of Nitrogen-Doped Monolayer and Multilayer Graphene on TEM Copper Grids. *Chem. Phys. Lett.* **2011**, *516* (4–6), 212–215. <https://doi.org/10.1016/j.cplett.2011.09.081>.
- (387) Zhang, L.; Huang, Z.; Liu, Y.; Shen, Y.; Li, K.; Cao, Z.; Ren, Z.; Jian, Y. Effects of Mechanical Ball Milling Time on the Microstructure and Mechanical Properties of Mo₂NiB₂-Ni Cermets. *Materials (Basel)*. **2019**. <https://doi.org/10.3390/ma12121926>.
- (388) Al-Sherbini, A. S.; Bakr, M.; Ghoneim, I.; Saad, M. Exfoliation of Graphene Sheets via High Energy Wet Milling of Graphite in 2-Ethylhexanol and Kerosene. *J. Adv. Res.* **2017**, *8* (3), 209–215. <https://doi.org/10.1016/j.jare.2017.01.004>.
- (389) Ouyang, W.; Zeng, D.; Yu, X.; Xie, F.; Zhang, W.; Chen, J.; Yan, J.; Xie, F.; Wang, L.; Meng, H.; et al. Exploring the Active Sites of Nitrogen-Doped Graphene as Catalysts for the Oxygen Reduction Reaction. *Int. J. Hydrogen Energy* **2014**, *39* (28), 15996–16005. <https://doi.org/10.1016/j.ijhydene.2014.01.045>.
- (390) Autthawong, T.; Chimupala, Y.; Haruta, M.; Kurata, H.; Kiyomura, T.; Yu, A. S.; Chairuang Sri, T.; Sarakonsri, T. Ultrafast-Charging and Long Cycle-Life Anode Materials of TiO₂-Bronze/Nitrogen-Doped Graphene Nanocomposites for High-Performance Lithium-Ion Batteries. *RSC Adv.* **2020**, *10* (71), 43811–43824. <https://doi.org/10.1039/d0ra07733j>.
- (391) Xing, T.; Li, L. H.; Hou, L.; Hu, X.; Zhou, S.; Peter, R.; Petravic, M.; Chen, Y. Disorder in Ball-Milled Graphite Revealed by Raman Spectroscopy. *Carbon N. Y.* **2013**, *57*, 515–519. <https://doi.org/10.1016/j.carbon.2013.02.029>.
- (392) Ma, X.; Zhao, Y. F.; Tian, W. J.; Qian, Z.; Chen, H. W.; Wu, Y. Y.; Liu, X. F. A Novel Al Matrix Composite Reinforced by Nano-AlN p Network. *Sci. Rep.* **2016**. <https://doi.org/10.1038/srep34919>.
- (393) Mohanavel, V.; Rajan, K.; Ravichandran, M. Synthesis, Characterization and Properties of Stir Cast AA6351-Aluminium Nitride (AlN) Composites. *J. Mater. Res.* **2016**. <https://doi.org/10.1557/jmr.2016.460>.
- (394) Cullis, C. F.; Yates, J. G. Reaction of Carbon with Nitrogen. *Trans. Faraday Soc.* **1964**, *60*, 141–148. <https://doi.org/10.1039/tf9646000141>.

- (395) Samal, P.; Vundavilli, P. R.; Meher, A.; Mahapatra, M. M. Recent Progress in Aluminum Metal Matrix Composites: A Review on Processing, Mechanical and Wear Properties. *Journal of Manufacturing Processes*. 2020, pp 131–152. <https://doi.org/10.1016/j.jmapro.2020.09.010>.
- (396) Wang, B.; Ruan, T.; Chen, Y.; Jin, F.; Peng, L.; Zhou, Y.; Wang, D.; Dou, S. Graphene-Based Composites for Electrochemical Energy Storage. *Energy Storage Materials*. 2020, pp 22–51. <https://doi.org/10.1016/j.ensm.2019.08.004>.
- (397) Tanisell, S.; Md Arshad, M. K.; Gopinath, S. C. B. Current State of Green Reduction Strategies: Solution-Processed Reduced Graphene Oxide for Healthcare Biodetection. *Materials Science and Engineering C*. 2019, pp 904–914. <https://doi.org/10.1016/j.msec.2018.11.062>.
- (398) Mahmood, F.; Sun, Y.; Wan, C. Biomass-Derived Porous Graphene for Electrochemical Sensing of Dopamine. *RSC Adv.* **2021**, *11* (25), 15410–15415. <https://doi.org/10.1039/d1ra00735a>.
- (399) Wei, Y.; Zhang, R.; Zhang, Y.; Zheng, X.; Cai, W.; Ge, Q.; Novoselov, K. S.; Xu, Z.; Jiang, T.; Deng, C.; et al. Thickness-Independent Energy Dissipation in Graphene Electronics. *ACS Appl. Mater. Interfaces* **2020**, *12* (15), 17706–17712. <https://doi.org/10.1021/acsami.0c00113>.
- (400) Le Ferrand, H.; Bolisetty, S.; Demirörs, A. F.; Libanori, R.; Studart, A. R.; Mezzenga, R. Magnetic Assembly of Transparent and Conducting Graphene-Based Functional Composites. *Nat. Commun.* **2016**, *7*. <https://doi.org/10.1038/ncomms12078>.
- (401) Clancy, A. J.; Au, H.; Rubio, N.; Coulter, G. O.; Shaffer, M. S. P. Understanding and Controlling the Covalent Functionalisation of Graphene. *Dalt. Trans.* **2020**, *49* (30), 10308–10318. <https://doi.org/10.1039/d0dt01589j>.
- (402) Fan, Q.; Gottfried, J. M.; Zhu, J. Surface-Catalyzed C-C Covalent Coupling Strategies toward the Synthesis of Low-Dimensional Carbon-Based Nanostructures. *Acc. Chem. Res.* **2015**, *48* (8), 2484–2494. <https://doi.org/10.1021/acs.accounts.5b00168>.
- (403) Nobile, M. R.; Raimondo, M.; Naddeo, C.; Guadagno, L. Rheological and Morphological Properties of Non-Covalently Functionalized Graphene-Based

- Structural Epoxy Resins with Intrinsic Electrical Conductivity and Thermal Stability. *Nanomaterials* **2020**, *10* (7), 1–23. <https://doi.org/10.3390/nano10071310>.
- (404) Hoa, H. T. M.; Lee, K. J.; Pham, H. P.; Doan, T. A.; Nguyen, H. H.; Nguyen, T. Q.; Tran, Q. T.; Cuong, T. V. Ammonia Gas Sensing Behavior of Hybridization between Reduced Graphene Oxide and Gold Nanoparticles. *J. Nanomater.* **2020**, *2020*. <https://doi.org/10.1155/2020/7680508>.
- (405) Wang, Z.; Xiao, J.; Li, X. Effects of Heteroatom (Boron or Nitrogen) Substitutional Doping on the Electronic Properties of Graphene Nanoribbons. *Solid State Commun.* **2012**, *152* (2), 64–67. <https://doi.org/10.1016/j.ssc.2011.11.002>.
- (406) Quan Tian, W.; Vincent Liu, L.; Kun Chen, Y.; Wang, Y. A. Electronic Properties and Reactivities of Perfect, Defected, and Doped Single-Walled Carbon Nanotubes. In *Challenges and Advances in Computational Chemistry and Physics*; 2010; Vol. 9, pp 421–471. https://doi.org/10.1007/978-1-4020-9785-0_16.
- (407) Naseer, A.; Ahmad, F.; Aslam, M.; Guan, B. H.; Harun, W. S. W.; Muhamad, N.; Raza, M. R.; German, R. M. A Review of Processing Techniques for Graphene-Reinforced Metal Matrix Composites. *Materials and Manufacturing Processes*. 2019, pp 957–985. <https://doi.org/10.1080/10426914.2019.1615080>.
- (408) Mombrú, D.; Romero, M.; Faccio, R.; Mombrú, Á. W. Electronic and Optical Properties of Sulfur and Nitrogen Doped Graphene Quantum Dots: A Theoretical Study. *Phys. E Low-Dimensional Syst. Nanostructures* **2019**, *113*, 130–136. <https://doi.org/10.1016/j.physe.2019.05.004>.
- (409) Lee, J. H.; Kwon, S. H.; Kwon, S.; Cho, M.; Kim, K. H.; Han, T. H.; Lee, S. G. Tunable Electronic Properties of Nitrogen and Sulfur Doped Graphene: Density Functional Theory Approach. *Nanomaterials* **2019**, *9* (2). <https://doi.org/10.3390/nano9020268>.
- (410) Suthar, J.; Patel, K. M. Processing Issues, Machining, and Applications of Aluminum Metal Matrix Composites. *Materials and Manufacturing Processes*. 2018, pp 499–527. <https://doi.org/10.1080/10426914.2017.1401713>.
- (411) Pérez-Bustamante, R.; Bolaños-Morales, D.; Bonilla-Martínez, J.; Estrada-Guel, I.;

- Martínez-Sánchez, R. Microstructural and Hardness Behavior of Graphene-Nanoplatelets/Aluminum Composites Synthesized by Mechanical Alloying. *J. Alloys Compd.* **2015**, *615* (S1), S578–S582. <https://doi.org/10.1016/j.jallcom.2014.01.225>.
- (412) Tian, W. ming; Li, S. mei; Wang, B.; Chen, X.; Liu, J. hua; Yu, M. Graphene-Reinforced Aluminum Matrix Composites Prepared by Spark Plasma Sintering. *Int. J. Miner. Metall. Mater.* **2016**, *23* (6), 723–729. <https://doi.org/10.1007/s12613-016-1286-0>.
- (413) Xie, Z.; Chen, M.; Peera, S. G.; Liu, C.; Yang, H.; Qi, X.; Kumar, U. P.; Liang, T. Theoretical Study on a Nitrogen-Doped Graphene Nanoribbon with Edge Defects as the Electrocatalyst for Oxygen Reduction Reaction. *ACS Omega* **2020**, *5* (10), 5142–5149. <https://doi.org/10.1021/acsomega.9b04146>.
- (414) Zhang, X.; Wang, S. Interfacial Strengthening of Graphene/Aluminum Composites through Point Defects: A First-Principles Study. *Nanomaterials* **2021**, *11* (3), 1–16. <https://doi.org/10.3390/nano11030738>.
- (415) Bumbrah, G. S.; Sharma, R. M. Raman Spectroscopy – Basic Principle, Instrumentation and Selected Applications for the Characterization of Drugs of Abuse. *Egyptian Journal of Forensic Sciences.* 2016, pp 209–215. <https://doi.org/10.1016/j.ejfs.2015.06.001>.
- (416) Ambrosi, A.; Chua, C. K.; Bonanni, A.; Pumera, M. Electrochemistry of Graphene and Related Materials. *Chemical Reviews.* 2014, pp 7150–7188. <https://doi.org/10.1021/cr500023c>.
- (417) Li, Z.; Fu, X.; Guo, Q.; Zhao, L.; Fan, G.; Li, Z.; Xiong, D. B.; Su, Y.; Zhang, D. Graphene Quality Dominated Interface Deformation Behavior of Graphene-Metal Composite: The Defective Is Better. *Int. J. Plast.* **2018**, *111*, 253–265. <https://doi.org/10.1016/j.ijplas.2018.07.020>.
- (418) Zhang, C.; Lu, C.; Michal, G.; Li, J.; Wang, R. Strong Strain Hardening in Graphene/Nanotwinned Metal Composites Revealed by Molecular Dynamics Simulations. *Int. J. Mech. Sci.* **2021**, *201*. <https://doi.org/10.1016/j.ijmecsci.2021.106460>.

- (419) Jiang, Y.; Xu, R.; Tan, Z.; Ji, G.; Fan, G.; Li, Z.; Xiong, D. B.; Guo, Q.; Li, Z.; Zhang, D. Interface-Induced Strain Hardening of Graphene Nanosheet/Aluminum Composites. *Carbon N. Y.* **2019**, *146*, 17–27. <https://doi.org/10.1016/j.carbon.2019.01.094>.
- (420) Du, X.; Du, W.; Wang, Z.; Liu, K.; Li, S. Defects in Graphene Nanoplatelets and Their Interface Behavior to Reinforce Magnesium Alloys. *Appl. Surf. Sci.* **2019**, *484*, 414–423. <https://doi.org/10.1016/j.apsusc.2019.04.111>.
- (421) Vishwakarma, V.; Keralavarma, S. M. Micromechanical Modeling and Simulation of the Loading Path Dependence of Ductile Failure by Void Growth to Coalescence. *Int. J. Solids Struct.* **2019**, *166*, 135–153. <https://doi.org/10.1016/j.ijsolstr.2019.02.015>.
- (422) Naragani, D. P.; Park, J. S.; Kenesei, P.; Sangid, M. D. Void Coalescence and Ductile Failure in IN718 Investigated via High-Energy Synchrotron X-Ray Tomography and Diffraction. *J. Mech. Phys. Solids* **2020**, *145*. <https://doi.org/10.1016/j.jmps.2020.104155>.
- (423) Ha, J.; Baral, M.; Korkolis, Y. P. Ductile Fracture of an Aluminum Sheet under Proportional Loading. *J. Mech. Phys. Solids* **2019**, *132*. <https://doi.org/10.1016/j.jmps.2019.103685>.
- (424) Jahromi, S. A. J. Transition in Fracture Micromechanism of SS70 Spray Cast Aluminum Alloy. *Mater. Manuf. Process.* **2003**, *18* (5), 803–810. <https://doi.org/10.1081/AMP-120024976>.
- (425) Pineau, A.; Benzerga, A. A.; Pardoën, T. Failure of Metals I: Brittle and Ductile Fracture. *Acta Mater.* **2016**, *107*, 424–483. <https://doi.org/10.1016/j.actamat.2015.12.034>.
- (426) Herrera, A.; Martínez-Madrid, M.; Horta, J.; Castaño, V. M. Effect of Solidification Times on Crack Opening Displacement of Aluminium Alloy Castings. *Mater. Manuf. Process.* **2003**, *18* (6), 979–992. <https://doi.org/10.1081/AMP-120025083>.

